Spatial Impact Trends on Debris Flow Fans in Southwestern British Columbia

by

Sophia Zubrycky

B.A.Sc. Geological Engineering, Queen's University, 2013

A THESIS SUBMITTED IN PARTIAL FULFILLMENT

OF THE REQUIREMENTS FOR THE DEGREE OF

Master of Applied Science

in

THE FACULTY OF GRADUATE AND POSTDOCTORAL STUDIES

(Geological Engineering)

The University of British Columbia

(Vancouver)

June 2020

The following individuals certify that they have read, and recommend to the Faculty of Graduate and Postdoctoral Studies for acceptance, the thesis entitled:

Spatial Impact Trends on Debris Flow Fans in Southwestern British Columbia

submitted by **Sophia Zubrycky** in partial fulfillment of the requirements for the degree of **Master of Applied Science** in **Geological Engineering**.

Examining Committee:

Dr. Scott McDougall, Assistant Professor, Geological Engineering, UBC
Supervisor

Dr. Erik Eberhardt, Professor, Geological Engineering, UBC
Supervisory Committee Member

Dr. Brett Eaton, Professor, Geography, UBC
Supervisory Committee Member

Dr. Matthias Jakob, Geoscientist, BGC Engineering Inc.
Supervisory Committee Member

Dr. Mitch D'Arcy, Assistant Professor, Department of Earth, Ocean and Atmospheric Sciences, UBC
Additional Examiner

Abstract

Forecasting the spatial impact of debris flows is challenging due to complex runout behaviour, such as variable mobility and channel avulsions. Practitioners often base the probability of runout exceedance on a fan, or define avulsion scenarios, on judgement. To support decision making, spatial impact trends were studied at thirty active debris flow fans in southwestern British Columbia (SWBC), Canada. 176 debris flow impact areas covering an average observation period of 74 years were mapped using orthorectified historical airphotos, satellite imagery, topographic basemaps, lidar, and field observations. A graphical plotting method was developed that converts geospatial mapping to spatial impact heatmaps normalized by the fan boundary, allowing for comparison of runout trends across fans in the dataset. Probability of spatial impact was analyzed in two components: runout down-fan (i.e., how far debris flows tend to travel past the apex toward the fan toe) and runout cross-fan (i.e., how far debris flows tend to deviate from the previous flow path). For fans in SWBC, there is a characteristic decay in spatial impact probability from the fan apex and the previous flow path, represented by a normal and log-normal distribution for normalized runout in the down-fan and cross-fan components, respectively. Differences in spatial impact trends can be explained, in part, by event volume, Melton ratio, fan truncation, and fan activity, however not by fan morphometrics, such as the slope or the point at which channelization is lost. A tool was created that transposes the empirical runout distributions onto a fan to assist in risk-based decision making. Future work may involve fitting functions to the spatial impact data for a more robust and adaptable forecasting tool.

Lay Summary

Debris flows are extremely rapid landslides comprised of debris and water that travel down steep mountain creeks. Estimating the chance of being impacted by a debris flow is important to understanding the risk to the public and infrastructure. This work is challenging because debris flows can travel long distances or suddenly change directions. To help with our understanding of likely future debris flow impacts, a historical record of debris flow impacts dating back to 1922 was mapped at 30 sites in southwestern British Columbia. By looking at these data in new ways, we can identify areas most susceptible to impacts, and what factors allow prediction of debris flow travel distance and flow paths. Debris flow volume and sediment mixture are key variables in explaining those two characteristics.

Preface

Some of the data presented in Figure 2.4 and Table 3.6 in Chapter 2 were published in conference paper Zubrycky, S., Mitchell, A., Aaron, J., and McDougall, S. (2019) Preliminary calibration of a numerical runout model for debris flows in southwestern British Columbia, in Debris-Flow Hazards Mitigation: Mechanics, Prediction, and Assessment (pp. 911–918), Golden, CO. Numerical model calibration was performed by A. Mitchell and I using methods and code developed by J. Aaron.

The database in Chapter 3 Section 3.1 was presented as part of a conference poster/extended abstract Zubrycky, S., Bonneau, D., McDougall, S., Jakob, M., and Hutchinson, J. (2018) Empirical prediction of debris flow avulsion and runout exceedance probability using a debris flow inventory from Southwestern British Columbia, poster session presented at the meeting of the 7th Canadian Geohazards Conference, Canmore, Alberta. The preliminary debris flow event database was compiled by D. Bonneau, which I subsequently edited and expanded.

A version of the material in Chapter 4 has been accepted to the XIII International Symposium on Landslides, with co-authors A. Mitchell and S. McDougall. I am the lead author of this work, responsible for all areas of major concept formation, data collection, analysis, and manuscript composition. A. Mitchell operated the lidar drone, processed the lidar data, helped with field work, and provided review. S. McDougall was the supervisory author, involved throughout the project in concept formation and manuscript edits.

Many of the airphotos in Table 3.2 were scanned with help from S. Ghadirianniari and K. Matson.

Figure 2.2 appears in this thesis with permission from John Wiley and Sons, and Figure 4.17 with permission from Elsevier. Debris flow lobe mapping presented in Figure 4.13 was adapted from de Haas et al. (2018a) with permission from the author.

Table of Contents

List of Tables

List of Figures

List of Supplementary Material

GIS data (Appendix B)

MATLAB code (Appendix C)

Supplementary material can be found on cIRcle (UBC digital repository).

Refer to appendices for description of data.

List of Acronyms

ALS Airborne laser scanning
BC British Columbia
BGC BGC Engineering Inc.
DEM Digital elevation model
ecdf Empirical cumulative distribution function
F-M Frequency-magnitude
GCP Ground control point
GIC Geographic Information Centre
GIS Geographic information system
GPS Global positioning system
KS Kolmogorov-Smirnov
Lidar Light detection and ranging
NDVI Normalized difference vegetation index
pdf Probability density function
PCIC Pacific Climate Impacts Consortium
QRA Qualitative risk assessment
RPAS Remotely piloted aerial system
SfM Structure from Motion
SLRD Squamish Lillooet Regional District
SWBC Southwestern British Columbia
TRIM Terrain Resource Information Management
UBC University of British Columbia
UTM Universal Transverse Mercator

Acknowledgments

I am very grateful and humbled to have been mentored by my supervisor, Scott McDougall. Without his wisdom, practical guidance, and unwavering support, this thesis would not have been possible. Scott follows in the footsteps (and fills the shoes of) the late Oldrich Hungr, who I would also like to acknowledge as a guiding force throughout my research. Thank you to my thesis and examining committee, Brett Eaton, Erik Eberhardt, and Matthias Jakob, for your stimulating discussions and thoughtful review.

To my office mates and colleagues, Jordan Aaron, Afshin Amini, Vincent An, Ally Brown, Vivian Cristina Dias, Sahar Ghadirianniari, Negar Ghahramani, Anya Leenman, Andrew Mitchell, Masoud Rahjoo, Brie Shaw, Lauren Vincent, and Siobhan (Whadcoat) Velazquez; thank you for your input, friendship, and keeping me sane. Special shout out to Andrew, who has been a brilliant collaborator, excellent field partner, and like a second supervisor to me.

I am also indebted to my field partners, and grateful for their patience and resilience during field work: David Bonneau, Bea Collier-Pandya, Vivian Cristina Dias, Carie-Ann Lau, Marin McDougall, Scott McDougall, Andrew Mitchell, Joshua Nicholas, Natalie Pedersen, José Pullarello, Stephanie Tarnai, and Bill and Siobhan Velazquez. I would also like to acknowledge Sahar Ghadirianniari and Kelsey Matson for their help scanning airphotos.

I am very fortunate to have had support from BGC, and mentorship from the people that make up BGC, including Bea Collier-Pandya, Kris Holm, Matthias Jakob, Carie-Ann Lau, Phil LeSueur, Emily Moase, and Alex Strouth. Special thank you to Alex for having my back and helping me see the bigger picture.

A lot of the data used in this thesis came from people and organizations who went out of their

way to help me. I would like to express my gratitude to David Bonneau and Jean Hutchinson from Queen's University, John Clague and Gioachino Roberti from Simon Fraser University, Trevor Evans from Canadian National Railway, Gord Hunter from the BC Ministry of Transportation and Infrastructure, Brian Menounos from the University of Northern British Columbia, Mike Tinholt from BC Hydro, Ryan Wainwright from the Squamish Lillooet Regional District, and John Whittall from BGC, for their generosity in sharing data. Lastly, I would like to acknowledge Erin and Rob Elliott, Sharon Kamenka, and the Ts'kw'aylaxw First Nation for land access permissions.

Finally, thank you to my family, friends, partners, and teammates; you have supported me in more ways than I can express.

Funding for this research was provided by the Natural Sciences and Engineering Research Council of Canada (NSERC) and scholarships given by The Department of Earth, Ocean and Atmospheric Sciences.

Chapter 1

Introduction

In this chapter, the overall context for the thesis is established by introducing the research problem, stating research objectives and hypotheses, and describing the overall research approach. These sections are followed by a general description of the study area.

1.1 Problem Statement

In mountainous regions, many communities and infrastructure projects are built on fans at the mouths of steep creeks, which may be subject to episodic debris flows. Forecasting the spatial impact of debris flows is an important part of hazard mapping, risk assessment, and mitigation design, but is challenging due to complex physical processes. Debris flow mobility, defined as the ability to travel long distances and/or inundate large areas, depends largely on volume (e.g., Corominas, 1996; Griswold & Iverson, 2008), but also flow composition and topographic controls to a certain extent. Rheological parameters used in semi-empirical numerical models such as Dan3D (McDougall & Hungr, 2004) or RAMMS (Christen et al., 2010) can be adjusted to simulate various flow mobility for a given volume, however, there is presently little guidance available to practitioners to do so (McDougall, 2017). These models are typically calibrated through back-analysis, requiring pre- and post-event data and objective calibration methods (e.g., Aaron et al., 2019). Empirical-statistical methods (e.g., Corominas, 1996; Griswold & Iverson, 2008; Rickenmann, 1999) provide a simple yet practical alternative, but must also be calibrated to local datasets. Additionally, empirical

relationships are prone to considerable scatter, although this variability can be used to establish limits of confidence in runout estimates for probabilistic assessments (McDougall, 2017).

Debris flows are prone to avulsion, defined as a sporadic deviation of flow from an established flow path. Avulsions are formative processes on debris flow fans, shifting the active channel and locus of deposition (and hazard) through space and time. Until recently, much of our understanding of avulsion processes is from observations of fluvial systems (de Haas et al., 2018a; Densmore et al., 2019). There is currently little guidance for predicting where and when the next avulsion might occur. Although three-dimensional numerical models can help indicate potential avulsion associated with superelevation and runup around channel bends, they currently lack the capability to simulate avulsions caused by sporadic channel blocking by coarse lobes or woody debris (McDougall, 2017). Estimating the probability of avulsion from direct observation may not be feasible due to long return periods for debris flows and even longer return periods for avulsion (de Haas et al., 2018a). Reconstructing fan history requires a significant amount of effort, and there are a limited number of well-studied fans in the literature to infer typical avulsion rates, which can be highly variable between fan settings (de Haas et al., 2018a).

In the study area of southwestern British Columbia (SWBC), debris flow hazard and risk assessments are becoming common to support planning and decision making. These include local fan studies (e.g., BGC, 2015; 2018b) and regional prioritization works (e.g., two case studies summarized by Sturzenegger et al. (2019) for central BC). In both these cases, expert judgement was an integral part of debris flow runout forecasting, such as selecting various mobility conditions, avulsion scenarios, and interpreting numerical modelling outputs. There must be a continued effort to bolster expert judgement, and in some cases, challenge practitioner bias, with empirical observations and statistical analyses. To date, there have been no systematic studies of runout evolution trends on fans in SWBC, and very few runout prediction methods in general that are either probabilistic, or consider flow deviation due to avulsion. This thesis aims to address these key knowledge gaps.

1.2 Research Objectives

To address the challenges described in Section 1.1, the main research objectives are:

1. Create a rich geospatial dataset documenting debris flow impacts with high spatial accuracy across numerous fans in SWBC.
2. Develop a systematic method to extract, visualize, and compare spatial impact trends across numerous fans.
3. Test statistical differences in spatial impact trends for groups of fans or events using easily measurable variables.
4. Provide data-driven guidance to practitioners for estimating probability of runout exceedance on a fan area using case studies in SWBC.

1.3 Research Hypothesis

Along with addressing the research objectives, the following hypotheses were tested:

1. Spatial impact trends relative to the previous flow path, both down and cross-fan, exist, and can be generalized for a group of fans.
2. Differences in spatial impact trends for groups of fans or events can be explained, in part, with morphometric or geotechnical characteristics.

1.4 Research Approach

First, a comprehensive literature review was completed to generate a conceptual model of what factors affect debris flow mobility and avulsion based on our current state of knowledge. Existing empirical runout methods were also summarized, and key challenges and knowledge gaps identified, to be addressed in this thesis and future work. The literature review is provided in Chapter 2.

The data compilation phase consisted of collecting high quality field and remote sensing data across 30 fans in SWBC. Impact areas and flow paths dating back to the beginning of the airphoto record were mapped with an ensemble of data sources, including airphotos, satellite imagery, lidar, and field observations. Event volumes were reconstructed where possible, and morphometric variables were calculated for each fan site. The dataset, along with the data compilation process, is described in Chapter 3.

Once the dataset was complete, spatial impact trends were aggregated across multiple fans using

the fan area as a normalizer, with the fraction of impacted areas a proxy for probability of impact. To simplify the data analysis, runout was considered in two components: runout down-fan (i.e., how far debris flows tend to travel past the apex toward the fan toe) and runout cross-fan (i.e., how far debris flows deviate from the previous flow path). Distributions of maximum down-fan and cross-fan runout are a proxy for mobility and avulsion behaviour, respectively. Regional and local trends are discussed, and differences in these distributions were tested using characteristics of the fan site or event as discriminators. Data analysis and interpretation of results is presented in Chapter 4.

Lastly, the main findings and implications for hazard and risk assessments were described, along with recommendations for future research. These conclusions are found in Chapter 5.

1.5 Study Area

1.5.1 Geologic Setting

The study area is located in southwestern British Columbia (SWBC), characterized by rugged mountains, deep valleys, and plateaus sculpted by Pleistocene glaciation. Most of the study sites are located in the southern Coast Mountains (Pacific Ranges) physiographic region, with a few sites in the Fraser Lowlands and bordering the northern Cascade Mountains and Thompson Plateau (Figure 1.1).

The study area is mostly underlain by Middle Jurassic to Eocene granitic rocks of the Coast Plutonic Complex, largely granodiorites with some quartz diorite and diorite, which overprint accretionary terranes of sedimentary and volcanic rocks of Middle Jurassic age and older (Bustin et al., 2013). High-grade regional metamorphism is closely associated with plutonism, as well as with major structures, consisting of northwest and north-trending contractional and strike-slip fault systems (Monger & Journeay, 1994). Quaternary volcanic rocks in the study area are part of the Garibaldi volcanic belt, the northern segment of the Cascade volcanic arc, characterized by a chain of intermediate composition volcanoes with evidence of extensive glaciovolcanism (Kelman et al., 2002).

During the most recent Pleistocene glacial episode, almost all of BC was covered by the

Cordilleran ice sheet, reaching its maximum extent about 17,000 years ago (Clague & Ward, 2011). Glaciation sculpted the Coast Mountains, shaping fjords and u-shaped valleys that dissect the terrain, depositing sequences of glacial till, glaciofluvial, glaciolacustrine, and minor glaciomarine sediments (Church & Ryder, 2010). Contemporaneous and post-glacial volcanism have formed prominent edifices, including Mount Garibaldi, Mount Cayley, and Mount Meager. Deglaciation was largely completed 11,500 years ago, accompanied by isostatic uplift and post-glacial dissection of valley-fill (Ryder, 1971; Ryder et al., 1991). Alpine glaciers are still present in the study area at high elevations, although these are vanishing with recent climate change (Walker & Pellatt, 2003). Following glacial debuttressing, mass wasting and fluvial reworking resulted in a pulse of sedimentation (paraglacial processes), followed by more stabilized slopes and a relaxation in sediment supply (Ballantyne, 2002; Church & Ryder, 2010). These processes formed talus slopes, colluvial cones, alluvial fans, dissected terraces, floodplains, and deltas that dominate the contemporary landscape. Debris flows are a dominant hillslope process by which sediments are delivered to valley floors, along with rockfalls and rock avalanches (Church & Ryder, 2010).

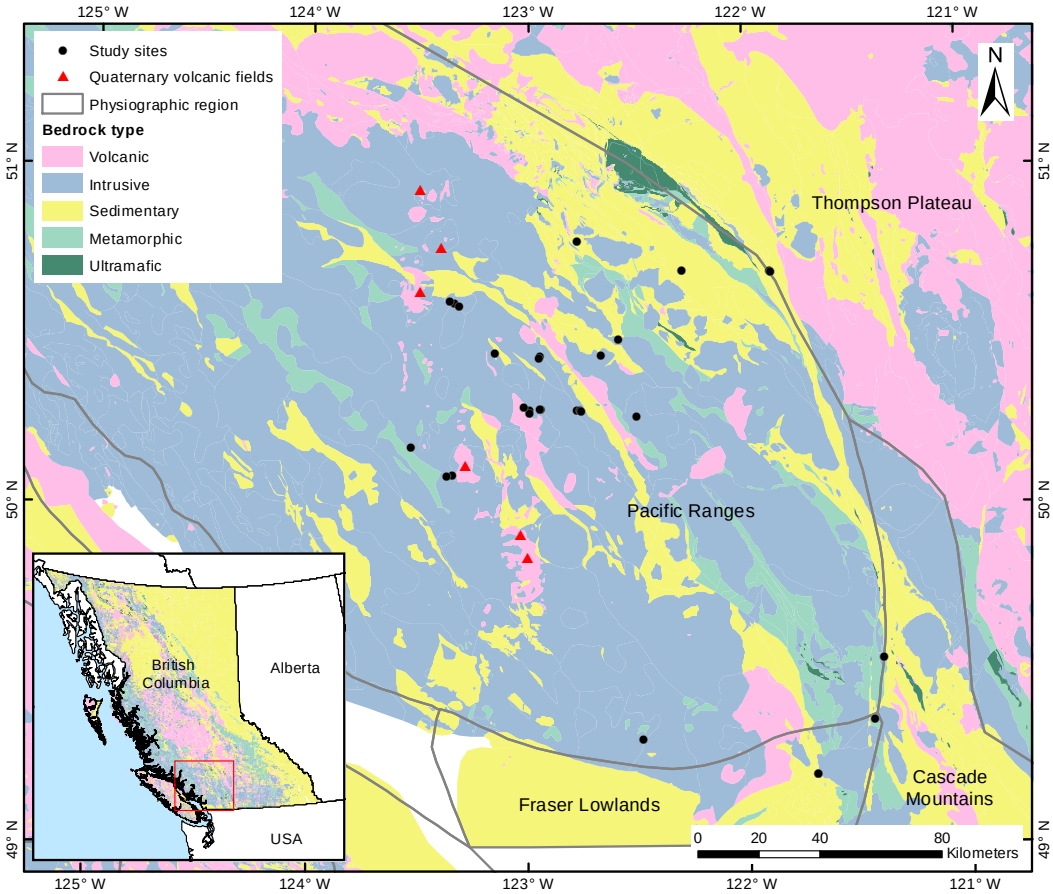

Figure 1.1. Regional geology and physiographic regions of the study area. Provincial digital bedrock geology accessed from Cui et al. (2017), physiographic regions for Canada accessed from Bostock (2014), and Quaternary volcanic fields from the Garibaldi volcanic belt assembled from Wilson (2019).

1.5.2 Climate

The climate of SWBC is generally moist and mild, but varies considerably across the study area. Pacific oceanic storms bring heavy rain and snow from late fall to winter along the coast of the Pacific Ranges. In the Lower Mainland, Pacific storms stalling against the mountains can also bring about intense, orographically enhanced, precipitation (Demarchi, 2011). Here, summers are typically dry and warm with occasional rainy periods. Further inland, the Interior Transition Ranges ecoregion lies in the rainshadow of the Coast Mountains, consisting of hot summers and cool, dry winters (Demarchi, 2011). Debris flows on the western flank of the Pacific Ranges can be

triggered by heavy rainfall or rain-on-snow events from October to December, while debris flows in the northeastern quadrant of the study area may be associated with spring rain-on-snow events or summer thunderstorms (Bovis & Jakob, 1999). Microscale weather processes in the catchments, such as cells of high intensity rainfall from orographic uplift and local wind pattern, are also important debris flow triggering mechanisms (Jakob & Lambert, 2009).

Figure 1.2 shows monthly climate normals from 1971-2000 at four stations across the study area accessed from the Pacific Climate Impacts Consortium (PCIC) data portal. Figure 1.3 shows gridded monthly precipitation data (PCIC, 2014) for the wettest (November) and driest (July) months, highlighting rain-shadow and topographic effects across the study area.

According to the PCIC Plan2Adapt Climate Information Tool (PCIC, 2012), projected climate changes for the study area over the next century include an increase in temperature and overall annual precipitation, with drier summers and wetter winters. These projections are based on the mean temperature and precipitation change from the 1961-1990 baseline using 30 climate change projections (15 Global Climate Models, two global greenhouse gas emission scenarios) for the Squamish Lillooet, Fraser Valley, and Metro Vancouver Regional Districts (PCIC, 2012). These climate projections could mean more wildfires, glacial and permafrost changes, beetle infestations, and more landslide triggering storms in the winters, all of which are known to influence debris flow activity (Jakob, 2019). A study by Jakob & Lambert (2009) also supports increased landslide frequency along the southwest coast of BC based on climate change models that predict increased antecedent and short-term precipitation in the twenty-first century.

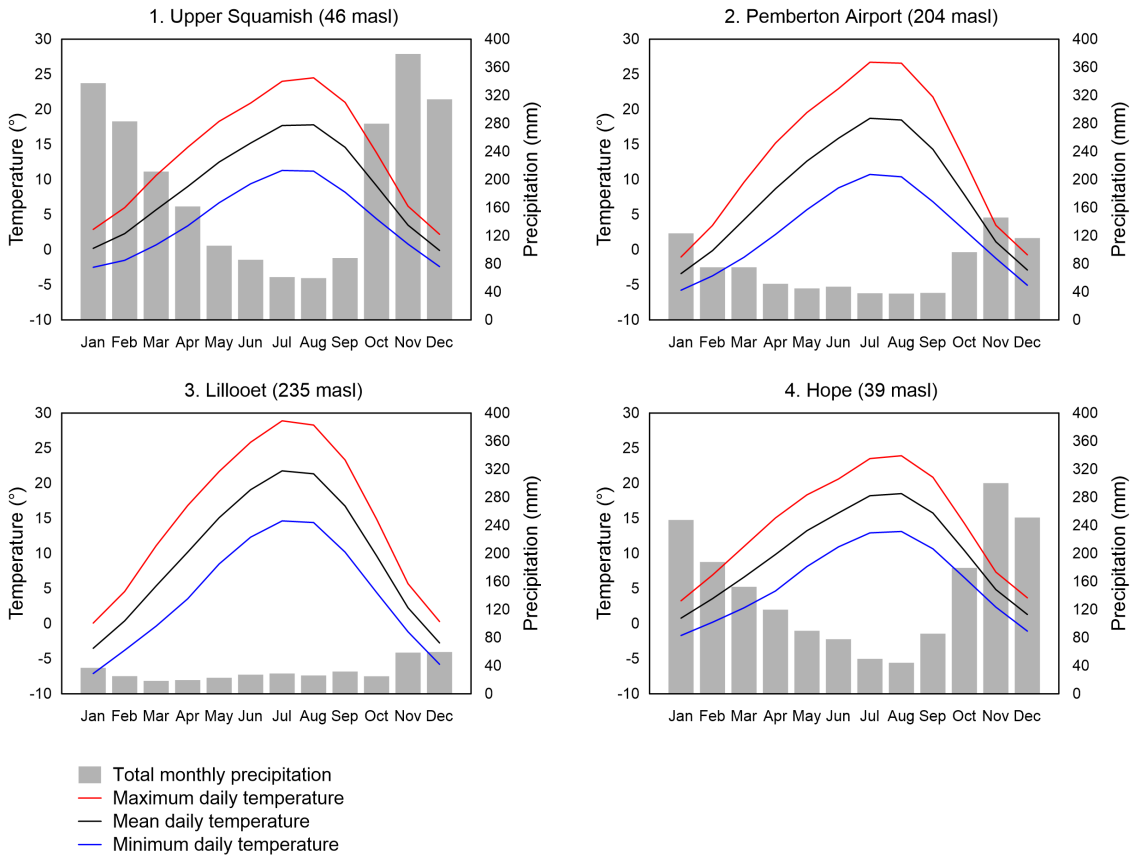

Figure 1.2. Monthly climate normals (1971-2000) for climate stations across the study area. Locations shown on map in Figure 1.3. Station data accessed from PCIC data portal.

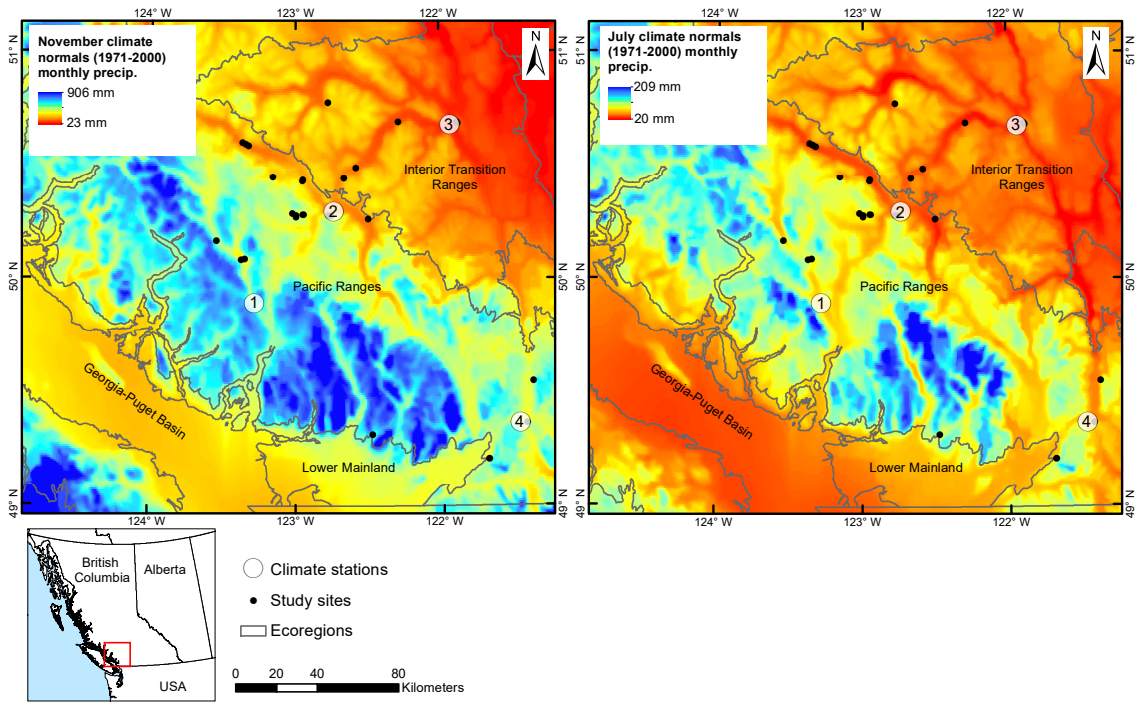

Figure 1.3. Gridded precipitation data for November (left) and July (right) climate normals (1971-2000) from PCIC (2014). High-resolution climatology grid with a pixel size of about 800 m is derived from station data interpolated using the Parameter-elevation Regressions on Independent Slopes Model (PRISM). Monthly climate station data shown in Figure 1.2. Ecoregions defined by Demarchi (2011).

1.5.3 Previous Research in the Study Area

To date, there have been no comprehensive studies of avulsion trends on debris flow fans in BC. Papers by Hungr et al. (1984) and VanDine (1985) laid the groundwork for debris flow hazard analysis and remedial measures in western Canada. The most relevant work related to debris flow runout in the study area is by Jordan (1994), who studied dynamic behaviour and physical properties of debris flows in the Squamish and upper Lillooet River drainages. Jakob et al. (1997) studied morphometric and geotechnical controls on debris flow frequency and magnitude, including many of the study sites in this thesis. Lau (2017) examined morphometric controls on scour depth on temperate alluvial fans in southern BC, including a detailed case study on a debris flow with extreme channel scour included in this inventory. Relevant research for coastal BC using a debris flow inventory from the Queen Charlotte Islands (Haida Gwaii) northwest of the study area include: empirical-statistical runout

models by Fannin & Rollerson (1993) and Fannin & Wise (2001); a study relating volume to slope length by Hungr et al. (2008); and an examination of controls on debris flow mobility by Guthrie et al. (2010).

Chapter 2

A Comprehensive Review of Debris Flow Runout

This literature review provides an overview of debris flow runout and avulsion processes on fans, focusing on implications for hazard and risk assessments. Here, debris flow and fan evolution processes are described, establishing a conceptual model for factors that affect debris flow mobility and avulsion. Components of a hazard and risk assessment are defined, and existing empirical methods for forecasting debris flow runout are discussed. Finally, the main challenges and knowledge gaps to be addressed in this thesis and future work are outlined.

2.1 Debris Flow Processes and Forms

A debris flow is defined by Hungr et al. (2014) as: "Very rapid to extremely rapid surging flow of saturated debris in a steep channel. Strong entrainment of material and water from the flow path". Debris is loose, unsorted material of low plasticity produced by mass wasting processes, weathering, glacier transport, explosive volcanism, or human activity (Hungr et al., 2001). Debris flows can be triggered by heavy precipitation, rapid snowmelt, mass movements in the catchment, and outburst flooding. Typically, most of the debris flow volume is derived from entrainment, with the initiating volume small in comparison (Hungr et al., 2014). A debris flow may be comprised of a single surge or many surges, which consist of a steep, coarse-grained front followed by a tail

of dilute sediment-charged (hyperconcentrated) afterflow (schematic in Figure 2.1) (e.g., Hungr, 2005; Iverson, 1997; Pierson, 1986). Thick surge fronts magnify the peak discharge, which can be an order of magnitude greater than the most extreme hydrological flood (Hungr et al., 2014). Velocities can range from 0.5 to 20 m/s (Lorenzini & Mazza, 2004) with measured and back-calculated peak velocities of 3 to 12 m/s recorded at some Canadian creeks (VanDine, 1985). Velocities are typically highest along steep and confined channel reaches of the catchment, decreasing at the fan apex where a loss in confinement and decrease in slope initiate deposition processes.

The schematic in Figure 2.1 helps depict the debris flow processes and forms described here. At the fan, narrow boulder levees typically form on either side of the flow path as coarse materials are advected to the flow edges (Blair & McPherson, 1998; Costa, 1984; Johnson et al., 2012). Debris can also be deposited in the channel as channel plugs (de Haas et al., 2018a; Whipple & Dunne, 1992). As the debris flow surges down-fan, accompanied by a reduction in slope, loss of channel confinement, and selective boulder depletion, the flow spreads and loses momentum, depositing as lobes (Blair & McPherson, 1998; de Haas et al., 2019). Debris flows are also prone to avulsion, where debris abandons the main channel, diverting flow to elsewhere on the fan (discussed further in Section 2.2). A watery afterflow may continue beyond the terminal lobes as the falling limb of the debris surge continues down slope, or as the catchment continues to drain rainfall (Blair & McPherson, 1998; Hungr, 2005). The upper fan is typically dominated by levee deposition while lobate forms are more common on the lower fan (Blair & McPherson, 1998). Fans are generally considered a depositional landform, but debris flows also erode and entrain fan sediments, governed by basal shear stresses, grain collisional stresses, or destabilization and collapse of channel banks (Schürch et al., 2011b, and references therein).

Debris flows are part of a wide and continuous spectrum of hydrogeomorphic processes with varying sediment sizes and particle-size distributions affecting flow properties (Pierson, 2004). In order of increasing sediment concentration, these processes include clear water floods, debris floods, hyperconcentrated flows, and mudflows/debris flows. Debris flows can be differentiated from the other processes by this definition by Hungr et al. (2014): "(1) the peak discharge is more than three times greater than that of a major flood flow, or (2) mean solids volume concentration at the surge

peak greater than about 60% and the water and solid phases thoroughly mixed". Mudflows are similar to debris flows but are distinguished texturally as containing a significant content of saturated plastic fines and lacking coarse fragments, typical in regions of deep weathering (Costa, 1984; Hungr et al., 2014). Hyperconcentrated flows are two-phase non-Newtonian fluids with sediment concentrations about 20-60% by volume (Pierson, 2005). Hungr et al. (2014) defines a debris flood as: "Very rapid flow of water, heavily charged with debris, in a steep channel. Peak discharge comparable to that of a water flood". The main difference between debris floods and hyperconcentrated flows/debris flows/mudflows is that flow properties are governed by fluid flow rather than the interaction of solid and fluid forces (Hungr et al., 2001; Iverson, 1997). Clear water/stream flow floods have less than 20% solids by volume with distinct sedimentary structures from fluid flow (e.g., stratified, well sorted, upward fining deposits, clast imbrication) (Costa, 1984; Wilford et al., 2004).

The distinction of hydrogeomorphic processes is important for hazard management because different hazard characteristics are associated with typical flow types (Wilford et al., 2004). Debris flows can be extremely destructive due to high velocities, flow depths, and the movement of large boulders. Except for catastrophic dam-breach outburst floods, debris floods usually do not develop impact forces comparable to debris flows (Hungr et al., 2001). Field evidence (described in Section 3.3.5) and morphometrics (described in Section 3.6.7) can help distinguish the dominant process type. In general, debris flow processes are more typical of steep drainages of less than a few square kilometers, while debris floods are associated with larger watersheds with greater hydrologic flood discharges (Hungr et al., 2014; Wilford et al., 2004). However, all processes may occur within a single drainage or may be present at different times during an event or a single surge (Costa, 1984).

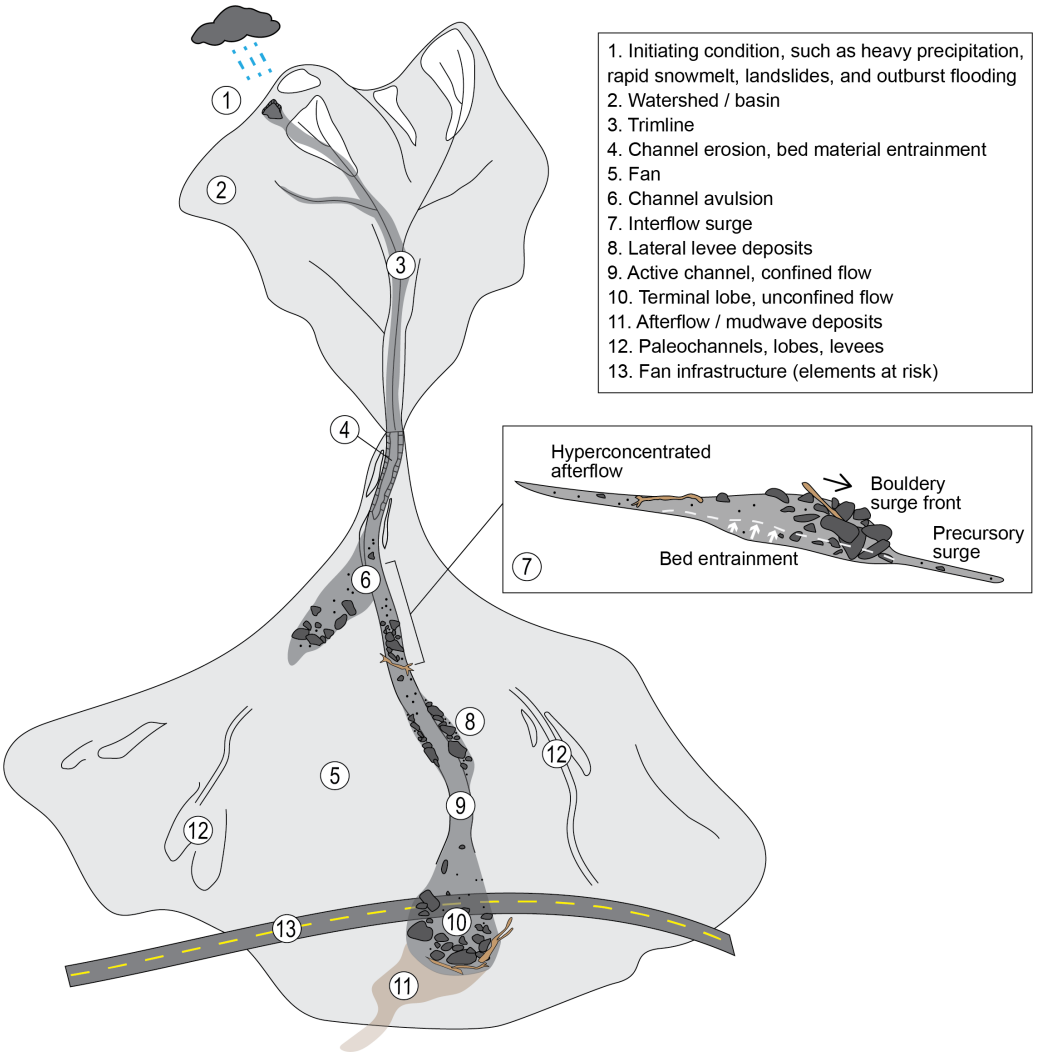

Figure 2.1. Schematic diagram of typical debris flow processes, forms, and impacts (not to scale). Adapted from Pierson (1986) and Lau (2017).

2.2 Debris Flow Fan Evolution

A fan's semi-conical morphology is the product of avulsion sequences that shift the active channel and locus of deposition through space and time (de Haas et al., 2018a; 2019). Until recently, there have been few systematic studies investigating controls on debris flow avulsion, and much of our understanding is from observations of fluvial systems (de Haas et al., 2018a; Densmore et al., 2019). Research on autogenic controls (internal thresholds and feedback response) on fluvial fan dynamics show that fan morphology evolves through repeated cycles of incision, backfilling, and

spreading/avulsion (Figure 2.2) (e.g., Reitz & Jerolmack, 2012; Schumm et al., 1987). Evidence from the fluvial literature suggests that avulsion rates increase with sediment supply (e.g., Ashworth et al., 2004; Bryant et al., 1995), with small aggrading floods critical to preconditioning avulsions by reducing channel capacity to some threshold (e.g., Field, 2001; Jones & Schumm, 1999).

de Haas et al. (2016) observed similar autogenic cycles on experimental debris flow fans, but with different processes (Figure 2.2). After upstream migration of the depocenter toward the fan apex (i.e., backstepping), an avulsion is triggered toward a topographically favourable path. After avulsing, backstepping recommences once debris flows reached a maximum runout, and the cycle repeats. One of the main differences between fluvial and debris flow end-members is that cycles on fluvial fans are controlled by progressive aggradation operating continuously in time, while debris flow deposition is more localized in space and time (de Haas et al., 2016). A single debris flow lobe can trigger an avulsion, leading to more chaotic avulsion patterns on debris flow fans compared to fluvial fan systems (de Haas et al., 2018a). Runoff erosion and secondary fluvial processes between debris flows were not replicated in the experiments by de Haas et al. (2016) since the watery tail-end of the experimental debris flow was prevented to bury or rework the initial deposit; these results represent an idealized end-member of the hydrogeomorphic process spectrum.

de Haas et al. (2018a) validated the experimental work with an analysis of spatio-temporal patterns on 16 well-studied fans from around the world. Patterns on natural fans were significantly more chaotic compared to the experimental findings due to variations in magnitude, composition, and rheology of the flows (de Haas et al., 2018a). Overall however, de Haas et al. (2018a) observed that debris flows on natural fans also follow cycles of channel plugging, backstepping of deposition towards the fan apex, avulsion towards a topographic low, and establishment of a new active channel. For the fans in that study, avulsions appeared to occur approximately every 3 to 8 flows, but this is very dependent on the fan environment; major channel shifts may require more flows between avulsion events, or a complete avulsion cycle could be initiated within a single event with multiple surge sequences (de Haas et al., 2018a).

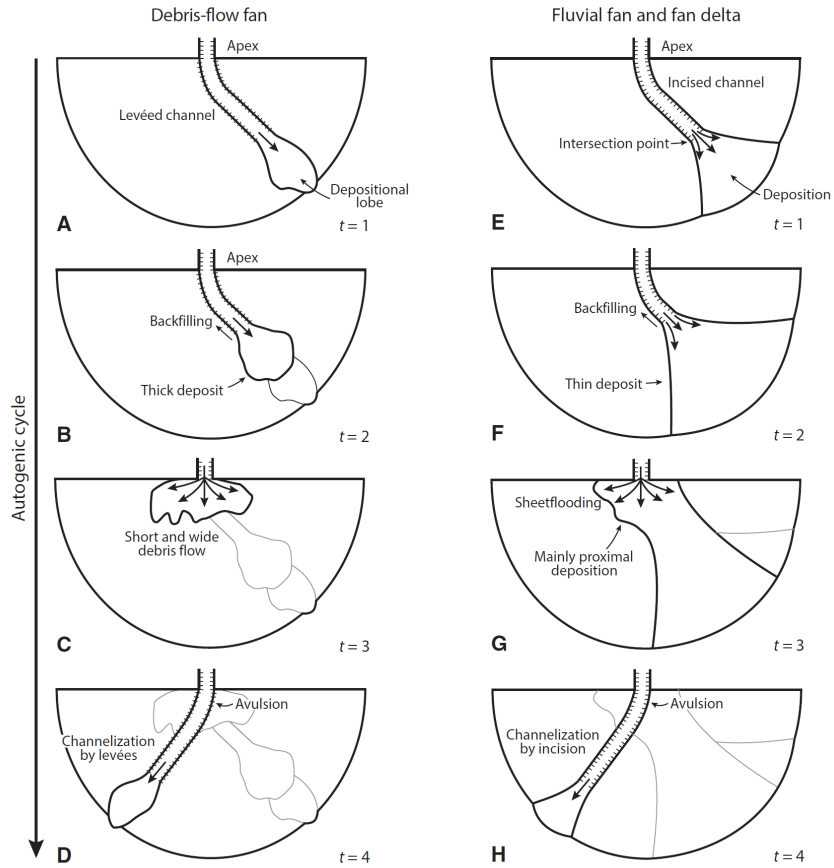

Figure 2.2. Schematic of autogenic cycles on experimental debris flow fans and fluvial fans and deltas from de Haas et al. (2016).

2.3 Debris Flow Hazard and Risk Assessment

In mountainous regions, communities and infrastructure are often built upon fans requiring detailed hazard and risk assessments to understand potential risks posed by hydrogeomorphic hazards. Risk is the probability of a hazardous event and its potential consequences. A quantitative risk assessment (QRA) is a systematic and quantitative framework for evaluating risk. Risk can be expressed analytically using Equation 2.1 or something similar (e.g., Corominas et al., 2014; Dai et al., 2002; Fell, 1994):

$$Risk = \sum_{i=1}^{n} P(H)_i \times P(S|H)_i \times P(T|S)_i \times V_i \times E \tag{2.1}$$

where, for i of n hazard scenarios, P(H) is the annual probability of the hazard occurring, P(S|H) is the spatial probability that the hazard will reach the element at risk, P(T|S) is the temporal probability that the element at risk will be present if the hazard reaches its location, V is the vulnerability or the probability of loss of life if the element is impacted, and E is the value of the element at risk or number of people at risk in the case of life loss risk.

Hazard assessments are generally limited to the P(H) and P(S|H) terms by considering the probability of a hazard occurring and its intensity without specifying the exposure or consequences to the elements at risk (Corominas et al., 2014). For debris flow hazard assessments, this usually involves identifying a potential debris flow hazard, determining event magnitudes for a range of return periods (i.e., developing frequency-magnitude (F-M) relationships), and conducting a runout assessment. A combination of P(H), P(S|H), and P(T|S) is sometimes referred to as encounter probability. The P(T|S) represent exposure to the hazard, while the V and E terms represent the consequences.

Defining a volume for a given return period is a sensitive parameter in the QRA as volume can propagate into other terms in Equation 2.1, such as P(S|H), where volume is typically an input for runout models. Establishing reliable F-M curves can be a costly and time-consuming endeavor, requiring detailed fan reconstructions using a variety of absolute and relative dating methods, supplemented by statistical analyses to extrapolate probabilities outside of the observed record (Jakob, 2019). When detailed studies are not practical, debris production has been correlated with catchment morphometrics, such as debris contributing areas, relief, drainage density, and ruggedness (e.g., Bovis & Jakob, 1999; D'Agostino & Marchi, 2001; de Haas & Densmore, 2019). Jakob et al. (2016) showed how regional F-M relationships might be developed by normalizing an ensemble of established F-M curves by fan volume or area.

Debris flow runout assessments involve forecasting debris flow motion, such as how far and how fast a debris flow will travel. Forecasting runout behaviour can be challenging due to the complexity of physical processes, as described in Section 2.1. There are many evolving tools and techniques, ranging from simple empirical methods (discussed further in Section 2.6) to analytical methods. Empirical methods are typically applied at the regional scale or for screening level studies,

while detailed QRAs or engineering design would more likely involve process-based modelling with numerical models, such as Dan3D (McDougall & Hungr, 2004), RAMMS (Christen et al., 2010), and FLOW-2D (O'Brien et al., 1993). Numerical models and GIS technologies are increasingly common for developing hazard and risk maps (Quan Luna et al., 2014). Numerical model outputs can be used to estimate vulnerability by associating building damage to debris flow intensity, calculated from numerical outputs such as flow depths, velocities, and impact pressures (e.g., Jakob et al., 2012; Kang & Kim, 2016; Quan Luna et al., 2011).

McDougall (2017) identified some challenges with modelling flow-like landslides, such as sensitivity to topographic resolution, selection of model input parameters, and simulating sudden channel obstructions causing avulsion. Semi-empirical models such as Dan3D (McDougall & Hungr, 2004) simulate bulk flow behaviour with a fixed rheology and a few calibrated parameters. Calibration through back-analysis requires detailed event documentation and pre-event topography. Even if calibrated, it is uncertain whether future events can be simulated with similar rheological models or calibrated parameters. Furthermore, although a fixed rheology may adequately simulate bulk flow, it does not capture flow heterogeneity inherent to debris flow processes (Iverson, 2003). Mathematical models such as D-Claw (George & Iverson, 2014) are able to simulate the effects of evolving dilatancy and flow phases from initiation to deposition, but require more model parameters. Numerical models may simulate avulsions associated with superelevation and runup, but avulsions caused by channel blockages from coarse deposits or woody debris require ad hoc topographic adjustments to simulate with a semi-empirical numerical model.

Many runout prediction methods are deterministic. Practitioners must use judgement to convert runout calculations or modelling outputs to a probability of runout exceedance, depending on anticipated mobility (irrespective of volume) or avulsion scenarios, depicted in Figure 2.3. A systematic way to account for different mobility or avulsion behaviours in a QRA is to identify credible sub-scenarios, assign a conditional probability, and model each sub-scenario separately. There is currently little guidance available to practitioners for identifying credible sub-scenarios and for assigning probabilities. A wide spectrum of mobility and avulsion behaviours make for a complicated event tree. Alternatively, varying mobility could be modelled with a Monte-Carlo style

analysis by sampling model parameters from probability density functions (PDF) (e.g., Aaron, 2017; Quan Luna, 2012; Scheidl & Rickenmann, 2010). Monte-Carlo style analyses require a rich database of systematically calibrated parameters to develop probability density functions, and would not be efficient for complex models that require hours to complete one model run.

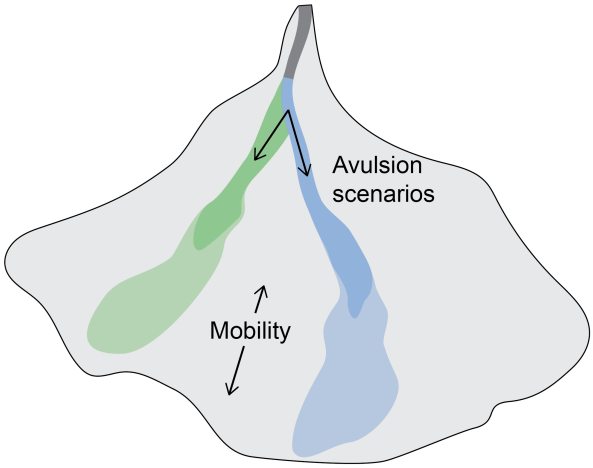

Figure 2.3. Conceptual debris flow avulsion scenarios and mobility that may be considered in a QRA.

Not all hazard and risk-based decision making follow the procedures outlined here. For instance, regional or preliminary studies often employ landslide susceptibility mapping. Landslide susceptibility, as defined by Fell et al. (2008), is "a quantitative or qualitative assessment of the classification, volume (or area), and spatial distribution of landslides which exist or potentially may occur in an area". In other words, a susceptibility analysis involves identifying the hazard and potential runout without explicitly considering a temporal probability. The Flow-R model (Horton et al., 2013) is a GIS-based regional susceptibility model with automatic source area delineation and flow propagation using a spreading algorithm and simple frictional laws. Since flow propagation calculations are based on a unit energy balance, there is no specification of event volumes or scenarios. Flow-R model outputs can be interpreted as areas that could potentially be reached by debris flows, with an associated relative susceptibility, but are not equivalent to a spatial probability of impact map.

In the context of hazard and risk, this thesis focuses on questions related to the P(S|H) term in Equation 2.1, and questions related to different mobility and avulsion scenarios shown in Figure 2.3.

2.4 Factors Affecting Debris Flow Mobility

Mobility is a measure of a landslide's ability to either runout long distances and/or inundate large areas. Controls on debris flow mobility have been studied extensively through experiments and field observations. Mechanistic interpretations from the literature are summarized here, forming a conceptual model for what factors affect debris flow mobility.

2.4.1 Event Conditions

It has been well established that debris flow volume has a large effect on runout, with greater volumes having more momentum and the tendency to spread further (e.g., Corominas, 1996; Griswold & Iverson, 2008; Legros, 2002). There is considerable scatter in these trends which may be attributed to other factors, discussed in the following Sections 2.4.2 and 2.4.3. A preliminary study by Zubrycky et al. (2019) using data from this thesis found a potential inverse correlation between a calibrated Voellmy friction coefficient and volume (Figure 2.4). A similar volume dependency was also observed by Schraml et al. (2015).

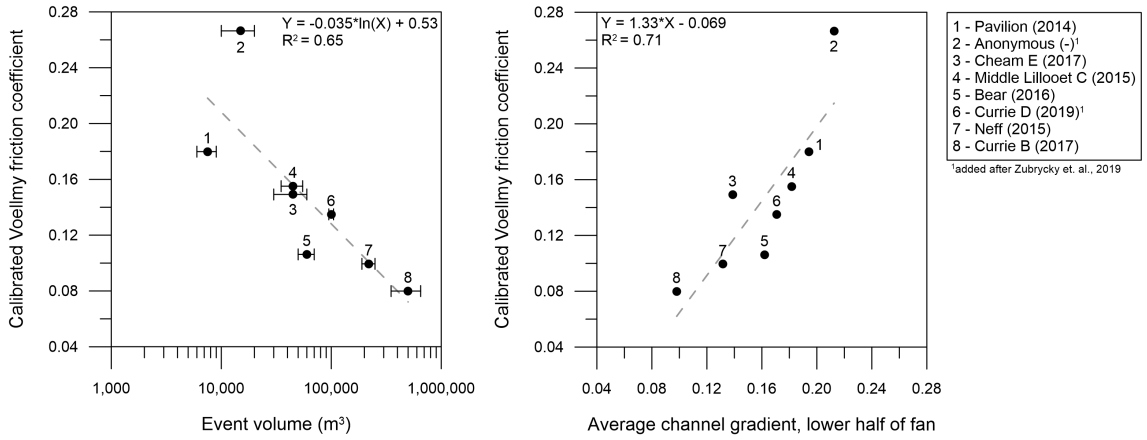

Figure 2.4. Preliminary correlations by Zubrycky et al. (2019) to calibrated Voellmy friction coefficient using data from debris flow events presented in this thesis. Numerical modelling was completed in Dan3D (McDougall & Hungr, 2004).

Other factors specific to an event scenario might also influence mobility, such as triggering conditions, discharge hydrograph (Whipple, 1992), number of surges (Chen et al., 2017), and degree volume generated from progressive entrainment (Frank et al., 2015). Flow height is influenced in part

by the flow hydrograph, which affects the degree of erosion and deposition (Schürch et al., 2011b). Chen et al. (2017) showed numerically that the inundated areas and runout distances of successive debris flows are smaller (i.e., a multi-surge event) than those of concurrent debris flows due to lower mobility of smaller individual events and blockage by the earlier debris flows. Although the mobility of an individual surge may be controlled by other factors, the total impact area of an entire event would be influenced by the number of surges, hypothetically.

2.4.2 Composition

Debris flow composition can be described by water content, grain-size distribution, lithology, and the amount of woody debris or organics. It has been well established in soil mechanics that pore-fluid pressures influence the strength of a sediment-water mixture. The effect of grain-size distribution on debris flow rheology has been studied experimentally (e.g., Major & Iverson, 1999; Parsons et al., 2001; Phillips & Davies, 1991) and observed geomorphically (e.g., Whipple & Dunne, 1992). Large-scale flume experiments by Major & Iverson (1999) show deposition at coarse grained flow margins is governed by frictional resistance in the absence of high pore-fluid pressure. Kaitna et al. (2016) found that the primary manner in which grain-size distribution controls excess pore pressure is in limiting pore pressure dissipation. Similarly, experimental findings by de Haas et al. (2015) show that increasing the coarse fraction enhances mobility to an extent, but an excess of coarse material enhances pore pressure diffusivity, increasing frontal friction and stalling the flow. Due to the grain-size heterogeneity within a single surge, debris flows should not be represented with a fixed rheology (Iverson, 2003). However, the bulk mobility of an event may be informed by the catchment lithology since weathering of the source rock would influence the grain-size distribution of a typical flow. Field evidence from the study area collected by Jordan (1994) found that fine-textured debris flows from weak, clay-rich Quaternary volcanic rocks exhibit long runout on gentle gradients compared to coarse-textured debris flows from granitic sources. A study by Tiranti & Deangeli (2015) showed how catchment lithology may help inform the selection of a rheological model.

Slurries with high proportions of silt and clay usually have lower yield strengths and viscosities making them generally more mobile (Whipple & Dunne, 1992). Lahars with high clay contents from

hydrothermally altered volcanic rocks have higher mobility than granular debris flows (Griswold & Iverson, 2008). Even within lahar populations, cohesive flows with more than 3 to 5 percent clay-sized sediment are more mobile compared to non-cohesive flows (Scott et al., 1995). Zhang et al. (2013) found that muddy debris flows in the Wenchuan Earthquake Zone with a higher fines content were more mobile compared to flows with larger clasts and less than 2 percent silt and clay, deriving different empirical runout equations based on the flow type. The experiments by de Haas et al. (2015) found that an increase in clay content enhances mobility due to retained excess pore pressures, however too much clay creates a viscous flow with reduced runout.

The effect of organics and woody debris on mobility are poorly understood. May (2002) found the runout length had a strong influence on the accumulation of wood as the flow traveled. Lancaster et al. (2003) hypothesized that one way in which large woody debris may reduce runout is by entanglement at the flow front causing wood jamming in channels.

2.4.3 Path Characteristics

Topography can also exert significant control on debris flow mobility (e.g., Corominas, 1996). Path characteristics that influence mobility include elevation loss, channel gradients, path curvature, channel confinement, obstacles, and interaction with forest stands. Many of these factors influence mobility by dissipating energy and promoting deposition. Debris flows that initiate higher in the watershed have higher potential energy, while those that interact with obstructions such as natural topographic features or human-made structures would dissipate energy. Dense forests have been found to suppress debris flow runout (e.g., Booth et al., 2020; Ishikawa et al., 2003), however this may only apply for debris flows up to a certain magnitude. Sharp channel bends also reduce flow velocity, thus limiting mobility (e.g., Benda & Cundy, 1990; Fannin & Wise, 2001).

Assuming steady, uniform, gravity-driven flow, yield stress can be calculated assuming a flow density, depth, and surface slope (e.g., Johnson & Rodine, 1984; Whipple & Dunne, 1992). It has been well observed that a decrease in slope initiates deposition and limits runout (e.g., Benda & Cundy, 1990; de Haas et al., 2015; Fannin & Wise, 2001; Miller & Burnett, 2008). However, factors that set the fan slope, such as lithology, grain-size, or process type (e.g., Blair & McPherson, 1998;

Hooke, 1968) may exert more of a control on mobility than the flow interacting with the slope itself. Based on a preliminary numerical model calibration exercise using data from this thesis, there is an apparent correlation between the calibrated Voellmy friction coefficient and the lower channel gradients (Figure 2.4). Scheidl & Rickenmann (2010) correlated empirical mobility coefficients to the average fan slope and the average channel slope. Experimental findings by de Haas et al. (2015) show that topographic controls, such as increased runouts with increased outflow plain slopes, were negligible compared to the effect of debris flow composition.

Channelized or confined flows typically exhibit longer runouts (e.g., Cannon, 1989; García-Ruiz et al., 1999; Zhang et al., 2013). Flow depths are thicker when concentrated in a channel, promoting entrainment and thus propagation down-fan; once unconfined, debris tends to spreads to some critical thickness, and movement is halted once all debris is deposited (Cannon, 1989; Fannin & Rollerson, 1993; Miller & Burnett, 2008; Schürch et al., 2011b). Along channelized reaches, water may be incorporated into the flow, further enhancing mobility. With a reduction in the channel capacity (cross-sectional area), frictional interactions with the channel sidewalls, such as boulder or log jamming, may lead to the formation of channel plugs (e.g., de Haas et al., 2018a).

2.5 Understanding Debris Flow Avulsion

Controls on debris flow avulsion are much less well studied than those affecting mobility. As described in Section 2.2, debris flow fan evolution processes can be chaotic and occur over various time scales. In this section, factors that may influence avulsion likelihood and location on a debris flow fan are described based on the current state of knowledge. Autogenic (intrinsic) controls on avulsion (e.g., de Haas et al., 2016) are the primary focus of this literature review, although allogenic (extrinsic) factors such as climate, base-level, and tectonics also play a role (Stouthamer & Berendsen, 2007).

2.5.1 Avulsion Triggers

There are various triggers, or physical drivers, that may cause a debris flow to avulse. These triggers may be considered in a hazard or risk assessment, or when describing an event forensically.

Avulsion triggers have been grouped into three general scenarios, as shown in Figure 2.5: 1) overtopping (e.g., de Haas et al., 2018b); 2) superelevation (e.g., Field, 2001); and 3) channel blockages (e.g., de Haas et al., 2018a, de Haas et al., 2019, Whipple & Dunne, 1992). Many of these triggers, or hybrids, may be at play during a single event, possibly interacting with one-another. Progressive aggradation is more typical of fluvial processes (e.g., Bryant et al., 1995; de Haas et al., 2016; Field, 2001), but might be an important trigger for mixed-process fans or debris flows with an abundance of inter-surge or precursory flooding. de Haas et al. (2019) found channel-plug formation to be the dominant mechanism for triggering avulsions in Saline Valley, California, while Millard et al. (2006) found channel crossing structures from forestry operations were associated with avulsions for debris flows in coastal BC. Bank failure has not been identified in the literature as a potential mechanism but is considered here conceptually.

1. Overtopping

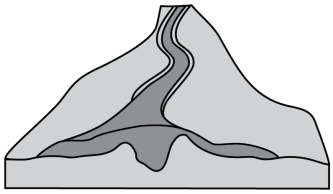

Peak discharge is significantly larger than the channel capacity.

2. Superelevation

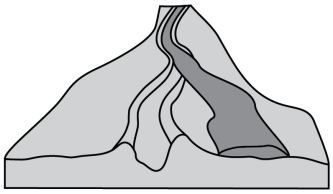

Flow height along the outside bend of a curved channel exceeds bank or levee height.

3. Channel blockages

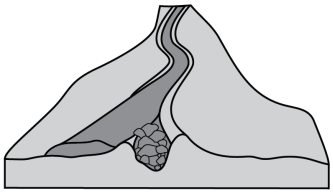

a) Debris plugs
Local deposition of debris diverting flow, possibly from the bouldery flow front, entangled wood, or a lobe from a previous surge.

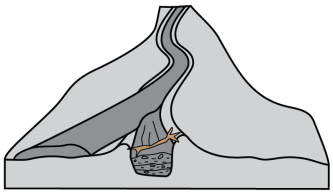

b) Progressive aggradation
Channel backfilling due to upward propogation of depositon (i.e., backwater effect), possiby from sequences of earlier surges.

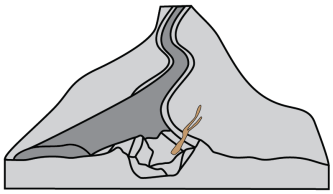

c) Bank failure
Collapse of channel walls causing a blockage. Highly erosive flows may undercut the channel triggering bank failure.

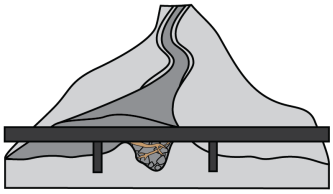

d) Structures
Boulder or wood jamming against structures such as bridges, culverts, roads, and dams.

Figure 2.5. Conceptual avulsion triggers.

2.5.2 Estimating Avulsion Probability

Estimating the probability of avulsion is challenging because avulsion rates vary between fan environments and through time. There are few fans that have been spatially and temporally reconstructed to help constrain typical avulsion recurrence intervals. Based on a study of four very active fans with frequent avulsions, de Haas et al. (2018a) found avulsions occurred every 3 to 8 flows. Studies at alluvial fans in Owens Valley, California (e.g., D'Arcy et al., 2015; Dühnforth et al., 2007) and at the Illgraben fan, Switzerland (Schürch et al., 2016) dated fan surfaces with a variety of techniques including cosmogenic radionucliides of boulders. These studies are useful for looking at the long-term evolution of fan sectors over thousands of years, but provide limited help to resolve the probability of an impending debris flow avulsing (de Haas et al., 2018a).

Certain fan environments may be more prone to avulsions than others. Fuller (2012) summarized physical variables that affect alluvial fan avulsions, including those related to flow discharge, sediment transport, fan physiography, channel condition, and allogenic factors. A recent study by Pederson et al. (2015) related compensational stacking, or the tendency to fill topographic lows through avulsion, to measurable fan characteristics. Based on the internal stratigraphy of three fans in Colorado, Pederson et al. (2015) found that areas with typical debris-flow characteristics (abundant coarse clasts, thick units, large lobes, high clay content) tend to stack more compensationally than areas with typical stream-flow characteristics (thinner deposits, less clay and coarse clasts) (Santi et al., 2017). Avulsions may be more likely at fans with characteristically thick lobes compared to their channel depths. As a proxy for probability of avulsion, de Haas et al. (2019) estimated the probability for a channel plug to have sufficient thickness to induce avulsion by comparing typical channel depths to lobe thicknesses across nine debris flow fans in Saline Valley, California.

Based on fan evolution studies by de Haas et al. (2016, 2018a) described in Section 2.2, fans with recent channel plugging in the active channel or a backward propagation of the depocenter may be a strong indicator of impending avulsion. An experimental study by de Haas et al. (2018b) showed that fans experiencing abundant small flows followed by a large flow were more likely to avulse; sequences of smaller flows cause channel plugging, while larger flows have sufficient volume to leave the active channel. However, flows with large flow depths may also erode the existing

channel, enhancing channelization and reducing the probability of avulsion (Densmore et al., 2019; Schürch et al., 2011b). There may be an optimal frequency-magnitude distribution for which avulsion frequency is maximized (de Haas et al., 2018a), but the possibility of erosion and self-channelization must somehow be accounted for. An experimental study by Deijns (2018) found that although the debris flow frequency-magnitude distribution seems to be the major controlling factor in fan development, changes in sediment composition also influence the avulsion behaviour on a timescale of a few events; gravel-rich flows (higher coarse-fraction) increased erosion and inhibited avulsion in the experiments, while gravel-poor experiments were more likely to plug the fan channel. Deijns (2018) describes that avulsion behaviour on experimental fans is controlled by an interplay between volume sequences, fan topography, and debris flow composition.

Considering the avulsion mechanism of boulder or wood jamming, fans with channel blocking structures (e.g., roads, bridges, culverts, check dams) would be more susceptible to avulsion.

2.5.3 Locating Avulsion Points

Currently, selecting avulsion points for a hazard or risk assessment is mostly based on expert judgement. In alluvial architecture modelling, avulsion points are simulated when some threshold is exceeded along a channel. Thresholds used in these models to induce river avulsions include the ratio between cross-valley slope and down-valley slope (e.g., Mackey & Bridge, 1995; Slingerland & Smith, 1998; Törnqvist & S. Bridge, 2002), and the ratio between superelevation (height difference between the levee crest and the average floodplain elevation) and the bankfull channel depth (e.g., Mohrig et al., 2000). Mackey & Bridge (1995) included the ratio of flood discharge to a flood discharge threshold to model avulsion probability along a channel length. Using this analog for debris flows, one could simply determine where along the channel the peak discharge is great enough to overwhelm the channel conveyance capacity. This may work for a single surge with a high peak discharge, but it assumes the channel capacity does not change during the course of an event. Due to complex flow sequencing, channel bed entrainment, and sporadic channel plugging, locating potential avulsions is not always straightforward.

A report by Millard et al. (2006) for fans in coastal BC found avulsions were most frequent

immediately downstream of the location at which the channel merges with the contemporary fan surface (i.e., the intersection point, as defined by Hooke (1967)), with frequency declining from this point toward the fan toe. Pederson et al. (2015) found avulsion tendency increased with distance from the fan apex, likely attributed to longitudinal variation in fan morphology, such as channel confinement decreasing down-fan.

The balance between typical lobe thickness and channel depth down-fan may be useful for identifying avulsion hotspots (de Haas et al., 2018a). Therefore, a likely avulsion point is related to the combined probability of a debris flow lobe stopping at a given location and having a thickness that approximately equals or exceeds the local channel depth (de Haas et al., 2019). From a study of nine debris flow fans in Saline Valley, California, de Haas et al. (2019) found that channel plugging has a similar likelihood at all radial distances from the fan apex, apart from areas of fan-head incision, since both lobe thickness and channel depth decrease with distance down-fan. For fans in coastal BC, Millard et al. (2006) found the channel depth did not appear to have a strong effect on the location of avulsions.

Given the avulsion triggers depicted in Figure 2.5, avulsion locations may be associated with channel bends (superelevation) or channel blocking structures. The possibility of these locations being credible avulsion points compared to any other location along the channel associated with other triggers is not well understood.

Rather than trying to predict avulsion locations, an understanding of avulsion dynamics could be used instead to delineate areas susceptible to impact from avulsion. Long-term avulsion prone sectors may be identified by analyzing radial variations in fan topography since deposition tends to gradually shift toward topographically lower parts on a fan (de Haas et al., 2018a). Paleochannels may also indicate preferential avulsion flow paths. Typical avulsion opening angles between old and new pathways have not been documented, so it is not clear whether an avulsion is more likely to gradually shift laterally or occupy a completely different fan sector (de Haas et al., 2018a; Densmore et al., 2019).

2.6 Empirical-Statistical Methods for Forecasting Debris Flow Runout

Empirical methods are a simple, practical, and widely used approach for estimating debris flow runout. They are derived from observation and guided by some knowledge of physical processes, where our understanding may be limited. Many of these methods are based on simple geometric correlations with easily obtainable predictor variables that can be calibrated to local datasets or transposed to similar environments. Empirical tools can be useful for preliminary local assessments and regional studies in the absence of site-specific data, detailed topographic data, and resources to undertake numerical modelling.

Empirical methods have been well summarized by Rickenmann (1999), Rickenmann (2005), Hürlimann et al. (2008), Scheidl & Rickenmann (2010), and others. Here, the most prominent relationships from the literature are highlighted, updated with some new approaches, followed by a discussion addressing challenges and limitations of these methods. Empirical relationships have been grouped into four general approaches, as shown in Figure 2.6:

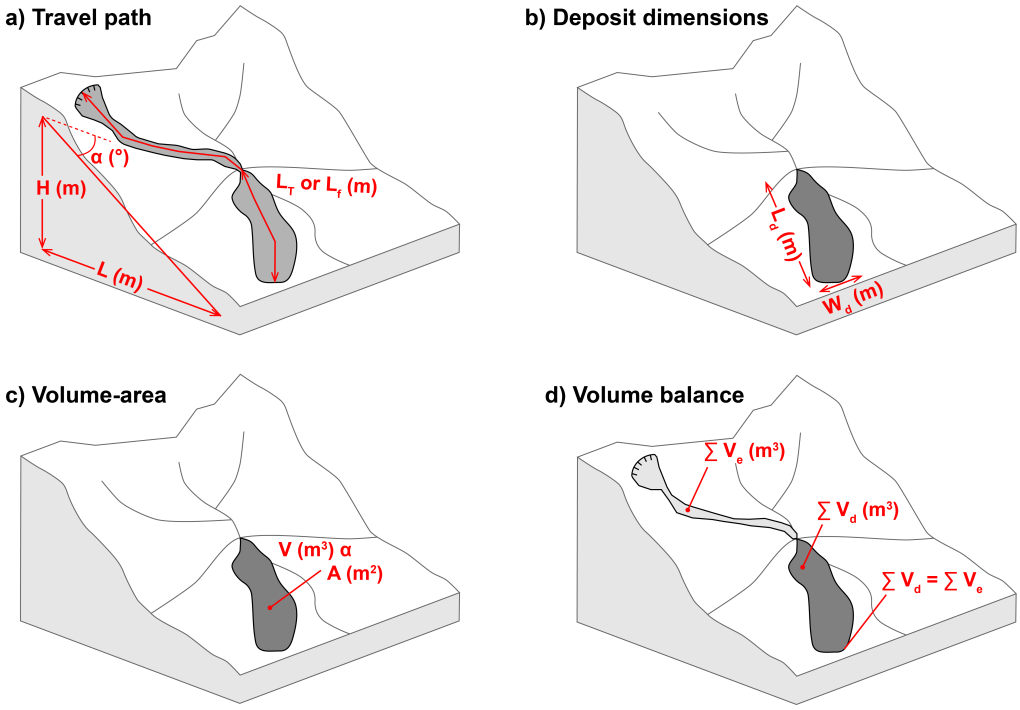

Figure 2.6. Schematic (not to scale) depicting empirical approaches for forecasting debris flow runout. **a)** Travel path, such as total travel path length (L_T), path length relative to the fan apex (L_f) (e.g., Rickenmann, 1999), or angle of reach (α) defined by the ratio of fall height (H) to horizontal travel distance (L) (e.g., Corominas, 1996); **b)** deposit dimensions, such as deposition length (L_d) and maximum lateral deposit width (W_d) (e.g., Tang et al., 2012); **c)** planimetric inundation area (A) correlated to debris flow volume (V) (e.g., Griswold & Iverson, 2008); and **d)** volume balance rules quantifying entrainment and deposition along a flow path, by which the total travel distance is defined where the cumulative flow volume is zero, i.e., the sum of the volume deposited (V_d) is equal to the sum of the volume entrained (V_e) (e.g., Fannin & Wise, 2001).

2.6.1 Travel Path

Runout is commonly represented by the angle of reach (α), or fahrböschung, which is the arctangent of the ratio of the fall height (H) to the horizontal travel distance (L), measured from the head of the source landslide to the furthest runout extent (Figure 2.6a). In other words, it is the inclination of the line projected from the landslide crest to the deposit toe. This parameter was first defined by Heim (1932), who designated α as a relative index of the mobility of rock avalanches, describing energy loss due to friction. Heim (1932), Scheidegger (1973), and many others have correlated α to landslide volume, showing an inverse relationship to event volume (V). Corominas

(1996) presented the first and most comprehensive review examining the effect of V on the H/L ratio for various landslide types including debris flows, finding a continuous reduction of H/L with an increase in V (m^3) (Equation 2.2). Equation 2.2 is from a dataset of 71 debris flows, debris slides, and debris avalanches (excluding mudflows and mudslides) triggered by storms in northern Spain (Corominas, 1996). Corominas (1996) found scattering in the relationship was mostly due to mechanisms of motion, obstacles or topographic constraints on the path.

$$\log(H/L) = -0.105\log(V) - 0.012 \tag{2.2}$$

Rickenmann (1999) derived relationships for L as a function of V and H, where the product of V and H can be considered as potential energy of the mass movement.

Regional angle of reach distributions can be used to define preliminary hazard zones without specifying hazard scenarios and associated volumes. Rickenmann & Zimmermann (1993) defined a minimum H/L ratio of 0.19 using a dataset of 600 debris flows in the Swiss Alps, which is comparable to a rule of thumb once used in Japan of 0.2 (Takahashi, personal communication, 1994, as cited in Bathurst et al., 1997). Minimum H/L ratios for matrix supported flows (0.07) were found to be lower than coarser-grained, clast supported flows (0.19) (Rickenmann & Zimmermann, 1993). Zimmermann et al. (1997) defined a lower envelope for H/L using the catchment area, where larger catchment areas are correlated to smaller H/L ratios (i.e., longer runout). A recent application of the angle α in hazard management tools is the GIS-based regional susceptibility model Flow-R (Horton et al., 2013). Flow propagation in Flow-R uses a spreading algorithm and energy balance laws, where energy loss due to friction can be parameterized by the angle of reach. Travel path length measured horizontally, such as the total travel path (L_T) or path relative to the fan apex (L_f) shown in Figure 2.6a, neglects the vertical component of energy loss. From a comprehensive study of various long runout landslides, Legros (2002) found that travel distance depends primarily on volume, while height just adds scatter to the correlation. A recent empirical study of rock avalanches by Mitchell et al. (2020) found contrary evidence, with predicted runout distances highly sensitive to the fall height, although initiating conditions for rock avalanches are unique to many debris flows.

Rickenmann (1999) provides a geometric scaling equation relating V (m^3) to L_f (m) based on a dataset of 140 debris flows from various sources (Equation 2.3). Rickenmann (1999) describes that runout is better represented by L_f since local changes in the channel geometry on the fan and different material properties are relatively more important compared to the entire travel path in the basin. Equation 2.3 is not recommended by Rickenmann (1999) for practical application as the scatter between predicted and observed values is too large.

$$L_f = 15V^{\frac{1}{3}} \tag{2.3}$$

A recent analysis of runout distances on depositional fans in the Wenchuan earthquake zone by Zhou et al. (2019) derived empirical multivariate equations suitable for prediction of L_f using two variables: volume and internal catchment relief.

Models that use stopping criteria based on path geometry to predict total runout (e.g., Benda & Cundy, 1990; Burton & Bathurst, 1998; Miller & Burnett, 2008) are generally used for sediment transport modelling in the catchment. Stopping criteria are based on the assumption that debris flows tend to deposit sediment where the channel gradient declines and/or at high tributary junction angles.

2.6.2 Deposit Dimensions

Predicting deposit dimensions, such as maximum deposit length (L_d) and maximum lateral deposit width (W_d) shown in Figure 2.6b, are important for hazard assessments on fans where debris flow transport in the catchment is of less importance compared to deposition patterns on the fan. Most of these relationships use volume as a predictor variable (e.g., Chen et al., 2007; Ikeya, 1981; Yu et al., 2006) as there is a natural scaling relationship (discussed further in Section 2.6.3). Chen et al. (2007) considered the effect of deposit shape on these relationships. Tang et al. (2012) used stepwise multiple regression analysis without volume as a candidate variable due to uncertainty in its estimation. Instead, the model by Tang et al. (2012) uses catchment area, catchment relief, and an estimate of the volume of removable sediment in the catchment to estimate maximum deposition width and length. Some of these models assume the onset of deposition starts at the fan apex, making L_d equivalent to L_f described previously.

2.6.3 Volume-Area Relationships

Assuming landslide deposits are geometrically similar, there is a ratio between volume (V, m^3) and the planimetric area (A, m^2) based on physical scaling laws that follows the power law relationship in Equation 2.4, where c is a calibrated coefficient (Hungr & Evans, 1993; Iverson et al., 1998). Griswold & Iverson (2008) calibrated this coefficient for rock avalanches and debris flows (c = 20), finding that power law equations with a specified slope of 2/3 are statistically indistinguishable from the best-fit power law regressions. Many other authors have calibrated the volume-area power law relationships to local and global debris flow datasets (e.g., Berti & Simoni, 2007; Booth et al., 2020; Crosta et al., 2003; D'Agostino et al., 2010; Scheidl & Rickenmann, 2008; Webb et al., 2008; Yu et al., 2006), as summarized in Figure 2.7.

$$A = cV^{2/3} \tag{2.4}$$

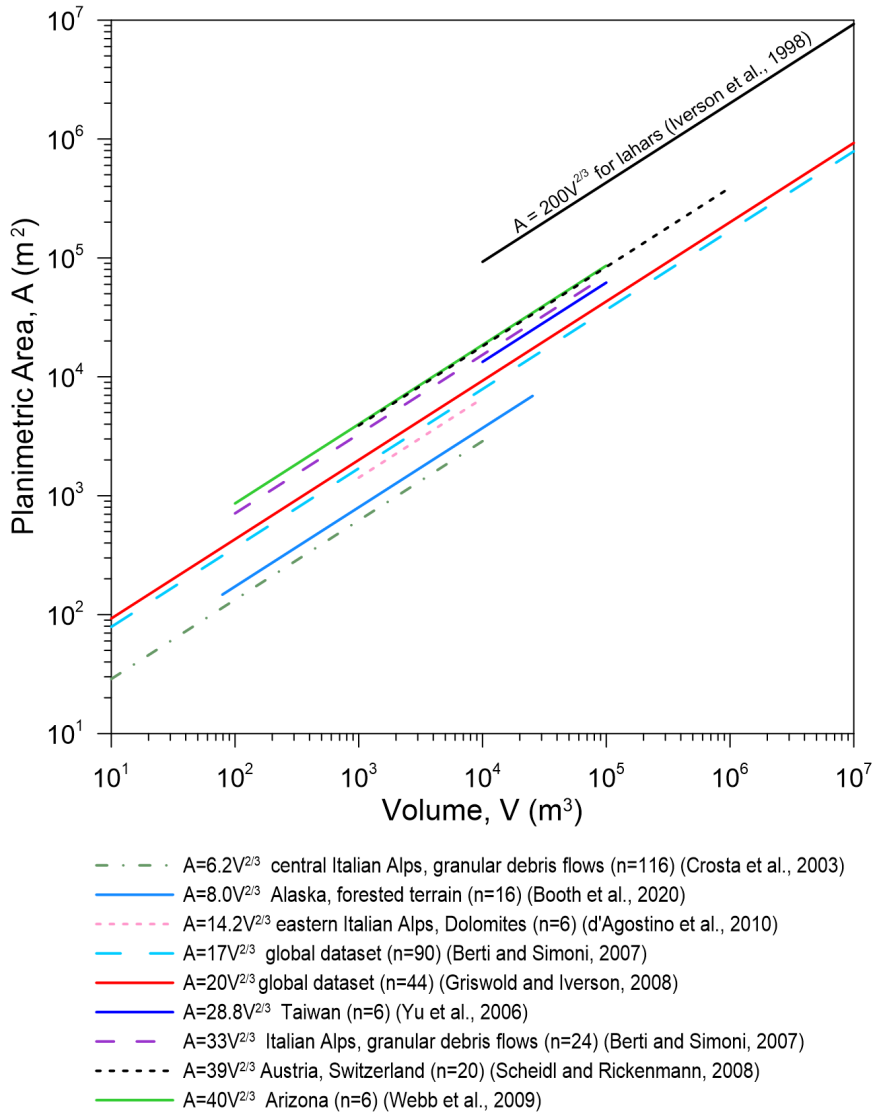

Figure 2.7. Power law scaling relationships with a 2/3 slope between volume and area for non-volcanic debris flows, over the domain of the respective volumes for each dataset. Trendline for lahars provided for reference.

The c coefficient can be interpreted as a mobility coefficient, irresepective of volume. As described in Section 2.4, mobility can be related to properties of the flow or topographic constraints. A c coefficient of 200 for lahars (debris flows from volcanoes) mean lahars typically inundate a planimetric area roughly ten times greater than a debris flow of the same volume. Scheidl & Rickenmann (2010) correlated c to the average fan slope and the average channel slope. The c

coefficients from the non-volcanic data sources shown in Figure 2.7 vary from 6.2 to 40. The variance could be related to many of the factors listed in Section 2.4, including different geology, climate, and geomorphic setting, or in part measurement inconsistency (Simoni et al., 2011). Landslide volumes are often estimated by multiplying an area covered by an estimated average thickness (Legros, 2002), so there is an inherent relationship between the two variables due to measurement.

Volume-area relationships are implemented in inundation mapping programs such as LAHARZ (Schilling, 1998), DFLOWZ (Berti & Simoni, 2014), and TopRunDF (Scheidl & Rickenmann, 2010). They are also used to reconstruct frequency-magnitude curves by associating a volume with a historical inundation area (Jakob, 2005).

2.6.4 Volume Balance

Volume balance methods determine the total runout based on the point at which volume entrained equals volume deposited (Figure 2.6d). Rulesets for erosion and deposition are based on the observation that debris flows tend to entrain material through steep, confined sections of the travel path, and deposit material at unconfined sections with lower gradients (Benda & Cundy, 1990; Fannin & Wise, 2001). Based on field survey data of 449 debris flows from glaciated hillslopes in coastal BC that were clear-cut logged, Fannin & Rollerson (1993) found the deposition of channelized events to be influenced by the ratio of channel width to channel gradient, with the onset of deposition expected when the ratio exceeds unity. Extending this work, Fannin & Wise (2001) developed an empirical-statistical model that calculates volume change based on reach geometry and slope angle for different flow types (unconfined, confined, and transition). Miller & Burnett (2008) calibrated entrained/deposited volumes and probability of debris flow termination to empirical data using the following attributes along the flow path: forest-cover class, gradient, flow path confinement, and junction angle.

2.6.5 Discussion

Empirical-statistical methods require a robust database of field observations for validation. The number of events in a dataset may be limited and biased since large magnitude debris flows are infrequent and smaller events often go undetected. Applying an empirical relationship outside of

the dataset area must be done with caution, and if so, the relationship should be from a comparable geographic area with similar geologic conditions (Rickenmann, 2005). Using observations of past events to forecast the runout of future events must also be done with caution as physical conditions (e.g., triggers, process type, topography, climate) will likely change with time.

From a review of 44 journal articles, conference papers, and technical reports, predictor variables used in various empirical runout models for debris flows (not including volcanic debris flows, such as lahars) are summarized in Figure 2.8. Although the count is biased by the empirical methods included here and the variables measured for each study, Figure 2.8 shows the variety of variables fit to explain runout for different datasets, with volume being the most common by far. For a discussion of the mechanisms that affect debris flow mobility, including some of these variables, refer to Section 2.4.

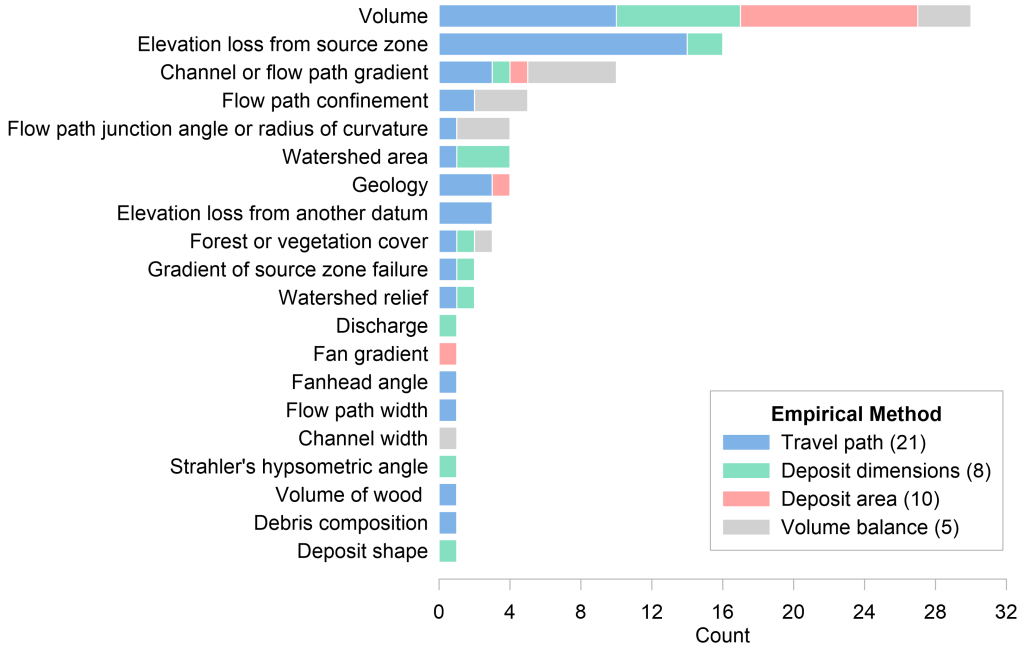

Figure 2.8. Predictor variables used in empirical debris flow runout relationships from a review of 44 published sources, categorized by methodology.

Debris flow volume is difficult to ascertain, both forensically and for forecasting purposes, resulting in high uncertainty with predictions. Forensically, in the absence of pre- and post-event lidar, volumes are typically estimated by multiplying an area covered by an estimated average

thickness (Legros, 2002). Deposits can be eroded or obscured by younger deposits, making event reconstruction prone to error (Jakob, 1996). Event reconstructions in the literature do not consistently include estimates of accuracy, precision, and error (Santi, 2014). Simoni et al. (2011) describes the scatter in the volume-area relationships for a homogeneous dataset is likely attributed to volume measurement errors rather than differences in flow mobility. There is considerable uncertainty when forecasting potential release volumes, and volume-based relationships are usually not practical for regional analyses.

The second most common predictor was elevation loss from a landslide source due to the number of relationships that use angle of reach. Estimating the location of the source zone can be challenging, especially if there are multiple source zones or if the debris flow volume is derived from progressive entrainment (e.g., Hungr et al., 2008). A few studies have used different datums, such as Prochaska et al. (2008) who defined the H/L ratio from the mid-point elevation of the drainage channel as it is more straightforward to identify. Similarly, Rickenmann (1999), Zhou et al. (2019), and others measure runout from the fan apex.

Due to the complexity and variability of debris flow processes, or perhaps measurement error, many of the empirical relationships show considerable scatter providing only order of magnitude estimates (Rickenmann, 1999). Variation within a dataset can be used to establish uncertainty for prediction, using prediction intervals as a proxy for probability of runout exceedance (McDougall, 2017; Mitchell et al., 2020).

Since uncertainty is inherent to natural processes like debris flows, deterministic estimates of runout cannot be reliable. As described in Section 2.3, risk assessments usually require runout estimates expressed as conditional probabilities. Different empirical approaches have been used to express debris flow runout probabilistically. Chen et al. (2007) derived different equations based on a non-exceedance probability using the cumulative distribution of the data. Simoni et al. (2011) assigned uncertainty factors to the volume-area relationship to associate probabilistic meaning to model results. The model by Fannin & Wise (2001) samples from a user-defined probability density function, with the number of simulations that surpass a given travel distance linked to the probability of exceedance. Bathurst et al. (1997) developed a logistic regression model for percentage of sediment

delivery to streams for shallow landslides that evolve into debris flows. Miller & Burnett (2008) assumed an exponential decrease in runout probability with distance travelled based on channel attributes.

Many of the flow path or volume balance models were developed for sediment transport in the watershed and may not be applicable for hazard management on developed fans. There were no relationships that directly addressed avulsion mechanisms on the fan since most of the methods are concerned with mobility away from a source, neglecting the possibility of major lateral diversions.

Schürch et al. (2011a) developed a novel stochastic fan evolution model based on empirical equations that attempts to model short and long-term fan behaviour driven by incision, aggradation, and avulsion over a sequence of events. In this model, flow volumes and sediment concentrations are sampled from probability density functions, a flow path is routed with a flow routing algorithm, empirical rules are applied for deposition, erosion, and stopping, and the process is iterated with an updated digital elevation model. Avulsions would be simulated when the topography is altered in such a way that a channel is blocked and/or there is a new topographically favourable flow path to a different part of the fan. Preliminary results show this model can be used to highlight locations in the channel network where avulsions are most likely to occur and what conditions are most likely to lead to avulsions (Schürch et al., 2011a). One foreseen limitation is having enough data to generate input probability density functions and to calibrate empirical coefficients, as well as observations on real fans to validate the overall results.

2.7 Challenges and Knowledge Gaps

Debris flows are complex, multi-phase processes with runout that varies in space and time. It has been well established that event volume increases mobility, but its effect on avulsion is more equivocal; a large peak discharge is more likely to overwhelm the channel capacity but it may also be erosive and self-channelizing. Irrespective of volume, flow composition and path characteristics affect debris flow mobility and avulsions, but it is unclear which variables are the most important to consider when forecasting runout. Although we are starting to understand avulsion mechanisms and indicators of impending avulsion, there is currently no broadly applicable, rigorous, and repeatable

way to define avulsion locations and associated probabilities.

Considering variability in debris flow mobility and avulsion scenarios, runout assessments should be probabilistic. Currently, most numerical models are unequipped to complete probabilistic analyses or simulate avulsions. Complex, multi-phase mathematical models may eventually simulate channel blockages, but these types of models are still in development. Empirical methods are a practical alternative based on observations of real events. There are currently no empirical methods for debris flows that consider flow deviation due to avulsion, and few that are probabilistic. Empirical model variables should be easy to obtain and measure with consistency and accuracy, however many of the existing relationships require a total volume and initiating point to be estimated a-priori, which are generally uncertain.

Although experimental and numerical studies can provide great insight into runout behaviour under controlled conditions, it is important to continue to collect data on natural debris flow fans, both for model validation, but also for developing empirical relationships and expert judgement. There remains a need to collect high-quality and consistent field measurements (with estimates of error) immediately following debris flow events to generate more reliable databases for statistical analysis.

2.8 Summary

- Debris flows are extremely rapid, surging, multi-phase mass movements down steep creeks that exhibit dynamic feedbacks between entrainment and deposition. They exist on a wide and continuous spectrum of hydrogeomorphic processes with varying water content and flow behaviour.
- Hazard and risk assessments on fans require forecasting debris flow motion, which should consider variability in mobility and the possibility of channel avulsions.
- Debris flow mobility is highly correlated to volume, but flow composition and interaction with the path have some effect too. Most generally, high volume events with high sustained pore fluid pressures travelling down steep, channelized, and unobstructed paths are highly mobile.
- Avulsions move deposition across a fan surface. They can be triggered by volume overwhelm-

ing the channel, superelevation of flow, and channel blockages. Despite recent advances in our understanding of these processes, there is still little evidence to help forecast avulsion locations and frequency on a fan.

- Empirical methods are a practical and widely used approach to forecast runout based on direct observation and guided by knowledge of physical processes, where our understanding may be limited. There are a wide variety of empirical tools, including angle of reach and volume-area scaling relationships, that provide insight into controls on mobility. Currently, there are no empirical methods that consider both down-fan and cross-fan variability in runout trends, which is important for risk-based decision making considering variable mobility and avulsion behaviours inherent to debris flow processes. This thesis addresses this key knowledge gap.

Chapter 3

Creating a Geospatial Dataset

The geospatial dataset consists of a historical archive of spatial impact areas and flow paths for 30 fans in SWBC. This chapter details the process of creating this dataset, including study site selection, geomorphic fan mapping methodologies, acquisition and processing of remote sensing data, and field methods. Methodology for calculating debris flow volumes and morphometric variables are described, along with data summaries. Data quality classes are presented to give the reader an intuition for mapping quality, followed by a discussion of the limitations of this dataset. The reliability of the analyses in Chapter 4 hinges on the quality and thoroughness of the data presented here. There remains a need to collect high-quality field and remote sensing data, both immediately following debris flows and back through time, to continue growing rich geospatial datasets; this chapter provides some guidance on how to do so. Mapping and field photographs for each fan site can be found in Appendix A, and geomorphic mapping shapefiles with metadata are provided in Appendix B.

3.1 Fan Site Selection

The 30 fans in this study were selected from a larger event database compiled as part of this work, consisting of 98 fans and hundreds of events (Figure 3.1). The event database was initiated in 2017 by D. Bonneau from Queen's University, who compiled data on events in Squamish Lillooet Regional District (SLRD) from news articles, DriveBC records, theses, publications, engineering reports,

satellite imagery, and personal observations (not published). Bonneau's preliminary inventory was manually checked and filtered to exclude rock avalanches, debris avalanches, and suspected flooding processes, and was expanded to include recorded events from the Metro Vancouver and Fraser Valley Regional Districts using similar sources listed above. The main references used to compile the inventory include: Hungr et al. (1984), Hungr et al. (1987), Evans & Lister (1984), VanDine (1985), Jordan (1994), Jakob (1996), Jakob et al. (1997), Jakob et al. (2016), Friele & Clague (2004), BGC (2004), Blais-Stevens & Septer (2008), and Sutton (2011). Well-documented and field mapped debris flows at Haida Gwaii (Queen Charlotte Islands) (Fannin & Rollerson, 1993; Fannin & Wise, 2001), and debris flows recorded elsewhere in western BC (e.g., Geertsema et al., 2009) were not included in this inventory due to their poor proximity for field work.

The fan sites selected for this study are shown in Figure 3.2 and listed in Table 3.1 (coordinates presented in NAD83 UTM Zone 10 N). The location of the anonymous case is undisclosed. These fan sites were manually chosen from the preliminary inventory using the following criteria:

- Presence of an active debris flow fan landform with minimal fan modification and a visible channel.
- A legacy of debris flows with impact areas on the fan visible in airphotos or satellite imagery, and/or well-preserved deposits, and/or well-documented debris flows that have been field mapped.

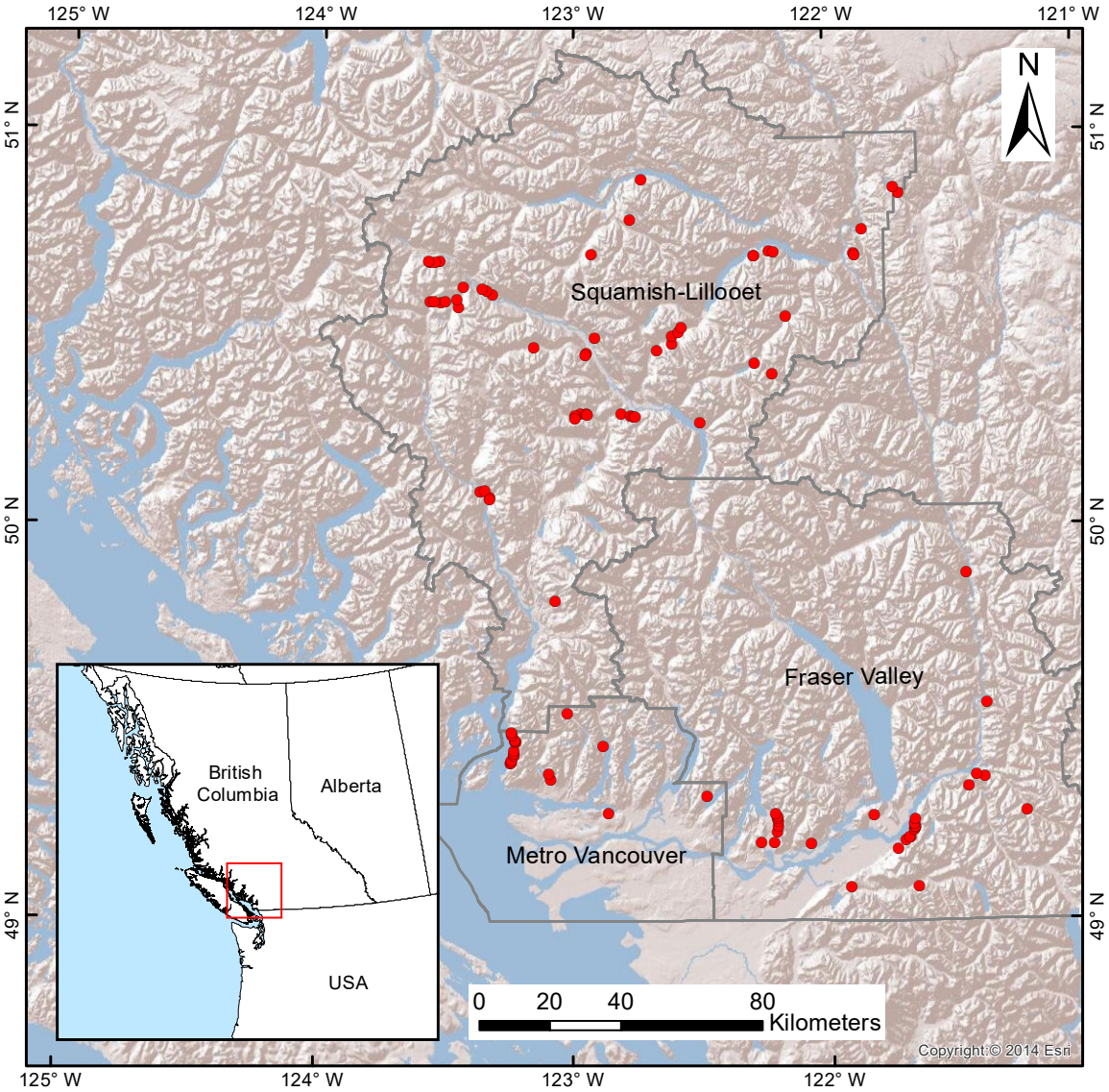

Figure 3.1. Location map of preliminary debris flow event inventory for SWBC. BC regional districts labelled for reference.

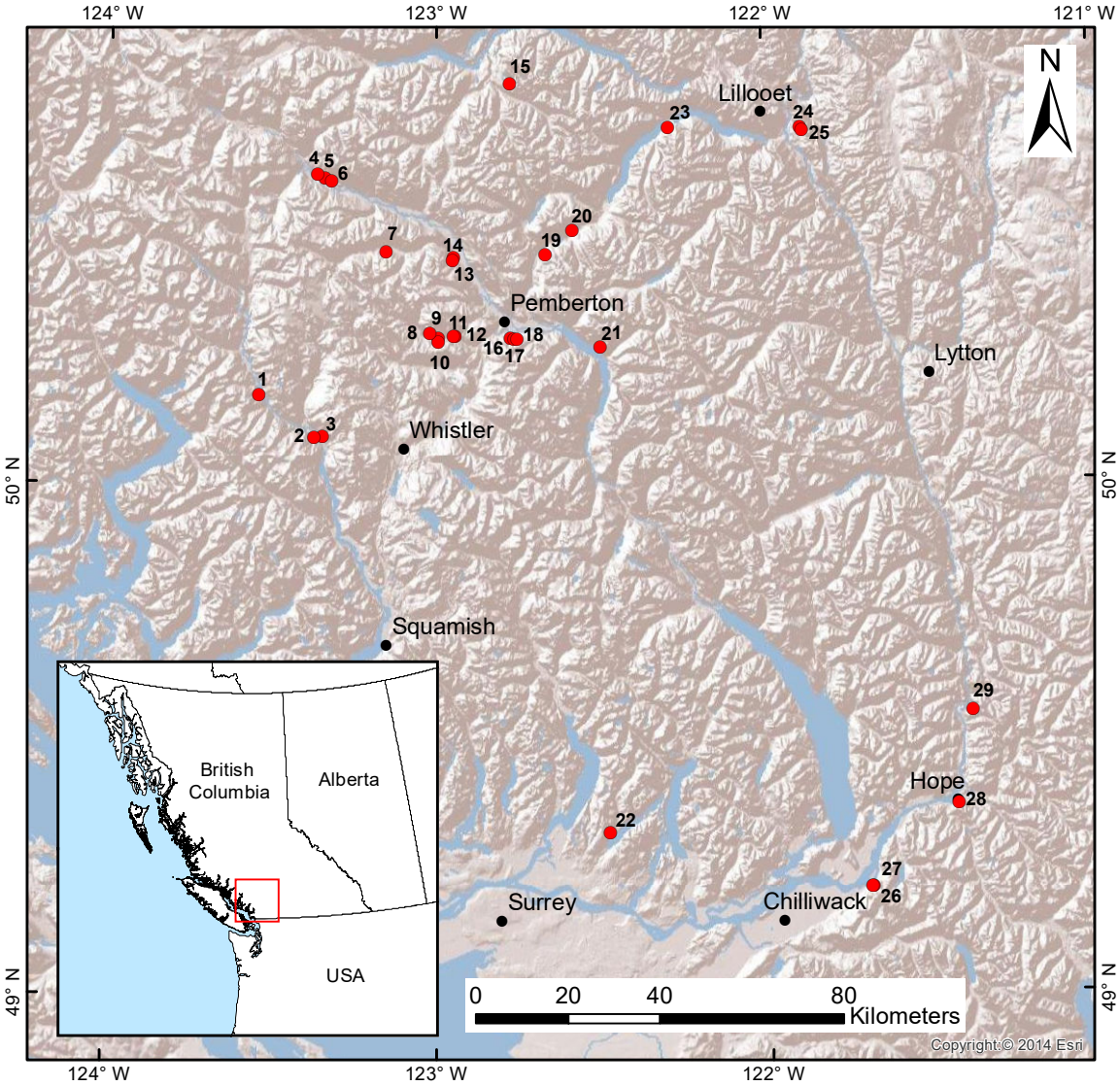

Figure 3.2. Location map of fan sites in this study.

Many of the fans in the study area have some form of fan modification (e.g., logging, development, roads, bridges, berms, channelization works), so this potential influence could not be fully avoided (e.g., Hope with an engineered deflection berm). Fans with large engineered barriers or filling basins were not included in this study. Debris flows that transport directly into a waterbody without much visible deposition on the fan, or where evidence of deposition is not preserved, were not good candidates for spatial impact mapping. This eliminated creeks along the Sea to Sky corridor (Blais-Stevens & Septer, 2008), with many events flowing directly into Howe Sound or filling engineered

Table 3.1. List of fan sites in this study.

Label	Name	Easting (m)	Northing (m)	Key Reference
1	Abandoned	461334	5558054	This thesis
2	Endurance	473304	5548766	Jakob (1996)
3	Terminal	475132	5549082	Jakob (1996)
4	Middle Lillooet W	474226	5606122	Jakob (1996), also known as Clearwater Creek
5	Middle Lillooet C	475684	5605380	Jordan (1994)
6	Middle Lillooet E	477147	5604529	Jordan (1994)
7	Petersen	488876	5589224	Jakob (1996)
8	Upper Rutherford	498423	5571312	This thesis
9	No Law	500317	5570349	Jakob (1996)
10	Sootip	500332	5569470	This thesis
11	Lower Rutherford W	503650	5570723	This thesis
12	Lower Rutherford E	503916	5570658	This thesis
13	Ross	503460	5587279	This thesis
14	Nightmare	503560	5587870	Jordan (1994), Jakob (1996), also known as Lower Ryan
15	Fergusson	515823	5625672	Jakob (1996)
16	Currie B	515965	5570375	BGC (2018a)
17	Currie C	516839	5570140	BGC (2018a)
18	Currie D	517411	5570114	BGC (2018a)
19	Deepa	523562	5588576	Jakob (1996)
20	Neff	529458	5593780	Lau (2017)
21	Catiline	535567	5568500	BGC (2015)
22	Fern	537775	5462900	This thesis
23	Bear	550167	5616375	BGC (2018b)
24	Fountain S	578798	5616465	Jordan (1994), Jakob (1996), also known as Gunbarrel II
25	Fountain N	579160	5615932	Jordan (1994), Jakob (1996), also known as Gunbarrel I
26	Cheam W	594952	5451397	DriveBC
27	Cheam E	595063	5451381	DriveBC
28	Hope	613674	5469474	Jakob et al. (1997)
29	Allard	616587	5489888	This thesis
-	Anonymous	-	-	This thesis

debris basins. Creeks at the Mount Meager volcanic complex, a Quaternary volcano in the study area with a history of large volcanic debris flows (e.g., Friele et al., 2008), were either well-incised into their fan surfaces, and/or consist of large multi-process fan complexes, including fans formed by rock avalanches. Moreover, it was difficult to distinguish individual events on very active fans due continuous overprinting of previous deposits. A debris flow creek dissecting a presumed rock avalanche deposit was also excluded since the debris flow fan was not well distinguished from the rock avalanche. Fans formed under paraglacial conditions were not candidates for this study since the fan area is not representative of recent debris flow activity. Paraglacial fans have been exposed to rapid shifts in base level and reduction of debris supply post-glaciation, causing erosion by trunk streams, fanhead trenching, and fan dissection, leaving large portions of the fan inactive (Ryder, 1971).

3.2 Geomorphic Fan Mapping

The following section describes the geomorphic features mapped to create this geospatial dataset. All mapping was completed in ArcGIS using an ensemble of remote sensing and field data described in Section 3.3, including airphotos, satellite imagery, lidar, contour basemaps, and field data. An example is shown in Figure 3.3. Mapping at each fan site can be found in Appendix A along with shapefiles in Appendix B.

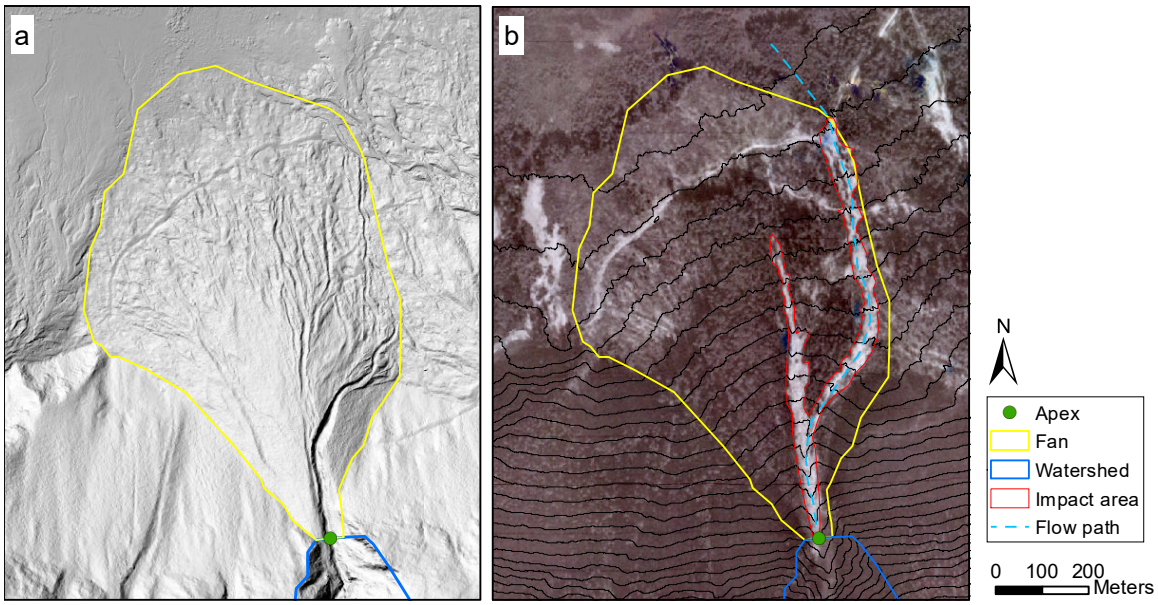

Figure 3.3. Example of geomorphic mapping at Currie C using **a)** lidar hillshade to define the apex and fan boundary; and **b)** 1996 airphoto orthomosaic to delineate an impact area and flow path (20 m contours derived from lidar). 2017 ALS bare earth hillshade courtesy of SLRD.

3.2.1 Fan Boundary

Fans are sloping, semi-conical landforms at the mouth of a mountain basin formed by the deposition of sediment discharged by hydrogeomorphic processes such as floods, debris floods, and debris flows. They are planimetrically fan-shaped with contours that bow in the down-slope direction (Bull, 1977). For geohazard risk assessments, the fan landform is often used as a zoning tool and represents an area susceptible to hydrogeomorphic hazard impact. The fan boundary can also be interpreted as a statistical upper-bound of its formative processes, except in cases where the fan has been eroded or buried. Given these descriptions, the fan boundary was mapped using the slope and shape of contours, and to include evidence of debris flow processes such as lobes, levees, and channels from the same sediment source. For coalescing fans, the orientations of channels and levees were used to differentiate sediment sources. For fans that coalesce with other landforms such as floodplains or talus slopes, the boundary was set to differentiate the dominant geomorphic process.

3.2.2 Fan Apex

The fan apex is the highest point of the fan landform. It represents a transition between mostly conveyance in the steep and confined drainages of the watershed to the onset of deposition at the fan. In the context of hazard and risk, elements at risk are typically located below this point since permanent development in the watershed is less common, especially in Canada. The fan apex was visually determined using contours and aerial imagery as the point of loss of lateral channel confinement from the basin valley slopes.

3.2.3 Impact Area

An impact area is defined here as any area below the fan apex that has been impacted by a debris flow, or multiple debris flows, over a certain time period. The impact area is distinguished from the deposit area as it represents any areas of debris flow erosion, transport, and deposition (see schematics in Figure 3.16). For the earliest observation record, the impact area is referred to as the "baseline" and represents the area most recently impacted by debris flows. Although it is possible that a spectrum of hydrogeomorphic process types are present within these defined areas, they have been referred to as debris flow impact areas for brevity (discussed further in Section 3.8). Mapping certainty was qualified for each impact area using classes defined in Section 3.7. In total, 176 impact areas (146 not including baseline impact areas) were mapped across 30 fans in this dataset. 110 of these impact areas were flagged as most likely an impact area associated with a single debris flow event (discussed further in Section 3.7).

3.2.4 Flow Path

The flow path is defined here as a line from the fan apex to the toe along either the active channel, the center of deposition if there is no defined channel, or the path of steepest descent past the toe of the deposit. If there were multiple active channels, the most active (i.e., most incised or most notable deposition) was selected (e.g., Figure 3.3). In the context of geohazard assessments, this line represents the most likely flow path of future hydrogeomorphic processes at a given time. A flow path was defined for each of the 176 impact areas in this dataset.

3.3 Data Sources

3.3.1 Airphotos

Hundreds of historical airphotos of the fan, watershed, and surrounding areas for each study site were scanned from the UBC Geographic Information Centre (GIC) Airphoto Library, as summarized in Table 3.2. The GIC airphoto archive includes over 2.5 million airphotos at various scales across BC dating back to 1922. An average of 15 observation points over an average span of 58 years were available from airphotos. Those lacking adequate scale to discern geomorphic features, or those obscured by clouds or snow, were not included. Some of the airphotos previously scanned at Catiline, Bear, Cheam E, and Cheam W were shared by BGC Engineering Inc. (BGC).

Airphotos were inspected for changes in erosion and deposition at the fan sites. Indicators of debris flow activity include the formation of levees and lobes, removal of vegetation, and changes in channelization including deepening/widening of channels, channel infilling, and migration by avulsion. Airphotos were selected for georeferencing if there was notable change since the previous photo, or as a baseline. An example of an impact area delineated using airphotos is shown in Figure 3.3.

Where possible, airphotos were orthorectified using Agisoft Metashape Professional (Metashape) (Agisoft LLC., 2019). Metashape is a commercial software that creates three-dimensional models from overlapping photographs using Structure from Motion (SfM). For this work, Metashape was used solely to orthorectify airphotos and not for reconstructing topography. Airphoto flight lines that were good candidates for orthorectifying in Metashape were those with three or more overlapping airphotos over the fan area, a small enough scale for accurate tie point selection (generally less than 1:30,000), and a large enough scale to cover variable terrain elevations (generally greater than 1:5,000). An example of an orthomosaic made at Fergusson with only 3 airphotos at a scale of 1:31,860 and a Digital Elevation Model (DEM) with a 25 m pixel size is shown in Figure 3.4. Other orthomosaics can be seen as basemap imagery in Appendix A for some of the fan sites. In total, about 60 orthomosaics were created in Metashape using the following workflow, adapted from Roberti (2018):

1. **Scan airphotos**. All airphotos were scanned at 800 dots per inch, which ensures about a 1 m pixel size given the upper bound of the expected model photo scale (1:30,000), following guidelines by Linder (2016). At least three overlapping airphotos over the fan site were used, but ideally more to include side overlap.
2. **Mask photos**. Photo frames and inscriptions were manually removed with "Intelligent Scissors".
3. **Align photos**. Metashape generates a sparse point cloud by matching features between photos. Photos were initially aligned with the "high" resolution setting, and re-aligned with a lower setting (less points) if the model was over-fitting and generated an unrealistic point cloud. Most photos were successfully aligned with the "medium" setting.
4. **Georeference**. Ground Control Points (GCP) were placed using lidar and imagery instead of being field-collected. In Metashape, the coordinate system was set to NAD83 UTM Zone 10 N. In ArcGIS, a point shapefile was created with the same coordinate system to store GCPs. One by one, GCPs were selected in ArcGIS and corresponding markers added to the airphotos in Metashape. If available, lidar and orthophotos were used to pick GCPs, otherwise, points were selected with DigitalGlobe satellite imagery (tile layer by Esri, 0.5 m resolution). Finding reliable GCPs was the most challenging and time-consuming step, especially with lower quality imagery or where the landscape has changed (e.g., forestry, construction, flooding, variable snow cover, etc.). Ideally GCPs are in flat, stable, and easily recognizable locations that constrain the coordinate in the x, y, and z directions (Roberti, 2018). For this work, GCPs were placed on the following features: corners of buildings or bridge abutments, road or path intersections, powerline footings, distinct bedrock features or lineations, bedrock creek junctions, large boulders, small ponds, or sometimes the end of a large fallen tree. Changing geomorphic features such as channels or river banks were not used. About 2-5 GCPs were chosen per airphoto, but this varied depending on the airphoto scale and availability of reliable GCPs. GCPs were also selected to be evenly spaced across the airphotos and to cover a range of elevations. After GCP selection, elevations were extracted to the point file in ArcGIS from a DEM, either lidar or TRIM. The point shapefile was exported from ArcGIS to a .csv file and

imported into Metashape to associate the x,y,z coordinates to each marker ID.

5. **Optimize**. Metashape adjusts camera alignment and updates the sparse cloud based on the GCPs to improve accuracy. Once optimized, the GCPs with the lowest planimetric accuracy were unselected, and the model was re-optimized to improve accuracy. This was an iterative process and sometimes additional GCPs were added, removed, or adjusted to attain a planimetric accuracy less than about 10 m for each GCP.
6. **Build dense point cloud**. Based on the camera positions, Metashape calculates a depth map to generate a dense point cloud. Aggressive depth filtering was used to omit outliers, which is recommended for aerial photography.
7. **Build mesh**. Metashape interpolates polygons between points to create a surface. The "Height field" setting that interpolates along the z axis (ideal for aerial photography) and a "high" polygon count was used, per recommendations by Roberti (2018).
8. **Build orthomosaic**. Default settings were used. Orthomosaic was exported as a .tif file for use in ArcGIS.

For scenes without sufficient overlap, airphotos were georeferenced in ArcGIS by aligning the airphoto image raster with control points. About 10 evenly distributed control points were selected for each airphoto using the methodology described above for Metashape (Step 4). Different transformations were tested to warp the image to match the control points. Although the resolutions of the ArcGIS georeferenced airphotos are higher than those of the Metashape orthomosaics, georeferencing in ArcGIS is not as reliable due to aerial photogrammetry distortions, such as varied terrain or camera tilt. It was found that the airphotos georeferenced in ArcGIS were subject to minor distortions or did not align with the base imagery along steep slopes. Since Metashape uses photogrammetry principles to preserve 3-dimensional scenes, the Metashape orthomosaics were more reliable as georeferenced base imagery. However, the airphotos georeferenced in ArcGIS were still useful for observing change and guiding mapping, in concert with other remote sensing data.

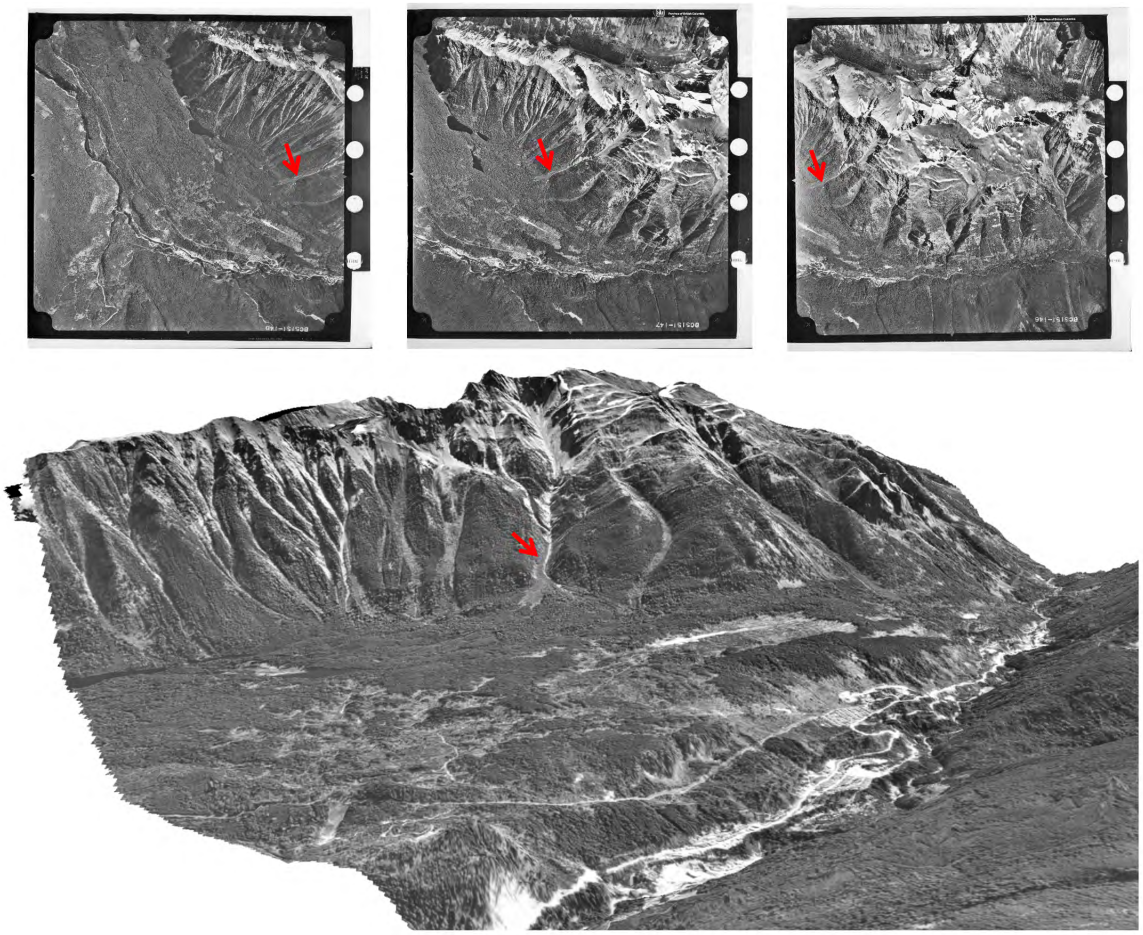

Figure 3.4. 1965 orthomosaic covering fan and watershed for Fergusson (red arrow) created with Metashape using three airphotos at a scale of 1:31,860 and TRIM DEM with a 25 m pixel size.

Table 3.2. Summary of airphoto and Metashape airphoto orthomosaic coverage at each fan site.

Fan site(s)	(Count) Airphoto years	(Count) Methashape orthomosaic years
Abandoned	(11) 1947, 1964, 1967, 1976, 1980, 1981, 1986, 1990, 1994, 1999, 2005	(5) 1947, 1967, 1976, 1986, 1994
Endurance and Terminal	(10) 1947, 1948, 1964, 1974, 1976, 1980, 1982, 1986, 1990, 1994	(5) 1947, 1964, 1976, 1986, 1994
Middle Lillooet W, C	(14) 1947, 1948, 1965, 1973, 1976, 1979, 1980, 1981, 1982, 1986, 1990, 1994, 1997, 2006	(7) 1965, 1973, 1976, 1979, 1986, 1990, 1994
Middle Lillooet E	(15) 1947, 1948, 1962, 1965, 1973, 1976, 1979, 1980, 1981, 1982, 1986, 1990, 1994, 1997, 2006	(7) 1965, 1973, 1976, 1979, 1986, 1990, 1994
Petersen	(15) 1947, 1948, 1962, 1964, 1969, 1973, 1978, 1981, 1982, 1986, 1987, 1994, 2005	(4) 1948, 1964, 1981, 1994
Upper Rutherford	(14) 1948, 1949, 1962, 1964, 1969, 1973, 1977, 1980, 1981, 1982, 1990, 1994, 2003, 2004	(4) 1948, 1973, 1981, 1994
No Law, Sootip	(13) 1948, 1949, 1962, 1964, 1969, 1973, 1980, 1981, 1982, 1990, 1994, 2003, 2004	(4) 1948, 1973, 1981, 1994
Lower Rutherford E, W	(12) 1947, 1948, 1962, 1964, 1969, 1973, 1977, 1980, 1981, 1990, 1994, 2003	(4) 1948, 1973, 1981, 1994
Ross, Nightmare	(14) 1946, 1965, 1969, 1973, 1976, 1977, 1978, 1980, 1981, 1982, 1986, 1990, 1994, 2005	(4) 1969, 1973, 1980, 1986
Fergusson	(10) 1947, 1964, 1965, 1975, 1978, 1979, 1987, 1993, 1997, 2005	(3) 1947, 1965, 1987
Currie B	(18) 1946, 1947, 1948, 1949, 1958, 1962, 1964, 1969, 1971, 1973, 1974, 1977, 1980, 1981, 1986, 1990, 1994, 2004	(7) 1946, 1958, 1964, 1969, 1980, 1990, 1994
Currie C, D	(19) 1946, 1947, 1948, 1949, 1958, 1962, 1964, 1966, 1969, 1971, 1973, 1974, 1977, 1980, 1981, 1986, 1990, 1994, 2004	(7) 1946, 1958, 1964, 1969, 1980, 1990, 1994
Deepa	(14) 1946, 1947, 1958, 1965, 1969, 1973, 1974, 1977, 1981, 1988, 1990, 1994, 1997, 2005	(3) 1946, 1958, 1969
Neff	(17) 1946, 1947, 1962, 1965, 1967, 1969, 1974, 1980, 1981, 1987, 1988, 1990, 1993, 1994, 1997, 2005, 2006	(4) 1946, 1969, 1988, 1993
Catiline	(13) 1948, 1962, 1967, 1969, 1979, 1980, 1981, 1987, 1990, 1993, 1994, 1997, 2005	(-)
Fern	(13) 1940, 1953, 1963, 1967, 1968, 1979, 1980, 1982, 1991, 1993, 1995, 1996, 2009	(1) 1982
Bear	(12) 1947, 1948, 1951, 1964, 1965, 1969, 1975, 1987, 1992, 1997, 2004, 2005	(1) 1948
Fountain N, S	(13) 1948, 1959, 1964, 1965, 1966, 1967, 1975, 1987, 1992, 1993, 1995, 1997, 2004	(7) 1948, 1959, 1964, 1975, 1993, 1997, 2004
Cheam W, E	(29) 1928, 1947, 1953, 1954, 1959, 1961, 1963, 1966, 1968, 1974, 1975, 1977, 1978, 1979, 1980, 1981, 1982, 1983, 1986, 1987, 1991, 1992, 1993, 1995, 1996, 1999, 2002, 2003, 2009	(5) 1928, 1947, 1953, 1961, 1968
Hope	(14) 1947, 1966, 1968, 1974, 1978, 1979, 1981, 1983, 1986, 1988, 1990, 1992, 1996, 2002	(1) 1996
Allard	(13) 1947, 1954, 1961, 1965, 1969, 1978, 1979, 1983, 1989, 1991, 1992, 1996, 2002	(5) 1947, 1961, 1969, 1983, 1996
Anonymous	(10) 1957, 1959, 1963, 1966, 1976, 1982, 1989, 1992, 1996, 2009	(-)

3.3.2 Satellite Imagery

Multispectral satellite imagery was accessed from Planet (2019) as part of Planet's Education and Research Program. Weekly to monthly 5-band RapidEye Ortho Tile imagery with a 5 m pixel size was available since 2009, and daily to weekly 4-band PlanetScope Scene imagery with a 3 m pixel size was available since 2016. Temporal resolutions varied depending on cloud cover or forest fire smoke, but monthly imagery since 2009 and weekly imagery since 2017 was reliably accessed for the entire study area from Planet. DigitalGlobe (tile layer by Esri) imagery within the last 3-5 years at a 0.5 m resolution was available for the entire study area. Satellite imagery hosted by Google Earth at various temporal and spatial resolutions was also used.

Planet (2019) satellite images were manually inspected in Planet Explorer to identify changes in deposition. For areas of visible change, pre- and post- event multispectral tiles were downloaded from Planet Explorer for mapping in ArcGIS. Change in brightness due to the removal of vegetation was often sufficient to delineate impact areas by visual inspection, but multispectral data was also used to supplement mapping. The normalized difference vegetation index (NDVI) is a spectral index commonly used for landslide detection and susceptibility mapping (e.g., Chen et al., 2018; Fiorucci et al., 2019; Martha et al., 2010; Miura, 2019; van Westen et al., 2008). NDVI is an indicator of green biomass and is calculated from near infrared (NIR) and red (R) spectral reflectances (unitless) (Equation 3.1, Rouse et al., 1974; Tucker, 1979). NDVI is an index from 0 to 1 with high values corresponding to dense vegetation and low values to bare rock or soil. In the event that a debris flow disturbs vegetation, a change in NDVI between n satellite images (dNDVI, Equation 3.2) may help with identifying an event and delineating impact extents.

$$NDVI = \frac{NIR - R}{NIR + R} \tag{3.1}$$

$$dNDVI = NDVI_n - NDVI_{n-1} \tag{3.2}$$

dNDVI calculated for three events is shown in Figures 3.5-3.7 with varying levels of success for impact area delineation. dNDVI was calculated with Planet satellite imagery in ArcGIS using

Image Analysis and Raster Math (i.e., pixel differencing). Low values (warm colours) indicate a decrease in vegetation, possibly due to the removal of vegetation or sedimentation, and high values (cool colours) indicate an increase in vegetation. Impact areas mapped using an ensemble of lidar change detection (where available), features in post-event lidar, orthophotos, satellite imagery, and/or field observations, are shown as a visual comparison to the dNDVI results.

The 2014 debris flows at Currie C and D fans shown in Figure 3.5 are visible in the dNDVI raster since these events impacted previously forested areas and sufficiently disturbed the canopy. Figure 3.5 is an example of ideal conditions for delineating impact areas with dNDVI. Figure 3.6 shows dNDVI compared to the lidar change detection results (described in Section 3.4.1) for a debris flow at Currie D in 2019. The dNDVI raster showed impacts to areas previously vegetated, such as the mudwave downstream of the main avulsion lobe, which was outside the limit of detection from the lidar change detection, but verified in the field. As expected, this method did not detect change where the lobe overprinted previous deposits. dNDVI greater than 0 in Figure 3.6 shows areas where lobes are starting to revegetate on adjacent fans. Lastly, the 2017 debris flows at Cheam E and W fans shown in Figure 3.7 were not well-delineated with dNDVI due to dense vegetation, except near the fan apex, which has been cleared by snow avalanches and debris, or along cutlines at the lower fan. dNDVI may be used as a way to automatically detect events and generate event inventories (discussed further in Section 5.3), however this was not attempted because of the limited availability and accessibility of pre- and post-event satellite imagery from Planet.

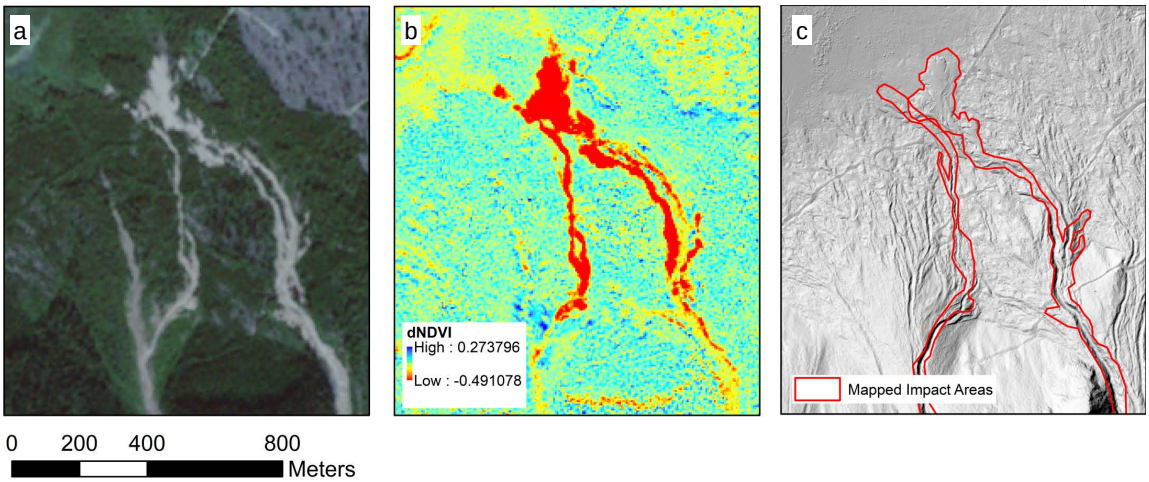

Figure 3.5. Debris flows at Currie C and D fans sometime between July and August 2014. **a)** RapidEye satellite imagery captured on August 7th, 2014 (Planet, 2019); **b)** dNDVI calculated between July and August 2014 RapidEye bands; and **c)** impact areas mapped using dNDVI results, field data, and features in post-event lidar. 2017 ALS bare earth hillshade courtesy of SLRD.

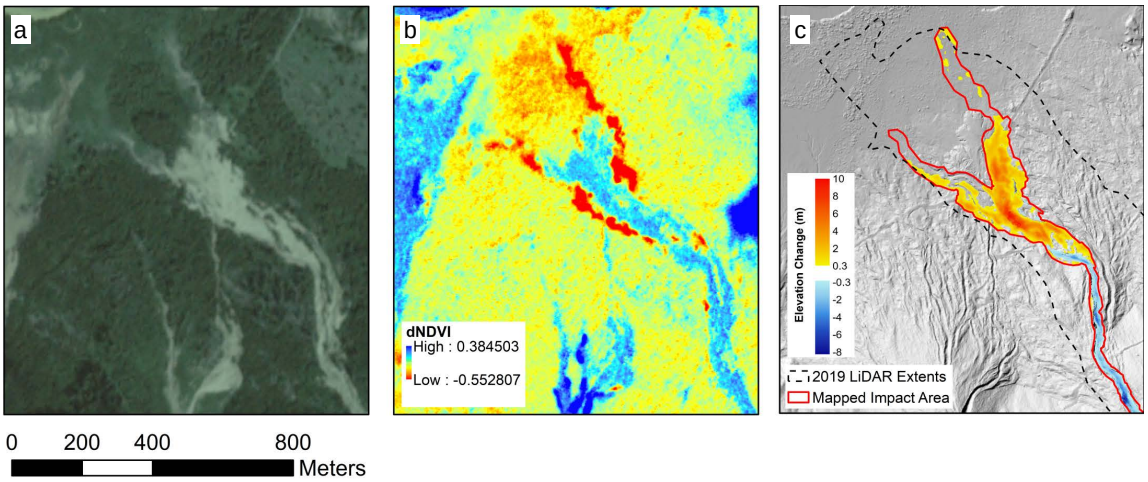

Figure 3.6. Debris flow at Currie D sometime between July 3 and 12, 2019. **a)** Planetscope satellite imagery captured on July 20th, 2019 (Planet, 2019); **b)** dNDVI calculated between May and July 2019 Planetscope bands; and **c)** results of lidar change detection between 2017 and 2019 surfaces (0.3 m limit of detection), and impact area mapped using field data, orthophotos, and lidar change detection results. 2017 ALS bare earth hillshade courtesy of SLRD.

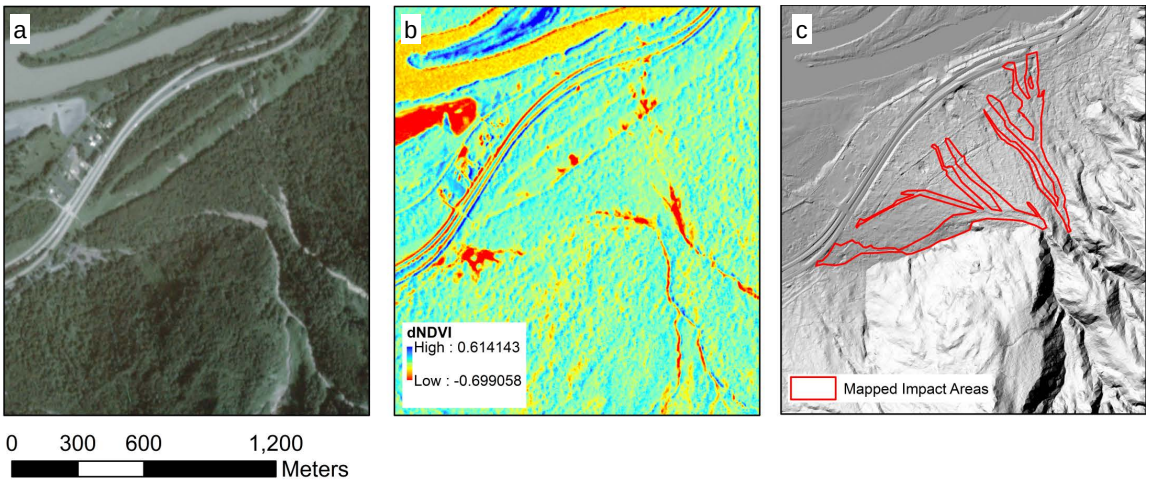

Figure 3.7. November 23, 2017 debris flows at Cheam E and W fans. **a)** Planetscope satellite imagery captured on July 5th, 2018 (Planet, 2019); **b)** dNDVI calculated between 2018 and 2017 Planetscope bands; and **c)** impact areas mapped using field data and high resolution Google Earth imagery. 2017 ALS bare earth hillshade courtesy of BC MOTI.

3.3.3 Lidar and Orthophotos

Lidar bare earth DEMs and orthophotos were available for 17 fan sites. Airborne laser scanning (ALS) lidar and orthophotos were acquired piecemeal from various agencies and institutions, as summarized in Table 3.3. Remotely piloted aerial system (RPAS, or drone) lidar and orthophotos at 3 fans were collected in September and October of 2019 using the UBC Geohazards Research Team drone. RPAS lidar details are summarized in Table 3.4. The platform is a Phoenix Lidar Systems MiniRanger ULS, which consists of a DJI Matrice M600 Pro drone equipped with a Riegl miniVUX laser scanner, Northrop Grumman uIMU, single-antenna dual frequency GNSS receiver, and a Sony A6000 camera with 16 mm prime lens. Data processing was completed using NovAtel Inertial Explorer v.8.80, Phoenix SpatialExplorer v.4.0.3, and TerraSolid v.019. A photo of RPAS data collection is shown in Figure 3.8, and an example of the final RPAS lidar product can be seen in Figure 3.9 as the bare earth hillshade.

Table 3.3. Summary of external ALS lidar data sources.

Fan site(s)	Year	Source	Coverage
Pavilion[1]	2011	BC Ministry of Transportation and Infrastructure	Fan
Catiline	2014	Squamish Lillooet Regional District	Fan and watershed
Allard	2015	Canadian National Railway	Fan and watershed
Neff	2015	BC Hydro	Fan
Middle Lillooet E, W, and C	2015	University of Northern British Columbia, Simon Fraser University	Fan
Cheam E and W, Hope	2017	BC Ministry of Transportation and Infrastructure	Fan and watershed
Currie B, C, and D, Bear	2017	Squamish Lillooet Regional District	Fan and watershed
Anonymous	2013, 2019	Metro Vancouver	Fan and watershed

[1]Fan site not part of this dataset except for volume-area relationship (Section 3.4.4).

Table 3.4. Summary of RPAS lidar data collected.

Fan site	Dates flown	Average point density (pts/m^2)	Average point spacing (m)	Fan area covered (km^2)
Currie D	October 1-2, 2019	6.7	0.38	0.50
Fountain N	October 23, 2019	8.1	0.35	0.95
Fountain S	September 18-19, 2019	8.1	0.35	0.44

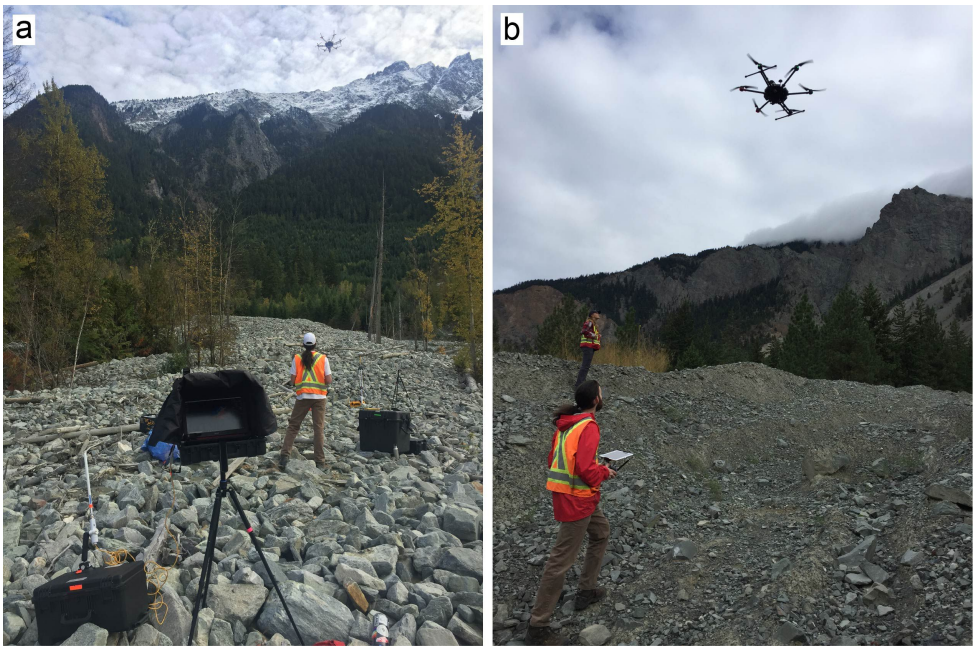

Figure 3.8. Photos of RPAS data collection at **a)** Currie D and **b)** Fountain S.

Lidar contours and hillshades were used to map impacts from debris flows, including levees, lobes, and channels, and to delineate the fan and watershed boundary. For three events in the dataset, pre- and post-event lidar was available for change detection analysis between the DEMs to estimate event volume and impact area, described further in Section 3.4.1.

In some cases, post-event lidar was used to confirm relative sequencing of recent lobe deposition based on cross-cutting relationships and superposition of lobes. An example of lobe superposition is shown in Figure 3.9 with well-preserved deposits at the lower Fountain S fan. Approximate dates and extents were first determined with satellite imagery (described in Section 3.3.2) and topographic features in the lidar DEM were used to refine mapping. The lower fan at Fountain S represents an idealized case. Further up-slope, the Fountain S fan is more channelized with many overlapping impact areas, so sequencing is not well-preserved in the topography. Deposition at the Fountain N lower fan is sheet-like, consisting of channelized surfaces rather than distinct lobes (Figure 3.9), so relative sequencing using topography was not possible here.

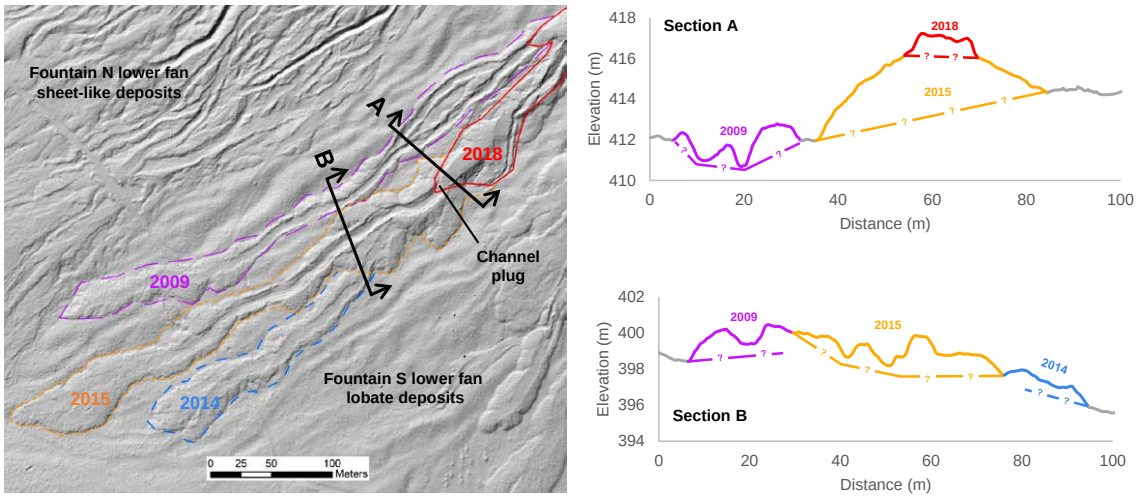

Figure 3.9. Interpretation of deposit sequencing at Fountain S lower fan based on Planet (2019) satellite imagery and topographic features in 2019 RPAS lidar DEM.

3.3.4 TRIM DEM

The Terrain Resource Information Management (TRIM) 1:20,000 DEM was used where lidar was not available. Elevation contours with a 20 m resolution and gridded map tiles with a 25 m pixel

size were accessed from the BC Geographic Data Catalogue.

3.3.5 Field Data

Geomorphic field mapping was completed at 18 of the 30 fans in the dataset over the period of July to November of 2018. Additional field observations at Currie D, Fountain N, and Fountain S were made during collection of RPAS lidar in September and October of 2019. Six additional fans were also visited in the field as part of this work, but were excluded from the final analysis, aside from the volume-area data at Pavilion (Section 3.4.4). Fans selected for field work were based on site accessibility, suspected recent debris flow activity, and priority to supplement or verify observations made using remote sensing data. A list of fan sites visited in the field is provided in Table 3.5. Field data from Catiline (BGC, 2015), Bear (BGC, 2018b), and the Anonymous site were collected and shared by BGC.

The main objective of the field work was to field-truth debris flow impact areas identified in airphotos and satellite imagery. Approximately 2-6 hours were spent at each fan with priority given to traversing recent flow paths and deposit boundaries. Field work consisted of hiking the fan to the fan apex and mapping debris flow lobes, levees, and channels. Fan boundaries, paleochannels, bedrock outcrops, and other landforms were recorded where possible. Any fan modifications were documented, including roads, bridges, berms, and culverts. Occasionally, the channel was hiked past the fan apex, but investigation of the watershed was beyond the scope of this work.

Topographic basemaps, georeferenced historical airphotos, satellite imagery, and lidar hillshades were accessed in the field with a GPS-enabled iPad tablet using the Avenza Maps app (Avenza Systems Inc.). Observation waypoints and tracks (e.g., Figure 3.10) were recorded with a Garmin GPSMAP 64s GPS unit with a position accuracy within 5 to 10 m under normal conditions. Hundreds of photos were taken during the field work and georeferenced to the GPS track timestamp to assist in mapping. Select field photos for each fan are shown in Appendix A, as well as throughout this thesis.

Where available, the following measurements and observations were made in the field:

- Deposition angle, superelevation angle, channel gradient, fan slope, and bank slope with a Suunto clinometer.

- Deposit thickness, levee dimensions, high water marks or mudlines, impact scar height, runup height, flow width, channel dimensions, and maximum cross-sections at bedrock controlled reaches with a measuring tape or Bushnell rangefinder.
- Description of debris, including grain-size (D50, D90, Dmax), sorting, structure, presence of organics, and clast lithology.

The following geomorphic (landform) and sedimentologic (deposit) evidence was used to identify debris flow processes on a fan (Costa, 1984; Giraud, 2005; Jakob, 2005; Lau, 2017; Pierson, 2004):

- Lateral levees along channel margins (Figure 3.11a).
- Trapezoidal to U-shaped channels with evidence of scour (Figure 3.11b).
- Paleochannels indicating previous flow paths (Figure 3.11c).
- Debris lobes, typically with positive relief (convex) and lobate margins (Figure 3.11d).
- Local damming by log jams or boulder clusters (channel plugs) (Figure 3.11e,f).
- Evidence of upstream runup, such as mud coatings and embedded gravel, on trees or other obstacles (Figure 3.11g).
- Inversely graded deposits lacking sorting or imbrication (Figure 3.11h).
- Matrix-supported deposits (Figure 3.11i), open-work structure also possible.
- Accumulation of coarse clasts at deposit margins or boulder studded surfaces (Figure 3.11j).
- Presence of megaclasts (Figure 3.11k).
- Buried logs with frayed ends (Figure 3.11l).

Impact area boundaries were delineated in the field where possible, which involved placing GPS waypoints or tracks along the edges of levees, lobes, and distal extents of muddy deposits (for recent events) (Figure 3.12). Observations of relative age helped with mapping, although these can be quite variable depending on the fan setting, fan activity, and climate. Given a distinguishable difference in relative age, and only where deposits have not been altered by subsequent flows, the following observations helped distinguish relative debris flow vintage in the field:

- Relative age of vegetation established on deposit surfaces.
- Degree of oxidation, moss cover, and lichen growth on deposit boulders (Figure 3.12).
- Channel activity, including scour, erosion, and deposition.

Table 3.5. Summary of field work completed.

Fan site	Easting (m)	Northing (m)	Date(s) of field work
Middle Lillooet W	474226	5606122	September 8, 2018
Middle Lillooet C	475684	5605380	September 8, 2018
Middle Lillooet E	477147	5604529	September 7, 2018
Upper Rutherford	498423	5571312	September 1, 2018
No Law	500317	5570349	August 31-September 1,2018
Lower Rutherford W	503650	5570723	August 29,2018
Lower Rutherford E	503916	5570658	September 1, 2018
Ross	503460	5587279	August 28-29, 2018
Currie B	515965	5570375	August 15, 2018
Currie C	516839	5570140	August 16, 2018
Currie D	517411	5570114	August 16, 2018; October 1-2, 2019
Neff	529458	5593780	August 7-8, 2018
Fern	537775	5462900	July 29, 2018
Fountain S	578798	5616465	September 23, 2018; September 18-19, 2019; October 23-24, 2019
Fountain N	579160	5615932	September 23, 2018; September 18-19, 2019; October 23-24, 2019
Cheam W	594952	5451397	September 13, 2018
Cheam E	595063	5451381	September 13, 2018
Anonymous	-	-	November 4, 2018
Pavilion[1]	589951	5634992	September 22, 2018

[1]Fan site not part of this dataset except for volume-area relationship (Section 3.4.4).

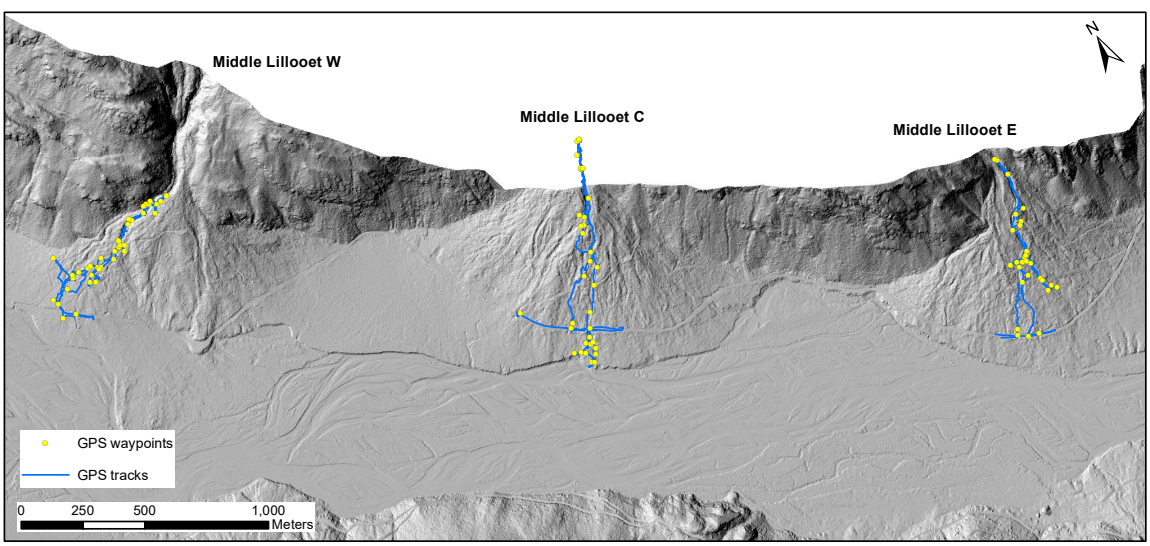

Figure 3.10. An example of GPS data from field traverses at three fan sites on the Lillooet River. 2015 ALS bare earth lidar hillshade courtesy of Brian Menounos from the University of Northern British Columbia, and John Clague and Gioachino Roberti from Simon Fraser University.

Figure 3.11. Examples of field evidence used to identify debris flow processes and delineate impact areas on fans. **a)** Lateral boulder levee; **b)** incised U-shaped channel; **c)** overgrown paleochannel; **d)** terminal lobe; **e)** log jam; **f)** bouldery channel plug; **g)** mudline; **h)** inverse grading; **i)** matrix supported deposits; **j)** boulder studded debris lobe; **k)** megaclast; and **l)** logs with frayed ends.

Figure 3.12. Examples of impact area boundaries such as **a)** edge of a channel levee; **b)** recent deposit abutting an older mossy lobe; and **c)** distal extent of mudwave impacts downslope of main deposit.

3.4 Estimating Event Volumes

Event volumes were estimated for 110 impact areas that were most likely from a single debris flow event (discussed further in Section 3.7). Volumes were estimated directly for 16 events with pre- and post-event lidar (Section 3.4.1), post-event lidar topography (Section 3.4.2), and field estimates of deposit thickness (Section 3.4.3). The direct estimates were used to develop local volume-area relationships to estimate volumes for the remaining 96 events in the dataset (Section 3.4.4).

3.4.1 Lidar Change Detection

The highest confidence volume estimates come from sites with pre- and post-event lidar. A change detection analysis was completed at Currie D between 2017 ALS and 2019 RPAS lidar datasets. A debris flow occurring sometime between July 3 and 12 of 2019 was identified using satellite imagery. Lidar and orthophotos were collected by RPAS on October 1 and 2, 2019 to capture post-event topography for part of the fan area (Figure 3.13). Change detection between the 2017 ALS and 2019 RPAS bare earth point clouds was completed in CloudCompare (2019) using the Multiscale Model to Model Cloud Comparison (M3C2) (Lague et al., 2013), with a limit of detection of ± 0.3 m based on the standard deviation of the differences between unchanged areas (Abellán et al., 2009). Negative change of 35,000 m^3 and positive change of 95,000 m^3 were calculated in CloudCompare between the 2.5D lidar surfaces. As shown in Figure 3.13, the muddy afterflow inundating the floodplain downstream of the main avulsion lobe was not detected in the lidar change

detection. An additional 5,000 m^3 of sediment was estimated based on field observations assuming an average mud thickness of 0.3 m across the inundation area mapped with aerial imagery and field GPS.

Volume estimates by change detection analysis were available for two other events in the dataset: BGC provided a volume estimate for the Anonymous event (pers. comm., J. Whittall, 2019), and the M3C2 analysis by Lau (2017) was used for the 2015 event at Neff. Field estimates of deposit thickness were used to verify the volume estimate by BGC, and field observations and post-event lidar features were used to adjust the volume estimate outside of the lidar overlap presented by Lau (2017).

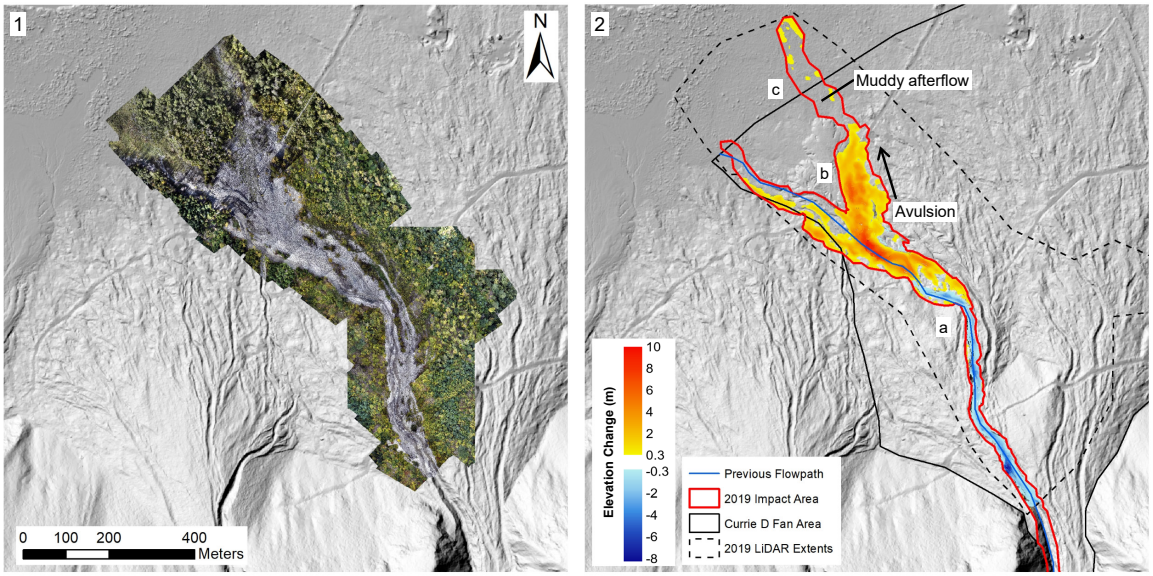

Figure 3.13. 2019 debris flow at Currie D. **1)** 2019 RPAS orthophoto and 2017 ALS bare earth hillshade; and **2)** M3C2 change detection analysis between 2019 RPAS point cloud and 2017 ALS point clouds, showing areas of a) scour, b) lobe deposition, but not c) muddy afterflow. Change detection clipped to 2019 impact area mapped with aerial imagery and field GPS. Representative photos of each area are shown in Figure 3.14. 2019 RPAS data processed by Andrew Mitchell and 2017 ALS lidar provided by SLRD.

Figure 3.14. Post-event photos of the 2019 debris flow at Currie D for different locations along the flow path (locations in Figure 3.13). **a)** Deeply incised channel at the upper fan, showing recent scour and bank erosion; **b)** thick, coarse, lobe deposit from main avulsion; and **c)** muddy afterflow deposits on the floodplain downstream of the fan toe.

3.4.2 Features in Post-Event Lidar

Deposit features preserved in post-event lidar topography were used to estimate volumes for three events in the dataset. Lobe volumes were estimated with ArcGIS assuming a planar deposit base (example shown in Figure 3.15). A polygon outside the lobe boundary was draped to the DEM and interpolated with a triangulated irregular network (TIN) to approximate the pre-event topography. The TIN was converted to a DEM and subtracted from the lidar DEM to create a coarse DEM of difference (difference raster), with the sum of the difference raster pixels used to approximate the lobe volume. The difference raster is also useful for approximating lobe or levee thicknesses without manually extracting cross sections. A similar approach was used by de Haas et al. (2019) to estimate lobe thickness from lidar elevation profiles assuming a planar base. There is significant error associated with this method since a deposit base cannot be approximated with a planar surface. As a test, this method was compared to the M3C2 analysis at Currie D (Figure 3.13) using a portion of the main avulsion lobe. In this case, the interpolation method using post-event lidar topography underestimated the total deposit volume by 30% compared to the change detection results. Deposits at Currie D and Fountain S were good candidates for this method because of thick, well-defined lobes with minimal post-event modification. Wide deposits that require long interpolation distances, lobes deposited in a channel, and deposits that have been subsequently modified or overprinted, are not good candidates for this method.

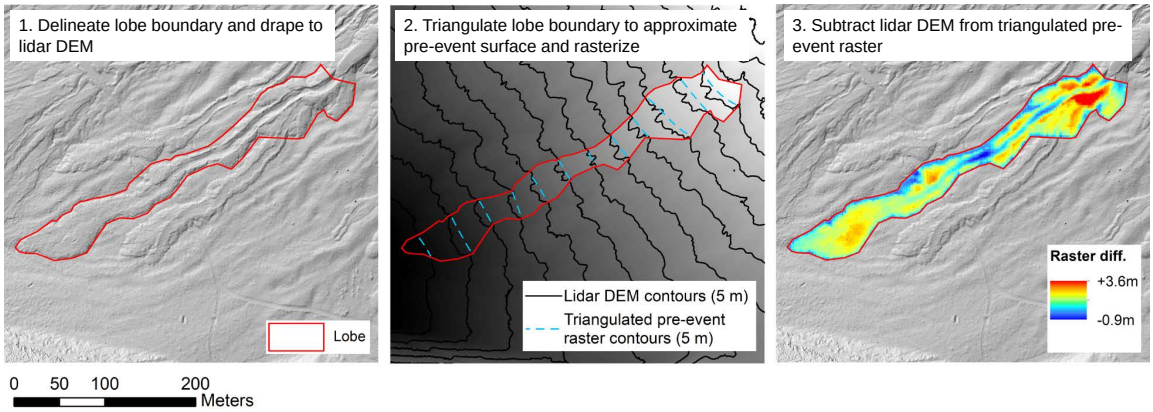

Figure 3.15. Workflow to approximate lobe thickness and volume with post-event lidar topography.

3.4.3 Field Measurements

Field measurements were used to constrain volumes for 10 events in the dataset. Five of these volumes were provided by others from post-event field inspections. For the other five events presented here, the sum of the mean deposit thickness multiplied by a representative deposit area were used to approximate the total volume. Field estimates of deposit thickness include measurements such as the height of debris piled against an obstacle, the thickness of a deposit layer exposed in channel walls, or the thickness of a lobe measured from a datum surface. Error of the volume estimate was calculated using the lower bound and upper bound deposit thickness estimates. Since this volume calculation is dependent on the sum of areas, there is an inherent relationship between the two variables, introducing some circularity to the volume-area relationship.

3.4.4 Volume-Area Relationship

A summary of the areas and volumes used to develop the volume-area relationship is provided in Table 3.6. The impact area is distinguished from the deposit area as it includes the entire area impacted on the fan below the fan apex, such as areas of erosion, transportation, and deposition (described in Section 3.2.3). Area error was estimated by multiplying the maximum cell-size of the data or imagery by the polygon perimeter, which accounts for measurement errors due to resolution, but not epistemic errors (e.g., cases where debris flow impacts are not visible through dense canopy,

evidence of deposition is removed or modified, etc.).

Volume-area relationships are shown in Figure 3.16 for debris flows in SWBC. Regressions for deposit area (A, m^2) and impact area (A_i, m^2) as a function of total volume (V, m^3) are provided in Equations 3.3 and 3.4, respectively. In Figure 3.17, volume-deposit area data for SWBC is compared to other local and global published power-law relationships (previously discussed in Section 2.6.3). The 2/3 exponent is preferable for the volume-deposit area relationship (Equation 3.3) because it follows a physical scaling relationship, and the quality of its fitting is comparable to the best-fit model, consistent with findings by Berti & Simoni (2007) and Griswold & Iverson (2008). For the volume-impact area relationship (Equation 3.4), the best-fit model is used because the physical scaling relationship is less relevant. Equation 3.4 was used to approximate volumes for the remaining events in the dataset since it is difficult to distinguish areas of deposition from erosion using remote sensing data. A histogram of event volumes for the resulting 110 event SWBC dataset is provided in Figure 3.18.

$$A = 33V^{2/3} \tag{3.3}$$

$$A_i = 12V^{0.78} \tag{3.4}$$

Table 3.6. Event volumes and areas.

Fan site	Event date	Deposit area (m^2)	Impact area (m^2)	Volume (m^3)	Area mapping method(s)	Volume estimation method
Middle Lillooet C	Sept or Oct 2015	31,500 ± 4,000	31,500 ± 4,000	45,000 ± 10,000	Field GPS, satellite imagery	Field estimates of deposit thickness
Middle Lillooet E	Oct 2015	16,500 ± 3,400	19,700 ± 4,100	20,000 ± 5,000	Field GPS, satellite imagery	Field estimates of deposit thickness
Currie B	Late fall 2016 or early 2017	304,000 ± 8,000	310,000 ± 7,900	500,000 ± 150,000	Lidar, orthophoto, field GPS	Features in post-event lidar, field estimates of deposit thickness
Currie D	July or Aug 2014	34,200 ± 1,800	103,900 ± 6,600	70,000 ± 20,000	Lidar, satellite imagery (dNDVI), field GPS	Features in post-event lidar, field estimates of deposit thickness
Currie D	Between July 3 and 12, 2019	76,500 ± 4,000	103,900 ± 6,600	100,000 ± 5,000	Lidar, orthophoto, field GPS, satellite imagery (dNDVI), Google Earth	RPAS lidar change detection, field estimates of deposit thickness, features in post-event lidar
Neff	Sept 20, 2015	140,500 ± 2,700	151,800 ± 4,100	220,000 ± 30,000	Lidar, orthophoto, field GPS	Lidar change detection (Lau, 2017), field estimates of deposit thickness, features in post-event lidar
Catiline	Sept 28, 2010	26,500 ± 3,700	35,300 ± 5,100	17,500 ± 2,500	Field GPS (Cordilleran, 2010)	Field estimates of deposit thickness (Cordilleran, 2010)
Catiline	Aug 30, 2013	24,000 ± 3,800	24,000 ± 3,800	17,500 ± 7,500	Field GPS (Cordilleran, 2013)	Field estimates of deposit thickness (Cordilleran, 2013)
Bear	July 30, 2016	98,100 ± 5,000	100,700 ± 5,700	67,000 ± 20,000	Lidar, orthophoto, GPS (BGC, 2018b), satellite imagery (dNDVI)	Field estimates of deposit thickness (BGC, 2018b)
Fountain S	Between Aug 2 and Aug 6, 2018	16,700 ± 3,600	23,700 ± 2,900	15,000 ± 5,000	Lidar, satellite imagery (dNDVI)	Features in post-event lidar
Fountain S[1]	Between Sept 11 and Sept 23, 2015	14,400 ± 2,000		15,000 ± 5,000	Lidar, satellite imagery (dNDVI), field GPS	Features in post-event lidar, field estimates of deposit thickness
Cheam W	November 23, 2017	86,000 ± 13,600	86,000 ± 13,600	65,000 ± 15,000	Field GPS, satellite imagery (dNDVI), Google Earth	Field estimates of deposit thickness
Cheam E	Nov 23, 2017	60,700 ± 10,400	60,700 ± 10,400	45,000 ± 15,000	GPS, satellite imagery (dNDVI), Google Earth	Field estimates of deposit thickness
Hope	Nov 8, 1995	29,900 ± 6,100	33,100 ± 7,200	50,000 ± 12,500	Orthorectified airphoto	Field estimates of deposit thickness (Jakob et al., 1997)
Anonymous	-	21,800 ± 1,800	23,000 ± 2,000	15,000 ± 5,000	GPS	Lidar change detection (courtesy of BGC), field estimates of deposit thickness
Pavilion[2]	Aug 20, 2014	9,400 ± 2,200	11,000 ± 2,900	7,500 ± 1,500	Field GPS, satellite imagery	Field estimates of deposit thickness
Pierce Creek[2]	Nov 28, 1995	52,500 ± 6,800	52,500 ± 6,800	63,000 ± 15,000	Orthorectified airphoto	Field estimates of deposit thickness (Jakob et al., 1997)

[1]Upper portions of the deposit overprinted by subsequent flows, so volume and deposit area associated with lower deposition lobes. Not included in impact volume-area relationship.
[2]Fan site not part of this dataset except for volume-area relationship.

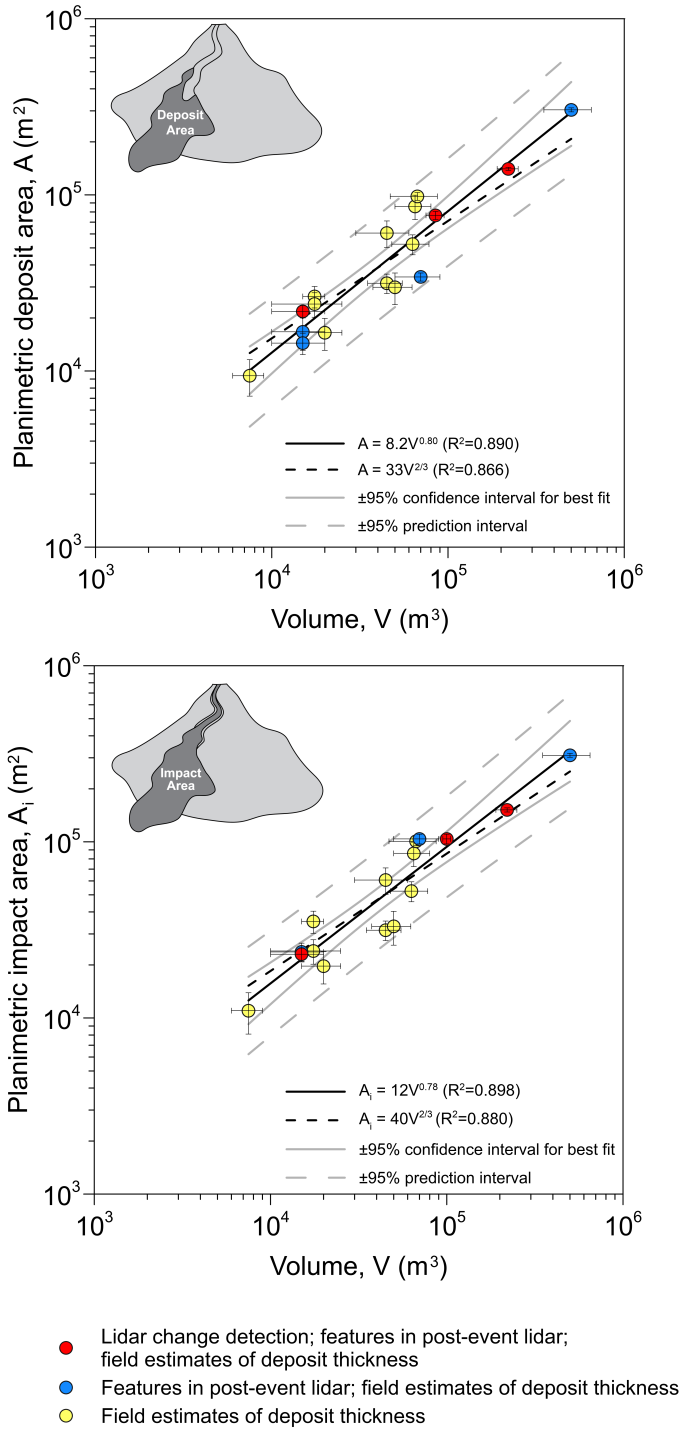

Figure 3.16. Volume-area relationships for debris flows in SWBC for deposit area (A) and impact area (A_i).

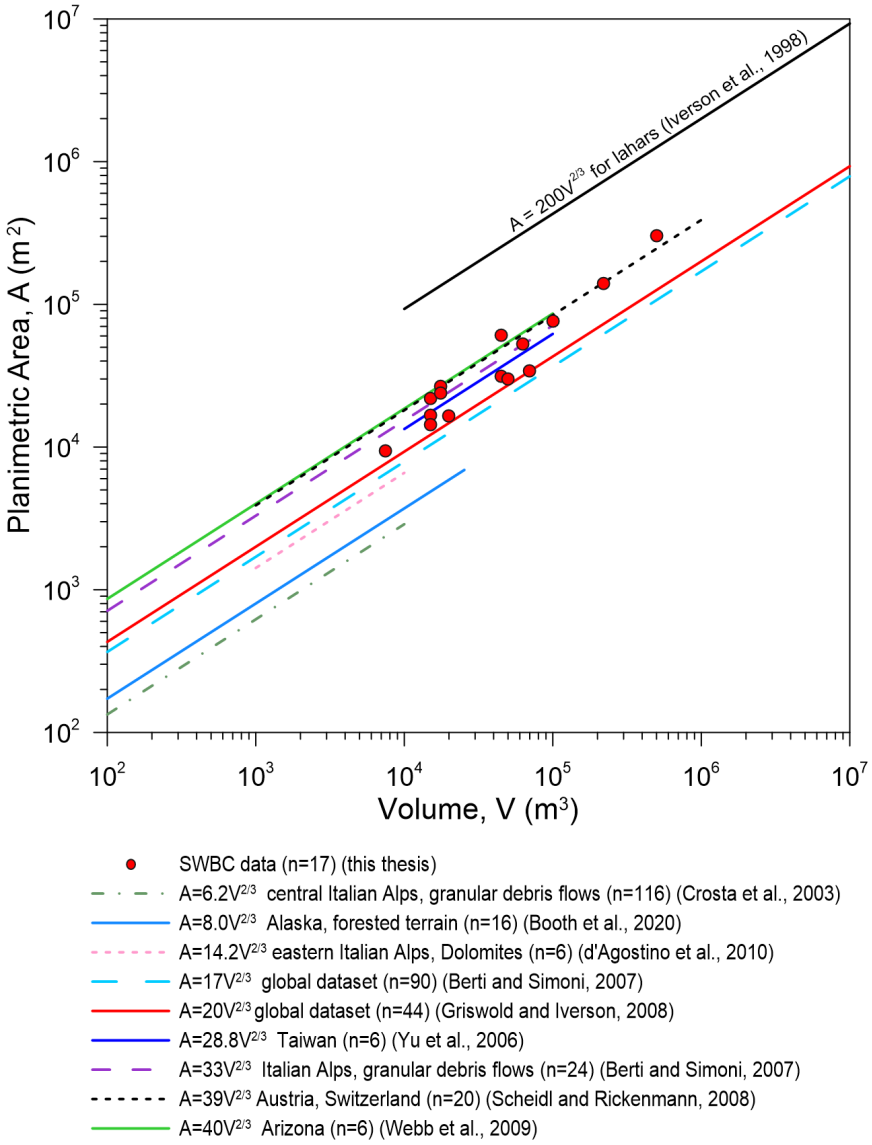

Figure 3.17. Comparison of SWBC volume-area data to empirical relationships for non-volcanic debris flows, over the domain of the respective volumes for each dataset. Trendline for lahars provided for reference.

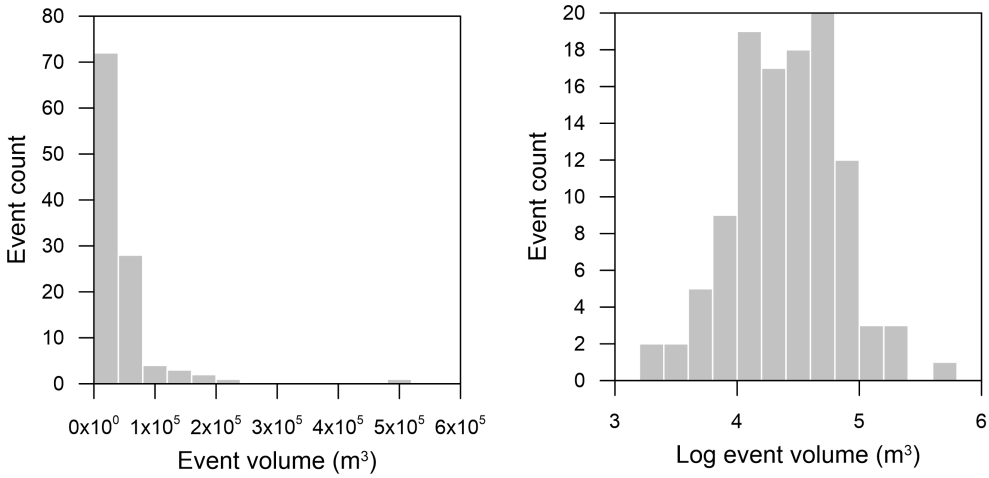

Figure 3.18. Distribution of event volumes for the SWBC dataset (110).

3.5 Avulsion Classification

In this work, an avulsion is defined as any deviation of flow from an established flow path during a debris flow. The classification scheme in Figure 3.19 was made to describe the types of avulsions (or lack thereof) observed in the dataset, based on the location, magnitude, and surface expression of debris flow impacts. During the mapping process, impact areas were assigned an avulsion class (or multiple classes), summarized in Figure 3.20. Out of the 146 impact areas (not including baseline impact areas), 86% were classified as having some form of avulsion or spreading across the fan, while 35% corresponded to a positional shift of the active channel on the fan (classes 4 and 5). Local channelized avulsions (class 3) were the most common, and often coincident with the other avulsion types. Major avulsions were more commonly initiated on the upper fan (class 5B), while lateral shifts were relatively more common on the lower fan (class 4A). The avulsion classification serves as a qualitative way to describe fan impacts from an empirical dataset; a quantitative analysis of runout and avulsion trends is presented in Chapter 4.

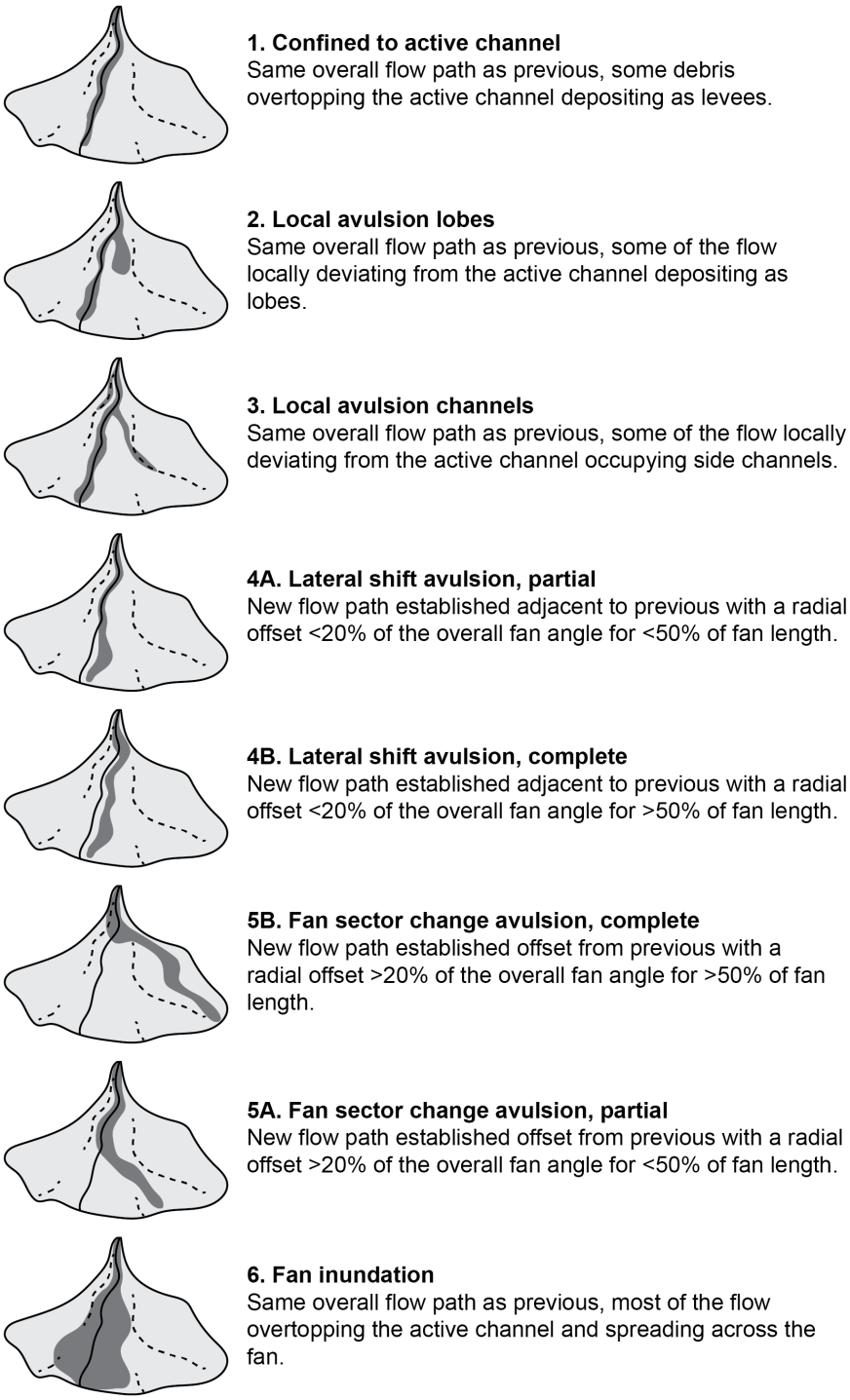

Figure 3.19. Debris flow avulsion classification scheme.

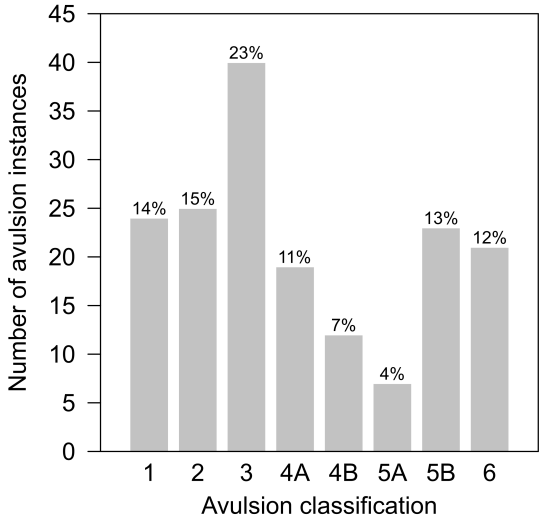

Figure 3.20. Distribution of avulsion classes (Figure 3.19) for impact areas in the SWBC dataset.

3.6 Fan Site Descriptors

This section presents the quantitative and qualitative variables used to describe the fan sites in the dataset, including definitions, calculations, and data sources. A data summary of all the variables is provided in Section 3.6.11.

Geomorphometry is the quantitative study of topography (Pike, 2000). Geomorphometric (morphometric) variables have been used to discriminate hydrogeomorphic process types (e.g., Wilford et al., 2004), predict debris flow activity (e.g., Bovis & Jakob, 1999), and as variables in empirical runout relationships (described in Section 2.6). Fan and watershed morphometric variables were calculated for each fan site for two purposes: 1) to describe the morphology of the fan sites and characterize dominant hydrogeomorphic process types; and 2) to be tested as discriminators to explain differences in mobility and avulsion trends (Section 4.4). Only a few variables were included in this work, in part due to the quality and variability of topographic data across the study area, but also to focus on variables that may be related to debris flow runout trends. Morphometric variables were selected based on results from previous studies that used morphometric variables to predict runout or scour (e.g., Lau, 2017; Scheidl & Rickenmann, 2010), and include Melton ratio, watershed

area, fan slope, average fan channel slope, fan elevation relief ratio, and fan intersection point. Other variables, such as measures of fan roughness, might be included in future work, as discussed in Section 5.3.

In addition to the morphometric variables, three qualitative variables (i.e., classifiers) were included as descriptors: source geology, fan truncation, and a relative fan activity class.

3.6.1 Melton Ratio

The Melton ratio (R), as defined by Melton (1965), is determined with Equation 3.5:

$$R = \frac{H_w}{\sqrt{A_w}} \tag{3.5}$$

where H_w is the watershed relief (km), and A_w is the planimetric watershed area (km^2). The Melton ratio is used to describe watershed ruggedness, with larger values corresponding to a more rugged (steep) watershed. The Melton ratio can be used to differentiate hydrogeomorphic process types, as shown in Section 3.6.7.

3.6.2 Watershed Area

The watershed area is the planimetric area of the watershed boundary upstream of the fan apex. Watershed boundaries were obtained from the Freshwater Atlas of BC (GeoBC, 2009), or calculated using Global Mapper™ (v18) "Create Watershed" tool with lidar or TRIM DEMs, and modified manually using elevation contours where necessary. Watershed shapefiles are provided in Appendix B GIS files.

3.6.3 Fan Slope

The fan slope was calculated as the slope of a straight line from the fan apex to the fan boundary through the fan centroid, with elevations derived from either lidar or TRIM DEMs. There are many ways to calculate fan slope, some of which have been explored here. Slopes calculated using four different methods across the 30 fans are compared in Figure 3.21. The first method uses the mean slope from a slope raster across the entire fan area. This method is sensitive to the DEM

resolution, with higher resolution DEMs capturing human-made cut slopes, channel sidewalls, or other geomorphic features included in the fan area. As shown in Figure 3.21, slopes calculated with the slope raster are lower compared to the other methods, likely because of the comparatively large area of the lower fan with gentler gradients. The second method is the slope of a straight line from the maximum to the minimum elevation along the fan boundary. Although this is straightforward to compute, it may result in steep slopes along a maximum relief across the fan. To consistently measure slope in the down-fan direction (i.e., radially away from the fan apex), the third method tried was the slope of a straight line from the apex to a point along the fan toe. The downside of this method is it requires differentiating the toe from the rest of the fan boundary. The fourth method, using a line from the apex through the fan centroid, was used for this study because the centroid be determined objectively, calculations are not very sensitive to DEM resolution, and the distribution of slopes was comparable to the third method.

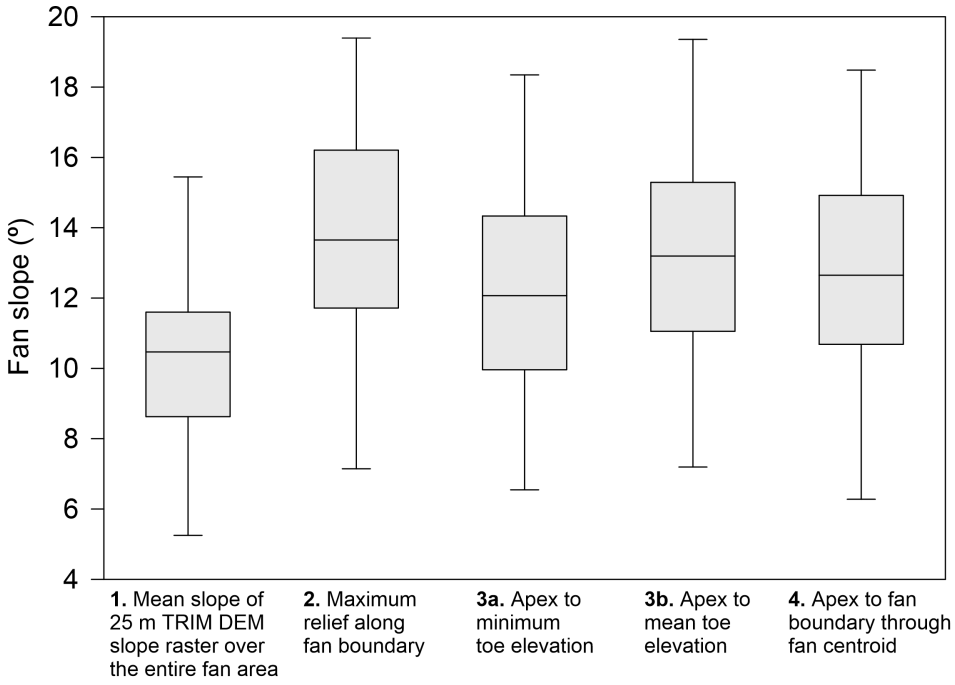

Figure 3.21. Box and whisker plot comparing different methods for calculating average fan slope across the fan sites. Elevations derived from TRIM DEM with a 25 m pixel size.

3.6.4 Average Fan Channel Slope

The average channel slope was calculated as the average slope between points along the length of the main channel from the fan apex to toe. A 25 m point sampling interval was used to match the coarsest DEM resolution (TRIM). Where available, the main channel was mapped with lidar topography following the guidelines for mapping flow paths described in Section 3.2.4. Otherwise, flow lines from the Freshwater Atlas of BC (GeoBC, 2009) were clipped to the fan area. As shown in Figure 3.22, the average fan channel slope is closely related to the overall fan slope, although typically lower since the channel slope is the average of slope segments along a curved path.

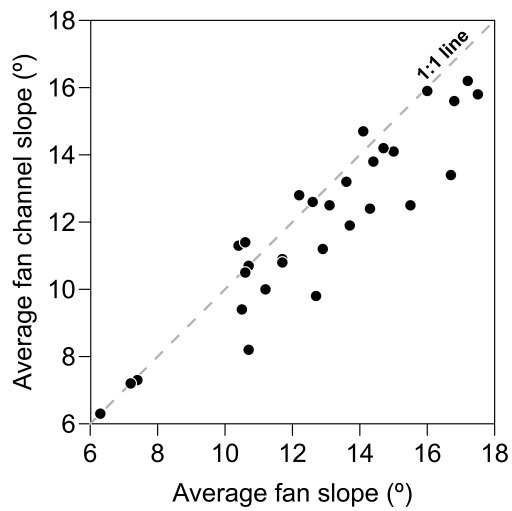

Figure 3.22. Comparison of overall fan slope to average slope along the fan channel.

3.6.5 Fan Elevation Relief Ratio

The elevation relief ratio (ERR) is defined by Equation 3.6 (Wood & Snell, 1960):

$$ERR = \frac{\bar{z} - z_{min}}{z_{max} - z_{min}} \tag{3.6}$$

where $\bar{z}$, z_{min}, and z_{max}, are the mean, minimum, and maximum elevation (m), respectively. The ERR is mathematically equivalent to the hypsometric integral (Pike & Wilson, 1971), both of which are used to approximate basin profile curvature. In this study, ERR is used as a very simple way to quantify the profile curvature of the fan, using elevations from the fan area instead of the watershed.

An ERR close to 0.5 corresponds to a more planar fan surface, while an ERR less than 0.5 is concave. There are other ways to quantify fan concavity, such as fitting curves to longitudinal elevation or slope profiles (e.g., Williams et al., 2006); these methods may be explored in future work with access to higher quality topographic data across all fans in the dataset.

3.6.6 Fan Intersection Point

The fan intersection point is where the main channel intersects the fan surface, usually somewhere mid-fan, and represents the transition from fan incision to deposition (Hooke, 1967). The intersection point is not a typical measurement used in morphometric analyses, and there is no objective way to calculate it with topographic data alone, but it is included here to quantify channel morphology and loss of confinement. The intersection point was defined manually using lidar DEMs and field observations. In this work, the intersection point is reported as the distance from the fan apex to the average intersection point (usually a range) normalized by the maximum fan length (i.e., average normalized position down-fan). Due to the availability of lidar data and field observations, the intersection point was determined for 23 of the 30 fans.

As an example, Figure 3.23 depicts how the intersection determined with a lidar DEM for Currie D. The active channel thalweg was offset to either side of the channel outside of the levees to represent the proximal average fan surface elevation, and the elevation difference between the thalweg and the average fan surface (i.e., relative channel fan incision) was calculated at each point along the channel. This is similar to the methodology applied by Lau (2017) for quantifying relative fan scour. The intersection is where the relative incision approaches zero. Representative cross-sections and photos in Figure 3.23 show fan incision for the channel up-slope of the intersection (A-A'), and deposition on top of the fan surface down-slope of the intersection (B-B').

Figure 3.24 depicts how the intersection was determined for fans without lidar using field observations. In Figure 3.24, the intersection is somewhere between points b and c, although the location may have been artificially modified since portions of the channel were excavated upslope of the logging road. In all cases, judgement was used to select the representative intersection location.

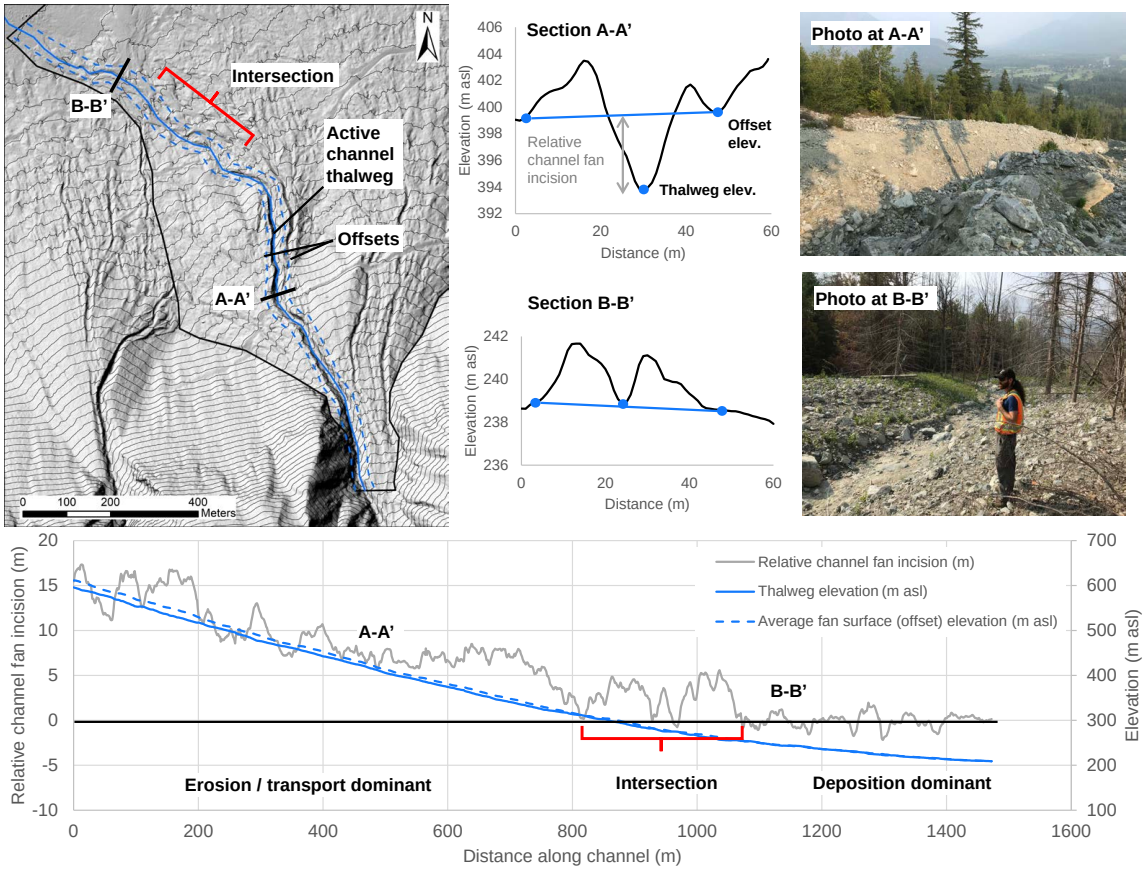

Figure 3.23. Intersection determined with lidar DEM at Currie D. 2017 ALS bare earth DEM courtesy of SLRD.

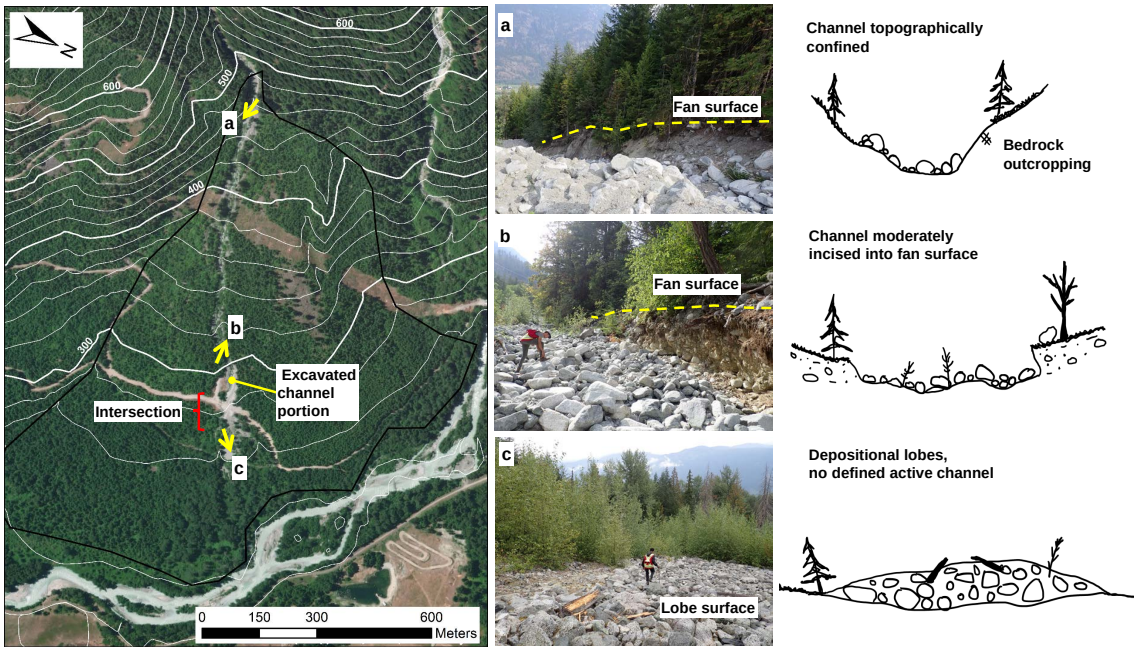

Figure 3.24. Intersection determined with field observations at Ross. 20 m contours derived from TRIM DEM. Sketches are based on field cross-sections and are not to scale.

3.6.7 Hydrogeomorphic Process Recognition

Morphometric variables were used to examine the dominant hydrogeomorphic processes for the fan sites using process boundaries by Wilford et al. (2004), Bardou (2002), and Bertrand et al. (2013) (Figure 3.25). The boundary by Bertrand et al. (2013) in Figure 3.25 discriminates debris flow and fluvial fans based on a statistical analysis of 620 catchments from a global dataset. In general, small, steep basins with higher Melton ratios are more typical of debris flow processes. Debris flows are the dominant classified flow type for most of the fan sites, with lesser debris flood/mixed-process fans. As described in Section 2.1, hydrogeomorphic processes exist on a spectrum, and all fans may be prone to all process types.

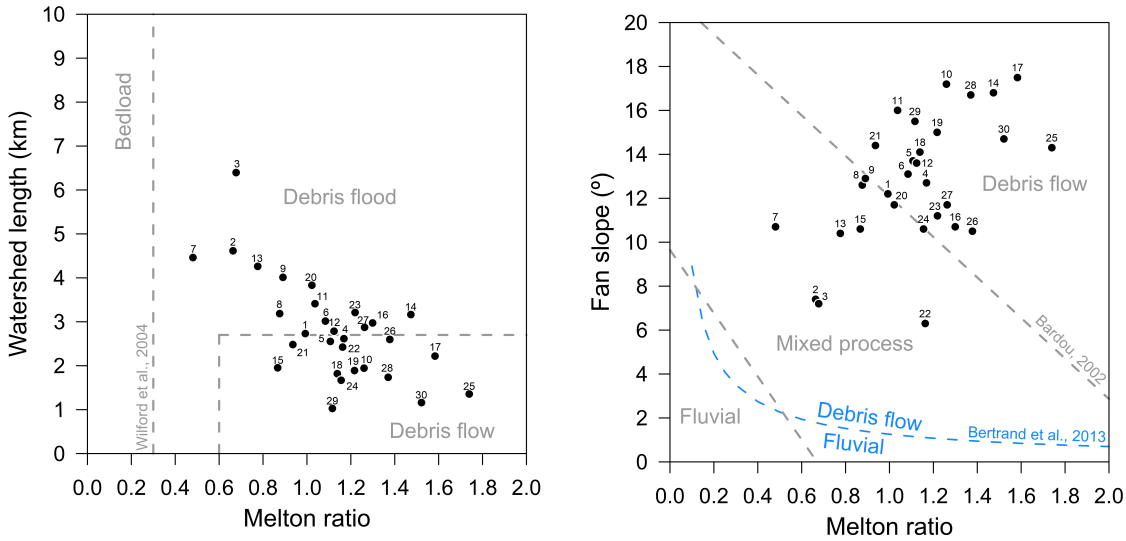

Figure 3.25. Fan sites plotted on typical hydrogeomorphic process recognition charts with boundaries by (left) Wilford et al. (2004) and (right) Bardou (2002) and Bertrand et al. (2013). Fan site labels correspond to Table 3.1.

3.6.8 Source Geology

Source (basin) geology was subdivided into four groups based on rock classes from provincial digital bedrock geology mapping at a scale of 1:50,000 to 1:250,000 (Cui et al., 2017): intrusive, sedimentary, volcanic, or metamorphic. For basins with multiple rock classes, classification was based on the geologic unit with the largest area. Basins were also classified as either supply-unlimited (i.e., transport-limited, almost an unlimited amount of sediment available), or supply-limited (i.e., weathering-limited, time is required to recharge channels with debris before the next event), as defined by Jakob (1996) and Bovis & Jakob (1999). Since the intrusive basins were classified as supply-limited due competent bedrock limiting sediment delivery, the source geology classifier is considered an adequate proxy for supply conditions in this study.

3.6.9 Fan Truncation

Fans in the SWBC dataset are situated in various geomorphic settings that may impact debris flow runout. As a preliminary way to describe the interactions of debris flows with geomorphic

processes beyond the fan extents, fans were classified as truncated if a body of water, such as a river or lake, abuts the fan toe. Erosion at the fan boundary may undersize the fan area, and evidence of impact is lost as debris flows enter the water body. Fans with mostly unconstrained deposition onto a floodplain or terrace, or where there is minimal geomorphic interaction with the body of water, are considered not truncated.

3.6.10 Fan Activity

Relative fan activity varies across the fan sites. The number of impact areas (not including the baseline) recorded at each fan ranges from 1 to 14, with an average of about 5 impact areas per fan over an average observation length of 74 years. The most active fans in the dataset are the ones at Mount Currie (Currie B, C and D) and Fountain Ridge (Fountain N and S), described further in Section 4.3. The impact recurrence period for each fan was calculated by dividing the length of the observation record by the number of mapped impact areas. This number is related to the number of available airphotos, the frequency of visible change in the airphoto and satellite record, and the number of debris flow events mapped in the field, and is not necessarily equivalent to the return period of debris flow activity at each fan. The average recurrence interval of mapped hydrogeomorphic change across the fan sites is about 24 years.

3.6.11 Summary of Variables

Histograms summarizing the distribution of quantitative and qualitative variables describing the fan sites are shown in Figure 3.26. Data for each fan site is summarized in Appendix A, and can be accessed digitally as shapefile metadata provided in Appendix B.

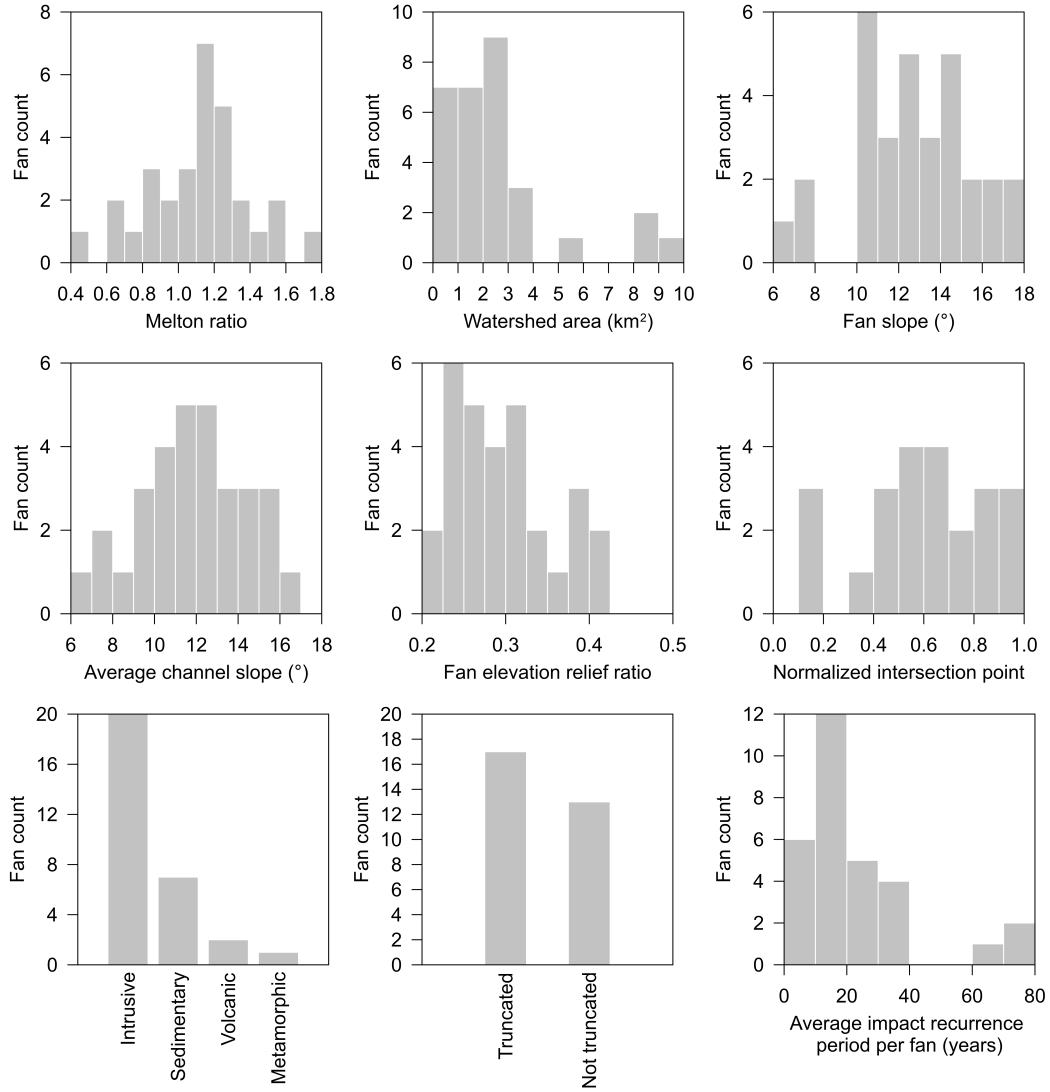

Figure 3.26. Distributions of morphometric and qualitative data describing the SWBC fan sites.

3.7 Mapping Certainty Classification

The certainty (i.e., quality) of impact area mapping was given a qualitative rating using the classes described in Table 3.7. The temporal certainty class reflects the observation frequency interval, and is somewhat related to the likelihood that the mapped impact area is from a single event. In other words, impact areas with dates that are approximately constrained are more likely (but not always) to be from multiple events, especially at very active fans. However, it is possible that an event constrained to a

Table 3.7. Description of impact area mapping certainty classes.

Class	Description	Temporal Certainty	Spatial Certainty
1	Well constrained	Eye witness account or event recorded; date constrained with imagery to within 1 year; date verified by other dating means.	Recent event with well-preserved deposits or flow markers verified in the field; pre- and post-event lidar or deposits visible in lidar; high quality pre- and post-event satellite imagery or orthophotos; sparse canopy or canopy removed by event.
2	Moderately constrained	Date constrained with imagery to within 10 years.	Less recent event with moderately preserved field evidence; some deposits or channels visible in lidar; moderate to high quality pre- and post- event satellite imagery or orthophotos; parts of the impact area obscured by canopy or fan disturbance.
3	Approximately constrained	Date constrained with imagery to within 10-20 years.	Impact area mapped using only airphotos or satellite imagery; moderate quality pre- and post- event satellite imagery or orthophotos; lidar unavailable or deposits obscured by subsequent events; impact area obscured by canopy or fan disturbance.

year with satellite imagery is the sum of a series of debris flows, or that an impact area constrained to a 20 year interval is from a single event. 110 of the 176 impact areas were flagged to be most likely associated with a single debris flow event. This distinction was made on a case-by-case basis considering the temporal certainty class and the relative activity of the fan.

The spatial certainty represents confidence in the impact area mapping, dictated by the quality of remote sensing data and field data. High volume events that disturbed large portions of the fan surface and were easy to observe in imagery, or those field mapped shortly after occurring, were considered well constrained. Figure 3.27 shows the number of impact areas for each class. There is an inverse distribution in the data certainty, with a lesser proportion of well spatially constrained impact areas compared to their temporal constraint. This is due, in part, to the nature of the imagery sources. Satellite data (Section 3.3.2) provides high temporal resolutions (weekly to monthly scenes) but at lower spatial resolutions (3-5 m pixel sizes), compared to the lesser amount of high resolution airphotos (Section 3.3.1) with inconsistent observation periods (about 1-20 years between photos). Out of the entire dataset, only 20 impact areas had both a temporal and spatial certainty class of 1. Data certainty classes for each impact area can be found as metadata with the GIS shapefiles provided in Appendix B.

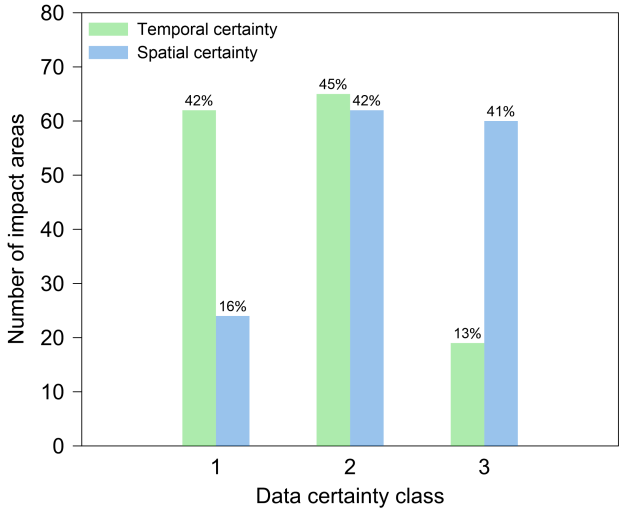

Figure 3.27. Distribution of data certainty classes for SWBC impact areas.

3.8 Dataset Limitations

The compiled dataset has limitations that should be considered throughout this thesis. Due to the ensemble of data sources used, mapping was completed at varying levels of confidence, as addressed by the data certainty classification defined in Section 3.7. The monitoring interval was not constant through time or consistent between fans, and it remains uncertain whether many of the impact areas are from multiple flows or a single event. There is data censoring since small channel-plugging events not visible in imagery or mappable in the field are underrepresented, although repeated RPAS lidar campaigns may fill this gap in the future. Since the airphoto record spans less than a century, the chances of capturing an extreme event on each fan are very low. Events that overprint previous deposits (e.g., Figure 3.6) or flow under dense canopy (e.g., Figure 3.7) are generally undetected in airphotos and satellite imagery. Distal debris flow impacts, such as the full extents of sheet flooding or mudwave deposits beyond the main deposit lobes (e.g., Figure 3.12c) may only be detected with high quality post-event satellite imagery or timely post-event field investigations. Post-depositional processes including damage cleanup or subsequent storm events may obfuscate evidence. Forestry road building, clear cutting, and snow avalanches may also obscure mapping. The spatial accuracy of geomorphic mapping is controlled by many factors, including the availability of lidar, accuracy of

the georeferencing process, pixel size of the imagery, and the accuracy of a handheld GPS. Although geomorphic mapping is subject to interpretation, effort was made to employ a consistent methodology, as described in Section 3.2.

Sometimes impacts from debris flows are difficult to distinguish from other hydrogeomorphic process types using imagery alone, in the absence of obvious lobes and levees. As shown in Section 3.6.7, morphometric variables were used to help distinguish the dominant hydrogeomorphic process types for the fans in this dataset, with most fans clustered close to debris flow processes. Trimlines or landslide scars were sometimes, but very rarely, identified in the watershed as an indicator of a possible debris flow initiating processes, and only some process types were field-truthed using the criteria listed in Section 3.3.5. Moreover, a spectrum of sediment concentrations and process types may be present within a single event or surge, as discussed in Section 2.1. Considering process type uncertainties, and whether a mapped change is from a single event or many, the impact areas represent the migration of debris flow-dominant hydrogeomorphic processes on debris flow fans.

There are other methods to reconstruct fan history for frequency-magnitude analysis, as summarized by Jakob (2005, 2013). Test trenching and borehole drilling, along with tephrachronology and radiocarbon dating methods, can determine a chronology of events and associated thickness dating back to the early fan record. Unfortunately, reconstructing 3-dimensional fan architecture is expensive, time consuming, and invasive. Dendrochronology can be used to reconstruct areas partially affected by debris flow inundation by dating tree ring growth reactions to external disturbances (Schneuwly-Bollschweiler & Stoffel, 2013). It is a less intensive method and provides a somewhat continuous record of debris flow activity over a few hundred years, given adequate conditions (Jakob, 2013). Lichenometry (e.g., Jomelli, 2013), cosmogenic radionuclides (e.g., Ivy-Ochs et al., 2013), and weathering fractures in boulders (D'Arcy et al., 2015), have also been used to date landforms. Although these methods provide a more continuous and complete data record for each fan, they lack the spatial detail awarded by airphoto analysis, lidar interpretation, and post-event field investigations for more recent flows, such as the delineation of flow paths and distal debris flow impacts.

As discussed in Section 3.4, there is a lot of uncertainty associated with estimating event volumes. Only three events in the dataset have pre- and post-event lidar available for a change detection analysis.

The volume-impact area relationship was based on 16 direct measurements, many of which involve using an area to estimate the volume assuming a representative thickness, introducing circularity in the relationship. To address these uncertainties, methodologies used to estimate volume have been described and estimates of error have been provided. In this study, the volumes are only used to place events in order-of-magnitude volume classes, and therefore the use of the volume-impact area relationship for the remaining 96 events is reasonable since the 95% prediction interval spans about half an order of magnitude (Figure 3.16).

Lastly, high quality topographic data was not available across the entire study area, and many morphometric variable calculations were completed with a 25 m resolution DEM. Therefore, only a few simple morphometric variables that were relatively insensitive to topographic resolution and easy to calculate have been included.

3.9 Summary

- 176 debris flow impact areas and flow paths were mapped across 30 fan sites dating back to 1928, with 110 impact areas likely associated with a single debris flow event. The average recurrence interval of mapped hydrogeomorphic change across the fan sites is about 24 years.
- 30 fan sites were selected from a larger debris flow event inventory compiled for SWBC based on the presence of a well-defined fan landform and a legacy of mappable debris flow events.
- Geomorphic mapping was completed in ArcGIS using an ensemble of remote sensing data and field data to define the fan boundary, fan apex, impact areas, and flow paths. The impact area is defined as any area below the fan apex that has been impacted by a debris flow, or multiple debris flows, over a certain time period. These areas represent the migration of hydrogeomorphic processes on debris flow fans.
- Remote sensing data consisted of hundreds of historical airphotos, satellite imagery, topographic basemaps, lidar, and orthophotos. About 60 airphoto scenes were orthorectified using Agisoft Metashape Professional (Agisoft LLC., 2019). Change detection with the spectral index NDVI (Normalized Difference Vegetation Index) was used for impact area mapping with satellite data, which consisted of daily to monthly images dating back to 2009 available through

Planet (2019). Lidar was available for 16 of the fan sites, including lidar and orthophotos collected during field work using a remotely piloted aerial system (RPAS, or drone) at three of the fan sites.

- Geomorphic field mapping was completed at 18 fan sites, in which the fan was hiked to the apex to delineate debris flow features, including lobes, levees, deposit boundaries, and channels.
- Event volumes were calculated for 16 events using lidar change detection, features in post-event lidar, and field data. This data was used to develop a local volume-impact area relationship to estimate volumes for the remaining 96 events in the dataset.
- A classification scheme was developed to describe the different types of avulsions (or lack thereof) based on the location, magnitude, and surface expression of debris flow impacts. 86% of the impact areas mapped involved some form of avulsion or spreading across the fan, while 35% corresponded to a positional shift of the active channel.
- The fan sites in the dataset were described by morphometric variables (Melton ratio, watershed area, fan slope, average fan channel slope, fan elevation relief ratio, and fan intersection point), source geology, truncation by a body of water, and fan activity. These variables will be used in Section 4.4 to stratify runout trends.
- Despite a dataset with varying levels of spatial and temporal accuracy, the compiled data is a unique and thorough record of spatial impacts on debris flow fans in SWBC.

Chapter 4

Extraction and Analysis of Spatial Impact Trends on Debris Flow Fans

This chapter is an analysis of the geospatial dataset described in Chapter 3. A novel method to extract and aggregate runout trends across fans is presented, creating fan-normalized spatial impact heatmaps. Using this method, regional spatial impact trends for the SWBC dataset are developed and compared to other data. Mobility and avulsion trends at five very active fans in the dataset are described. Using the entire SWBC dataset, differences in runout distributions grouped by event volume, morphometric variables, and other descriptors, are tested to examine which variables discriminate different mobility and avulsion trends. Lastly, a simple tool that transposes the empirical data onto another fan is presented, showing potential applications for data-driven runout assessments.

4.1 Creating Fan-Normalized Spatial Impact Heatmaps

A new graphical method is presented to extract and visualize spatial impact trends on debris flow fans. This method builds on metrics proposed by Densmore et al. (2019), where avulsion size is quantified by the opening angle of the avulsion and the radial distance of the avulsion site, as well as techniques used by de Haas et al. (2018a) to summarize deposition patterns over time based on runout distance and flow angle measured from the fan apex.

Impact areas are extracted using a circular grid centered on the fan apex and normalized by

the maximum fan length and fan arc length. The maximum fan dimensions can be interpreted as statistical upper-bounds of its formative debris flows. In the measurement grid, zones of increasing radii represent mobility down-fan, and arc length offsets represent lateral shifts across the fan relative to two datums: the fan axis (Section 4.1.1) or the previous flow path (Section 4.1.2). Multiple normalized impact area plots are summed to create a heatmap for a fan or a group of fans. The data extraction process is described in more detail in the code workflow in Section 4.1.3.

4.1.1 Relative to the Fan Axis

The fan axis is a line bisecting the fan through the apex and the fan centroid. Although the fan axis is determined planimetrically, it can be interpreted as a reasonable proxy for the overall depocenter of the fan landform (considered here as the location of maximum deposit thickness) since cross-fan profiles tend to be convex (e.g., Blair & McPherson, 1998; Whipple & Dunne, 1992). As shown in Figure 4.1, the fan axis is used as a datum for measuring cross-fan offsets for individual impact area polygons. The overlapping impact area polygons are summed to create a heatmap, with "hotspots" used to identify areas on an individual fan most impacted based on the data record.

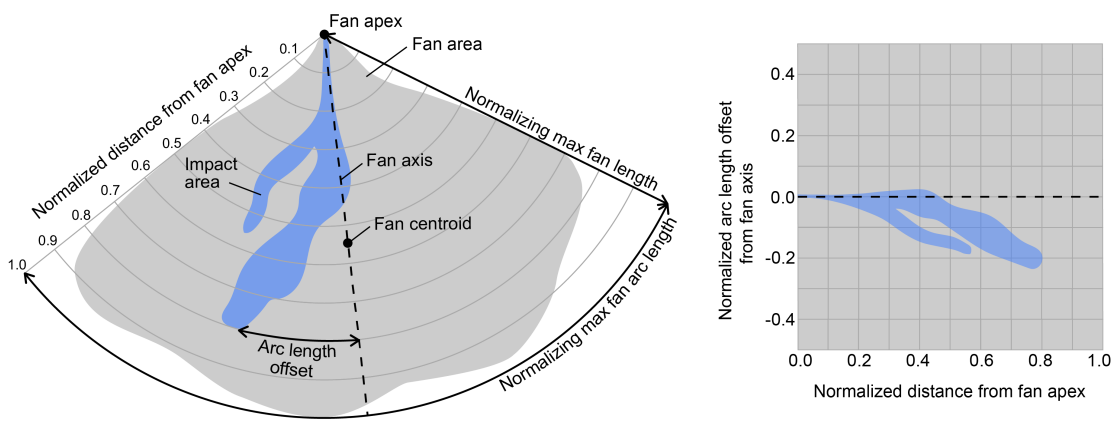

Figure 4.1. Example of the fan-normalized plotting method for one impact area relative to the fan axis.

4.1.2 Relative to the Previous Flow Path

For each impact area, a flow path was defined from apex to toe using imagery and topography as either the active channel, or the center of deposition if there is no defined channel, or the path of

steepest descent past the toe of the deposit. As shown in Figure 4.2, the impact area plotted relative to the previous flow path highlights flow path deviations, including locations and extents of avulsions. A spatio-temporal component is captured since the datum is relative to impacts from a previous time. Using the impact area in Figure 4.2 as an example, the flow avulsed from the channel about a third of the way down-fan, extending across almost half of the maximum fan arc length. Avulsion trends are thus recorded in these plots, which are typically difficult to ascertain when looking at impact area mapping in GIS, and tedious to measure manually for many events. When impact areas are summed creating a heatmap, hotspots represent areas most likely impacted relative to a current channel configuration based on historical data. Interpretations and applications of these plots are discussed throughout this chapter.

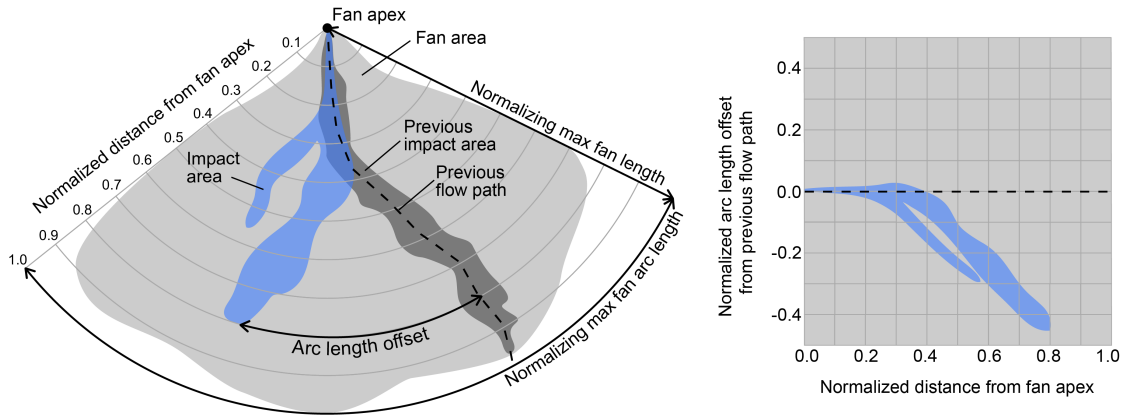

Figure 4.2. Example of the fan-normalized plotting method for one impact area relative to the previous flow path.

4.1.3 Code Workflow

The following steps briefly describe the code workflow for converting GIS mapping to fan-normalized spatial impact heatmaps for a site. The code was implemented in MATLAB (R2019b).

1. **Load shapefiles.** For a fan site with *i* impact areas, the fan apex (1 point), fan boundary (1 polygon), impact areas (*i* polygons, ordered sequentially), and flow paths (*i* polylines, ordered sequentially) are loaded as separate shapefiles in UTM coordinates (Figure 4.3). The fan polygon, impact area polygons, and flow path polylines should intersect the fan apex.

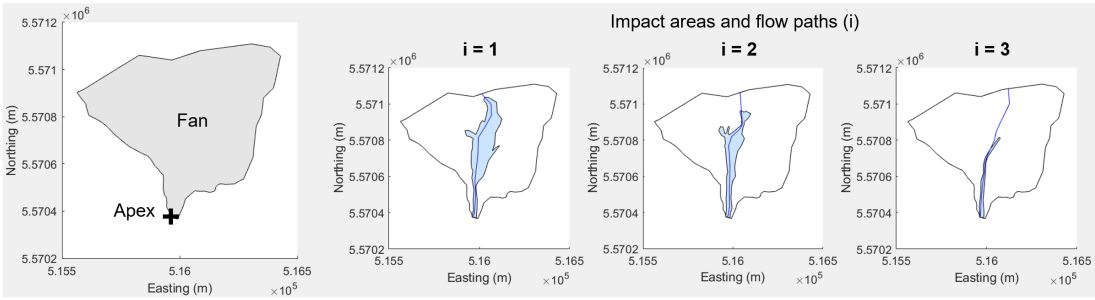

Figure 4.3. Example shapefile inputs for plotting.

2. **Initialize a measurement grid centered on the fan apex.** The grid resolution is specified by the number of nodes down the maximum fan length (x') and across the maximum fan angle (y'). A grid resolution of 500 was used in this study. The grid is sized to span twice the length of the fan in the radial component to measure runout past the fan toe, $x \in \{0, 2x'\}$, and 360 degrees in the angular component to capture all fan orientations, $y \in \{0, 360\}$. The number of radial (n) and angular (m) increments in the grid are calculated using the specified grid resolution, and the grid nodes are stored in an $m \times n$ array. Grid dimensions are shown in Figure 4.4. The y component can be converted from degrees to arc lengths using the angle and radius at each node (equation in Figure 4.4c). Due east was set as an arbitrary datum for 0 degrees.

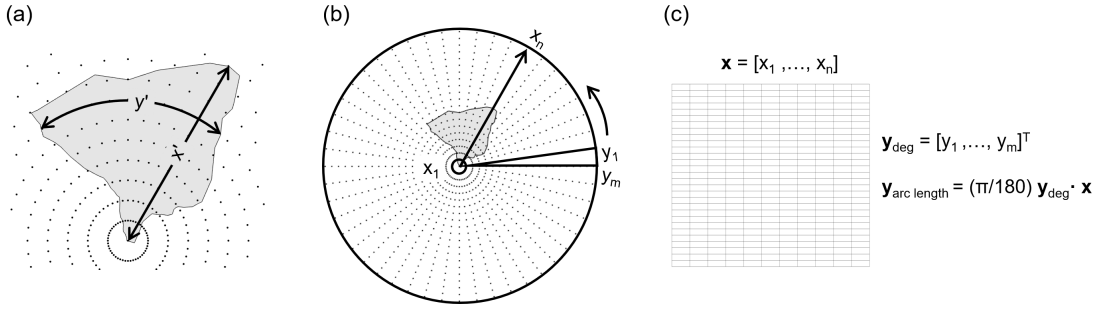

Figure 4.4. Initializing measurement grid. **a)** Normalizing fan dimensions; **b)** circular measurement grid with n radial increments in the x dimension, and m angular increments in the y dimension; and **c)** grid nodes stored in an $m \times n$ array.

3. **Intersect impact area shapefiles with grid**. Arrays are populated with ones and zeros to indicate if the grid node intersects the shapefile, forming the z dimension. An example for one impact area is shown in Figure 4.5a.

4. **Reorder and sum impact area arrays:**

   - **Relative to fan axis.** Columns are reordered relative to the bearing of a line connecting the fan apex to the fan centroid (Figure 4.5b).
   - **Relative to previous flow path.** The bearing to each node along a flow path (n) for each flow path (i) is stored in an $i \times n$ array. For each impact area array (i), each column (n) is reordered relative to the bearing along the previous flow path ($i-1$) (Figure 4.5c).

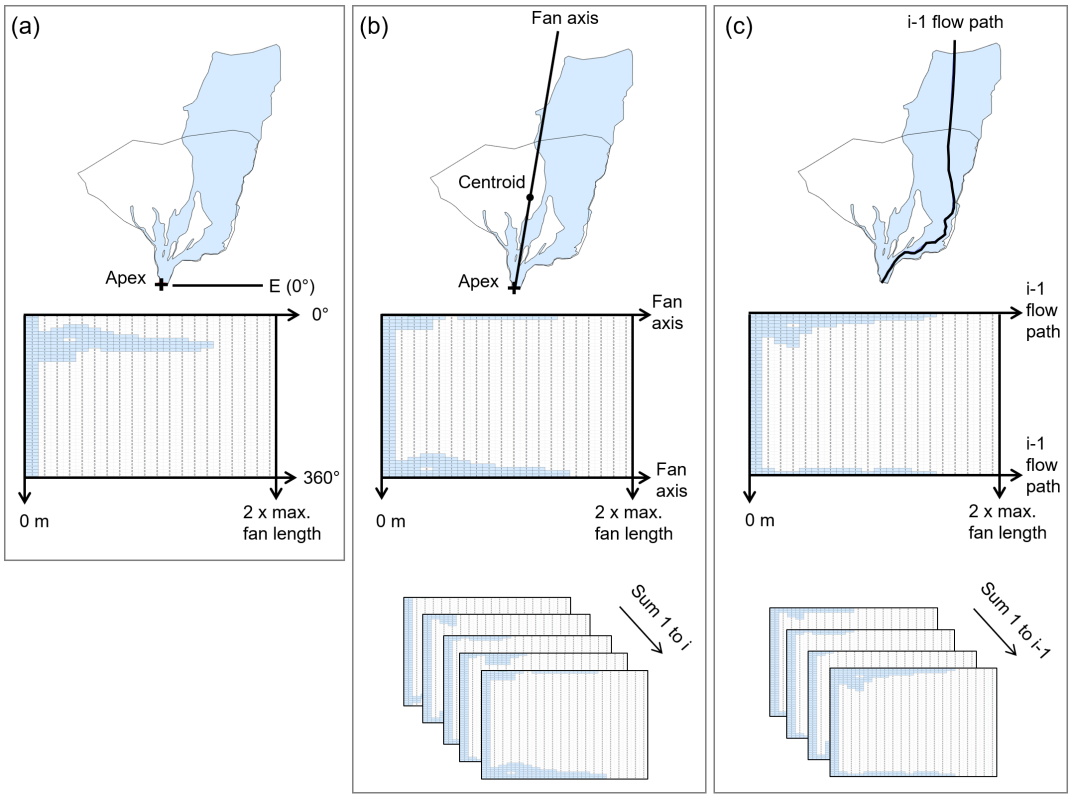

Figure 4.5. Reshaping and summing impact area arrays. **a)** Intersection of an impact area with the measurement grid; **b)** re-ordering impact area array relative to fan axis and summing; and **c)** re-ordering impact area array relative to previous flow path ($i-1$) and summing.

5. **Plot summed arrays on normalized axes.** The x component is normalized by the maximum fan length (x'), calculated as the maximum planimetric distance from the apex to a point on the fan boundary. The y component is normalized by the maximum fan arc length (y'), calculated as the maximum arc length intersecting the fan along the measurement grid. Normalizing fan dimensions are shown in Figure 4.4a. The z summation arrays are re-sampled over the

normalized $x \in \{0, 2\}$ and $y \in \{-1, 1\}$ vectors at the specified grid resolution to reduce the size of the array (500 used in this study). Fan-normalized spatial impact heatmaps (summation plots) for one fan are shown in Figure 4.6.

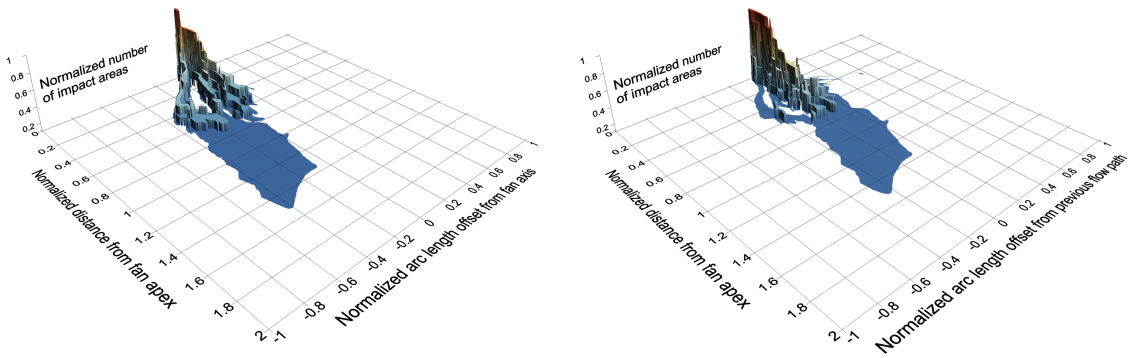

Figure 4.6. Examples of summed and normalized impact area plots for one fan site, relative to the (left) fan axis and (right) previous flow path.

4.1.4 Limitations

Aside from mapping and data record uncertainties (described in Section 3.8), the main limitations associated with the fan-normalized spatial impact heatmaps are related to normalization and reference datums. The fan boundary is an imperfect normalizer because fans truncated by valleys, rivers, glacial features, and/or coalescing fans would be undersized, whereas fans formed largely under paraglacial conditions may be oversized, potentially skewing trends (although paraglacial fans were not included in this dataset). Not all fans are idealistic semi-conical shapes, and in some cases, normalizing dimensions reflect external geomorphic and topographic constraints rather than debris flow runout trends. Topography is not considered since all measurements are planimetric. This method is not ideal for fans with bifurcating channels or flows with multiple flow paths since measurements from the previous flow path are relative to a single line. The heatmaps treat all impacts as equal; there is no differentiation between impact energy based on flow thickness, composition, or speed. Future work incorporating flow intensity is discussed in Section 5.3. Lastly, different fan environments (i.e., geology, climate, topography, fan morphology) may preclude aggregating impact areas across multiple fans, which is made possible with normalized axes. As with any empirical method, discretion is required when interpreting regional heatmap aggregates.

4.2 Regional Spatial Impact Trends on Fans in Southwestern British Columbia

4.2.1 Spatial Impact Heatmaps

Spatial impact heatmaps comprised of 176 impact areas across 30 fans in SWBC are shown in Figure 4.7, relative to the fan axis (a,b) and relative to the previous flow path (c,d). The heatmap relative to the fan axis shows the variety (and chaos) of impacts and flow paths across the fan space. The heatmap relative to the previous flow path shows how most impact areas follow the previous flow path, with some deviations from avulsion and/or lateral spreading. Plots b and d in Figure 4.7 are not normalized by the fan dimensions, and preserve scaling. From the fan apex, almost all debris flows impact within $\pm 60^\circ$ relative to the fan axis or previous flow path.

Overall, the heatmaps in Figure 4.7 show a decay in the fraction of impacted areas away from the fan apex, and for the plots relative to the previous flow path, a decay away from the active channel. Figure 4.8 shows smoothing of the fan-normalized heatmap (surface) using filters in Surfer ® (Golden Software, LLC, 2018). The plots in Figure 4.8 are an oblique view of a symmetrical version of Figure 4.7c, where directionality was removed by transposing impacted grid cells along the $y = 0$ axis. The general shape of the surfaces in Figure 4.8 can be interpreted as a bivariate empirical cumulative runout exceedance distribution function, representing the fraction of events exceeding a certain distance relative to an active channel. Isolines extracted from the fan-normalized heatmaps (i.e., draped incrementally along both axes of the fan-normalized spatial impact surface) are shown in Figure 4.9.

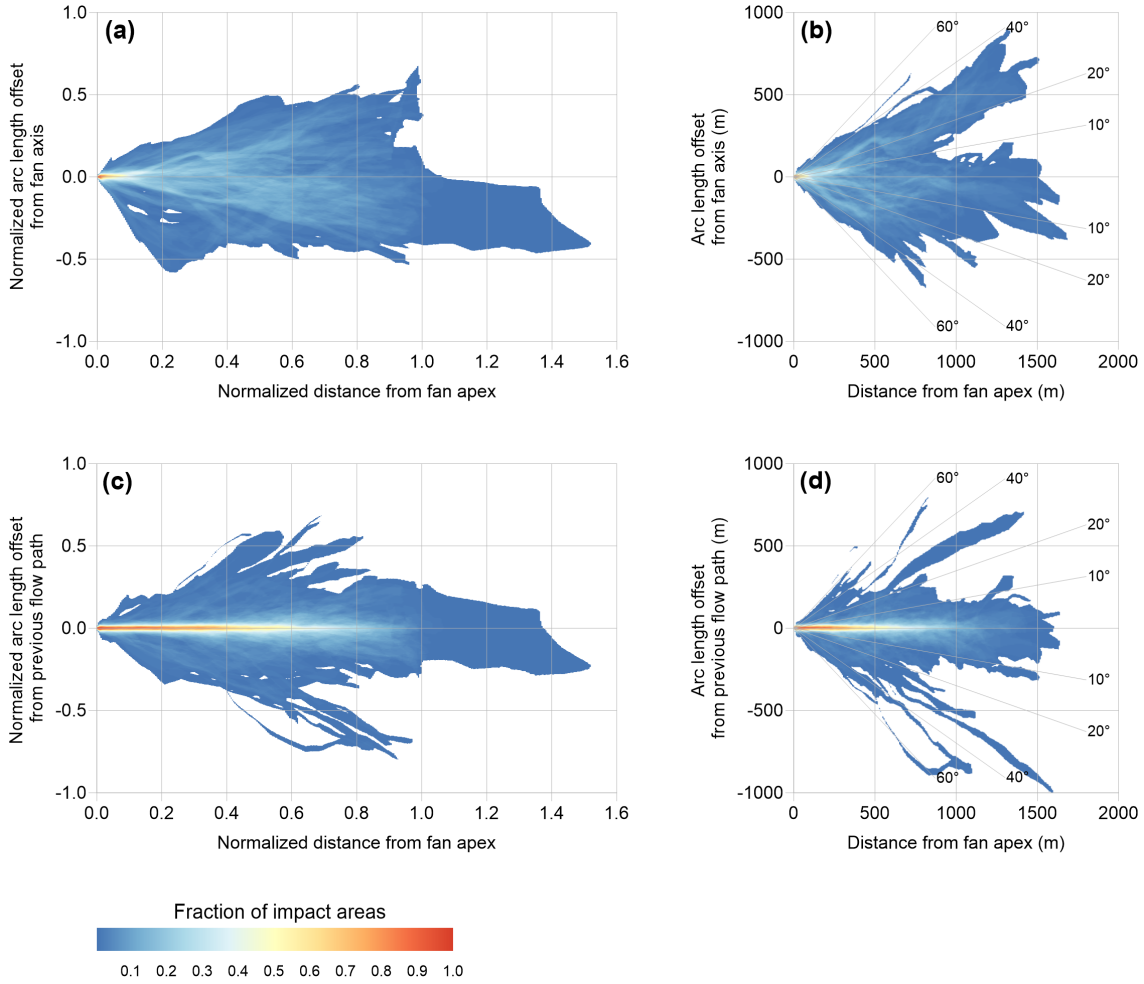

Figure 4.7. Regional debris flow spatial impact heatmaps for SWBC based on 176 mapped impact areas across 30 fans. **a)** Fan-normalized, arc lengths measured relative to the fan axis; **b)** unnormalized, arc lengths measured relative to the fan axis; **c)** fan-normalized, arc lengths measured relative to the previous flow path; and **d)** unnormalized, arc lengths measured relative to the previous flow path.

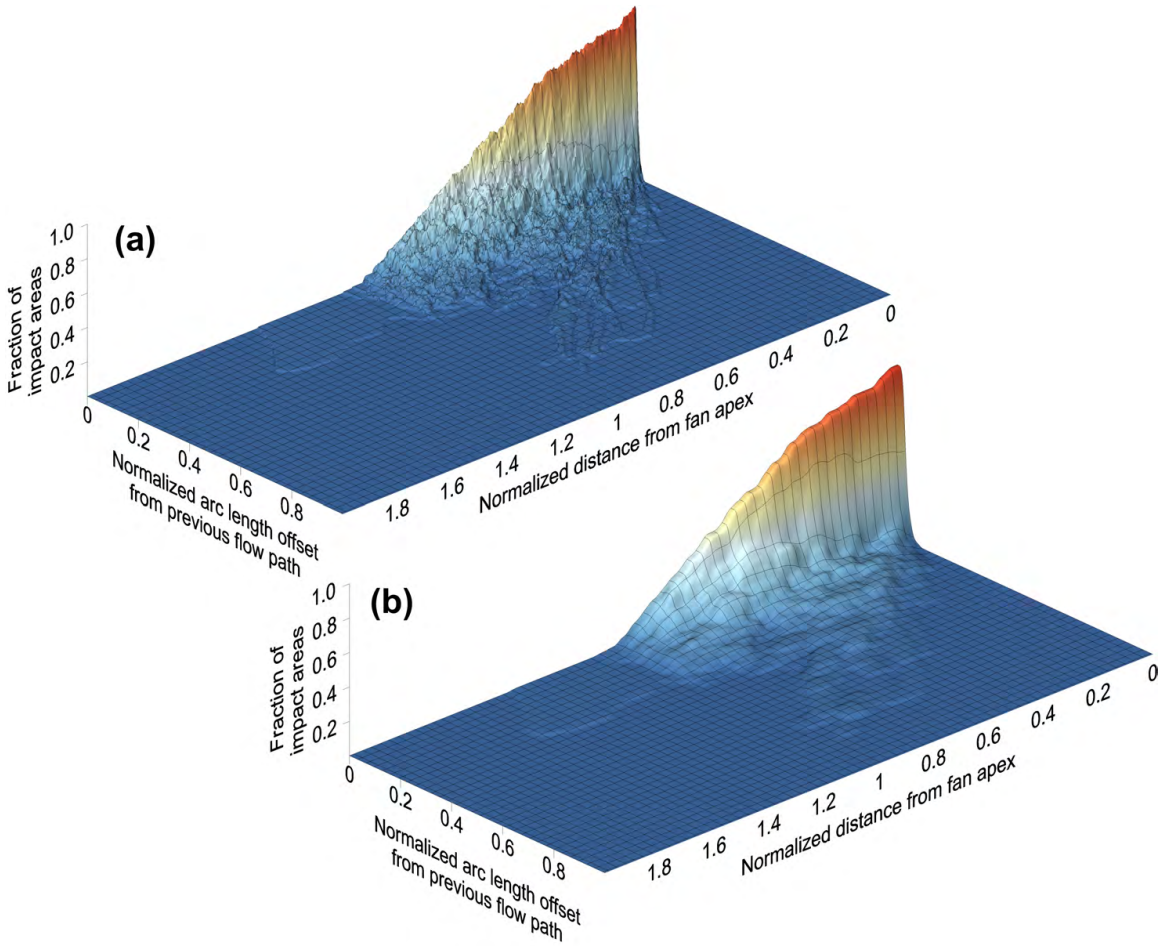

Figure 4.8. Smoothing of the fan-normalized spatial impact surface (heatmap relative to the previous flow path, non-directional) using filters in Surfer ® (Golden Software, LLC, 2018). **a)** Raw data; and **b)** 3 passes of a 5×5 maximum value filter and 10 passes of a Gaussian low-pass filter.

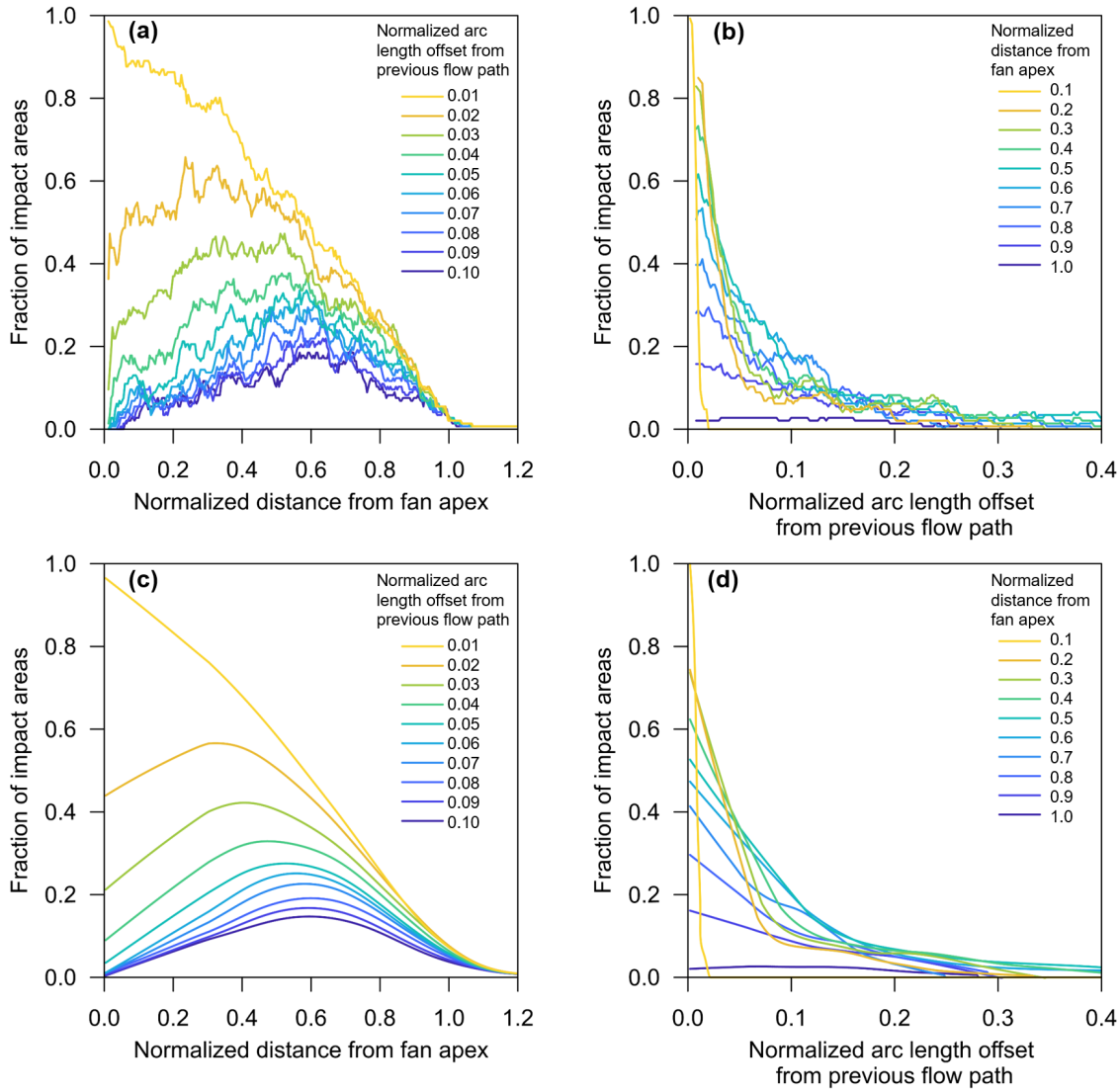

Figure 4.9. Isolines extracted from regional fan-normalized spatial impact heatmap. **a,b)** Raw data; and **c,d)** data smoothed in MATLAB using LOWESS (locally weighted scatterplot smoothing).

4.2.2 Maximum Runout Distributions

Distributions of maximum runout in the down-fan (x) and cross-fan (y) components were extracted from the spatial impact heatmaps relative to the previous flow path. Probability density functions (pdf) and empirical cumulative runout exceedance distribution functions (ecdf', or cumulative runout exceedance for short) are shown in Figure 4.10 (fan-normalized) and Figure 4.11 (unnormalized)

for the SWBC dataset. Runout exceedances are presented instead of a non-exceedance probability typical of an empirical cumulative distribution function (ecdf) due to the applicability in hazard and risk calculations, specifically, the probability that a hazard will reach the element at risk (see Section 2.3). The ecdf' (also known as the complementary cumulative distribution function) is equal to $1-$ecdf.

Statistical distributions were fit to the data using the maximum likelihood estimation method and selected based on goodness of fit metrics (e.g., Akaike information criterion, Bayesian information criterion). Fan-normalized distributions (Figure 4.10) follow normal and log-normal distributions in the down-fan and cross-fan components, respectively. Although the logistic distribution marginally out-performed the normal distribution for maximum runout in the down-fan component, the normal distribution is presented here due to similarities with the log-normal distribution, such as calculating the location (mean, μ) or scale (standard deviation, σ) parameters. The unnormalized distributions shown in Figure 4.11 generally follow a similar distribution to the fan-normalized data, although the maximum runout in the down-fan component is better represented by a Gamma distribution with heavier tails and a positive skew. Based on the SWBC dataset, about 90% of the debris flows impacted past 50% of the maximum length down the fan, while less than 10% avulsed beyond 50% of the maximum arc length across the fan.

Since the cumulative runout exceedance curves are projections of the maximum runout in the down-fan and cross-fan dimensions, the probabilities cannot be directly combined for a spatial probability of impact at a location on a fan. Instead, a two-dimensional cumulative runout exceedance distribution can be represented by either the heatmap in Figure 4.8, the isolines in Figure 4.9, or a bivariate distribution fit to the data in Figure 4.12. An example of how the fan-normalized spatial impact heatmaps can be transformed for use in hazard and risk calculations is described in Section 4.5.1.

There is a steep reduction in impact areas with runout recorded past the maximum fan length ($x = 1$), as shown by the normalized pdf for the down-fan component in Figure 4.10. The paucity of debris flow impacts here might be a result of fan truncation by a water body, such as a lake or river, or another topographic or physical obstacle. Debris flows may have runout further if unconstrained

by these features, with a hypothetical distribution resembling the bell-shaped tail of the normal distribution (implications of fan truncation is discussed further in Section 4.4.9). Data censoring may also be present at the upper tail of the distribution (closer to the fan apex, $0 < x < 0.4$). Smaller, less mobile events that mostly deposit in the upper-fan channel are not discernible in aerial imagery, and thus would not be captured in the data record. Similarly, debris flows that remained in the active channel may be underrepresented in the cross-fan distribution. Without data censoring, the peak of the cross-fan distribution in Figure 4.10 might be closer to the previous flow path ($y = 0$), with a higher density of impact areas between $0 < y < 0.1$.

There is a slight positive covariance between the two orthogonal runout dimensions (Figure 4.12), indicating that debris flows that deviate from the previous flow path also typically have longer runouts in the down-fan direction. The covariance is partly explained because arc lengths are calculated with a radius (i.e., the position down-fan), but there are many impact areas where the points of maximum runout for each dimension are at different locations, such as those with bifurcating flow paths or a variable spreading width. Figure 4.12 provides evidence that debris flow mobility and avulsion might be related. A possible physical interpretation for this relationship is related to event volume, in which large magnitude events with sufficient energy travel long distances down-fan (e.g., Corominas, 1996) are also likely to avulse the channel (e.g., de Haas et al., 2018b). The relationship between volume and runout is discussed further in Section 4.4.

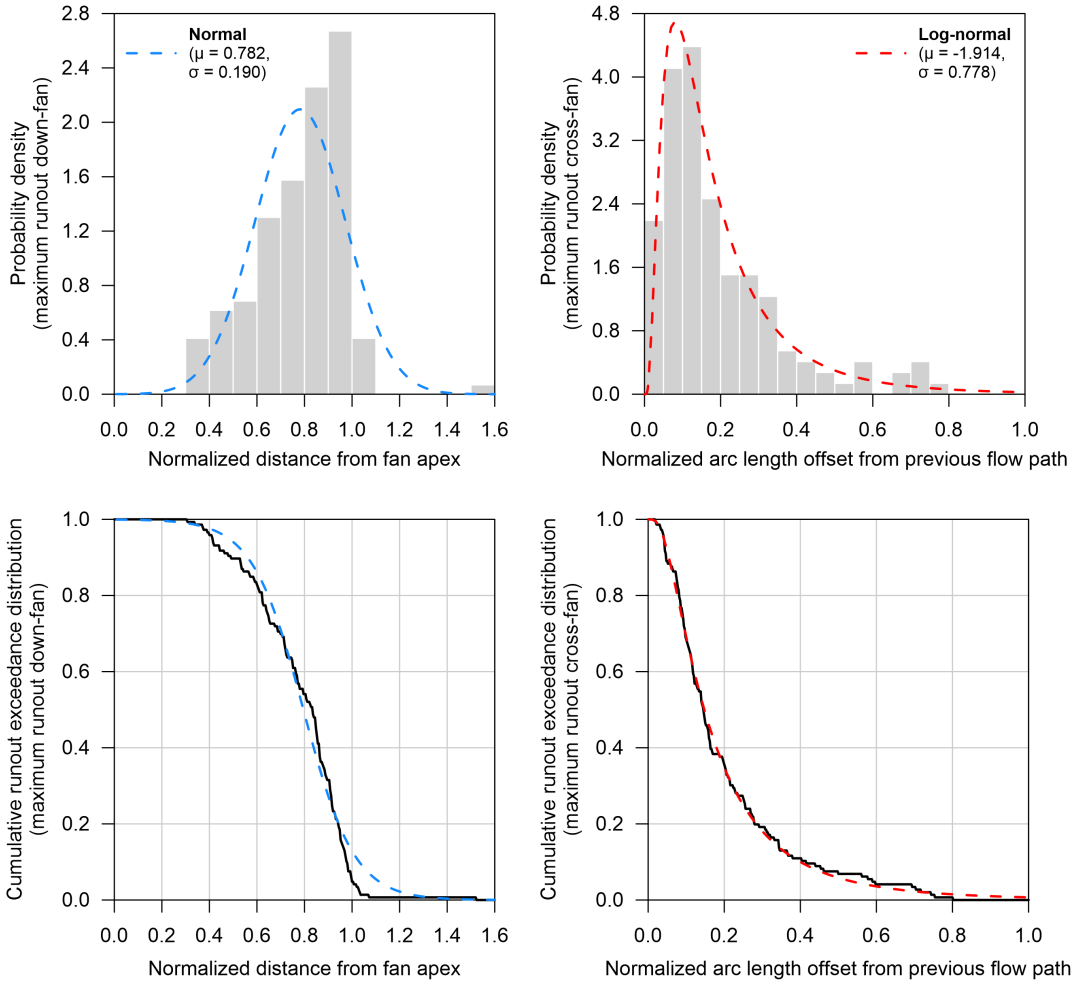

Figure 4.10. Fan-normalized maximum runout distributions for the down-fan (left) and cross-fan (right) components based on 30 fans in SWBC.

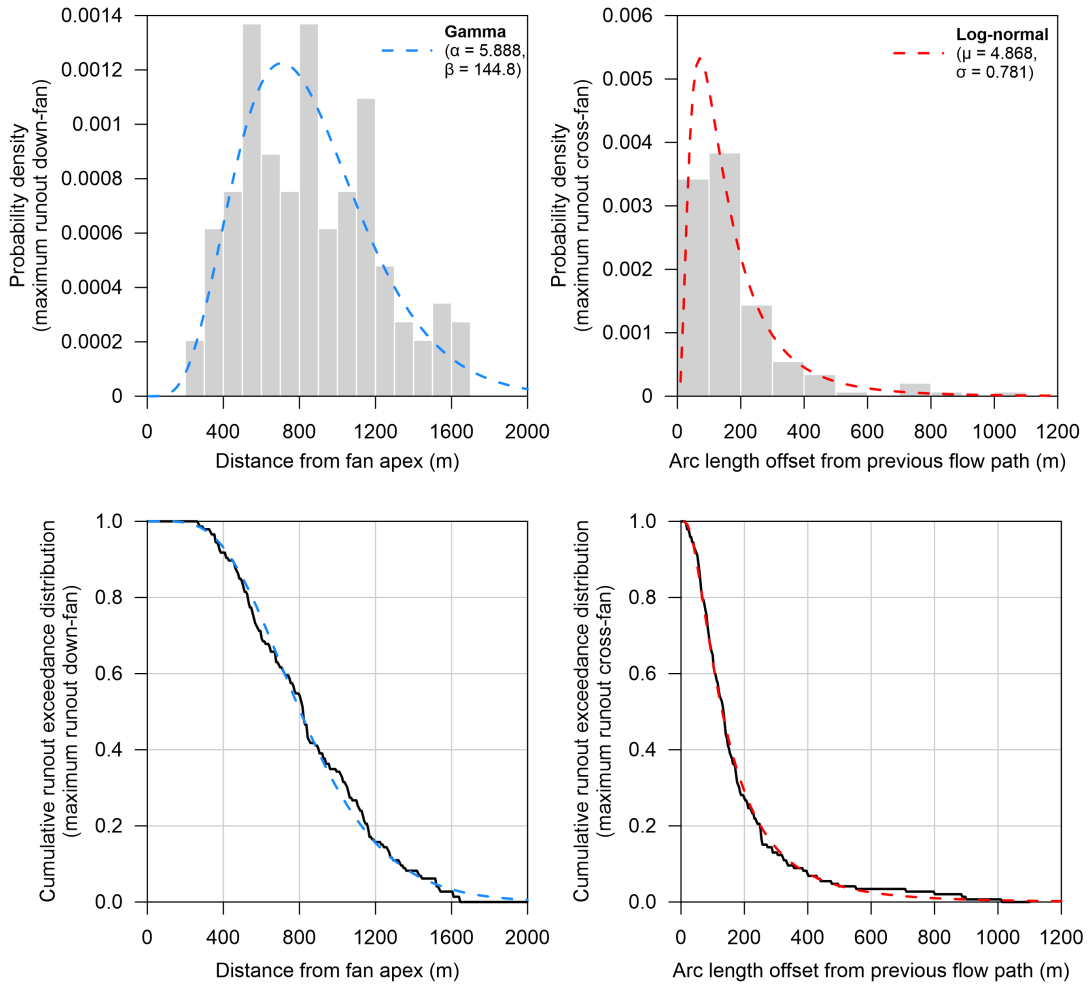

Figure 4.11. Maximum runout distributions for the down-fan (left) and cross-fan (right) components based on 30 fans in SWBC.

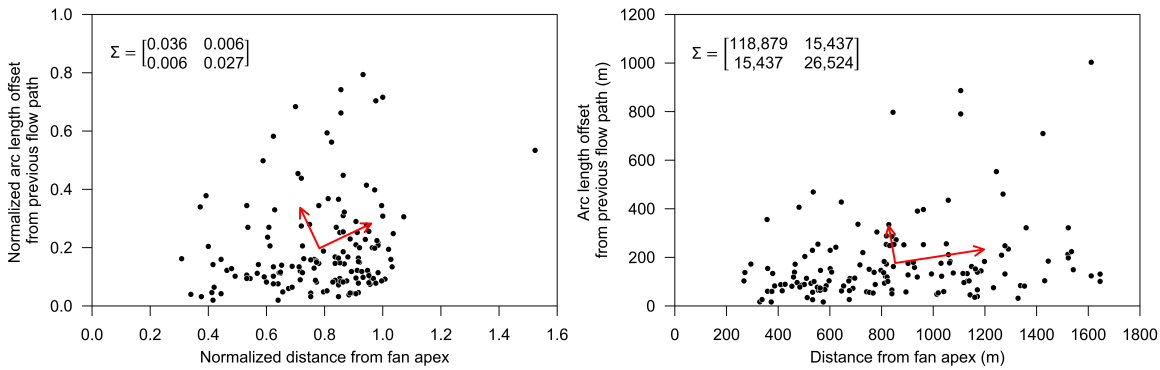

Figure 4.12. Relationship between maximum runout in the down-fan (x) and cross-fan (y) components, with normalized (left) and unnormalized (right) scales. Eigenvectors of the covariance matrix (Σ) scaled by the respective eigenvalue are plotted in red.

4.2.3 Comparison to an External Case Study: Kamikamihori Fan, Japan

The regional SWBC distributions were compared to runout distributions at the Kamikamihori fan, a well-studied and monitored debris flow creek on the slopes of the active volcano Mount Yakedake in the northern Japanese Alps (e.g., Suwa et al. 2009; Suwa et al. 2011; de Haas et al. 2018a). Over ten debris flows per year occurred in the decade following the last phreatic eruption in 1962, and an observation station installed in 1970 has recorded data from upwards of 91 debris flow events (Suwa et al., 2011). Although the geologic conditions differ from the SWBC dataset, the Kamikamihori fan was chosen because deposit extents have been mapped following each event since 1978.

The Kamikamihori fan dataset consists of 17 events over a span of 27 years. Depositional history from 1978 to 2005 compiled by de Haas et al. (2018a) was manually georeferenced (Figure 4.13) and the polygons converted into fan-normalized spatial impact heatmaps (Figure 4.14). Lobe sequences corresponding to a single event were combined into one impact area, and boundaries were extended to the fan apex following contours or channels, consistent with impact area mapping for the SWBC dataset. Since aerial photos, satellite images, or field data were not available for these events, flow paths were approximated as the center of the impact area path in the down-fan direction. The approximate fan area and apex were estimated using contour maps and satellite imagery.

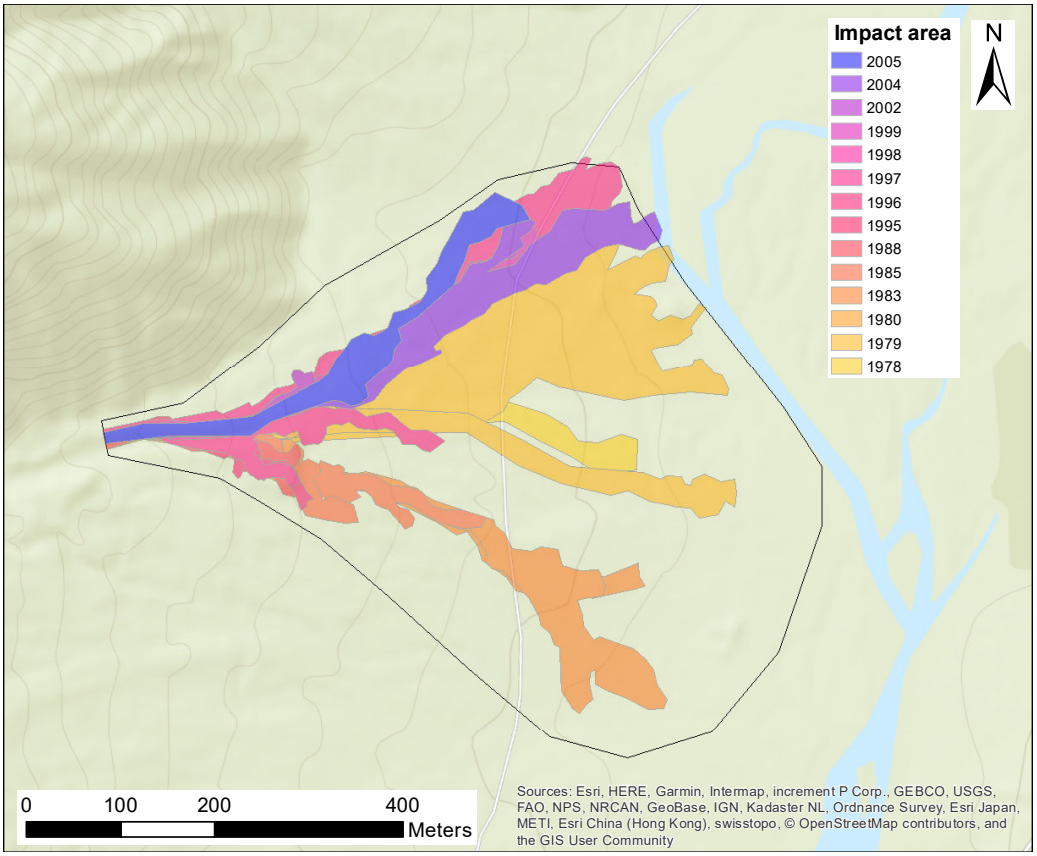

Figure 4.13. Depositional history at the Kamikamihori fan, Japan. Impact areas adapted and mapped using figures compiled by de Haas et al. (2018a).

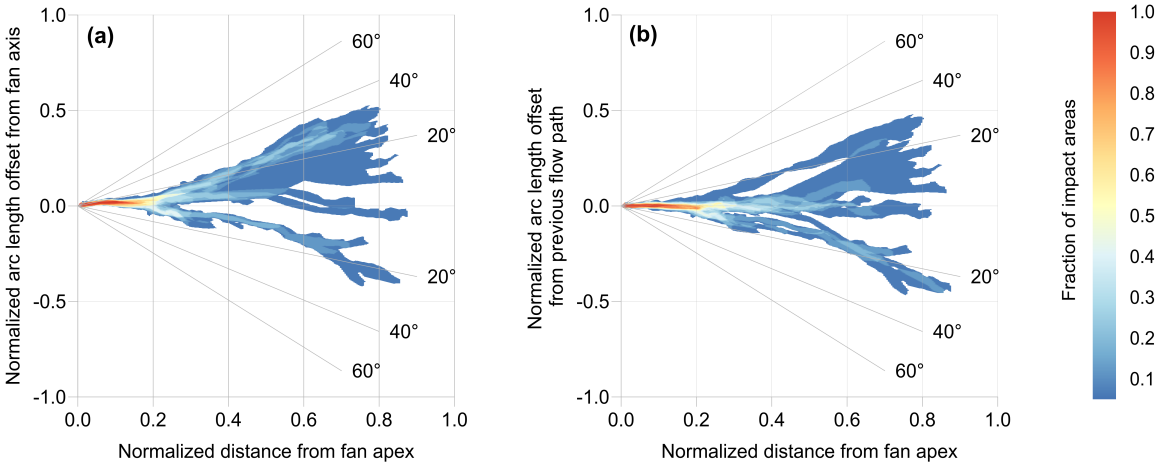

Figure 4.14. Fan-normalized spatial impact heatmaps **a)** relative to the fan axis; and **b)** relative to the previous flow path, for the Kamikamihori fan based on 17 impact areas.

Figure 4.15 shows the maximum runout distributions at the Kamikamihori fan (blue) compared to the entire SWBC dataset (grey). The distribution of normalized runout in the cross-fan component is similar to the SWBC dataset, however, there is a clear difference in the down-fan component; a much higher proportion of debris flows recorded at Kamikamihori terminate closer to the fan apex. As summarized by de Haas et al. (2018a), the deposition on the Kamikamihori fan follows patterns of channel plugging, backstepping, and avulsion, with successive deposits migrating up-fan until a flow of sufficient magnitude initiates a large avulsion. An example of this pattern is the four low mobility channel-blocking events from 1985 to 1996, followed by a relatively large debris flow in 1997 diverting flow from the south to the north side of the fan. Debris flow lobes at the Kamikamihori fan have been distinguished into two groups: "swollen" (steep bouldery fronts, clast-supported, fan-proximal) and "flat" (thin deposits lacking steep fronts, matrix-supported) (Suwa et al. 2009; Suwa et al. 2011). The relative proportion of these two groups is interpreted to be reflected in the two peaks of the down-fan pdf near 0.2 and 0.8 of the normalized fan length (Figure 4.15). Channel-blocking lobes with steep fronts and open-work structure have also been observed at the SWBC fans (e.g., Figure 4.16), however, these localized channel-blocking events are difficult to distinguish in aerial imagery compared to large magnitude events and/or major avulsions. Futhermore, some of the impact areas from the SWBC dataset might be the sum of a few smaller events, the runouts of which would not be documented. The characteristic down-fan runout exceedance curve with a higher proportion of fan-proximal deposits afforded by a continuously monitored debris flow channel may provide justification for adjusting the upper tail of the regional SWBC distribution.

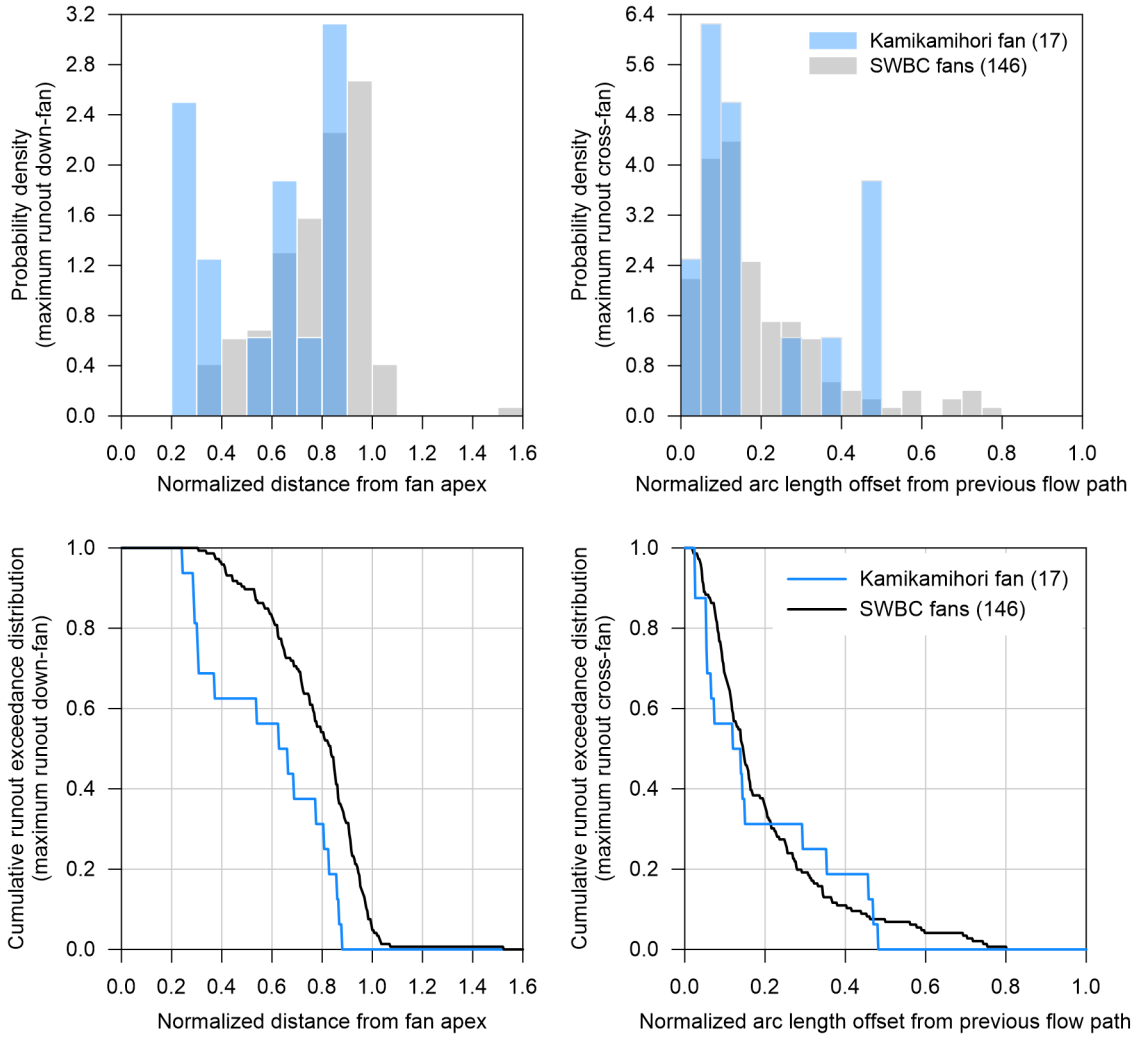

Figure 4.15. Comparison of maximum runout distributions in the down-fan and cross-fan components for the Kamikamihori fan (17 impact areas) to the regional SWBC dataset (176 impact areas, 30 fans).

Figure 4.16. Steep, bouldery, clast-supported, deposit front plugging the channel on the proximal fan at Currie D (evidence of localized debris flow impacts not visible in aerial imagery).

4.2.4 Comparison to Conceptual Avulsion Scenarios

In a recent study of the spatio-temporal evolution of debris flow fans, de Haas et al. (2018a) postulated conceptual avulsion patterns, as observed on fans from around the world. Figure 4.17 by de Haas et al. (2018a) illustrates conceptually the influence of flow volume sequencing and fan topography on runout and avulsion patterns. de Haas et al. (2018a) presented three scenarios: a) backstepping from a sequence of smaller flows followed by an avulsion during a large flow; b) avulsion through multiple channels, with the most topographically favourable flow path forming the main channel, followed by progressive backfilling of side channels; and c) gradual lateral shifting towards a topographic low during a sequence of similar-sized flows.

For illustrative purposes, fan-normalized cumulative runout exceedance distributions were extracted for the three conceptual scenarios in Figure 4.17 using the methods described in Section 4.1. Conceptual cumulative runout exceedance distributions in both down-fan and cross-fan components are shown in Figure 4.18 compared to empirical data. The conceptual distributions appear as step functions since only one cycle with three events per scenario is plotted, but a characteristic curve

shape can be idealized from them. As identified by de Haas et al. (2018a), scenario (a) cycles are observed on the Kamikamihori fan (Section 4.2.3), with a higher proportion of short runout events due to backstepping processes toward the fan apex. Conceptual scenario (b) is distinguished from the other distributions as having the largest area under the runout exceedance curve in the cross-fan component; this curve shape is due to multiple channels becoming activated, and therefore debris flow impacts directed further away from the previous flow path. Fan analogues for scenario (b) from the SWBC dataset are Abandoned or Cheam E, but are not shown in Figure 4.18 (refer to Appendix A for individual plots). The Currie D runout exceedance distribution closely resembles the runout patterns of scenario (c), particularly in the cross-fan component. Debris flows at Currie D mostly follow the previous flow path, with gradual lateral shifting and overprinting of previous deposits. Spatial impact trends at Currie D are described in more detail in Section 4.3.1. The SWBC aggregate distribution lies somewhere between the conceptual curves, showing an ensemble of avulsion patterns. Based on this preliminary work, the conceptual patterns described by de Haas et al. (2018a) are realistic analogues of spatial runout patterns observed on real debris flow fans.

It is likely that these conceptual avulsion patterns evolve through time with changing climate, supply conditions, and fan topography. Furthermore, many cycles may occur during a single event, or a cycle may be disrupted by extreme system perturbations or stochastic processes. The average runout distribution can be represented by an ensemble, as shown by the SWBC aggregate in Figure 4.18, but theoretical distributions based on topography (relative location of steepest descent) and flow volume sequencing may be derived to refine runout forecasting. This approach is shown conceptually in Figure 4.18 based on the work by de Haas et al. (2018a), but future work may involve developing these conceptual runout exceedance curves.

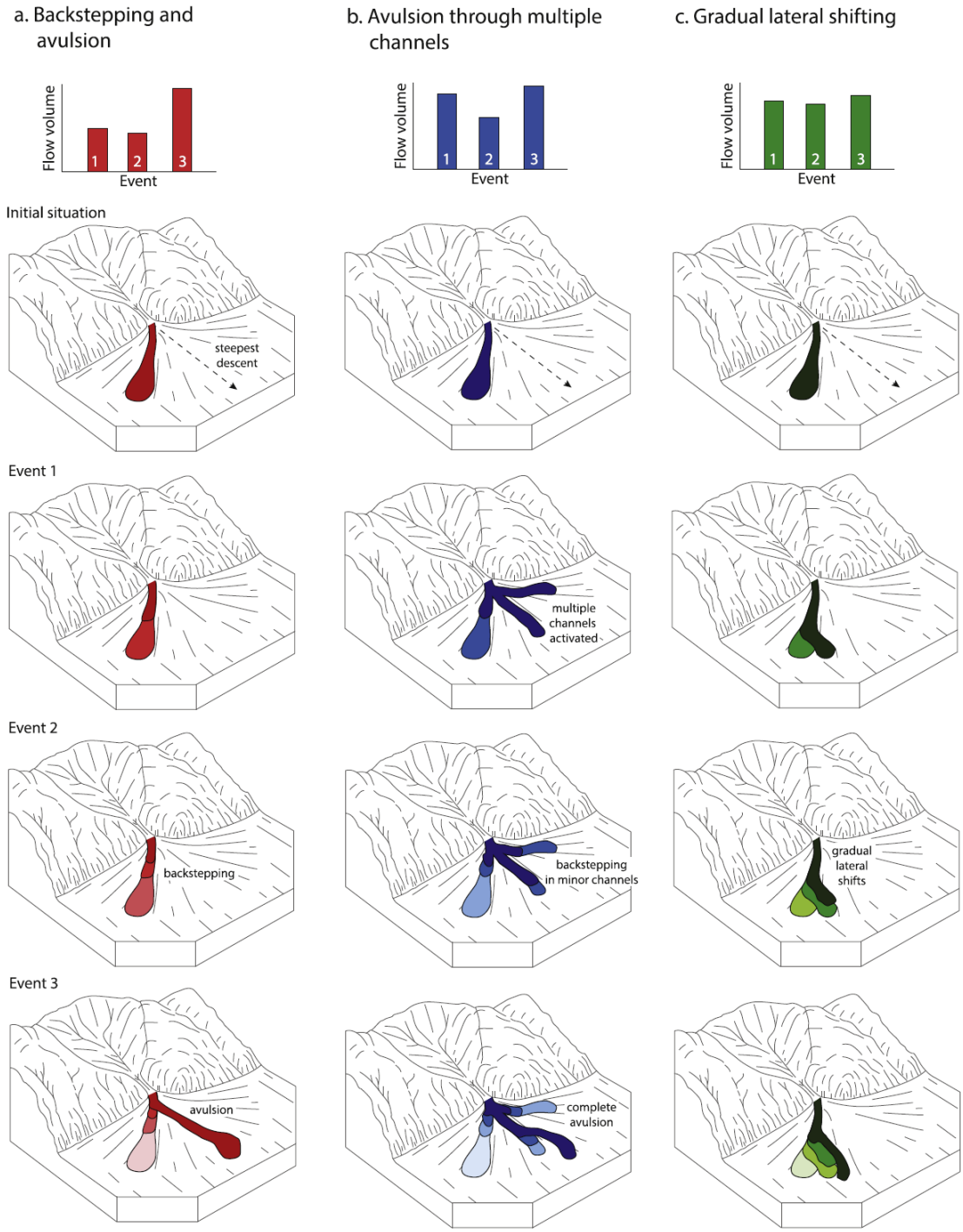

Figure 4.17. Figure from de Haas et al. (2018a) illustrating conceptual avulsion patterns based on varying flow volume sequences.

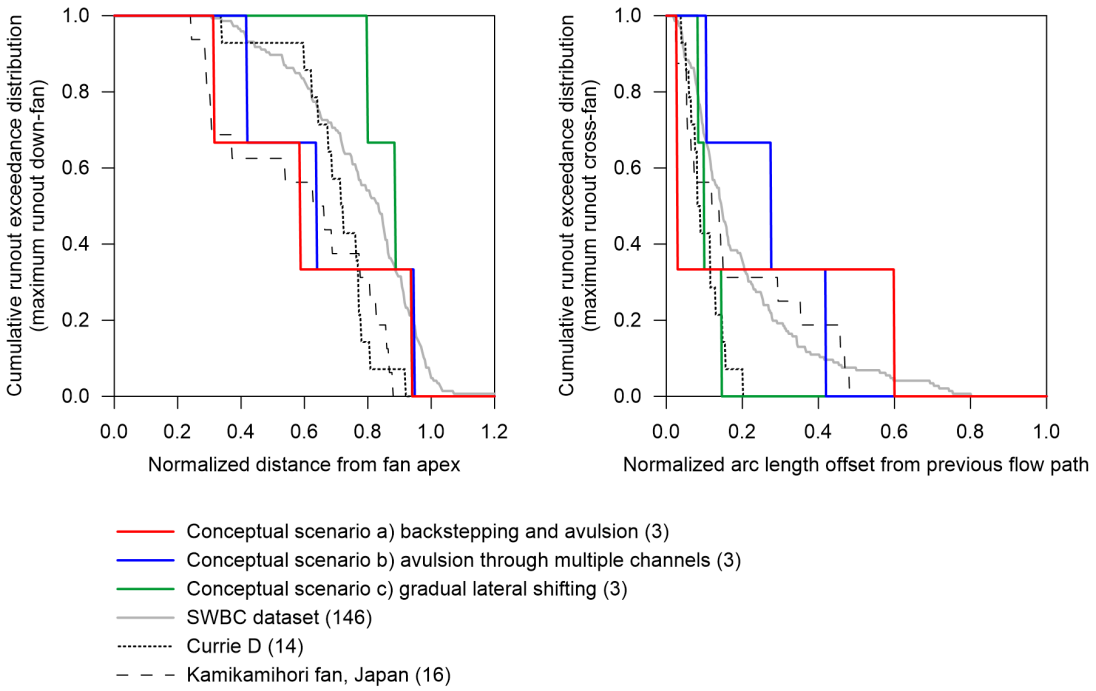

Figure 4.18. Fan-normalized cumulative runout exceedance distributions for conceptual avulsion scenarios proposed by de Haas et al. (2018a) (Figure 4.17) compared to empirical data.

4.3 Local Spatial Impact Trends at Two Locations in Southwestern British Columbia

In this section, local spatial impact trends are examined more closely at two locations from the SWBC dataset: three fans at Mount Currie near Pemberton, and two fans at Fountain Ridge near Lillooet (Figure 4.19). These sites were selected because of high rates of debris flow activity (10-15 impact areas at each fan), as well as the presence of lidar data and field observations to support a more detailed analysis.

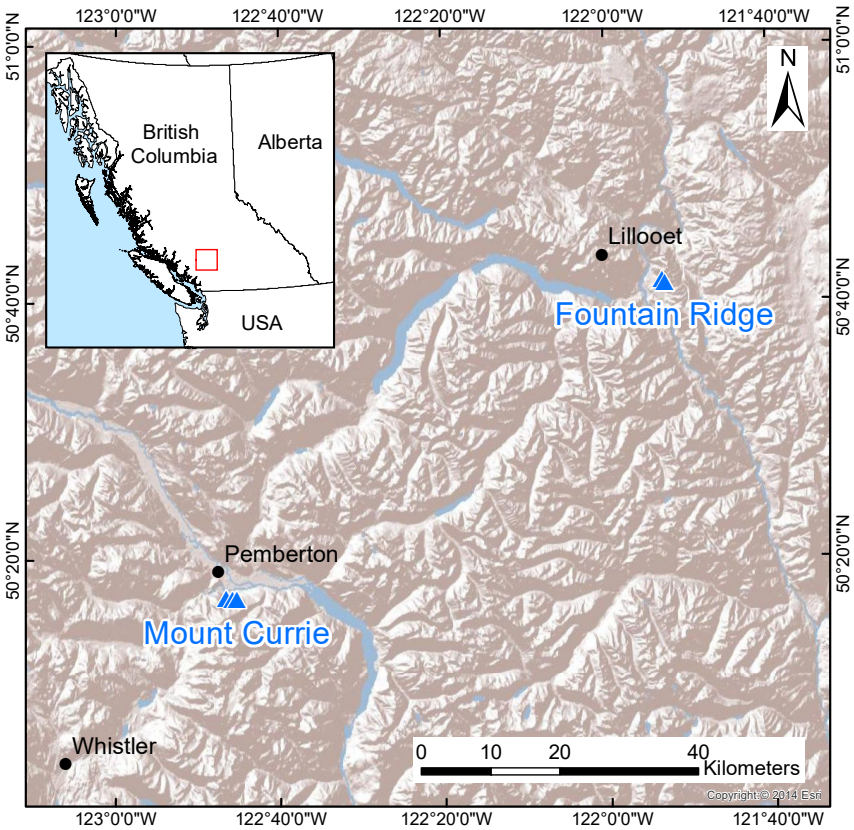

Figure 4.19. Location map of Mount Currie and Fountain Ridge fans.

4.3.1 Mount Currie

Three conjoined fans emanate from the steep, precipitous, north facing slopes of Mount Currie (Figure 4.20). Mount Currie is a northeast trending glacial arête ridge consisting of foliated quartz diorites with a strong joint control of relief (Bovis & Evans, 1995). The mountain ridge is dissected by linear tension cracks, scarps, and trenches, with a prominent 1.7 km long linear scarp oblique to the ridge axis (shown on the lidar in Figure 4.20) likely associated with gravitational movement (Bovis & Evans, 1995; Thompson et al., 1997). Frequent rockfalls, rock slides, and debris slides fill the watershed gullies with colluvium (BGC, 2018a). In addition to debris flows, snow avalanches commonly reach the fan. Despite Currie B having the largest watershed area, Currie D has the largest fan area. Although differences in fan areas might be attributed to different weathering rates or kinematic mechanisms in the respective watersheds, it is more likely a portion of the Currie B fan

was buried by floodplain sediments (anabranches of the Green River are seen abutting the fan toe of Currie B in the early airphoto record).

The fans are highly channelized, with large bouldery levees present at the upper fans, cobbly deposits with a sandy matrix typical on the lower fans, and evidence of sediment plumes inundating the Green River floodplain. The active channels are incised 10 to 15 m into the fans near their apexes. Typical debris flow features and deposits at the Mount Currie fans are shown in Figure 4.21.

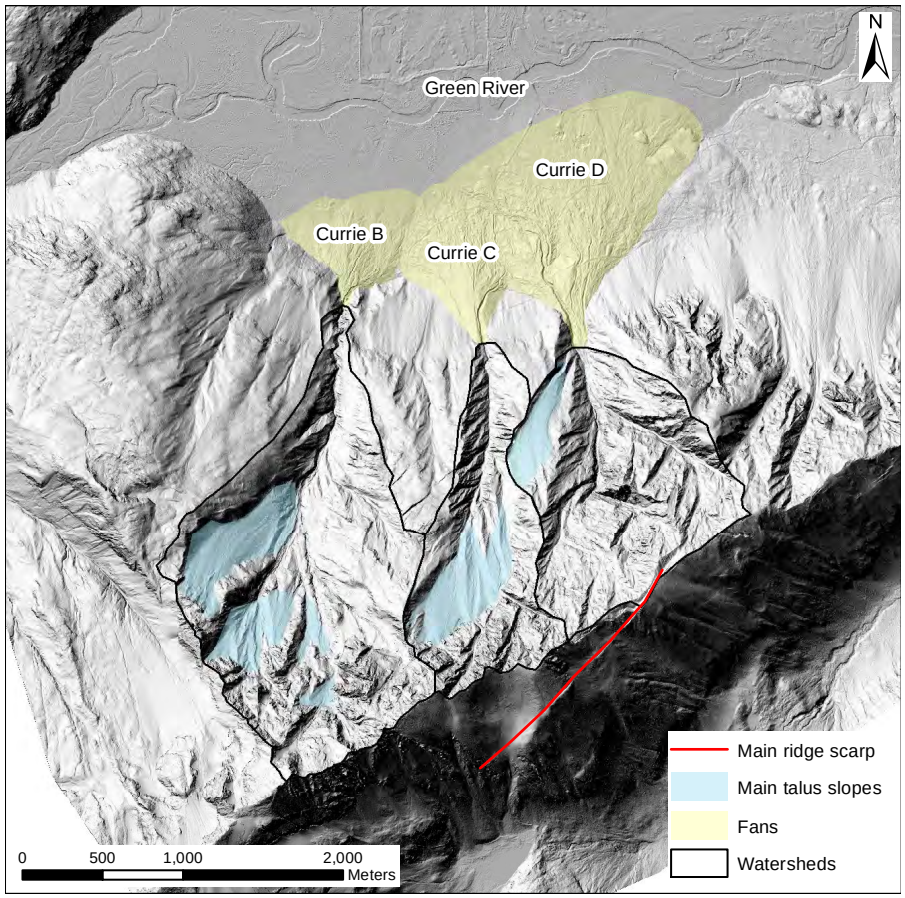

Figure 4.20. Overview of Mount Currie with main geomorphic features mapped. 2017 ALS bare earth hillshade courtesy of SLRD.

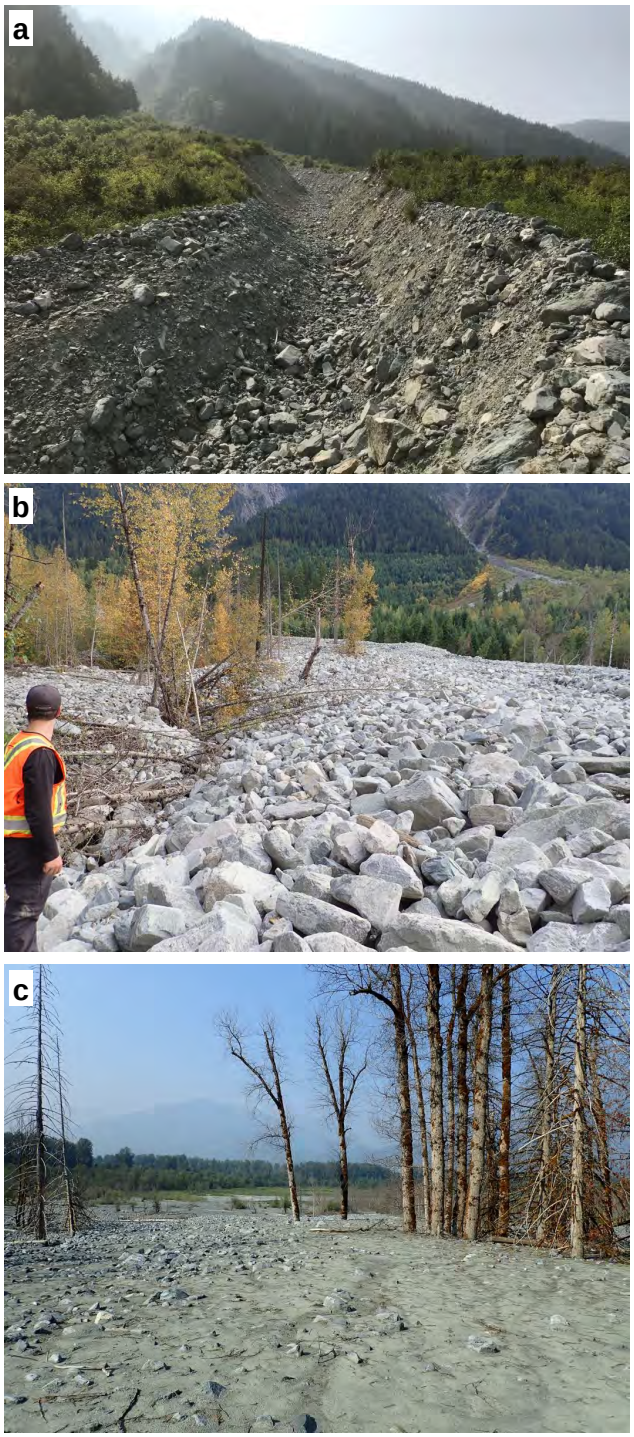

Figure 4.21. Mount Currie field photographs. **a)** Incised channel at the upper fan of Currie C; **b)** bouldery lobe, mid to lower fan at Currie D; and **c)** boulder-studded sandy deposit at the lower fan of Currie B, Green River floodplain in the distance.

Impact area mapping at the Mount Currie fans is shown in Figure 4.22, and spatial impact heatmaps in Figure 4.23. The largest debris flow in the dataset occurred at Currie B, with a volume of approximately 500,000 m^3. Part of the flow avulsed from the main channel at the channel bend downslope of the apex, while the bulk of the deposit followed the previous flow path, inundating the floodplain (sandy debris field pictured in Figure 4.21c). Debris flows recorded at Currie C are markedly of smaller magnitudes and more channelized compared to the other fans. The most impact areas mapped at any of the fans in the dataset is at Currie D (15), the most recent of which occurred during the summer of 2019 with a volume of about 100,000 m^3 (see Section 3.4.1 for change detection results). Debris flows recorded at Currie D remain channelized at the upper fan, and often deposit thick, coarse-grained terminal lobes at the distal fan, overlapping and side-stepping previous deposits here. No major avulsions shifting deposition to the east side of the fan were observed at Currie D in the airphoto record.

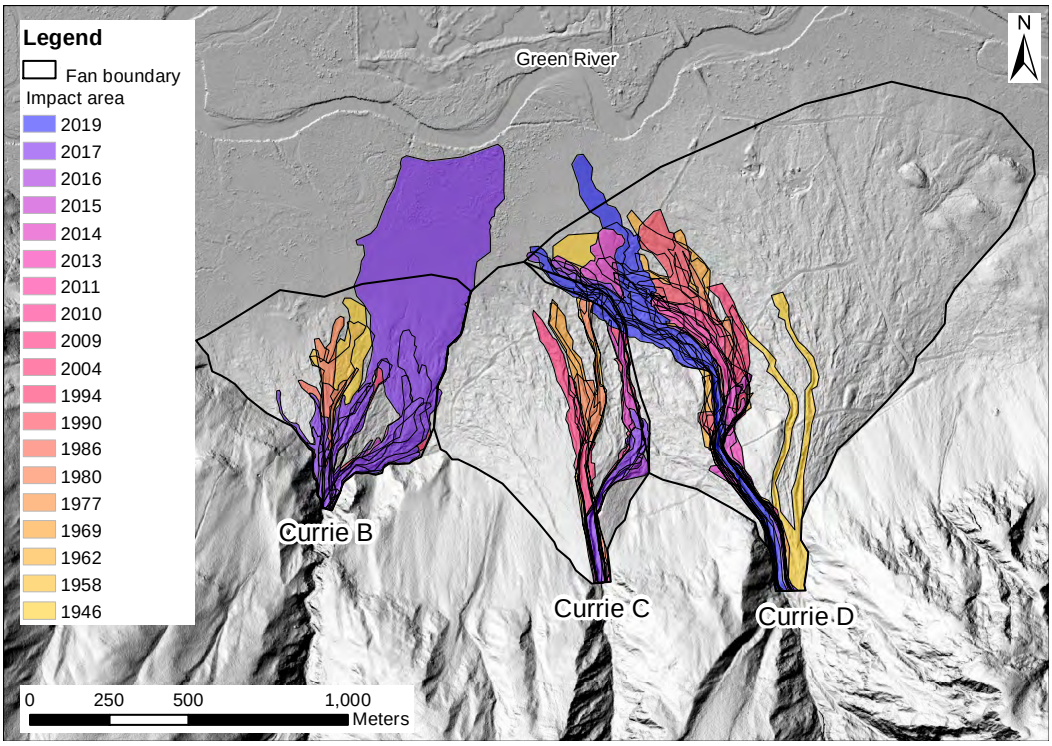

Figure 4.22. Debris flow impact area mapping at Mount Currie fans. 2017 ALS bare earth hillshade courtesy of SLRD.

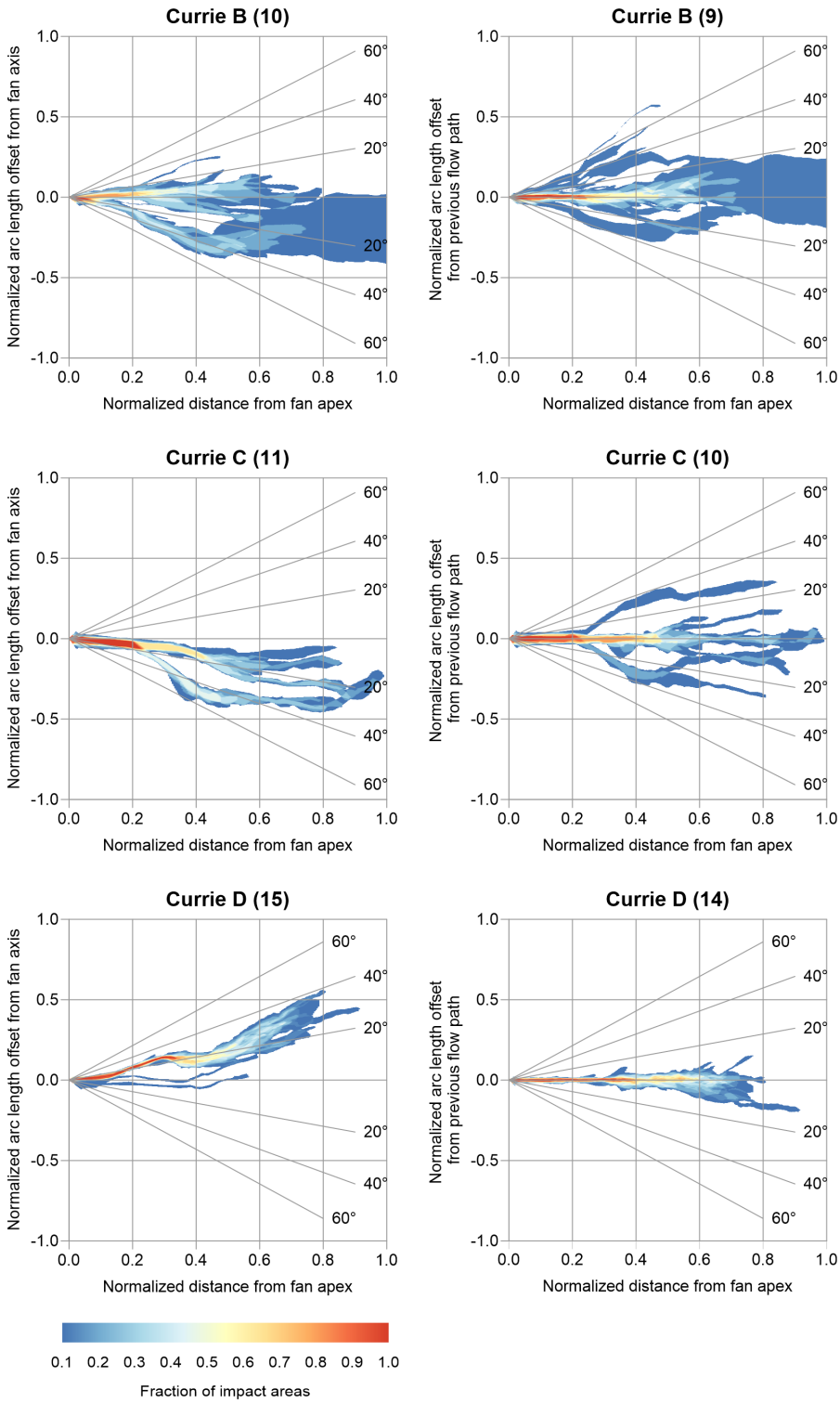

Figure 4.23. Fan-normalized spatial impact area heatmaps relative to the fan axis (left) and the previous flow path (right) for the Mount Currie fans.

4.3.2 Fountain Ridge

Fountain Ridge is a north-northwest trending ridge of folded, deformed, and highly weathered sedimentary rocks of the Jackass Mountain Group, including greywackes, argillites, and conglomerates (Duffell & McTaggart, 1952). Two very active conjoined debris flow fans have formed on top of a river terrace east of the Fraser River, and are truncated by a kame terrace to the south (Figure 4.24) (Ryder, 1969). Debris flow channels are fed by constant raveling of extensive talus slopes from steep, small basins (Jordan, 1994).

Jordan (1994) found that debris flows at Fountain Ridge appear to have relatively low velocities, high viscosities, and deposit most of their sediment load in well-developed levees. This morphology and flow behaviour is common of arid environments with lower water contents (Jordan, 1994; Whipple & Dunne, 1992). Typical debris flow features and deposits at Fountain Ridge are shown in Figure 4.25. Debris flows form narrow levee-confined channels with small lobes that break through the levees, or thin (less than 2 m thick) terminal lobes of uniform thickness on the distal fans, consisting of mostly gravels and cobbles. Based on one grain-size sample taken by Jordan (1994), 32% of the debris was matrix (smaller than 4 mm), and 21% was cobbles and boulders. Cemented, matrix-supported flow sequences were preserved in near-vertical channel banks at Fountain N (Figure 4.25b), showing inverse grading.

Differences in deposit textures and morphology at Fountain N and S are shown in Figure 4.26. Deposition at the lower Fountain N fan is more sheet-like, consisting of thin and wide deposits with channelized surfaces, while deposits at Fountain S tend to be self-channelizing and lobate. Based on field observations, the grain-size of the terminal lobes at Fountain S appear to be coarser and more uniformly graded compared to the deposits at Fountain N. Geomorphic evidence corroborating a higher coarse fraction for the Fountain S flows is the formation of prominent levees from coarse materials advected to the flow edges.

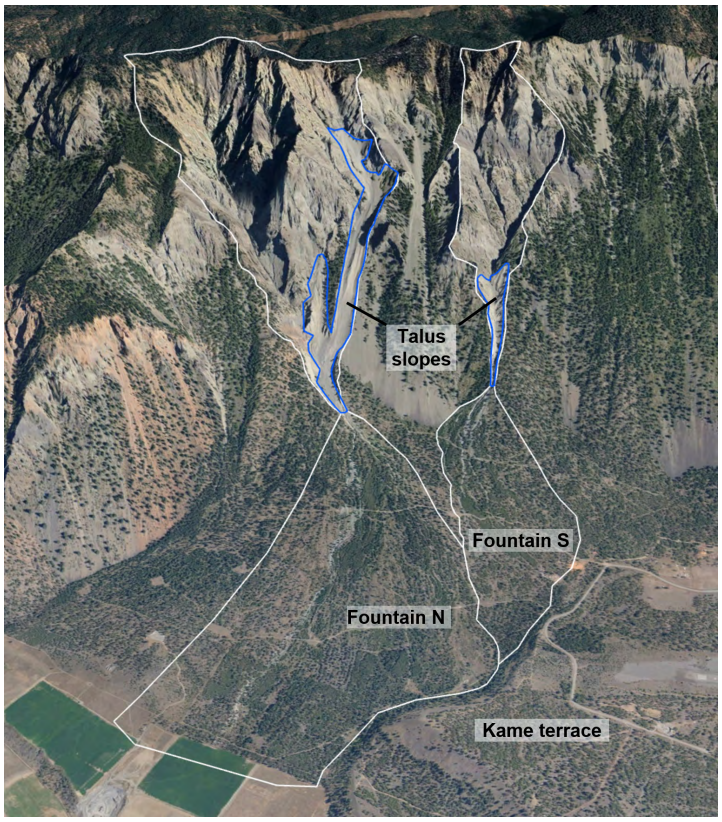

Figure 4.24. Oblique view of Fountain Ridge in Google Earth. Fans and watersheds are outlined in white, and talus slopes in blue. Fountain N is supplied by a 1.2 km long talus chute.

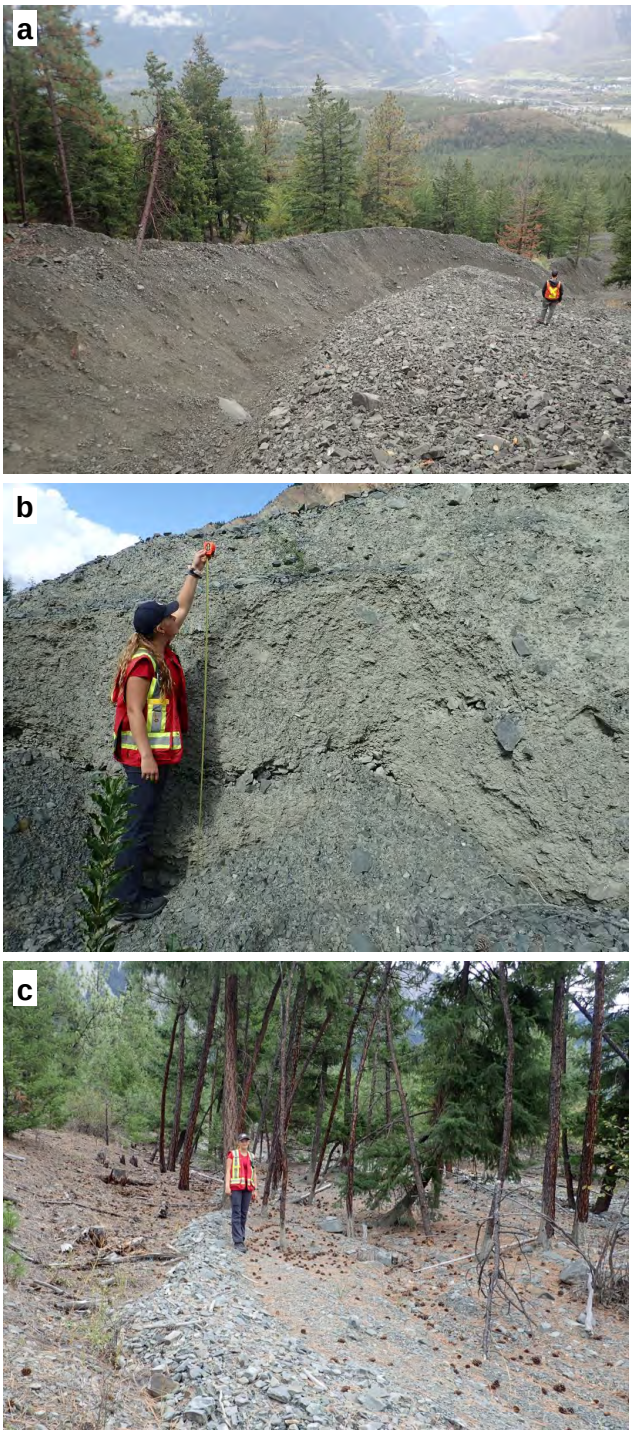

Figure 4.25. Fountain Ridge field photographs. **a)** Channelized reach on the upper Fountain N fan; **b)** near-vertical cemented channel side-wall exposing flow sequences and inverse grading, mid-fan Fountain N; and **c)** thin terminal lobe, distal Fountain N fan.

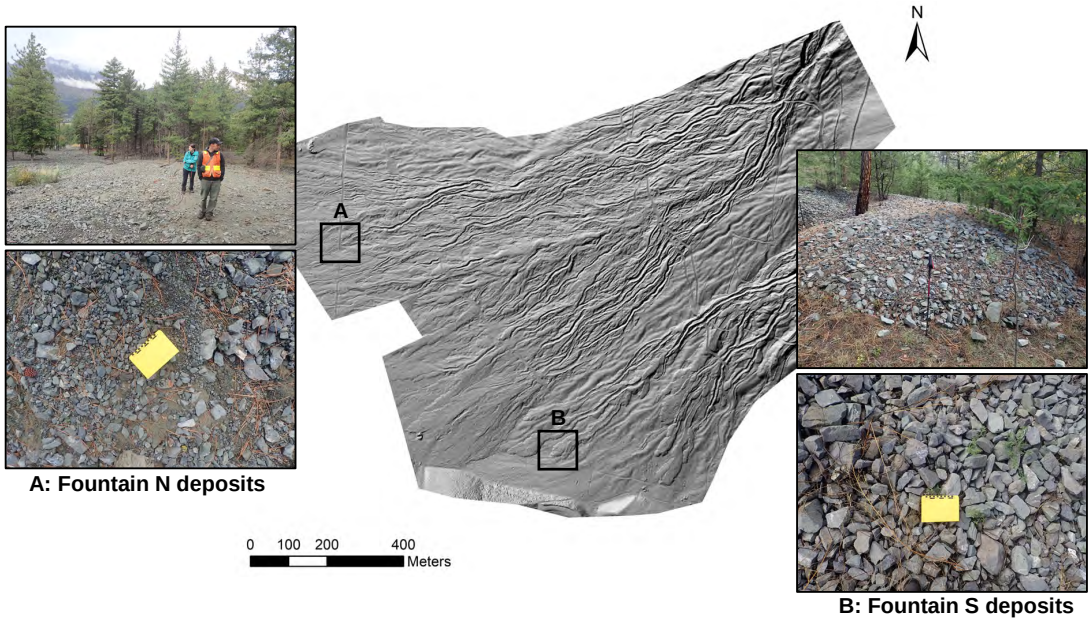

Figure 4.26. Comparison of debris flow deposit morphology and textures at the distal Fountain Ridge fans. Sheet-like deposits more typical at Fountain N, compared to lobate, coarser-grained deposits at Fountain S. 2019 bare earth lidar collected by RPAS (drone).

Impact area mapping at the Fountain Ridge fans is shown in Figure 4.27, and spatial impact heatmaps are shown in Figure 4.28. The largest event is estimated to be approximately 170,000 m^3 at Fountain N, while flows at Fountain S are less than 40,000 m^3. Avulsions are common at both fans. At Fountain N, major avulsions occur near the fan apex, causing back-and-forth switches between the north and south sectors, while avulsions at Fountain S occur at various locations down-fan as lobes break through levees. The two main avulsion paths at Fountain N are aligned roughly with the orientations of the main basin drainage and the talus chute. Debris flow runout distances are markedly longer at Fountain N (up to 1.7 km long, the furthest in the SWBC dataset), resulting in a large fan area.

Differences in deposit morphology, mobility, and avulsion patterns at Fountain N and S cannot be attributed to different source geologies or climates. A possible reason for these differences is the presence of a 1.2 km long talus slope in the comparatively larger watershed at Fountain N, providing a constant and unlimited supply of fine-grained material directly to the fan (Figure 4.24). The channel is incised 10-15 m into a Holocene fan near the apex, providing additional sediment from entrainment.

At Fountain N, it is likely that progressive aggradation or plugging near the fan apex primes the channel for avulsions.

Spatial impact trends at Fountain S are affected by both the texture of the sediment supply and topography. Fountain S has a much less extensive talus source and a smaller watershed compared to Fountain N. Debris with a slightly lower fines content is more diffusive of excess pore pressures, resulting in less mobile flows (e.g., de Haas et al., 2015; Whipple & Dunne, 1992). Although the Fountain S fan abuts a kame terrace, contemporary debris flow lobes typically terminate short of it, whereas debris flows at Fountain N runout further at comparable fan gradients. Fountain S flow paths are topographically forced to the south away from the depositionally-dominant northern fan system.

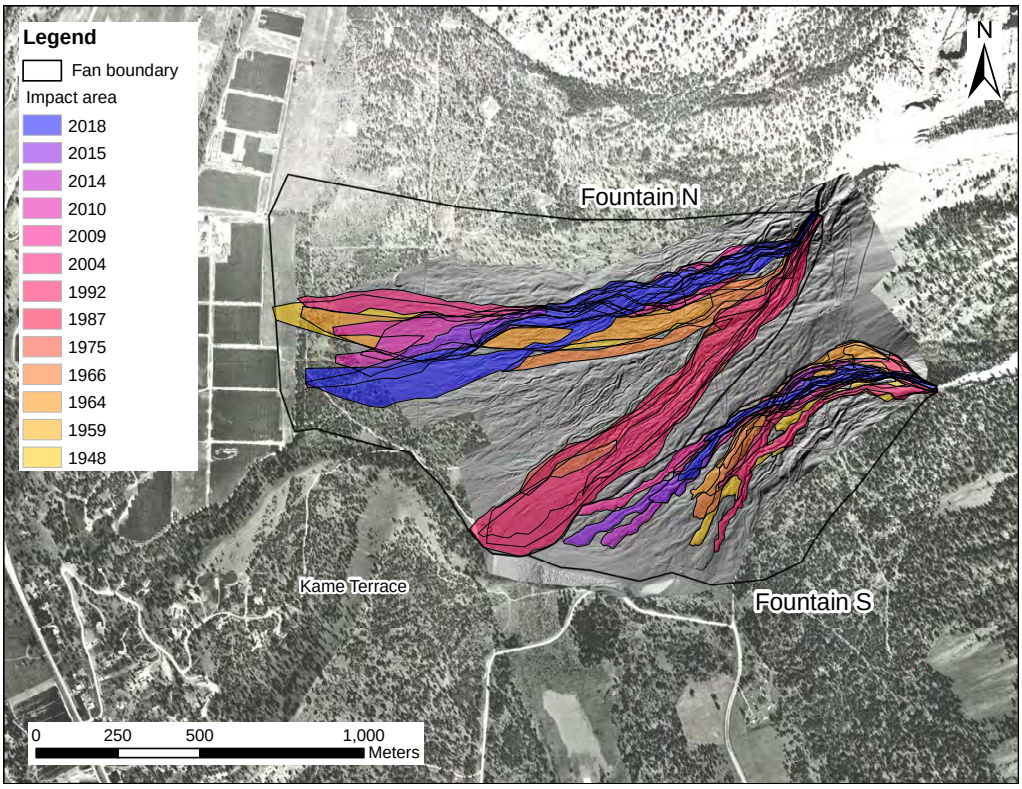

Figure 4.27. Debris flow impact area mapping at Fountain Ridge fans. 2019 bare earth lidar collected by RPAS (drone) overlain on 1997 orthorectified airphoto scene.

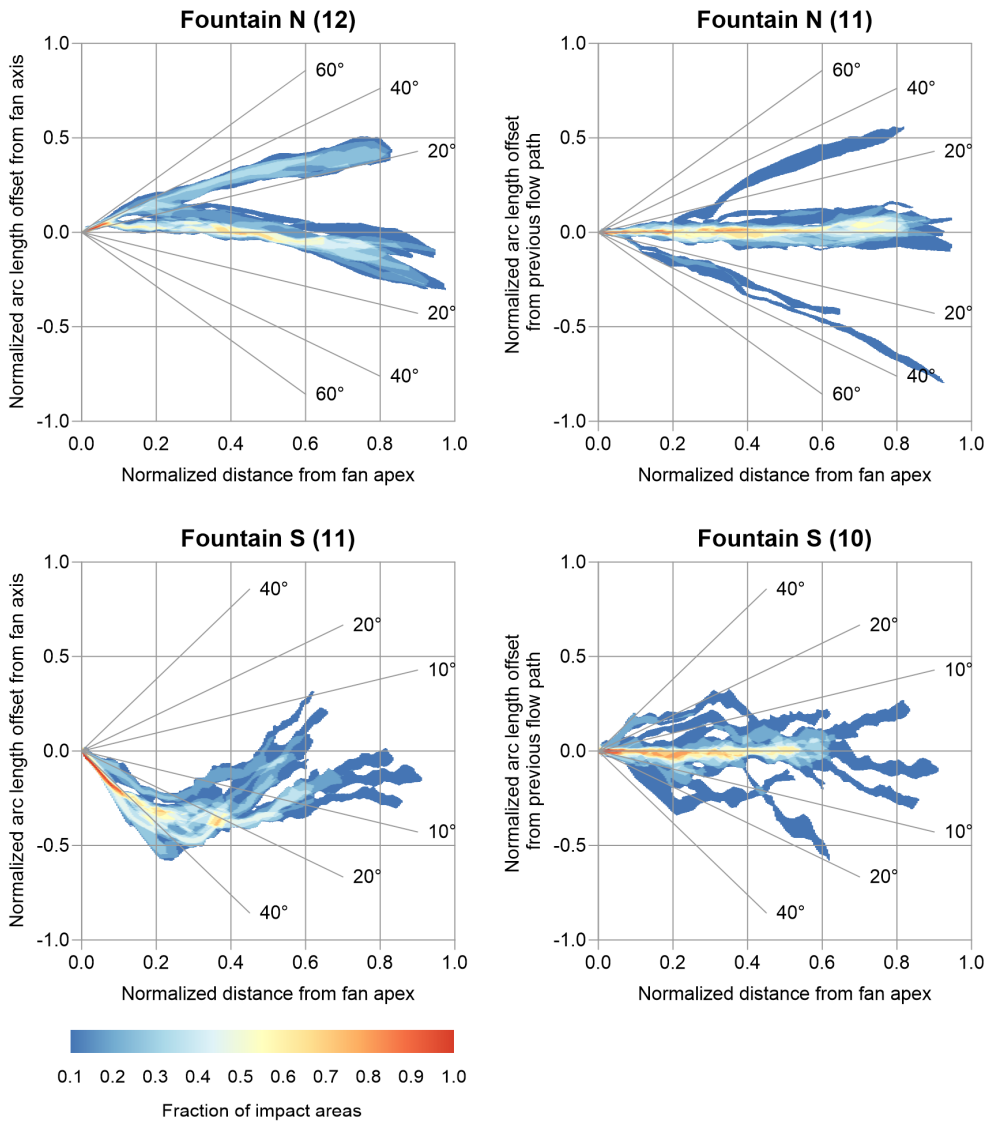

Figure 4.28. Fan-normalized spatial impact area heatmaps relative to the fan axis (left) and the previous flow path (right) for the Fountain Ridge fans.

4.3.3 Comparison and Discussion

Mount Currie and Fountain Ridge are very active fan complexes with distinctive geologic settings and climates. Morphometric variables at each fan site are summarized in Table 4.1. As described in the previous sections, debris at Mount Currie is comprised of cobbly, bouldery crystalline rock, while Fountain Ridge debris is derived from weathered sedimentary rocks, and is comparatively

Table 4.1. Summary of morphometric variables at Mount Currie and Fountain Ridge fans.

Fan site	Fan area (km^2)	Overall fan slope (°)	Average fan channel slope (°)	Watershed area (km^2)	Watershed relief (km)	Melton ratio
Currie B	0.4	10.7	8.2	2.7	2.1	1.3
Currie C	0.4	17.5	15.8	1.2	1.7	1.6
Currie D	1.3	14.1	14.7	1.7	1.5	1.1
Fountain N	1.2	10.6	11.4	0.9	1.1	1.2
Fountain S	0.4	14.3	12.4	0.4	1.0	1.7

fine-textured. Mount Currie receives more precipitation, while Fountain Ridge is located in a more arid region of SWBC (see Section 1.5.2 for climate data).

Comparing the spatial impact heatmaps for Mount Currie in Figure 4.23, hotspots are more concentrated along the previous flow path and near the fan apex. At Mount Currie, channels are steep and deeply incised, with major avulsions more typical past 20% of the maximum fan length (except for large volume events at Currie B). In contrast, spatial impact heatmaps for Fountain Ridge in Figure 4.28 show less concentrated impact area hotspots, indicating frequent shifts in flow paths; channels on the upper fan at Fountain Ridge are less stable, and avulsions are common near the fan apex.

Figure 4.29 shows a time series of maximum fan-normalized runout extents. The apparent increase in frequency after 2009 is due to access to Planet satellite imagery with high temporal resolution. Based on the impact area mapping, there are no obvious patterns of backstepping in the down-fan component followed by an avulsion, although it is likely smaller channel plugging events have been censored. There appears to be a correlation between event volume and runout distance, although the largest avulsion magnitudes at Fountain N and S were associated with relatively small volumes. Figure 4.29 shows cycles of high magnitude avulsions at Fountain N (frequency and amplitude of the cross-fan time series), whereas the other fans exhibit more gradual cycles of fan migration.

Fan-normalized and unnormalized cumulative runout exceedance distributions between the fan sites are compared in Figure 4.30. Fountain N has the longest runout distances in both down-fan and cross-fan dimensions, which might be attributed to larger event volumes, enhanced mobility from

high fines content, and a constant sediment supply from watershed talus slopes priming channels for avulsion. Currie D, with similar down-fan runout distances and event volumes to Fountain N, has a markedly lower cross-fan mobility, with most events remaining channelized until the distal fan. The comparatively different runout trends at Currie D might be related to many factors, including failure mechanisms and source geology. For instance, rock toppling and sliding in the upper watershed could trigger debris flows with large peak discharges and high velocities; evidence of high impact energies was observed in the field, including the destruction and burial of large trees, and splintered logs with frayed ends buried in debris. These types of debris flows are more likely to erode the channel into its steep fan (itself a product of coarse-grained, granitic debris with a high friction angle), therefore channelizing the flow, and only deviating from the flow path at the distal fan where confinement is lost, or if there is an event with sufficient peak discharge to overwhelm the channel capacity.

At a high level, a comparison of spatial impact trends at two very active debris flow fans with differing geologic settings help add to the conceptual model of factors that influence debris flow mobility (Section 2.4) and avulsion (Section 2.5). Based on observations at Mount Currie and Fountain Ridge, debris flow volumes and peak discharge, source geology, sediment supply conditions, grain-size distribution, fan topography, and fan incision, influence the migration of impact areas through time. Climate differences between the two sites may also affect runout trends, but were not explored as part of this work. In Section 4.4, a statistical approach is taken to test what variables are associated with different runout trends using the entire SWBC dataset.

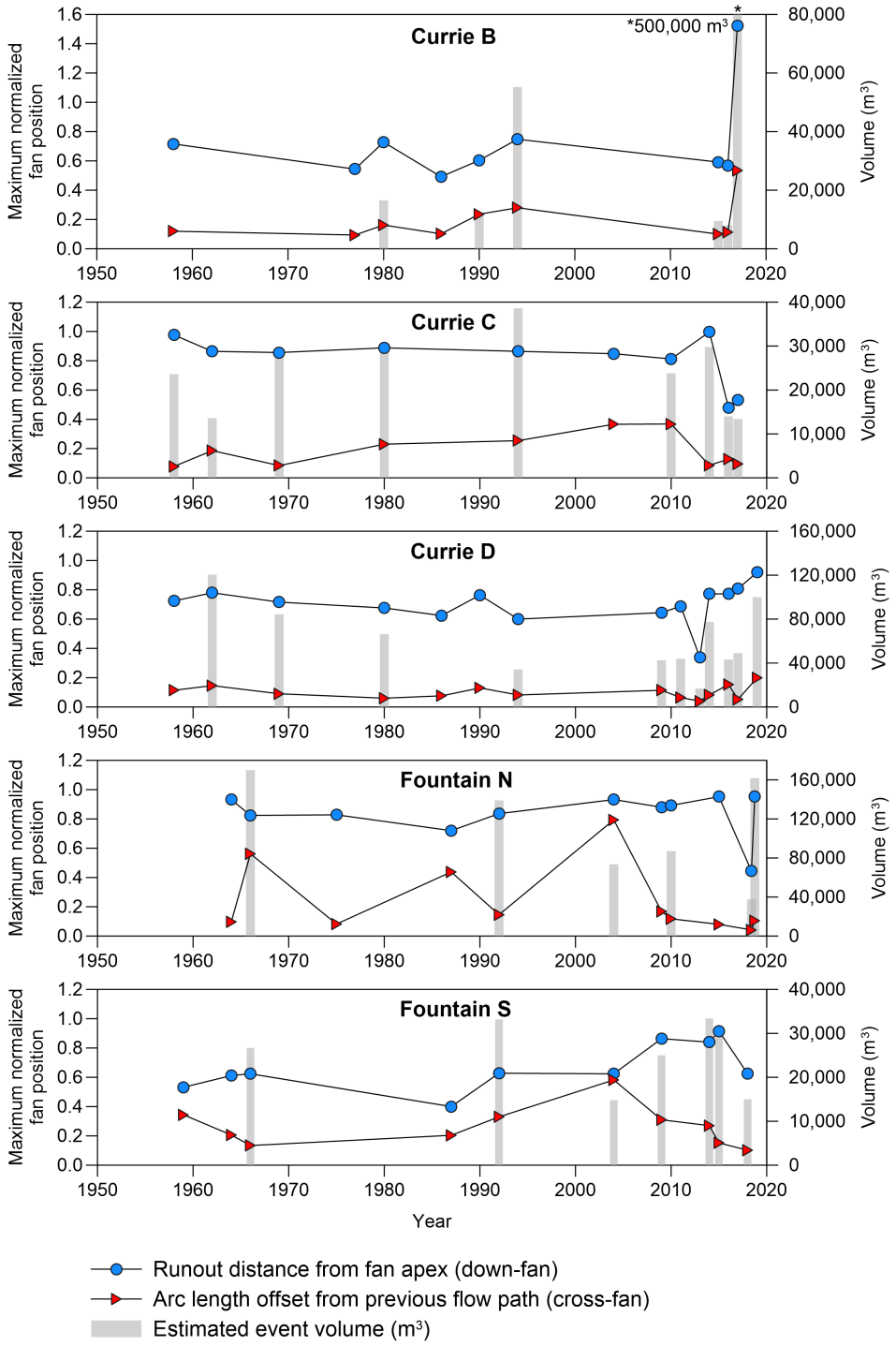

Figure 4.29. Time series showing the evolution of maximum debris flow runout in both down-fan and cross-fan components, along with volume estimates where available (see Section 3.4), at Mount Currie and Fountain Ridge fans.

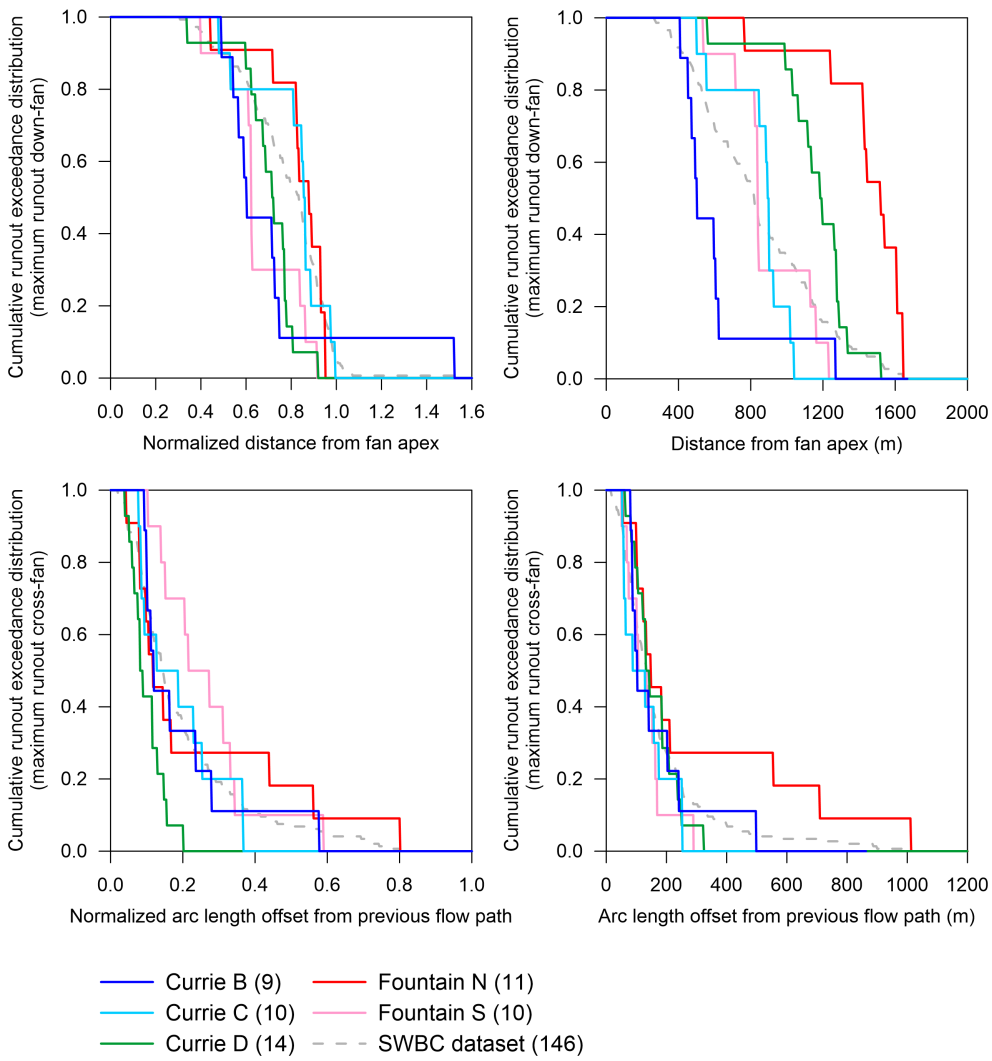

Figure 4.30. Comparison of cumulative runout exceedance distributions at Mount Currie and Fountain Ridge fans.

4.4 Factors Affecting Spatial Impact Trends on Fans in SWBC

4.4.1 Statistical Approach

To test the research hypothesis that differences in debris flow spatial impact trends can be explained, in part, with morphometric or geotechnical characteristics, the following statistical approach was taken:

1. Impact areas from the SWBC dataset were separated into groups based on event volume (Section 3.4), and site characteristics described by morphometric variables, source geology, fan truncation, and rates of debris flow activity (Section 3.6). Variables were limited to those that were relatively simple to obtain given the availability of data across all fan sites, and that might be related to mobility and avulsion based on the literature review (Sections 2.4 and 2.5). Partitioning impact areas by event volume is not fan-specific, whereas the other variables stratify trends by fan site. For continuous variables, the population was split into 3 groups using the lower (Q1) and upper (Q3) quartiles. In this preliminary analysis, quartiles were selected as a simple way to compare upper and lower sample groups without sacrificing the sample size. For categorical variables, the dataset was split into two groups to maximize sample size.
2. Cumulative runout exceedance distributions relative to the previous flow path were generated for each group, for both the down-fan and cross-fan components, and with fan-normalized and unnormalized runout distances.
3. A two-sample Kolmogorov-Smirnov (KS) test was used to test if there is a statistically significant difference in the distributions of the sample groups for each variable. The KS test is non-parametric (i.e., does not assume a distribution) and the test statistic is the maximum absolute distance between the empirical cumulative distribution functions. The null hypothesis is that both samples come from the same distribution; if the null hypothesis is rejected (p-value < 0.05), the samples are from different distributions, and the variable used to separate the sample might explain variation in runout trends. For continuous variables, the difference between the lower ($<$Q1) and upper quarters ($>$Q3) are considered. The two-sample KS test was completed in MATLAB.

Results of the statistical analysis are displayed in Figures 4.31, 4.32 and 4.33. P-values are bold where the null hypothesis is rejected (p-value < 0.05), indicating the variable might be a discriminator for the spatial impact metric. Conversely, a case where the null hypothesis is accepted might indicate that the ensemble distribution adequately represents the probability of runout exceedance, regardless of the discriminating variable. A discussion for each variable is provided in the following sections.

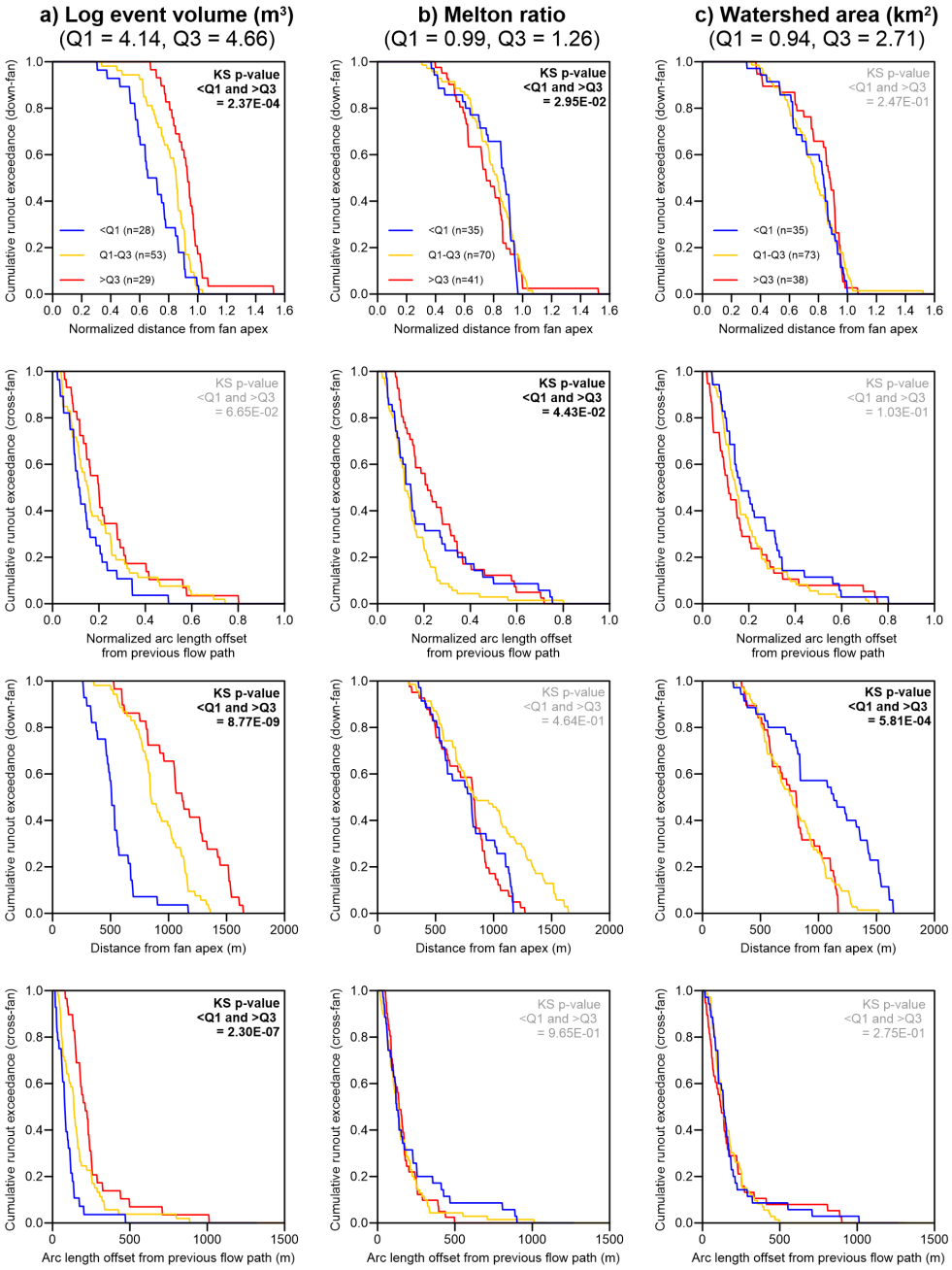

Figure 4.31. Comparison of cumulative runout exceedance distributions using sub-samples of impact areas from the SWBC dataset. Each column of plots corresponds to a variable by which the samples are separated, and each row is a different runout metric (down-fan or cross-fan; normalized or unnormalized). Sample groups are partitioned by variable quartiles (Q1, Q3). KS test p-value between upper and lower quarters are bold if the samples are from different distributions (p-value < 0.05).

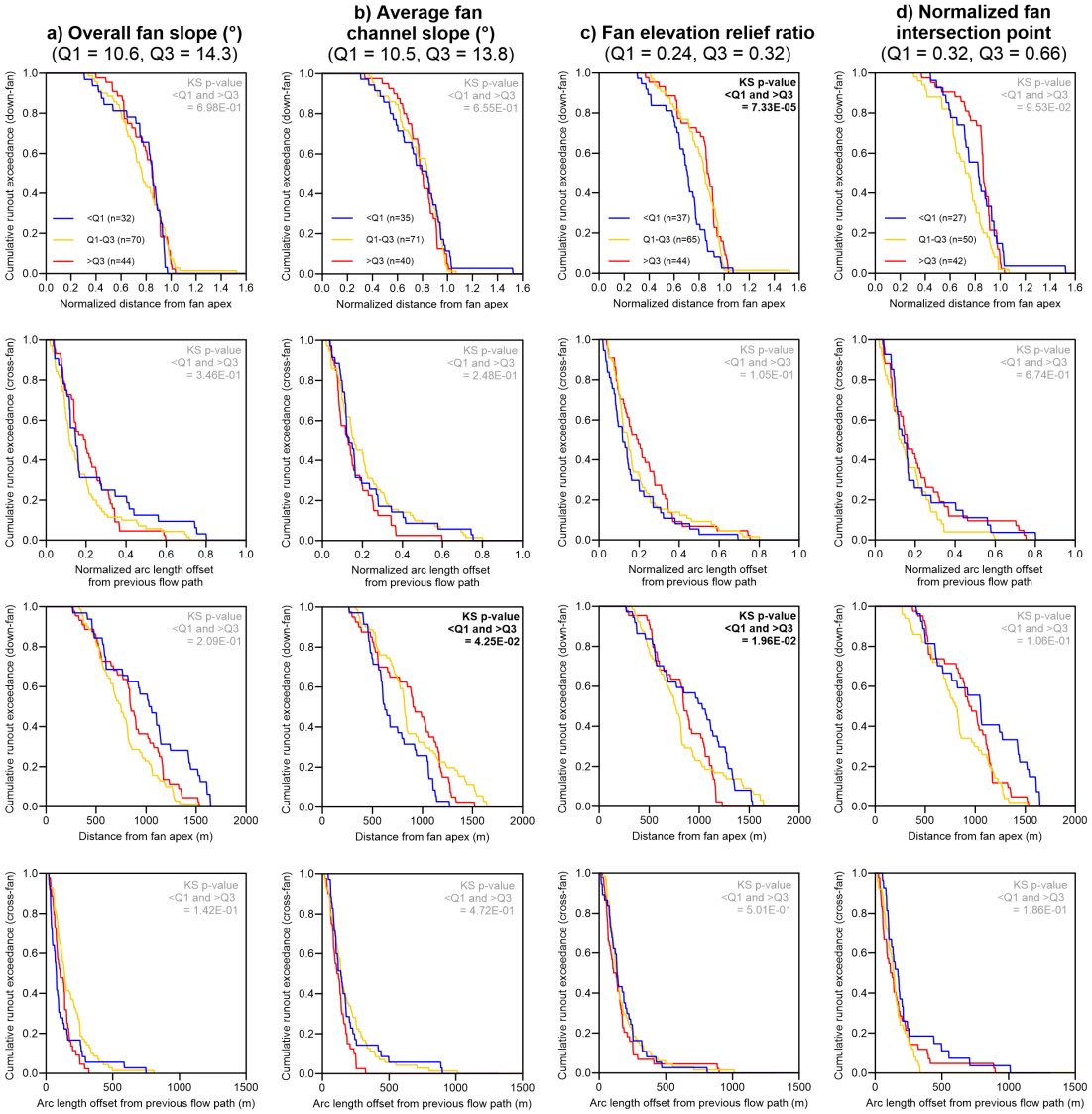

Figure 4.32. Comparison of cumulative runout exceedance distributions using sub-samples of impact areas from the SWBC dataset. Each column of plots corresponds to a variable by which the samples are separated, and each row is a different runout metric (down-fan or cross-fan; normalized or unnormalized). Sample groups are partitioned by variable quartiles (Q1, Q3). KS test p-value between upper and lower quarters are bold if the samples are from different distributions (p-value < 0.05).

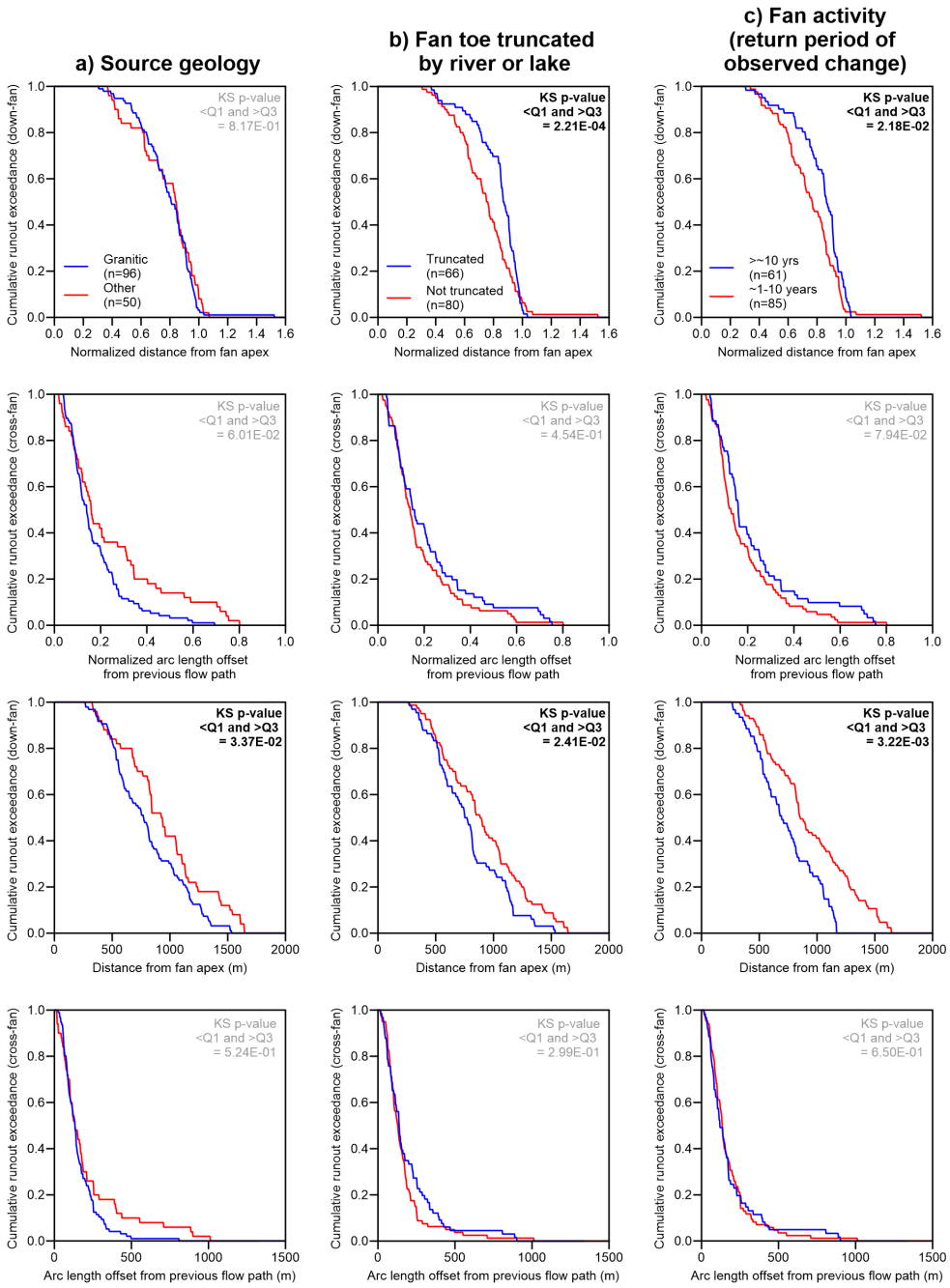

Figure 4.33. Comparison of cumulative runout exceedance distributions using sub-samples of impact areas from the SWBC dataset. Each column of plots corresponds to a variable by which the samples are partitioned, and each row is a different runout metric (down-fan or cross-fan; normalized or unnormalized). KS test p-value are bold if the samples are from different distributions (p-value < 0.05).

4.4.2 Event Volume

There is a positive correlation between volume and maximum runout distributions, with larger magnitude events typically travelling farther in the down-fan and cross-fan dimensions (Figure 4.31a). This result is consistent with empirical findings from the literature (e.g., Corominas, 1996; Griswold & Iverson, 2008). Since volume was estimated using the planimetric impact area for a majority of the events in this study, there is an inherent relationship between the maximum runout extents and volume. For fan-normalized runout, the results show that larger magnitude events are more mobile in the down-fan direction relative to other fan-formative events. Although there is a weak positive correlation for normalized runout in the cross-fan component, the differences are not statistically significant. The implications of these findings are that the volume of a debris flow may not be as significant when forecasting the probability of avulsion compared to mobility in the down-fan direction. Examples of this finding can be seen at the Fountain N and Fountain S fans, where the largest magnitude avulsions were not associated with the largest event volumes in their respective data record (refer to Figure 4.29). Competing mechanisms may explain the weaker correlation between volume and avulsions; although large magnitude events would have a sufficient peak discharge to overtop the active channel, they may also erode the channel bed, enhancing channelization (e.g., Schürch et al., 2011b).

4.4.3 Melton Ratio

There is a statistically significant difference in the normalized runout distributions for fans grouped by Melton ratio (Figure 4.31b). In the down-fan component, lower Melton Ratios (less rugged watersheds) are associated with events that terminate closer to the fan toe, whereas higher Melton ratios (more rugged watersheds) have a higher proportion of short-runout events. A possible interpretation for this trend is through the association of Melton ratio with hydrogeomorphic process type (e.g., Jackson et al., 1984; Wilford et al., 2004) (see Section 3.6.7). Events on mixed-process fans (lower Melton ratios), possibly debris flow-flood hybrids, would have higher water contents and thus higher mobility, whereas debris flows with high sediment concentrations are more likely to form channel plugs, terminating mid-fan. Secondary processes, such as stream-flow and flooding

between debris flow events, may also erode debris flow deposits and redistribute sediment down-fan, enhancing connectivity to the distal fan. The normalized cross-fan runout trends corroborate this interpretation; there is a higher proportion of events that follow the previous flow path for the lowest Melton ratios compared to the highest Melton ratios (although the inter-quartile range has very few high magnitude avulsions). Debris flows have characteristically higher peak discharges compared to debris floods (Hungr et al., 2014), which may increase the probability of the channel capacity being overwhelmed. Similar distinction between process type was found by Pederson et al. (2015) through stratigraphic analysis; deposits with typical debris flow characteristics tended to stack more compensationally (i.e., avulse) compared to areas with typical stream-flow characteristics (Santi et al., 2017).

4.4.4 Watershed Area

Runout distributions stratified by watershed area mirror trends found by the Melton ratio (since watershed area is used to calculate the Melton ratio), but were not statistically significant from one another, except for the unnormalized data in the down-fan component (Figure 4.31c). A likely reason for the unnormalized down-fan component outlier (<Q1) is because the Fountain N and S fans are included in this sample, with characteristically long runout lengths and small watershed areas. The watershed area is hypothesized to influence spatial impact trends in different, potentially competing, ways. Large watersheds generate higher water discharges, and therefore more fluidized, mobile flows (Tang et al., 2012); for this reason, watershed area has been used as a variable to predict runout distances in some empirical runout relationships (e.g., Tang et al., 2012; Zimmermann et al., 1997). Larger watersheds might (but not always) contain more contributing debris flow source areas, and higher sediment inputs would aggrade fan channels through time, triggering subsequent avulsions. Conversely, larger watersheds are associated with debris flood and stream-flow processes (e.g., Millard et al., 2006; Wilford et al., 2004), and therefore deposits that stack less compensationally (i.e, less likely to avulse) (Pederson et al., 2015). Lau (2017) found watershed area to be an important variable contributing to channel scour for alluvial fans in SWBC, which could hypothetically reduce cross-fan impacts due to increased confinement.

4.4.5 Fan and Channel Slope

Neither the fan slope nor channel slope discriminate differences in runout exceedance distributions (Figure 4.32a,b). Although the fan and channel slope are closely related (see Figure 3.22), they were calculated differently (refer to Sections 3.6.3 and 3.6.4), and have slightly different physical interpretations. The fan slope represents the overall slope of the fan landform, whereas the average channel slope is more representative of contemporary processes along the active channel. The channel slope, and to some extent the overall fan slope, fluctuate in time, and future studies with pre-event topographic measurements may yield different results.

It is hypothesized that fans with gentler slopes are correlated to higher mobility because they are associated with both finer-grained flows (Blair & McPherson, 1998) and mixed-process fans (Bardou, 2002; Bertrand et al., 2013; Scheidl & Rickenmann, 2010). A preliminary numerical modelling study by Zubrycky et al. (2019) using debris flow events from this thesis found a potential positive correlation between calibrated Voellmy friction coefficients and channel gradients (see Figure 2.4). However, this trend may be moderated by the interaction of topography with the flowing mass, in which a decrease in slope initiates deposition. Hypothesized causative links to runout in the cross-fan component are also enigmatic; either steep fans are reflective of debris flow-dominant processes that generate coarse-grained, channel plugging events that trigger avulsions (de Haas et al., 2018a; Pederson et al., 2015), or steep fans are more likely to be incised, in which flow is concentrated along the active channel (Lau, 2017).

4.4.6 Fan Elevation Relief Ratio

For groups separated by the fan ERR, statistically significant differences were found between the runout exceedance distributions in the down-fan component (Figure 4.32c). For the normalized data, events reaching the distal fan were more common for the (relatively) more planar fan surfaces (i.e., fans with higher ERRs). A theoretical interpretation explaining the high proportion of debris flows terminating mid-fan with higher concavity is the reduction in fan slope exerts a centripetal acceleration, stalling the flowing mass. Williams et al. (2006) found planar fan slopes to be associated with debris flow processes, while concave-upward shapes are more typical of fluvially-fed fans.

Given this association, the runout trends contradict trends found using the Melton Ratio, where high mobility events reaching the distal fan were more common for mixed-process watersheds. It should be acknowledged that the range of fan ERRs is narrow (0.21-0.42), with all fans being concave-upward. Further research with a wider range of fan profiles and different measures of concavity are recommended to validate these results.

4.4.7 Normalized Fan Intersection Point

Based on the position at which the main channel intersects the fan surface, there is no statistically significant difference in the runout exceedance distributions for the SWBC dataset (Figure 4.32d). Since the normalized fan intersection point is a reasonable proxy for the extent of fan incision along the fan length, it was hypothesized that fans with intersection points on the distal fan would have lower cross-fan runout magnitudes compared to fans where flow confinement is lost on the upper fan. By accepting the null hypothesis however, the degree of channelization on a fan may not be a strong indicator for forecasting spatial impact trends. The intersection point fluctuates in time, and future work using pre-event topography for measures of fan incision and channelization should be considered to further these results.

The relationship between the fan intersection point and the avulsion node (position on the fan where the avulsion path deviates from the previous flow path) is shown in Figure 4.34 for the SWBC dataset. Although there is no trend between the two locations, most of the avulsion nodes in the SWBC dataset occur upstream of the intersection point, contrary to findings by Millard et al. (2006), who found avulsions were most frequent immediately downstream of the intersection point for fans in coastal BC. Based on the distribution of avulsion node positions down the fan, avulsions were most frequent immediately downstream of the fan apex and at around 30% of the maximum fan length, and declining toward the fan toe.

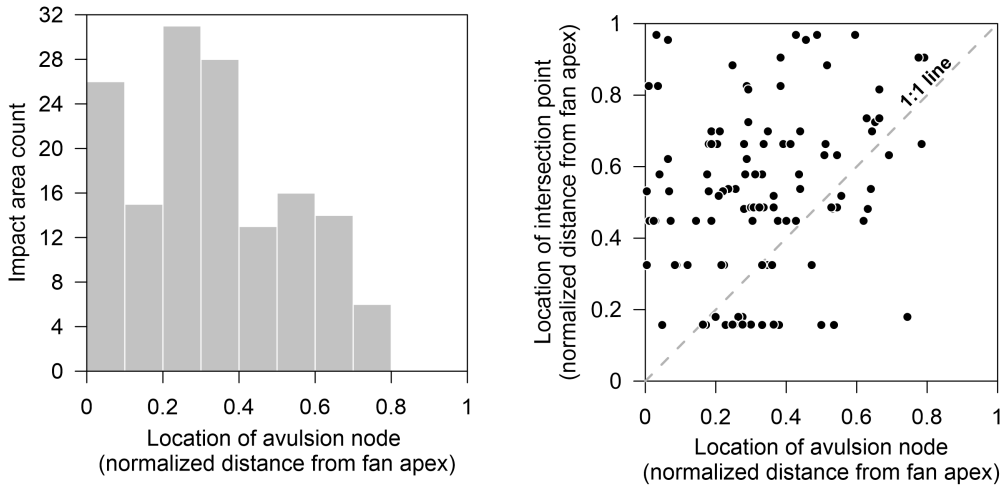

Figure 4.34. (Left) Distribution of avulsion nodes along the longitudinal position on the fan and (right) relationship between longitudinal position of the avulsion node on the fan relative to the fan intersection point.

4.4.8 Source Geology

Impact areas were separated into two groups based on source geology: granitic rocks, and non-granitic rocks (sedimentary, metamorphic, and volcanic rock types). The potential effects of source geology on spatial impact trends is previously discussed in Section 4.3, comparing Mount Currie fans (granodiorites) to Fountain Ridge fans (weathered sedimentary rocks). Based on data from the entire study area, there is a statistically significant difference in the absolute down-fan runout distribution between source geology groups (Figure 4.33a). This finding is consistent with the understanding that coarse-grained, frictional, granitic debris flows have typically shorter runouts compared to debris comprised of sedimentary or volcanic rocks with a larger proportion of fine-grained material and higher clay contents. However, fan-normalized runout exceedance curves in the down-fan direction are very similar for both groups of rock types, which supports the use of fan-normalized runout exceedance distributions, irrespective of source geology.

It is hypothesized that supply conditions influence cross-fan runout distributions, in that supply-unlimited basins with a more constant sediment feed would plug or aggrade the channel, providing optimal conditions for avulsion. Since granitic basins in the dataset were classified as supply limited

(Jakob, 1996), the source geology groups are a reasonable proxy for supply conditions, in addition to grain-size distributions and rheological properties. For the SWBC dataset, granitic debris flows appear to have shorter cross-fan mobility compared to the other rock types, however the difference is not statistically significant.

4.4.9 Fan Truncation

Impact areas separated by fan toe truncation have different distributions in the down-fan component (Figure 4.33b). Longer absolute runouts are observed on the non-truncated fans, but when runout is normalized by the fan boundary, the truncated fans have a higher proportion of debris flows that terminate closer to the mapped fan boundary. In comparison, maximum runouts for non-truncated fans have a more normal distribution, with a mean closer to 75% of the maximum fan length (Figure 4.35). These differences may be attributed to normalizing with a shorter fan length, where the true fan boundary reflective of a fan's formative debris flows has been inundated or eroded by a water body. Furthermore, debris flows that runout past the fan toe would not be captured in the data record, resulting in a high proportion of mapped impact areas terminating at the fan toe. Spatial impact trends grouped by fan truncation may also reflect interaction with downstream conditions, such as backwater effects caused by an impounded water body, or fan entrenchment from river incision at the toe, requiring further study.

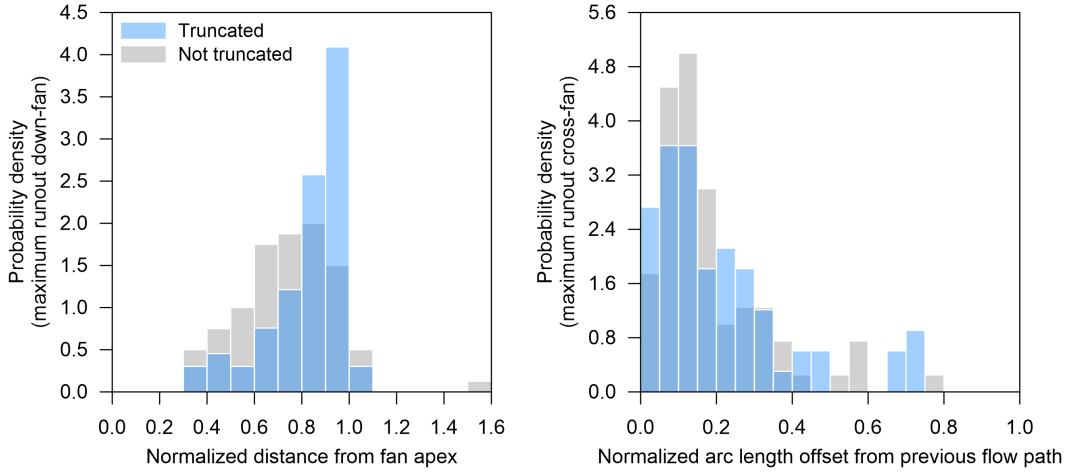

Figure 4.35. Probability density of fan-normalized maximum runouts grouped by fan truncation.

4.4.10 Fan Activity

de Haas et al. (2018a) and de Haas et al. (2018b) show avulsion trends might be influenced by frequency-magnitude distributions; fans with abundant, small, channel-plugging events followed by a large magnitude event with sufficient volume to overwhelm the channel capacity are ideal for high rates of avulsion. Due to the limited data record, frequency-magnitude relationships were not derived for the SWBC dataset. Instead, the relative fan activity (Section 3.6.10) was tested as a discriminator using two groups: observed change from debris flow processes every 1 to 10 years (very active fans), or greater than 10 years (relatively less active fans). The only distributions that were statistically different were runout in the down-fan direction, where the more active fans had characteristically longer absolute runout distances, but with a comparatively lower proportion reaching the distal fan (Figure 4.33c). In other words, for the SWBC dataset, fans with higher rates of activity experience more debris flows that terminate short of the fan boundary. Based on the work by de Haas et al. (2018a) and de Haas et al. (2018b), these relatively low mobility events may serve to backfill channels, causing subsequent debris flows to avulse; although we see a slight increase in normalized cross-fan runouts for the more active fans in the dataset, the difference is not statistically significant.

4.4.11 Summary and Implications

Differences in runout distributions in the down-fan and cross-fan components for the SWBC dataset were tested using simple variables that describe the event and fan characteristics. The purpose of the statistical analysis was to test the hypothesis that certain morphometric and geotechnical characteristics influence mobility and avulsion trends on fans. The results have implications for runout analyses; variables that discriminate spatial impact trends can be used to stratify the empirical dataset for forward prediction, whereas variables with no discernable effect may not be as relevant.

From this preliminary study, event volume had the most significant impact on debris flow mobility, consistent with findings from the literature. However, volume may not be as significant when forecasting the probability of avulsion compared to mobility in the down-fan direction.

Some differences were found for spatial impact trends stratified by variables related to hydrogeo-

morphic process type (Melton ratio, watershed area), in which runouts on mixed-process fans were more mobile in the down-fan component, but not in the cross-fan component (i.e., less avulsions). Spatial impact trends from a wider range of alluvial fan types should be studied to test this hypothesis since most of the fans in the SWBC dataset are classified as debris flow-dominant (Section 3.6.7). Overall, most of the morphometric variables related to the fan (fan slope, channel slope, and intersection point) did not separate the runout distributions into statistically significant groups. One interpretation of this result is the fan morphometric variables used are incongruent with the time scale of this dataset (e.g., if the average channel slope fluctuates on the decadal scale, or conversely, the fan slope is more representative of centuries of debris flow activity).

Source geology, fan truncation, and fan activity had no impacts on the cross-fan runout distributions. In the down-fan component, normalized runout trends for granitic rocks were statistically similar to those of the other geology types in the study area, supporting the use of fan-normalized distributions irrespective of source geology. Normalized trends in the down-fan component differed for fans truncated by a waterbody, which might be related to an undersized fan length normalizer and debris flow impacts not being recorded past the fan toe. Lastly, more active fans appeared to have a higher proportion of events terminating on the upper fan.

Overall, the statistical assessment presented here is a preliminary effort to test differences in mobility and avulsion trends using a rich geospatial dataset. The results are meant to enhance practitioner judgement when using empirical data in forward analyses (Section 4.5.1), and to form hypotheses that should continue to be tested using different datasets or methods (Section 5.3).

4.5 Fan-Normalized Empirical Runout Estimator Tool

This section describes a tool that transposes the fan-normalized spatial impact heatmaps derived in this chapter onto another fan relative to an active channel. The tool is useful for visualizing empirical runout trends across a fan, and may be applicable for preliminary hazard assessments, regional prioritization studies, or supporting expert judgement. The fan used as an example (Catiline) is part of the empirical dataset; it is used strictly to illustrate the methodology, and not as a validation exercise, nor are the results to be interpreted for any risk assessment.

4.5.1 Code Workflow

The workflow for converting fan-normalized spatial impact heatmaps to probability of runout exceedance contours for a fan relative to an active channel is described below. The code was implemented in MATLAB (R2019b), and is provided in Appendix C, along with sample shapefiles and empirical grids (i.e., fan-normalized spatial impact heatmaps relative to the previous flow path).

1. **Load shapefiles.** For a fan site, the fan apex (1 point), fan boundary (1 polygon), and flow path (1 polyline), are loaded as separate shapefiles in UTM coordinates (Figure 4.36a). The flow path must intersect the apex and extend past the fan toe.
2. **Initialize a measurement grid centered on the fan apex.** For a specified grid resolution and radius size, grid nodes are created along a series of circles centered on the fan apex. Grid x and y coordinates are stored in an array, including nodes along the flow path. A grid with 50 nodes down and across the maximum fan extents, and sized 1.2 $\times$ the maximum fan length, is shown in Figure 4.36b.
3. **Load empirical data**. A fan-normalized spatial impact heatmap grid relative to the previous flow path is selected as the empirical data (Figure 4.36c), with dimensions $x \in \{0,2\}$, $y \in \{0,1\}$, and $z \in \{0,1\}$. The empirical data can be a subset of the full dataset depending on the application (e.g., volume class, geology), as described in Section 4.4. Grids were filtered in another MATLAB script and smoothed in Surfer® (Golden Software, LLC, 2018). Empirical grids for the entire SWBC dataset are provided in Appendix C: one of the raw data, and one smoothed (5 passes of a 5$\times$5 maximum value filter and 10 passes of a Gaussian low-pass filter).
4. **Sample empirical data.** For each grid node, the normalized distance from fan apex (x) and normalized arc length offset from the flow path (y) are calculated, and a z value is extracted from the empirical grid.
5. **Export raster.** Measurement grid nodes are interpolated over a raster with a specified pixel size (m) and exported as a GeoTIFF or Surfer® grid file. Figure 4.36d shows the output raster clipped to the fan area and contoured in ArcGIS.

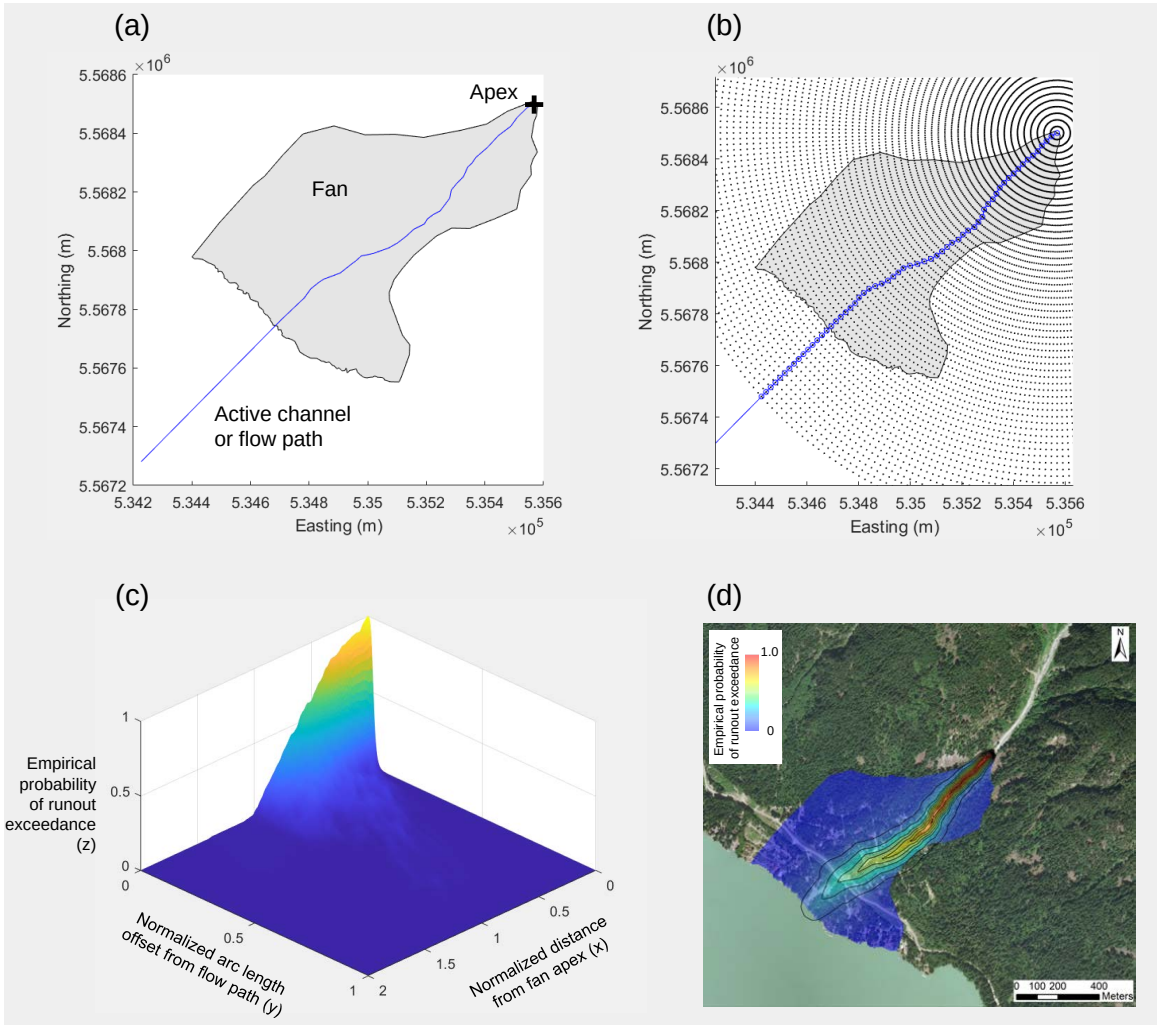

Figure 4.36. Components of the empirical runout estimator tool. **a)** Input shapefiles; **b)** measurement grid centered on fan apex, including nodes along flow path; **c)** empirical data source: filtered and smoothed fan-normalized spatial impact heatmap; and **d)** empirical data sampled at each measurement grid node and exported as a georeferenced raster, where it can be contoured, clipped, or used for calculations in GIS.

4.5.2 Application

The main application of the empirical runout exceedance tool is to visualize the fan-normalized spatial impact heatmaps onto another fan space for forecasting purposes. The output grid and contours represent an empirical probability of runout exceedance; although a statistical model has not been fit to the data at this stage, the raw empirical data is useful for risk-based decision making.

In a regional study, empirical runout distributions can be used to prioritize fan sites for further study. For instance, the probability of runout exceedance derived from a regional dataset multiplied by an average annual probability of occurrence (for a debris flow of any size) approximates the overall encounter probability for any location on the fan without explicitly modelling different volume or avulsion scenarios. This encounter probability applies for an impending debris flow event, while long term fan evolution studies would require a different approach to what is described here.

Figure 4.37 shows an example of the empirical data partitioned into different volume classes, showing varying spatial impact distributions for each. For local studies, the shape and extents of the empirical contours can provide guidance to practitioners for converting numerical modelling results into probability of spatial impact for risk calculations. In a Bayesian statistical framework, an expert opinion (prior), based on a local observations, site-specific interpretations, or modelling results, can be updated with the empirically derived probability of runout exceedance contours (likelihood), to form a posterior distribution of spatial impact probabilities. A similar Bayesian approach was used by Nolde & Joe (2013) to incorporate expert judgement for more precise estimates of debris flow return periods.

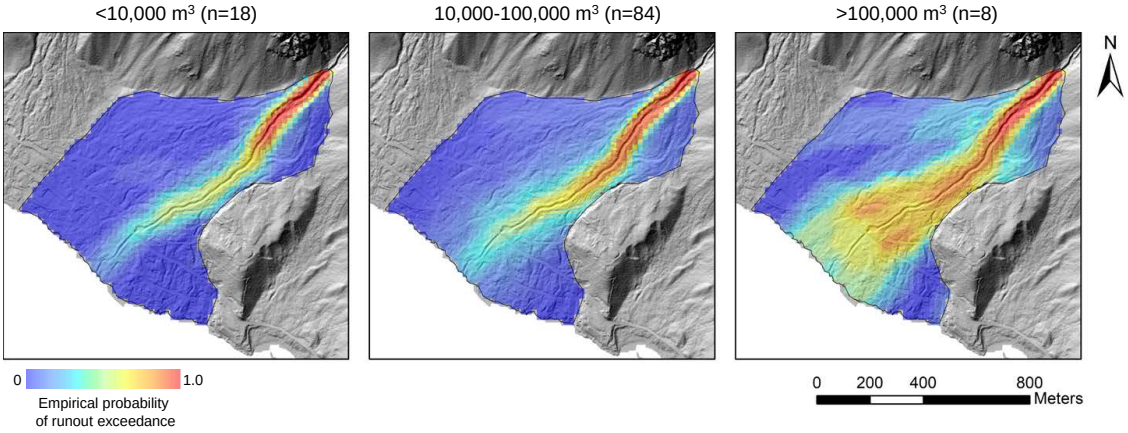

Figure 4.37. Probability of runout exceedance heatmaps derived from subsets of the SWBC dataset based on volume class. The Catiline fan is used as an example prediction space. 2014 ALS bare earth lidar hillshade courtesy of SLRD.

4.5.3 Limitations

The empirical runout exceedance tool shares the limitations with creating the fan-normalized spatial impact heatmaps, such as normalizing assumptions, discussed previously in Section 4.1.4. This tool is not meant for predicting fan-specific avulsion paths, rather, a possible distribution of runout extents from an empirical sample. Results depend on the selection of a flow path a-priori, which may not always be clear. The tool does not work for multiple or bifurcating flow paths, nor would it be appropriate for channels with mitigation structures. Runout exceedance for flow paths with sharp channel bends may not be realistic because x and y measurements would be oblique to the measurement grid. Since arc length offsets are measured relative to a line, the channel width is not taken into account; there may be some cases where the probability of runout exceedance decays prematurely in the cross-fan component for wide channel sections, and vice versa. Probability of runout exceedance heatmaps and contours are sensitive to the number of samples in the empirical dataset, smoothing of the empirical grid, number of nodes in the measurement grid, and the pixel size of the output raster. If the empirical grid is not smoothed enough, or a small sub-sample is used, artefacts of avulsion pathways from one fan in the dataset will be spuriously projected onto the prediction fan space; an example of this effect can be seen in Figure 4.37 for the $>$100,000 m^3 volume class since it only has 8 events in the subset. To avoid overfitting, future work may involve fitting three dimensional functions or statistical models, rather than projecting the data itself, discussed further in Section 5.3. As is the case with any empirical tool, judgement must be used when interpreting outputs and presenting results.

4.6 Summary

1. A new graphical method is developed to extract and summarize debris flow runout trends, creating spatial impact heatmaps. The main application is to aggregate trends across different fans creating an empirical runout distribution normalized by the fan boundary. The heatmaps are also useful in highlighting avulsion “hotspots” and measuring avulsion magnitudes.
2. The maximum fan-normalized runout distributions relative to the previous flow path follow a normal distribution in the down-fan component, and a lognormal distribution in the cross-fan

component. These distributions provide an understanding of relative down-fan and cross-fan mobility calibrated to an empirical dataset. Based on the SWBC dataset, about 90% of the debris flows impacted past 50% of the maximum length down the fan, while less than 10% avulsed beyond 50% of the maximum arc length across the fan.

3. In comparing the SWBC fan-normalized maximum runout distributions to a monitored fan in Japan, cross-fan impact trends were found to be similar, but the distributions of runout in the down-fan component were not; a higher proportion of debris flows terminating on the upper fan were recorded at the monitored fan, and may justify adjusting the upper tail of the SWBC dataset distribution to account for missing data (such as smaller debris flows not detected in aerial imagery).
4. Runout distributions based on theoretical avulsion cycles were compared to case studies, showing conceptually that these patterns are observed on real debris flow fans.
5. Runout and avulsion trends were analyzed and compared for groups of fans at two locations with very high rates of debris flow activity (Mount Currie and Fountain Ridge). Debris flow volume, peak discharge, source geology, sediment supply, grain-size distribution, fan topography, and fan incision, are hypothesized to influence the migration of impact areas through time for these case studies.
6. The following variables were tested as discriminators for differences in down-fan and cross-fan runout distributions: event volume, Melton ratio, watershed area, fan slope, channel slope, fan elevation relief ratio, fan intersection point, source geology, fan truncation, and fan activity. Event volume had the most significant impact stratifying spatial impact trends, with larger magnitudes corresponding to more mobile runout in the down-fan component. Volume was not a statistically significant indicator for cross-fan runout offsets. Fans with lower Melton ratios tend to have impacts more concentrated along the previous flow path and reaching the distal fan extents. Most fan morphometrics and source geology had no significant impact on normalized runout patterns. Down-fan runout distributions were unique for fans truncated by a water body, although the differences might be attributed to a truncated fan length and runout not recorded past the fan toe. Fans with higher event frequencies also had more events

terminating short of the fan boundary.

7. Avulsion nodes (locations) were most common immediately downstream of the fan apex, and about 30% of the maximum fan length, with frequencies declining toward the fan toe.
8. A tool was developed to transpose fan-normalized spatial impact heatmaps from the SWBC empirical dataset onto another fan for guidance in risk-based decision making. The code and data are provided in Appendix C.

Chapter 5

Conclusions and Recommendations

This chapter summarizes the work completed and highlights the main findings, addressing the research objectives and hypotheses. More detailed summaries are provided at the end of each chapter in Sections 2.8, 3.9, and 4.6. Implications for practitioners are discussed, followed by a list of ideas for future work.

5.1 Summary of Main Findings

This work was undertaken to better understand spatial impact trends on debris flow fans. Currently, there is little research guiding practitioners in estimating probability of spatial impacts on a fan considering various mobility and avulsion scenarios. A comprehensive literature review was completed to form a conceptual model of factors that affect debris flow runout. According to the literature, high mobility events are generally associated with large volumes and fall heights, high sustained pore pressures, and steep, channelized travel paths. Avulsions are comparatively less understood, but there is some evidence that debris composition, lobe thickness, preceding events, and the frequency-magnitude distribution also influence the probability of avulsion. Based on descriptions from the literature, avulsion triggers were grouped into three scenarios: overtopping, superelevation, and various channel blocking mechanisms, including channel plugs and progressive aggradation. From a literature review of 44 empirical runout relationships with various runout assessment methodologies, volume was by far the most common predictor, followed by elevation loss from the source

zone (i.e., fall height), both of which can be difficult to ascertain. Very few of the methods reviewed were probabilistic, and none consider cross-fan impacts via avulsion mechanisms explicitly.

One of the major contributions from this work is the creation and documentation of a unique spatial record of debris flow impacts in SWBC, which can be continuously added to and used for future analyses. This geospatial dataset consists of 176 debris flow impact areas and flow paths across 30 fan sites. In this work, an impact area is defined as any area below the fan apex that has been impacted by a debris flow, or multiple debris flows, over a certain time period. Geomorphic mapping was completed using an ensemble of remote sensing and field data, including hundreds of historical airphotos dating back to 1928, satellite imagery with high temporal resolution dating back to 2009, topographic basemaps, lidar, and orthophotos. Change detection with the spectral index NDVI was useful for delineating impact areas with satellite imagery in some cases, working best on sparsely forested or clearcut fans, and for debris flows that disturb the canopy and do not overprint recent deposits. Lidar was available for 16 of the fan sites, including lidar and orthophotos collected during field work with a RPAS (drone) at three fans. Geomorphic field mapping was completed at 18 fan sites to delineate lobes, levees, and channels. Field observations were documented, including flow depths, superelevation angles, deposit thickness, deposition angles, and debris composition. The geospatial dataset also consists of fan and watershed boundaries, fan apex locations, and morphometric variables calculated with lidar or freely available DEMs. A classification scheme was developed to describe the different types of avulsions (or lack thereof) based on the location, magnitude, and surface expression of debris flow impacts. Of all the impact areas mapped, 86% had some form of avulsion or spreading across the fan, with local channelized avulsions the most common type. 35% of the impact areas corresponded to a shift in the position of the channel on the fan. Data certainty classes were also defined to give the reader a sense of spatial and temporal accuracy of the impact area mapping. The dataset, including GIS shapefiles with associated metadata, are provided in Appendix B.

As part of the data compilation process, local volume-area relationships were derived based on lidar change detection, features in post-event lidar, and field data. Impact areas, deposit areas, and approximate event volumes, along with estimates of error, have been documented for 16 events in the dataset. The volume-area relationship for SWBC was compared to nine other relationships

for non-volcanic debris flows from the literature and had the same regression coefficient as the relationship for granular debris flows from the Italian Alps. The volume-impact area relationship (differentiated from the volume-deposit area relationship) was used to approximate volumes for the remaining events in the dataset using the mapped impact areas.

A novel plotting method was devised to extract runout trends from the geospatial data in both the down-fan and cross-fan components using a circular grid centered on the fan apex. Zones of increasing radii on the grid represent runout down-fan, and arc length offsets represent lateral shifts across the fan relative to the fan axis or previous flow path. Spatial impact heatmaps were created by summing the plotted impact areas. Heatmaps across different fans were combined by normalizing runout to the maximum fan length (down-fan) and arc length (cross-fan). The ensemble heatmap for all the SWBC impact areas shows that most debris flows impact along the previous flow path, with the probability of impact decaying from the apex and away from the active channel. Almost all debris flows impact within $\pm 60^\circ$ relative to the fan axis or previous flow path.

Maximum runouts in the down-fan and cross-fan components were extracted from the dataset. Based on the SWBC dataset, about 90% of the debris flows impacted past 50% of the maximum length down the fan, while less than 10% avulsed beyond 50% of the maximum arc length across the fan. Avulsions were most common immediately downstream of the fan apex and at about 30% of the maximum fan length, with instances decreasing toward the fan toe. Maximum normalized runout in the down-fan component can be represented by a normal distribution, while the cross-fan follows a log-normal distribution.

From a more thorough comparison of spatial impact at five very active fans, it appears that debris flow volume, peak discharge, source geology, sediment supply conditions, grain-size distribution, fan topography, and fan incision, play a role in mobility and avulsion patterns. For two coalescing fans with the same climate and source geology, the effect of sediment supply and grain-size distribution on spatial-temporal impacts is made apparent. As is the case for alluvial fans, a more constant sediment supply was the likely cause of a very laterally unstable fan system, shown by one of the case studies with an extensive talus slope. The other case study had coarser-grained and more uniformly graded debris flows, forming lobate deposits with characteristically shorter runouts.

Using the entire SWBC dataset, a preliminary statistical analysis was completed to test the hypothesis that differences in spatial impact trends for groups of fans or events can be explained, in part, with morphometric or geotechnical characteristics. Event volume, unsurprisingly, had a significant influence stratifying spatial impact trends, with larger magnitude volumes corresponding to more mobile runout in the down-fan component. Volume was not a statistically significant discriminator for normalized runout in the cross-fan component, as some of the largest magnitude avulsions in the dataset were not associated with the largest magnitude volumes. There were statistically significant differences based on the Melton ratio, which is compelling for the interpretation that impacts on mixed-process fans tend to reach further down-fan but remain closer to the active channel. Differences in mobility and avulsion, however, were not explained by fan morphometrics, such as the slope or the point at which channelization is lost. Granitic debris flows tended to travel shorter distances, although when runout is normalized by the fan, the distributions were statistically similar to the other source geology types. Separating down-fan runout distributions based on fan truncation or fan activity is warranted given statistically significant differences between the two populations. Overall, there was no clear morphometric discriminator for spatial impact trends on debris flow fans, warranting further study.

Lastly, a tool was developed that transposes the empirical runout distributions from the SWBC dataset onto a fan to assist in risk-based decision making. The code and empirical forecasting data are provided in Appendix C.

5.2 Implications for Hazard and Risk Assessments

Estimating the probability of debris flow impact is an important part of calculating risk for land zoning or hazard mitigation efforts on fans. This work provides a new perspective on debris flow fan susceptibility to impact based on real debris flow events. The methods used here are different from other empirical methods in that runout trends are represented on the fan space and in two dimensions. By measuring cross-fan runouts from the previous flow path, typical avulsion locations and angles are uncovered.

The maximum fan boundary can be interpreted as a statistical upper-bound of runout from its

formative debris flows. Normalizing by the fan boundary allows for runout trends on groups of fans to be compared and combined. Although the fan boundary is an imperfect normalizer (e.g., in the case of truncated fans), the fan landform can be identified somewhat consistently for forward prediction. As shown in Section 4.5.1, normalized regional aggregates can be transferred to other fans to estimate encounter probability on a fan using empirical data. With enough reconstructed fans in the dataset, the ensemble heatmap captures regional frequency-magnitude distributions, mobility behaviours, and avulsion scenarios, without having to specify these a priori. The regional spatial impact heatmaps could be useful for validating hazard maps made with other methods, regional fan susceptibility mapping, or prioritization studies. In a preliminary statistical assessment, discriminators including the Melton ratio, fan truncation, and fan activity might be site-specific variables to consider when customizing fan-normalized trends. Future work should involve fitting functions to the data for a more robust and adaptable forecasting tool, as described in Section 5.3. It should be made explicit that use of this data for forecasting purposes applies to the next debris flow event, and not long term fan evolution directly.

Considering numerical modelling for a specific volume and flow path, the cumulative runout exceedance curves in the down-fan component for a certain volume class could be used to transform modelling outputs from deterministic to probabilistic. When modelling an avulsion, the conditional probability could be approximated using the cumulative runout exceedance curves in the cross-fan component, considering an anticipated avulsion path. Although there was a clear relationship between flow volume and down-fan mobility, the probability of avulsion may not be as sensitive to flow volume.

The potential applications proposed here are not meant to replace expert judgement or the need for numerical modelling in certain cases, rather, the empirical spatial impact trends are another resource available to support risk-based decision making.

5.3 Recommendations for Future Work

Opportunities to improve and extend the work presented in this thesis are as follows:

1. **Semi-automated inventory generation.** Rather than manually inspecting satellite images, a

semi-automated workflow could be developed to detect debris flow events on fans. A recent study by Deijns et al. (2020) used NDVI calculated from Lansat imagery to determine the timing of landslides over a 33-year period. For a debris flow fan area, a time series of high-resolution satellite data (maximum 5 m pixel size) could be extracted, and differences in spectral indices calculated as an indicator of change (refer to Section 3.3.2 for examples). This method might perform poorly for densely vegetated fans or fans with logging and frequent snow avalanches, and the model would have to be trained to filter for cloud cover, geometric distortions, and seasonality. Feature detection using high resolution DEMs is also an emerging field, and could be used to associate lobe boundaries with dates detected from the satellite data. Similar to concepts used by Eisank et al. (2014) for delineating drumlins, debris flow lobe shapes could be detected in lidar, and methods used in Section 3.4.2 could be used to constrain the event volume from lobes. Fountain S would be an ideal test fan for generating debris flow inventories with satellite and lidar data.

2. **Incorporating other dating methods.** Methods such as dendrochronology and surface exposure dating methods could be used to extend the data record for long-term debris flow evolution studies, at the cost of lower spatial accuracy. Dendrochronology might be used to constrain some of the events in this dataset to a year.
3. **Continued monitoring campaigns.** There remains a need to collect high quality and consistent field and remote sensing data immediately following debris flow events. It is recommended that annual RPAS (drone) lidar scans are continued at Mount Currie at Fountain Ridge for more accurate estimates of debris flow volume and erosion, and to capture events undetected with satellite imagery. Baselines should be established at other fans in this dataset. Ideally, ALS scans should be taken following major events to measure volume change in the watershed. Monitoring equipment, such as cameras, geophones, and rain gauges, would be useful at the most active fans (e.g., Currie D and Fountain N) to alert a research team when an event occurs for timely field investigations. This equipment would also generate useful data for future research, such as information about surge sequencing, velocity measurements, and storm data.
4. **Expanding the dataset.** More fans and impact areas should be added to the dataset to capture

variability in runouts and a larger spectrum of event magnitudes. Repeating the statistical analysis for fans outside the study area with different climates and geologic settings, or to include a wider range of hydrogeomorphic processes, would provide more opportunity to test the hypotheses.

5. **Expanding the predictor variables.** Due to the limited topographic data available across the fan sites, only a limited selection of morphometric variables was practical for this work. Upon access to high quality lidar data across more of the fan sites, future work may incorporate more accurate measures of fan incision and curvature. Other variables that would be compelling to test, as available, include fan roughness, number of channels on a fan, channel curvature, area of contributing source zones in the watershed, grain-size distributions, climate variables such as annual precipitation, intensity and duration of rainfall during an event, number of surges during an event, peak discharge, location and volume of the initiating mass, and the runout of the previous event(s).
6. **Deriving statistical distributions or functions for probability of runout exceedance.** Future work may involve fitting three dimensional functions or statistical models to the impact area heatmaps (i.e., bivariate empirical cumulative runout exceedance distribution functions), resulting in robust and adaptable models for runout prediction, without overfitting to the empirical data. For instance, statistical model parameters (e.g., location, scale, shape) could be a function of site-specific attributes or theoretical avulsion sequence patterns.
7. **Testing and validation with laboratory flume table experiments.** Spatial impact heatmaps could be compared to flume table debris flow experiments, applying the same measurement approach with a grid centered on the fan apex and avulsions measured relative to the previous flow path. Extending the work by de Haas et al. (2015) and de Haas et al. (2018b), variables such as the peak discharge, number of surges, grain-size distribution, and water content, could be systematically changed to test the impacts on debris flow avulsion and mobility trends. Furthermore, experimental work allows the opportunity to measure the fan topography and channel geometry before and after every event, which can be used to examine the interaction of debris flows with their path.

8. **Methods to estimate probability of avulsion based on longitudinal channel threshold exceedance.** Although this thesis begins to elucidate fan-scale avulsion "hotspots", methods to estimate the location and conditional probability of an avulsion along a channel are still undeveloped. Future research might involve determining discharge thresholds at which an avulsion is imminent for a given channel configuration. Another approach might involve determining the probability of avulsion versus conveyance with a logistic regression function calibrated to variables related to the flow (depth, velocity, grain-size) and channel (slope, cross-sectional area, planimetric curvature). A similar philosophy was applied with volume-balance runout models by Miller & Burnett (2008) and Fannin & Wise (2001), in which the probability of erosion versus deposition was estimated using path characteristics. Numerous case studies with pre- and post-event lidar topography (e.g., 2019 event at Currie D), or flume table experiments, would be required to calibrate these types of models.
9. **Extending the statistical analysis.** The preliminary statistical analysis presented in this thesis is meant to unearth general runout trends with the available data, and to examine what variables should be considered for future work. With more data, the statistical analysis might be extended to include other classification and regression techniques. Rather than splitting the predictor variables into groups based on quartiles, future work may involve optimizing the value at which a variable maximizes the differences between groups. Discriminant analyses, decision tree algorithms, and various clustering approaches might be considered for predicting spatial impact distributions.
10. **Incorporating intensity mapping.** In this work, spatial impact was treated as a binary variable (impacted/not impacted) without consideration of flow intensity used to estimate vulnerability in a QRA. Effort should be undertaken to document the impact energy of debris flows, such as measures of structural damage, extent of vegetation removal, velocity estimates (e.g., runup, superelevation), grain-size, and flow depths, as an additional dimension to scale the spatial impact heatmaps. This documentation was completed for a few events in the dataset, but not extensively enough for a statistical analysis.
11. **Hosting the dataset and code online.** The geospatial dataset and code should be hosted

online through an open-source web application. A workflow could be created that allows users to add their own data, filter the empirical dataset or use pre-calibrated functions, and export custom probability of runout exceedance contours for a fan or group of fans.

5.4 Closure

This work was undertaken to better understand debris flow fan hazard susceptibility through empirical observation. The research objectives (Section 1.2) have been accomplished: a geospatial dataset documenting debris flow impacts was created, and spatial impact trends extracted for use in forecasting. The research hypotheses (Section 1.3) have been tested: spatial impact distributions were fit for runout in both down-fan and cross-fan components, and variables that discriminate runout trends were tested. Much research remains to be done before debris flow avulsion and mobility can be routinely predicted, however, the work presented here provides a unique empirical approach for such analysis.

References

Aaron, J. (2017). *Advancement and Calibration of a 3D Numerical Model for Landslide Runout Analysis*. Ph.D Thesis, University of British Columbia, Vancouver, BC. → page 19

Aaron, J., McDougall, S., & Nolde, N. (2019). Two methodologies to calibrate landslide runout models. *Landslides*, *16*(5), 907–920, https://doi.org/10.1007/s10346-018-1116-8. → page 1

Abellán, A., Jaboyedoff, M., Oppikofer, T., & Vilaplana, J. M. (2009). Detection of millimetric deformation using a terrestrial laser scanner: experiment and application to a rockfall event. *Natural Hazards and Earth System Sciences*, *9*(2), 365–372, https://doi.org/10.5194/nhess-9-365-2009. → page 64

Agisoft LLC. (2019). Agisoft Metashape Professional (Version 1.5.2) (Software) https://www.agisoft.com/downloads/installer/. → pages 49, 87

Ashworth, P. J., Best, J. L., & Jones, M. (2004). Relationship between sediment supply and avulsion frequency in braided rivers. *Geology*, *32*(1), 21–24, https://doi.org/10.1130/G19919.1. → page 15

Ballantyne, C. K. (2002). Paraglacial geomorphology. *Quaternary Science Reviews*, *21*(18-19), 1935–2017, https://doi.org/10.1016/S0277-3791(02)00005-7. → page 5

Bardou, E. (2002). *Methodologie de diagnostic des laves torrentielles sur un bassin versant alpin*. Ph.D Thesis, École Polytechnique Fédérale de Lausanne, Lausanne, Switzerland. → pages xiii, 80, 81, 132

Bathurst, J. C., Burton, A., & Ward, T. J. (1997). Debris Flow Run-Out and Landslide Sediment Delivery Model Tests. *Journal of Hydraulic Engineering*, *123*(5), 410–419, https://doi.org/10.1061/(ASCE)0733-9429(1997)123:5(410). → pages 31, 37

Benda, L. E. & Cundy, T. W. (1990). Predicting deposition of debris flows in mountain channels. *Canadian Geotechnical Journal*, *27*(4), 409–417, https://doi.org/10.1139/t90-057. → pages 22, 32, 35

Berti, M. & Simoni, A. (2007). Prediction of debris flow inundation areas using empirical mobility relationships. *Geomorphology*, *90*(1-2), 144–161, https://doi.org/10.1016/j.geomorph.2007.01.014. → pages 33, 68

Berti, M. & Simoni, A. (2014). DFLOWZ: A free program to evaluate the area potentially inundated by a debris flow. *Computers & Geosciences*, *67*, 14–23, https://doi.org/10.1016/j.cageo.2014.02.002. → page 35

Bertrand, M., Liébault, F., & Piégay, H. (2013). Debris-flow susceptibility of upland catchments. *Natural Hazards*, *67*(2), 497–511, https://doi.org/10.1007/s11069-013-0575-4. → pages xiii, 80, 81, 132

BGC (2004). *Preliminary Debris Flow Hazard Assessment of Field, Carratt, Eng, McNab, and Dale Creeks, Hatzic Valley*. Technical Report Project No. 0378-001-03. → page 42

BGC (2015). *Catiline Creek Debris-Flow Hazard and Risk Assessment*. Technical Report Project No. 1358001. → pages 2, 45, 60

BGC (2018a). *Mount Currie Landslide Risk Assessment*. Technical Report Project No. 1358004. → pages 45, 111

BGC (2018b). *Seton Portage Area Integrated Hydrogeomorphic Risk Assessment*. Technical Report Project No. 1358005. → pages 2, 45, 60, 69

Blair, T. C. & McPherson, J. G. (1998). Recent debris-flow processes and resultant form and facies of the Dolomite alluvial fan, Owens Valley, California. *Journal of Sedimentary Research*, *68*(5), 800–818, https://doi.org/10.2110/jsr.68.800. → pages 12, 22, 90, 132

Blais-Stevens, A. & Septer, D. (2008). *Historical accounts of landslides and flooding events along the Sea to Sky Corridor, British Columbia, from 1855-2007*. Open-File 5741, Geological Survey of Canada. → pages 42, 44

Booth, A. M., Sifford, C., Vascik, B., Siebert, C., & Buma, B. (2020). Large wood inhibits debris flow runout in forested southeast Alaska. *Earth Surface Processes and Landforms*, https://doi.org/10.1002/esp.4830. → pages 22, 33

Bostock, H. (2014). *Physiographic regions of Canada*. Open-File Geological Survey of Canada "A" Series Map 1254A. Scale 1:5,000,000. → pages xi, 6

Bovis, M. J. & Evans, S. G. (1995). Rock slope movements along the Mount Currie "fault scarp", southern Coast Mountains, British Columbia. *Canadian Journal of Earth Sciences*, *32*(12), 2015–2020, https://doi.org/10.1139/e95-154. → page 111

Bovis, M. J. & Jakob, M. (1999). The role of debris supply conditions in predicting debris flow activity. *Earth Surface Processes and Landforms*, *24*(11), 1039–1054, https://doi.org/10.1002/(SICI)1096-9837(199910)24:11⟨1039::AID-ESP29⟩3.0.CO;2-U. → pages 7, 17, 74, 81

Bryant, M., Falk, P., & Paola, C. (1995). Experimental study of avulsion frequency and rate of deposition. *Geology*, *23*(4), 365–368, https://doi.org/10.1130/0091-7613(1995)023⟨0365:ESOAFA⟩2.3.CO;2. → pages 15, 24

Bull, W. B. (1977). The alluvial-fan environment. *Progress in Physical Geography: Earth and Environment*, *1*(2), 222–270, https://doi.org/10.1177/030913337700100202. → page 47

Burton, A. & Bathurst, J. C. (1998). Physically based modelling of shallow landslide sediment yield at a catchment scale. *Environmental Geology*, *35*(2-3), 89–99, https://doi.org/10.1007/s002540050296. → page 32

Bustin, A. M., Clowes, R. M., Monger, J. W., & Journeay, J. M. (2013). The southern Coast Mountains, British Columbia: New interpretations from geological, seismic reflection, and gravity data. *Canadian Journal of Earth Sciences*, *50*(10), 1033–1050, https://doi.org/10.1139/cjes-2012-0122. → page 4

Cannon, S. (1989). *An evaluation of the travel-distance potential of debris flows*. Miscellaneous Publication 89-2, Utah Geological and Mineral Survey, Salt Lake City, Utah. → page 23

Chen, H. X., Zhang, L. M., Gao, L., Yuan, Q., Lu, T., Xiang, B., & Zhuang, W. L. (2017). Simulation of interactions among multiple debris flows. *Landslides*, *14*(2), 595–615, https://doi.org/10.1007/s10346-016-0710-x. → pages 20, 21

Chen, J., Chang, S., Tsang, Y., & Shieh, C. (2007). Empirical relationships for deposited length of debris flows - A case study in Taiwan. In C. Chen & J. Major (Eds.), *Debris-Flow Hazards Mitigation: Mechanics, Prediction, and Assessment* (pp. 525–530). Chengdu, China. → pages 32, 37

Chen, Z., Zhang, Y., Ouyang, C., Zhang, F., & Ma, J. (2018). Automated Landslides Detection for Mountain Cities Using Multi-Temporal Remote Sensing Imagery. *Sensors*, *18*(3), https://doi.org/10.3390/s18030821. → page 54

Christen, M., Kowalski, J., & Bartelt, P. (2010). RAMMS: Numerical simulation of dense snow avalanches in three-dimensional terrain. *Cold Regions Science and Technology*, *63*(1-2), 1–14, https://doi.org/10.1016/j.coldregions.2010.04.005. → pages 1, 18

Church, M. & Ryder, J. M. (2010). Physiography of British Columbia. In R. G. Pike, T. E. Redding, R. D. Moore, R. D. Winkler, & K. D. Bladon (Eds.), *Compendium of Forest Hydrology and Geomorphology in British Columbia*, volume 1 of 2 of *Land Management Handbook 66* (pp. 17–45). Victoria, BC: Ministry of Forests and Range Forest Science Program. → page 5

Clague, J. J. & Ward, B. (2011). Pleistocene glaciation of British Columbia. In J. Ehlers, P. Gibbard, & P. Hughes (Eds.), *Quaternary Glaciations - Extent and Chronology*, volume 15 of *Developments in Quaternary Sciences* (pp. 563–573). Elsevier. → page 5

CloudCompare (2019). CloudCompare (version 2.10) [GPL Software]. Retrieved from http://www.cloudcompare.org/. → page 64

Cordilleran (2010). *Catalina Creek emergency debris flow assessment*. Memo to Ministry of Forests and Range, Squamish, BC. → page 69

Cordilleran (2013). *Catalina Creek debris flow, August 30, 2013*. Memo to Ministry of Forests, Lands and Natural Resource Operations, Squamish, BC. → page 69

Corominas, J. (1996). The angle of reach as a mobility index for small and large landslides. *Canadian Geotechnical Journal*, *33*, https://doi.org/10.1139/t96-005. → pages xi, 1, 20, 22, 30, 31, 100, 130

Corominas, J., et al. (2014). Recommendations for the quantitative analysis of landslide risk. *Bulletin of Engineering Geology and the Environment*, *73*(2), 209–263, https://doi.org/10.1007/s10064-013-0538-8. → pages 16, 17

Costa, J. (1984). Physical geomorphology of debris flows. In J. Costa & P. Fleisher (Eds.), *Developments and Applications of Geomorphology* (pp. 268–317). Springer. → pages 12, 13, 61

Crosta, G. B., Cucchiaro, S., & Frattini, P. (2003). Validation of semi-empirical relationships for the definition of debris-flow behaviour in granular materials. In D. Rickenmann & C. Chen (Eds.), *Debris-Flow Hazards Mitigation: Mechanics, Prediction, and Assessment* (pp. 821–831).: Millpress, Rotterdam. → page 33

Cui, Y., Schiarizza, P., & Diakow, L. (2017). *British Columbia digital geology*. Open-File 2017-8, British Columbia Ministry of Energy, Mines and Petroleum Resources. Data version 2019-12-19. → pages xi, 6, 81

D'Agostino, V., Cesca, M., & Marchi, L. (2010). Field and laboratory investigations of runout distances of debris flows in the Dolomites (Eastern Italian Alps). *Geomorphology*, *115*(3-4), 294–304, https://doi.org/10.1016/j.geomorph.2009.06.032. → page 33

D'Agostino, V. & Marchi, L. (2001). Debris flow magnitude in the Eastern Italian Alps: Data collection and analysis. *Physics and Chemistry of the Earth, Part C: Solar, Terrestrial & Planetary Science*, *26*, 657–663, https://doi.org/10.1016/S1464-1917(01)00064-2. → page 17

Dai, F. C., Lee, C. F., & Ngai, Y. Y. (2002). Landslide risk assessment and management: an overview. *Engineering Geology*, *64*(1), 65–87, https://doi.org/10.1016/S0013-7952(01)00093-X. → page 16

D'Arcy, M., Roda Boluda, D. C., Whittaker, A. C., & Carpineti, A. (2015). Dating alluvial fan

surfaces in Owens Valley, California, using weathering fractures in boulders. *Earth Surface Processes and Landforms*, *40*(4), 487–501, https://doi.org/10.1002/esp.3649. → pages 26, 86

de Haas, T., Braat, L., Leuven, J. R., Lokhorst, I. R., & Kleinhans, M. G. (2015). Effects of debris flow composition on runout, depositional mechanisms, and deposit morphology in laboratory experiments. *Journal of Geophysical Research: Earth Surface*, *120*(9), 1949–1972, https://doi.org/10.1002/2015JF003525. → pages 21, 22, 23, 120, 150

de Haas, T. & Densmore, A. L. (2019). Debris-flow volume quantile prediction from catchment morphometry. *Geology*, *47*(8), 791–794, https://doi.org/10.1130/G45950.1. → page 17

de Haas, T., Densmore, A. L., den Hond, T., & Cox, N. J. (2019). Fan-Surface Evidence for Debris-Flow Avulsion Controls and Probabilities, Saline Valley, California. *Journal of Geophysical Research: Earth Surface*, *124*(5), 1118–1138, https://doi.org/10.1029/2018JF004815. → pages 12, 14, 24, 26, 28, 66

de Haas, T., Densmore, A. L., Stoffel, M., Suwa, H., Imaizumi, F., Ballesteros-Cánovas, J., & Wasklewicz, T. (2018a). Avulsions and the spatio-temporal evolution of debris-flow fans. *Earth-Science Reviews*, *177*, 53–75, https://doi.org/10.1016/j.earscirev.2017.11.007. → pages v, xiv, 2, 12, 14, 15, 23, 24, 26, 27, 28, 89, 103, 104, 105, 107, 108, 109, 110, 132, 136

de Haas, T., Kruijt, A., & Densmore, A. L. (2018b). Effects of debris-flow magnitude–frequency distribution on avulsions and fan development. *Earth Surface Processes and Landforms*, *43*(13), 2779–2793, https://doi.org/10.1002/esp.4432. → pages 24, 26, 100, 136, 150

de Haas, T., van den Berg, W., Braat, L., & Kleinhans, M. G. (2016). Autogenic avulsion, channelization and backfilling dynamics of debris-flow fans. *Sedimentology*, *63*(6), 1596–1619, https://doi.org/10.1111/sed.12275. → pages xi, 15, 16, 23, 24, 26

Deijns, A. A. (2018). The effect of debris-flow sediment composition change on avulsion behavior and debris-flow fan development. Master's thesis, Universiteit Utrecht, Utrecht, Netherlands. → page 27

Deijns, A. A., Bevington, A. R., van Zadelhoff, F., de Jong, S. M., Geertsema, M., & McDougall, S. (2020). Semi-automated detection of landslide timing using harmonic modelling of satellite imagery, Buckinghorse River, Canada. *International Journal of Applied Earth Observation and Geoinformation*, *84*, 101943, https://doi.org/10.1016/j.jag.2019.101943. → page 149

Demarchi, D. A. (2011). *An Introduction to the Ecoregions of British Columbia*. Victoria, BC: Ecosystem Information Section, Ministry of Environment, 3rd edition. → pages xi, 6, 9

Densmore, A. L., de Haas, T., McArdell, B., & Schürch, P. (2019). Making sense of avulsions on debris-flow fans. In J. Kean, J. Coe, P. Santi, & B. Guillen (Eds.), *Debris-Flow Hazards Mitigation: Mechanics, Prediction, and Assessment* (pp. 637–644). Golden, CO. → pages 2, 14, 27, 28, 89

Duffell, S. & McTaggart, K. (1952). *Ashcroft map-area, British Columbia*. Memoir 262, Geological Survey of Canada. → page 116

Dühnforth, M., Densmore, A. L., Ivy-Ochs, S., Allen, P. A., & Kubik, P. W. (2007). Timing and patterns of debris flow deposition on Shepherd and Symmes creek fans, Owens Valley, California, deduced from cosmogenic 10Be. *Journal of Geophysical Research: Earth Surface*, *112*(F3), https://doi.org/10.1029/2006JF000562. → page 26

Eisank, C., Smith, M., & Hillier, J. (2014). Assessment of multiresolution segmentation for delimiting drumlins in digital elevation models. *Geomorphology*, *214*(100), 452–464, https://doi.org/10.1016/j.geomorph.2014.02.028. → page 149

Evans, S. G. & Lister, D. R. (1984). The geomorphic effects of July 1983 rainstorms in the southern

Cordillera and their impact on transportation facilities. In *Current Research, Part B* (pp. 223–235). Geological Survey of Canada. Paper 84-1B. → page 42

Fannin, R. J. & Rollerson, T. P. (1993). Debris flows: some physical characteristics and behaviour. *Canadian Geotechnical Journal*, *30*(1), 71–81, https://doi.org/10.1139/t93-007. → pages 10, 23, 35, 42

Fannin, R. J. & Wise, M. P. (2001). An empirical-statistical model for debris flow travel distance. *Canadian Geotechnical Journal*, *38*(5), 982–994, https://doi.org/10.1139/cgj-38-5-982. → pages xi, 10, 22, 30, 35, 37, 42, 151

Fell, R. (1994). Landslide risk assessment and acceptable risk. *Canadian Geotechnical Journal*, *31*(2), 261–272, https://doi.org/10.1139/t94-031. → page 16

Fell, R., Corominas, J., Bonnard, C., Cascini, L., Leroi, E., & Savage, W. Z. (2008). Guidelines for landslide susceptibility, hazard and risk zoning for land use planning. *Engineering Geology*, *102*(3), 85–98, https://doi.org/10.1016/j.enggeo.2008.03.022. → page 19

Field, J. (2001). Channel Avulsion on Alluvial Fans in Southern Arizona. *Geomorphology*, *37*, 93–104, https://doi.org/10.1016/S0169-555X(00)00064-7. → pages 15, 24

Fiorucci, F., Ardizzone, F., Mondini, A. C., Viero, A., & Guzzetti, F. (2019). Visual interpretation of stereoscopic NDVI satellite images to map rainfall-induced landslides. *Landslides*, *16*(1), 165–174, https://doi.org/10.1007/s10346-018-1069-y. → page 54

Frank, F., McArdell, B. W., Huggel, C., & Vieli, A. (2015). The importance of entrainment and bulking on debris flow runout modeling: examples from the Swiss Alps. *Natural Hazards and Earth System Sciences*, *15*(11), 2569–2583, https://doi.org/10.5194/nhess-15-2569-2015. → page 20

Friele, P. & Clague, J. J. (2004). Large Holocene landslides from Pylon Peak, southwestern British Columbia. *Canadian Journal of Earth Sciences*, *41*(2), 165–182, https://doi.org/10.1139/e03-089. → page 42

Friele, P., Jakob, M., & Clague, J. J. (2008). Hazard and risk from large landslides from Mount Meager volcano, British Columbia, Canada. *Georisk: Assessment and Management of Risk for Engineered Systems and Geohazards*, *2*(1), 48–64, https://doi.org/10.1080/17499510801958711. → page 46

Fuller, J. E. (2012). *Evaluation of avulsion potential on active alluvial fans in central and western Arizona*. Arizona Geological Survey Contributed Report CR-12-D. → page 26

García-Ruiz, J. M., Beguería, S., Lorente, A., & Martí, C. (1999). *Comparing Debris Flow Relationships in the Alps and in the Pyrenees*. Technical Report EVG1-CT-1999-00007, Instituto Pirenaico de Ecología, Zaragoza, Spain. → page 23

Geertsema, M., Schwab, J., Blais-Stevens, A., & Sakals, M. (2009). Landslides impacting linear infrastructure in west central British Columbia. *Natural Hazards: Journal of the International Society for the Prevention and Mitigation of Natural Hazards*, *48*(1), 59–72, https://doi.org/10.1007/s11069-008-9248-0. → page 42

GeoBC (2009). Freshwater Atlas of British Columbia https://www2.gov.bc.ca/gov/content/data/geographic-data-services/topographic-data/freshwater. → pages 75, 77

George, D. L. & Iverson, R. M. (2014). A depth-averaged debris-flow model that includes the effects of evolving dilatancy. II. Numerical predictions and experimental tests. *Proceedings of the Royal Society A: Mathematical, Physical and Engineering Sciences*, *470*(2170), https://doi.org/10.1098/rspa.2013.0819. → page 18

Giraud, R. (2005). *Guidelines for the geologic evaluation of debris-flow hazards on alluvial fans in*

Utah. Miscellaneous Publication 06-6, Utah Geological Survey. → page 61
Golden Software, LLC (2018). Surfer v15.5 www.goldensoftware.com. → pages xiv, 95, 97, 138
Griswold, J. P. & Iverson, R. M. (2008). *Mobility statistics and automated hazard mapping for debris flows and rock avalanches*. Open-File Report 2007–5276, U.S. Geological Survey, Reston, Virginia. → pages xi, 1, 20, 22, 30, 33, 68, 130
Guthrie, R. H., Hockin, A., Colquhoun, L., Nagy, T., Evans, S. G., & Ayles, C. (2010). An examination of controls on debris flow mobility: Evidence from coastal British Columbia. *Geomorphology*, *114*(4), 601–613, https://doi.org/10.1016/j.geomorph.2009.09.021. → page 10
Heim, A. (1932). *Bergsturz und Menschenleben (Landslides and Human Lives)*. Vancouver: Bitech Press. Translated by N. Smermer, 1989. → page 30
Hooke, R. L. (1967). Processes on Arid-Region Alluvial Fans. *The Journal of Geology*, *75*(4), 438–460, https://doi.org/10.1086/627271. → pages 28, 78
Hooke, R. L. (1968). Steady-state relationships on arid-region alluvial fans in closed basins. *American Journal of Science*, *266*(8), 609–629, https://doi.org/10.2475/ajs.266.8.609. → page 23
Horton, P., Jaboyedoff, M., Rudaz, B., & Zimmermann, M. (2013). Flow-R, a model for susceptibility mapping of debris flows and other gravitational hazards at a regional scale. *Natural Hazards and Earth System Science*, *13*(4), 869–885, https://doi.org/10.5194/nhess-13-869-2013. → pages 19, 31
Hungr, O. (2005). Classification and terminology. In M. Jakob & O. Hungr (Eds.), *Debris-flow Hazards and Related Phenomena* (pp. 9–23). Berlin, Heidelberg: Springer Praxis Books. 10.1007/3-540-27129-5_2. → page 12
Hungr, O. & Evans, S. G. (1993). *The Failure Behaviour of Large Rockslides in Mountainous Regions*. Open-File 2598, Geological Survey of Canada. → page 33
Hungr, O., Evans, S. G., & Hutchinson, I. N. (2001). A Review of the Classification of Landslides of the Flow Type. *Environmental & Engineering Geoscience*, *7*(3), 221–238. → pages 11, 13
Hungr, O., Leroueil, S., & Picarelli, L. (2014). The Varnes classification of landslide types, an update. *Landslides*, *11*(2), 167–194, https://doi.org/10.1007/s10346-013-0436-y. → pages 11, 12, 13, 131
Hungr, O., McDougall, S., Wise, M. P., & Cullen, M. (2008). Magnitude–frequency relationships of debris flows and debris avalanches in relation to slope relief. *Geomorphology*, *96*(3), 355–365, https://doi.org/10.1016/j.geomorph.2007.03.020. → pages 10, 37
Hungr, O., Morgan, G. C., & Kellerhals, R. (1984). Quantitative analysis of debris torrent hazards for design of remedial measures. *Canadian Geotechnical Journal*, *21*(4), 663–677, https://doi.org/10.1139/t84-073. → pages 9, 42
Hungr, O., Morgan, G. C., VanDine, D. F., & Lister, D. R. (1987). Debris flow defenses in British Columbia. In J. E. Costa & G. F. Wieczorek (Eds.), *Debris Flows/Avalanches: Process, Recognition, and Mitigation*, volume 7 of *Reviews in Engineering Geology* (pp. 201–222). Geological Society of America. https://doi.org/10.1130/REG7. → page 42
Hürlimann, M., Rickenmann, D., Medina, V., & Bateman, A. (2008). Evaluation of approaches to calculate debris-flow parameters for hazard assessment. *Engineering Geology*, *102*(3-4), 152–163, https://doi.org/10.1016/j.enggeo.2008.03.012. → page 29
Ikeya, H. (1981). A method of designation for area in danger of debris flow. In *Erosion and Sediment Transport in Pacific Rim Steeplands*, volume 132 (pp. 578–588). Christchurch, New

Zealand. → page 32

Ishikawa, Y., Kawakami, S., Morimoto, C., & Mizuhara, K. (2003). Suppression of debris movement by forests and damage to forests by debris deposition. *Journal of Forest Research*, *8*(1), 37–47, https://doi.org/10.1007/s103100300004. → page 22

Iverson, R. M. (1997). The physics of debris flows. *Reviews of Geophysics*, *35*(3), 245–296, https://doi.org/10.1029/97RG00426. → pages 12, 13

Iverson, R. M. (2003). The debris-flow rheology myth. In D. Rickenmann & C. Chen (Eds.), *Debris-flow Hazards Mitigation: Mechanics, Prediction, and Assessment* (pp. 303–314). → pages 18, 21

Iverson, R. M., Schilling, S. P., & Vallance, J. W. (1998). Objective delineation of lahar-inundation hazard zones. *Geological Society of America Bulletin*, *110*(8), 972–984, https://doi.org/10.1130/0016-7606(1998)110⟨0972:ODOLIH⟩2.3.CO;2. → page 33

Ivy-Ochs, S., Dühnforth, M., Densmore, A. L., & Alfimov, V. (2013). Dating Fan Deposits with Cosmogenic Nuclides. In M. Schneuwly-Bollschweiler, M. Stoffel, & F. Rudolf-Miklau (Eds.), *Dating Torrential Processes on Fans and Cones: Methods and Their Application for Hazard and Risk Assessment* (pp. 243–263). Dordrecht: Springer Netherlands. → page 86

Jackson, L., Kostaschuk, R., & MacDonald, G. (1984). Identification of debris flow hazard on alluvial fans in the Canadian Rocky Mountains. *Review in Engineering Geology*, *7*, 115–124, https://doi.org/10.13140/2.1.2321.1206. → page 130

Jakob, M. (1996). *Morphometric and Geotechnical Controls of Debris Flow Frequency and Magnitude in Southwestern British Columbia*. Ph.D Thesis, University of British Columbia, Vancouver, BC. → pages 37, 42, 45, 81, 135

Jakob, M. (2005). Debris-flow hazard analysis. In M. Jakob & O. Hungr (Eds.), *Debris-flow Hazards and Related Phenomena* (pp. 411–443). Berlin, Heidelberg: Springer Praxis Books. 10.1007/3-540-27129-5_17. → pages 35, 61, 86

Jakob, M. (2013). Events on Fans and Cones: Recurrence Interval and Magnitude. In M. Schneuwly-Bollschweiler, M. Stoffel, & F. Rudolf-Miklau (Eds.), *Dating Torrential Processes on Fans and Cones: Methods and Their Application for Hazard and Risk Assessment* (pp. 95–108). Dordrecht: Springer Netherlands. → page 86

Jakob, M. (2019). Debris-flow hazard assessments - a practitioner's view. In J. Kean, J. Coe, P. Santi, & B. Guillen (Eds.), *Debris-Flow Hazards Mitigation: Mechanics, Prediction, and Assessment* (pp. 716–723). Golden, CO. → pages 7, 17

Jakob, M., Bale, S., McDougall, S., & Friele, P. (2016). Regional debris-flow and debris-flood frequency-magnitude curves. In *Proceedings of GeoVancouver 2016 Conference* Vancouver, BC. → pages 17, 42

Jakob, M., Hungr, O., & Thompson, B. (1997). Two debris flows with anomalously high magnitude. In C. Chen (Ed.), *Debris-Flow Hazards Mitigation: Mechanics, Prediction, and Assessment* (pp. 382–394). San Francisco, CA. → pages 9, 42, 45, 69

Jakob, M. & Lambert, S. (2009). Climate change effects on landslides along the southwest coast of British Columbia. *Geomorphology*, *107*(3-4), 275–284, https://doi.org/10.1016/j.geomorph.2008.12.009. → page 7

Jakob, M., Stein, D., & Ulmi, M. (2012). Vulnerability of buildings to debris flow impact. *Natural Hazards*, *60*(2), 241–261, https://doi.org/10.1007/s11069-011-0007-2. → page 18

Johnson, A. & Rodine, J. (1984). Debris flow. In D. Brunsden & D. Prior (Eds.), *Slope Instability* (pp. 257–361). New York: John Wiley & Sons Inc. → page 22

Johnson, C. G., Kokelaar, B. P., Iverson, R. M., Logan, M., LaHusen, R. G., & Gray, J. (2012). Grain-size segregation and levee formation in geophysical mass flows. *Journal of Geophysical Research: Earth Surface*, *117*(F1), https://doi.org/10.1029/2011JF002185. → page 12

Jomelli, V. (2013). Lichenometric Dating of Debris Avalanche Deposits with an Example from the French Alps. In M. Schneuwly-Bollschweiler, M. Stoffel, & F. Rudolf-Miklau (Eds.), *Dating Torrential Processes on Fans and Cones: Methods and Their Application for Hazard and Risk Assessment* (pp. 211–224). Dordrecht: Springer Netherlands. → page 86

Jones, L. S. & Schumm, S. A. (1999). Causes of avulsion: an overview. In N. Smith & J. Rogers (Eds.), *Fluvial Sedimentology VI* (pp. 171–178). John Wiley & Sons Inc. → page 15

Jordan, R. P. (1994). *Debris flows in the southern Coast Mountains, British Columbia: dynamic behaviour and physical properties*. Ph.D Thesis, University of British Columbia. → pages 9, 21, 42, 45, 116

Kaitna, R., Palucis, M. C., Yohannes, B., Hill, K. M., & Dietrich, W. E. (2016). Effects of coarse grain size distribution and fine particle content on pore fluid pressure and shear behavior in experimental debris flows. *Journal of Geophysical Research: Earth Surface*, *121*(2), 415–441, https://doi.org/10.1002/2015JF003725. → page 21

Kang, H. & Kim, Y. (2016). The physical vulnerability of different types of building structure to debris flow events. *Natural Hazards*, *80*(3), 1475–1493, https://doi.org/10.1007/s11069-015-2032-z. → page 18

Kelman, M. C., Russell, J. K., & Hickson, C. J. (2002). Effusive intermediate glaciovolcanism in the Garibaldi volcanic belt, southwestern British Columbia, Canada. *Geological Society, London, Special Publications*, *202*(1), 195–211, https://doi.org/10.1144/GSL.SP.2002.202.01.10. → page 4

Lague, D., Brodu, N., & Leroux, J. (2013). Accurate 3D comparison of complex topography with terrestrial laser scanner: Application to the Rangitikei canyon (N-Z). *ISPRS Journal of Photogrammetry and Remote Sensing*, *82*, 10–26, https://doi.org/10.1016/j.isprsjprs.2013.04.009. → page 64

Lancaster, S., Hayes, S., & Grant, G. (2003). Effects of wood on debris flow runout in small mountain watersheds. *Water Resources Research*, *39*, 1168, https://doi.org/10.1029/2001wr001227. → page 22

Lau, C.-A. (2017). Channel scour on temperate alluvial fans in British Columbia. Master's thesis, Simon Fraser University. → pages xi, 9, 14, 45, 61, 65, 69, 74, 78, 131, 132

Legros, F. (2002). The mobility of long-runout landslides. *Engineering Geology*, *63*, https://doi.org/10.1016/S0013-7952(01)00090-4. → pages 20, 35, 37

Linder, W. (2016). *Digital Photogrammetry: A Practical Course*. Berlin Heidelberg: Springer-Verlag, 4th edition. https://doi.org/10.1007/978-3-662-50463-5. → page 50

Lorenzini, G. & Mazza, N. (2004). *Debris flow: Phenomenology and rheological modelling*. Wit Press. → page 12

Mackey, S. D. & Bridge, J. S. (1995). Three-dimensional model of alluvial stratigraphy; theory and applications. *Journal of Sedimentary Research*, *65*(1b), 7–31, https://doi.org/10.1306/D42681D5-2B26-11D7-8648000102C1865D. → page 27

Major, J. J. & Iverson, R. M. (1999). Debris-flow deposition: Effects of pore-fluid pressure and friction concentrated at flow margins. *Geological Society of America Bulletin*, *111*, 1424–1434, https://doi.org/10.1130/0016-7606(1999)111⟨1424:DFDEOP⟩2.3.CO;2. → page 21

Martha, T. R., Kerle, N., Jetten, V., van Westen, C. J., & Kumar, K. V. (2010). Characterising spectral, spatial and morphometric properties of landslides for semi-automatic detection using object-oriented methods. *Geomorphology*, *116*(1), 24–36, https://doi.org/10.1016/j.geomorph.2009.10.004. → page 54

May, C. L. (2002). Debris flows through different forest age classes in the central Oregon Coast Range. *Journal of the American Water Resources Association*, *38*(4), 1097–1113, https://doi.org/10.1111/j.1752-1688.2002.tb05549.x. → page 22

McDougall, S. (2017). 2014 Canadian Geotechnical Colloquium: Landslide runout analysis — current practice and challenges. *Canadian Geotechnical Journal*, *54*(5), 605–620, https://doi.org/10.1139/cgj-2016-0104. → pages 1, 2, 18, 37

McDougall, S. & Hungr, O. (2004). A model for the analysis of rapid landslide motion across three-dimensional terrain. *Canadian Geotechnical Journal*, *41*(6), 1084–1097, https://doi.org/10.1139/t04-052. → pages xi, 1, 18, 20

Melton, M. A. (1965). The Geomorphic and Paleoclimatic Significance of Alluvial Deposits in Southern Arizona. *The Journal of Geology*, *73*(1), 1–38, https://doi.org/10.1086/627044. → page 75

Millard, T., Wilford, D., & Oden, M. (2006). *Coastal fan destabilization and forest management*. Technical Report TR-034, Research Section, Coast Forest Region, BC Ministry of Forests, Nanaimo, BC. → pages 24, 27, 28, 131, 133

Miller, D. J. & Burnett, K. M. (2008). A probabilistic model of debris-flow delivery to stream channels, demonstrated for the Coast Range of Oregon, USA. *Geomorphology*, *94*(1-2), 184–205, https://doi.org/10.1016/j.geomorph.2007.05.009. → pages 22, 23, 32, 35, 38, 151

Mitchell, A., McDougall, S., Nolde, N., Brideau, M.-A., Whittall, J., & Aaron, J. B. (2020). Rock avalanche runout prediction using stochastic analysis of a regional dataset. *Landslides*, *17*(4), 777–792, https://doi.org/10.1007/s10346-019-01331-3. → pages 31, 37

Miura, H. (2019). Fusion Analysis of Optical Satellite Images and Digital Elevation Model for Quantifying Volume in Debris Flow Disaster. *Remote Sensing*, *11*(9), https://doi.org/10.3390/rs11091096. → page 54

Mohrig, D., Heller, P. L., Paola, C., & Lyons, W. J. (2000). Interpreting avulsion process from ancient alluvial sequences: Guadalope-Matarranya system (Northern Spain) and Wasatch formation (Western Colorado). *Bulletin of the Geological Society of America*, *112*(12), 1787–1803, https://doi.org/10.1130/0016-7606(2000)112⟨1787:IAPFAA⟩2.0.CO;2. → page 27

Monger, J. W. & Journeay, J. M. (1994). *Guide to the Geology and Tectonic Evolution of the Southern Coast Mountains*. Open-File 2490, Geological Survey of Canada. → page 4

Nolde, N. & Joe, H. (2013). A Bayesian extreme value analysis of debris flows: Extreme Value Analysis of Debris Flows. *Water Resources Research*, *49*(10), 7009–7022, https://doi.org/10.1002/wrcr.20494. → page 140

O'Brien, J. S., Julien, P. Y., & Fullerton, W. T. (1993). Two-dimensional water flood and mudflow simulation. *Journal of Hydraulic Engineering*, *119*(2), 244–261, https://doi.org/10.1061/(ASCE)0733-9429(1993)119:2(244). → page 18

Parsons, J. D., Whipple, K. X., & Simoni, A. (2001). Experimental study of the grain-flow, fluid-mud transition in debris flows. *The Journal of Geology*, *109*(4), 427–447, https://doi.org/10.1086/320798. → page 21

PCIC (2012). Plan2Adapt Climate Information Tool

https://pacificclimate.org/analysis-tools/plan2adapt/. → page 7

PCIC (2014). High Resolution Climatology https://data.pacificclimate.org/portal/bc_prism/map/. → pages xi, 7, 9

Pederson, C. A., Santi, P. M., & Pyles, D. R. (2015). Relating the compensational stacking of debris-flow fans to characteristics of their underlying stratigraphy: Implications for geologic hazard assessment and mitigation. *Geomorphology*, *248*, 47–56, https://doi.org/10.1016/j.geomorph.2015.06.030. → pages 26, 28, 131, 132

Phillips, C. J. & Davies, T. R. H. (1991). Determining rheological parameters of debris flow material. *Geomorphology*, *4*(2), 101–110, https://doi.org/10.1016/0169-555X(91)90022-3. → page 21

Pierson, T. C. (1986). Flow behavior of chanellized debris flows, Mount St. Helens, Washington. In A. Abrahams (Ed.), *Hillslope Processes* (pp. 269–296). Boston: Allen & Unwin. → pages xi, 12, 14

Pierson, T. C. (2004). *Distinguishing between Debris Flows and Floods from Field Evidence in Small Watersheds*. Fact Sheet 2004-3142, U.S. Geological Survey. → pages 12, 61

Pierson, T. C. (2005). Hyperconcentrated flow — transitional process between water flow and debris flow. In M. Jakob & O. Hungr (Eds.), *Debris-flow Hazards and Related Phenomena* (pp. 159–202). Berlin, Heidelberg: Springer Praxis Books. 10.1007/3-540-27129-5_8. → page 13

Pike, R. J. (2000). Geomorphometry - diversity in quantitative surface analysis. *Progress in Physical Geography: Earth and Environment*, *24*(1), 1–20, https://doi.org/10.1177/030913330002400101. → page 74

Pike, R. J. & Wilson, S. E. (1971). Elevation-relief ratio, hypsometric integral, and geomorphic area-altitude analysis. *Bulletin of the Geological Society of America*, *82*(4), 1079–1084, https://doi.org/10.1130/0016-7606(1971)82[1079:ERHIAG]2.0.CO;2. → page 77

Planet (2019). Planet Application Program Interface: In Space for Life on Earth. San Fransisco, CA. https://api.planet.com. → pages xii, 54, 56, 57, 59, 88

Prochaska, A. B., Santi, P. M., Higgins, J. D., & Cannon, S. H. (2008). Debris-flow runout predictions based on the average channel slope (ACS). *Engineering Geology*, *98*(1-2), 29–40, https://doi.org/10.1016/j.enggeo.2008.01.011. → page 37

Quan Luna, B. (2012). *Chapter 6: Application of a Monte Carlo method to debris flow run-out modeling*. Ph.D Thesis, University of Twente, Enschede, Netherlands. → page 19

Quan Luna, B., Blahut, J., van Westen, C. J., Sterlacchini, C. J. S., van Asch, T. W., & Akbas, S. O. (2011). The application of numerical debris flow of modelling for the generation physical vulnerability curves. *Natural Hazards and Earth System Sciences*, *11*, 2047–2060, https://doi.org/10.5194/nhess-11-2047-2011. → page 18

Quan Luna, B., et al. (2014). Methods for debris flow hazard and risk assessment. In T. Asch, J. Corominas, S. Greiving, J.-P. Malet, & S. Sterlacchini (Eds.), *Mountain Risks: From Prediction to Management and Governance* (pp. 133–177). Springer. → page 18

Reitz, M. D. & Jerolmack, D. J. (2012). Experimental alluvial fan evolution: Channel dynamics, slope controls, and shoreline growth. *Journal of Geophysical Research: Earth Surface*, *117*(F2), https://doi.org/10.1029/2011JF002261. → page 15

Rickenmann, D. (1999). Empirical Relationships for Debris Flows. *Natural Hazards*, *19*, 47–77, https://doi.org/10.1023/A:1008064220727. → pages xi, 1, 29, 30, 31, 32, 37

Rickenmann, D. (2005). Runout prediction methods. In M. Jakob & O. Hungr (Eds.), *Debris-flow Hazards and Related Phenomena* (pp. 305–324). Berlin, Heidelberg: Springer Praxis Books. 10.1007/3-540-27129-5_13. → pages 29, 36

Rickenmann, D. & Zimmermann, M. (1993). The 1987 debris flows in Switzerland: documentation and analysis. *Geomorphology*, *8*(2-3), 175–189, https://doi.org/10.1016/0169-555X(93)90036-2. → page 31

Roberti, G. (2018). *Mount Meager, a glaciated volcano in a changing cryosphere: hazards and risk challenges*. Ph.D Thesis, Simon Fraser University. → pages 49, 50, 51

Rouse, J. J., Haas, R., Schell, J., Deering, D., & Harlan, J. (1974). *Monitoring the vernal advancements and retrogradation (green wave effect) of natural vegetation*. Type I Progress Report - Number 7, Texas A&M University, Remote Sensing Center, College Station, TX. → page 54

Ryder, J. M. (1969). *Alluvial fans of post-glacial environments within British Columbia*. Ph.D Thesis, University of British Columbia, Vancouver, BC. → page 116

Ryder, J. M. (1971). Some Aspects of the Morphometry of Paraglacial Alluvial Fans in South-central British Columbia. *Canadian Journal of Earth Sciences*, *8*(10), 1252–1264, https://doi.org/10.1139/e71-114. → pages 5, 46

Ryder, J. M., Fulton, R., & Clague, J. J. (1991). The Cordilleran Ice Sheet and the Glacial Geomorphology of Southern and Central British Colombia. *Géographie Physique et Quaternaire*, *45*(3), 365–377, https://doi.org/10.7202/032882ar. → page 5

Santi, P. M. (2014). Precision and Accuracy in Debris-Flow Volume Measurement. *Environmental & Engineering Geoscience*, *20*(4), 349–359, https://doi.org/10.2113/gseegeosci.20.4.349. → page 37

Santi, P. M., Pyles, D., & Pederson, C. (2017). Debris Flow Avulsion. *International Journal of Erosion Control Engineering*, *10*(1), 67–73, https://doi.org/10.13101/ijece.10.67. → pages 26, 131

Scheidegger, A. (1973). On the prediction of the reach and velocity of catastrophic landslides. *Rock Mechanics*, *5*, https://doi.org/10.1007/BF01301796. → page 30

Scheidl, C. & Rickenmann, D. (2008). Depositional characteristics and runout of alpine debris flows. In *Interpraevent'08*, volume 1 (pp. 477–488). Dornbirn, Austria. → page 33

Scheidl, C. & Rickenmann, D. (2010). Empirical prediction of debris-flow mobility and deposition on fans. *Earth Surface Processes and Landforms*, *35*(2), 157–173, https://doi.org/10.1002/esp.1897. → pages 19, 23, 29, 34, 35, 74, 132

Schilling, S. (1998). *LAHARZ: GIS programs for automated mapping of lahar-inundation hazard zones*. Open-File Report 98-638, U.S. Geological Survey, Vancouver, Washington. → page 35

Schneuwly-Bollschweiler, M. & Stoffel, M. (2013). Dendrogeomorphology – Tracking Past Events with Tree Rings. In M. Schneuwly-Bollschweiler, M. Stoffel, & F. Rudolf-Miklau (Eds.), *Dating Torrential Processes on Fans and Cones: Methods and Their Application for Hazard and Risk Assessment* (pp. 165–178). Dordrecht: Springer Netherlands. → page 86

Schraml, K., Thomschitz, B., McArdell, B. W., Graf, C., & Kaitna, R. (2015). Modeling debris-flow runout patterns on two alpine fans with different dynamic simulation models. *Natural Hazards and Earth System Sciences*, *15*(7), 1483–1492, https://doi.org/10.5194/nhess-15-1483-2015. → page 20

Schumm, S. A., Mosley, M. P., & Weaver, W. (1987). *Experimental Fluvial Geomorphology*. New York, NY: John Wiley & Sons Inc. → page 15

Schürch, P., et al. (2016). Quantitative reconstruction of late Holocene surface evolution on an alpine debris-flow fan. *Geomorphology*, *275*, 46–57, https://doi.org/10.1016/j.geomorph.2016.09.020. → page 26

Schürch, P., Densmore, A. L., Rosser, N., & McArdell, B. (2011a). A novel debris-flow fan evolution model based on debris flow monitoring and LiDAR topography. In R. Genevois, D. Hamilton, & A. Prestininzi (Eds.), *Debris-Flow Hazards Mitigation: Mechanics, Prediction, and Assessment* (pp. 263–272). Padua, Italy. https://doi.org/10.4408/IJEGE.2011-03.B-031. → page 38

Schürch, P., Densmore, A. L., Rosser, N. J., & McArdell, B. W. (2011b). Dynamic controls on erosion and deposition on debris-flow fans. *Geology*, *39*(9), 827–830, https://doi.org/10.1130/G32103.1. → pages 12, 21, 23, 27, 130

Scott, K. M., Vallance, J. W., & Pringle, P. T. (1995). *Sedimentology, behavior, and hazards of debris flows at Mount Rainier, Washington*. Professional Paper 1547, U.S. Geological Survey. → page 22

Simoni, A., Mammoliti, M., & Berti, M. (2011). Uncertainty of debris flow mobility relationships and its influence on the prediction of inundated areas. *Geomorphology*, *132*(3-4), 249–259, https://doi.org/10.1016/j.geomorph.2011.05.013. → pages 35, 37

Slingerland, R. & Smith, N. D. (1998). Necessary conditions for a meandering-river avulsion. *Geology*, *26*(5), 435–438, https://doi.org/10.1130/0091-7613(1998)026⟨0435:NCFAMR⟩2.3.CO;2. → page 27

Stouthamer, E. & Berendsen, H. J. (2007). Avulsion: the relative roles of autogenic and allogenic processes. *Sedimentary Geology*, *198*(3-4), 309–325, https://doi.org/10.1016/j.sedgeo.2007.01.017. → page 23

Sturzenegger, M., Holm, K., Lau, C.-A., & Jakob, M. (2019). Semi-automated regional scale debris-flow and debris-flood susceptibility mapping based on digital elevation model metrics and Flow-R software. In J. Kean, J. Coe, P. Santi, & B. Guillen (Eds.), *Debris-Flow Hazards Mitigation: Mechanics, Prediction, and Assessment* (pp. 855–862). Golden, CO. → page 2

Sutton, E. (2011). Influence of Hydrometeorological Controls on Debris Flows Near Chilliwack, British Columbia. Master's thesis, Simon Fraser University, Vancouver, BC. → page 42

Suwa, H., Okano, K., & Kanno, T. (2009). Behavior of debris flows monitored on test slopes of Kamikamihorizawa Creek, Mount Yakedake, Japan. *International Journal of Erosion Control Engineering*, *2*(2), 33–45, https://doi.org/10.13101/ijece.2.33. → pages 103, 105

Suwa, H., Okano, K., & Kanno, T. (2011). Forty years of debris flow monitoring at Kamikamihorizawa Creek, Mount Yakedake, Japan. In R. Genevois, D. Hamilton, & A. Prestininzi (Eds.), *Debris-Flow Hazards Mitigation: Mechanics, Prediction, and Assessment* (pp. 605–613). Padua, Italy. → pages 103, 105

Tang, C., Zhu, J., Chang, M., Ding, J., & Qi, X. (2012). An empirical–statistical model for predicting debris-flow runout zones in the Wenchuan earthquake area. *Quaternary International*, *250*, 63–73, https://doi.org/10.1016/j.quaint.2010.11.020. → pages xi, 30, 32, 131

Thompson, S. C., Clague, J. J., & Evans, S. G. (1997). Holocene Activity of the Mt. Currie Scarp, Coast Mountains, British Columbia, and Implications for its Origin. *Environmental and Engineering Geoscience*, *III*(3), 329–348, https://doi.org/10.2113/gseegeosci.III.3.329. → page 111

Tiranti, D. & Deangeli, C. (2015). Modeling of debris flow depositional patterns according to the catchment and sediment source area characteristics. *Frontiers in Earth Science*, *3*, 8, https://doi.org/10.3389/feart.2015.00008. → page 21

Tucker, C. J. (1979). Red and photographic infrared linear combinations for monitoring vegetation. *Remote Sensing of Environment*, *8*(2), 127–150,

https://doi.org/10.1016/0034-4257(79)90013-0. → page 54

Törnqvist, T. & S. Bridge, J. (2002). Spatial variation of overbank aggradation rate and its influence on avulsion frequency. *Sedimentology*, *49*, 891–905, https://doi.org/10.1046/j.1365-3091.2002.00478.x. → page 27

van Westen, C. J., Castellanos, E., & Kuriakose, S. L. (2008). Spatial data for landslide susceptibility, hazard, and vulnerability assessment: An overview. *Engineering Geology*, *102*(3), 112–131, https://doi.org/10.1016/j.enggeo.2008.03.010. → page 54

VanDine, D. F. (1985). Debris flows and debris torrents in the Southern Canadian Cordillera. *Canadian Geotechnical Journal*, *22*(1), 44–68, https://doi.org/10.1139/t85-006. → pages 9, 12, 42

Walker, I. R. & Pellatt, M. G. (2003). Climate Change in Coastal British Columbia — A Paleoenvironmental Perspective. *Canadian Water Resources Journal*, *28*(4), 531–566, https://doi.org/10.4296/cwrj2804531. → page 5

Webb, R. H., Magirl, C. S., Griffiths, P. G., & Boyer, D. E. (2008). *Debris Flows and Floods in Southeastern Arizona from Extreme Precipitation in July 2006-Magnitude, Frequency, and Sediment Delivery*. Open-File Report 2008-1274, U.S. Geological Survey, Reston, Virginia. → page 33

Whipple, K. X. (1992). Predicting debris-flow runout and deposition on fans: the importance of the flow hydrograph. In *Erosion, Debris-Flows and Environment in Mountain Regions: Proceedings of the Chengdu Symposium. International Association of Hydrological Sciences*, volume 209 (pp. 337–345). → page 20

Whipple, K. X. & Dunne, T. (1992). The influence of debris-flow rheology on fan morphology, Owens Valley, California. *Geological Society of America Bulletin*, *104*(7), 887–900, https://doi.org/10.1130/0016-7606(1992)104⟨0887:TIODFR⟩2.3.CO;2. → pages 12, 21, 22, 24, 90, 116, 120

Wilford, D., Sakals, M., Innes, J., Sidle, R., & Bergerud, W. (2004). Recognition of debris flow, debris flood and flood hazard through watershed morphometrics. *Landslides*, *1*, 61–66, https://doi.org/10.1007/s10346-003-0002-0. → pages xiii, 13, 74, 80, 81, 130, 131

Williams, R. M. E., Zimbelman, J. R., & Johnston, A. K. (2006). Aspects of alluvial fan shape indicative of formation process: A case study in southwestern California with application to Mojave Crater fans on Mars. *Geophysical Research Letters*, *33*(10), https://doi.org/10.1029/2005GL025618. → pages 78, 132

Wilson, A. (2019). *Glaciovolcanism in the Garibaldi volcanic belt: supplementary material*. Ph.D Thesis, University of British Columbia, Vancouver, BC. https://doi.org/10.14288/1.0388500. → pages xi, 6

Wood, W. F. & Snell, J. (1960). *A Quantitative System for Classifying Landforms*. U.S. Army Techical Report EP-124, Quartermaster Research & Engineering Command. → page 77

Yu, F.-C., Chen, C.-Y., Chen, T.-C., Hung, F.-Y., & Lin, S.-C. (2006). A GIS Process for Delimitating Areas Potentially Endangered by Debris Flow. *Natural Hazards*, *37*(1-2), 169–189, https://doi.org/10.1007/s11069-005-4666-8. → pages 32, 33

Zhang, S., Zhang, L.-M., Chen, H.-X., Yuan, Q., & Pan, H. (2013). Changes in runout distances of debris flows over time in the Wenchuan earthquake zone. *Journal of Mountain Science*, *10*(2), 281–292, https://doi.org/10.1007/s11629-012-2506-y. → pages 22, 23

Zhou, W., Fang, J., Tang, C., & Yang, G. (2019). Empirical relationships for the estimation of debris flow runout distances on depositional fans in the Wenchuan earthquake zone. *Journal of*

Hydrology, *577*, https://doi.org/10.1016/j.jhydrol.2019.123932. → pages 32, 37

Zimmermann, M., Mani, M., Gamma, P., Gsteiger, P., Heiniger, O., & Hunziker, G. (1997). *Murganggefahr und Klimaänderung - ein GIS-basierter Ansatz.* Zürich: vdf Hochschulverlag AG, 1st edition. (in German). → pages 31, 131

Zubrycky, S., Mitchell, A., Aaron, J., & McDougall, S. (2019). Preliminary calibration of a numerical runout model for debris flows in southwestern British Columbia. In J. Kean, J. Coe, P. Santi, & B. Guillen (Eds.), *Debris-Flow Hazards Mitigation: Mechanics, Prediction, and Assessment* (pp. 911–918). Golden, CO. → pages xi, 20, 132

Appendix A

Fan Site Summaries

A one page data summary is provided for each fan in the dataset, including impact area mapping, fan site descriptor variables, spatial impact heatmaps, cumulative runout exceedance distributions, and field photographs (if available).

Site 1: Abandoned

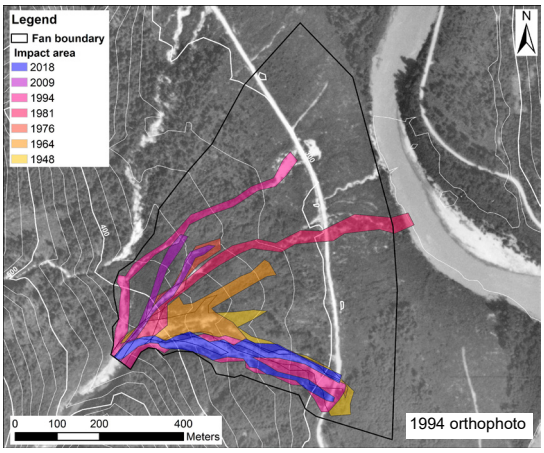

Easting (m)	461334
Northing (m)	5558054
No. impact areas:	7
No. events:	2
Normalizing fan length (m):	910
Normalizing fan arc-length (m):	943
Normalizing fan angle (°)	82
Watershed area (km^2):	2.68
Melton ratio:	0.99
Fan area (km^2):	0.41
Fan slope (°):	12.2
Average channel slope (°):	12.8
Fan ERR:	0.23
Normalized intersection point:	-
Truncated:	Yes
Bedrock geology:	Intrusive

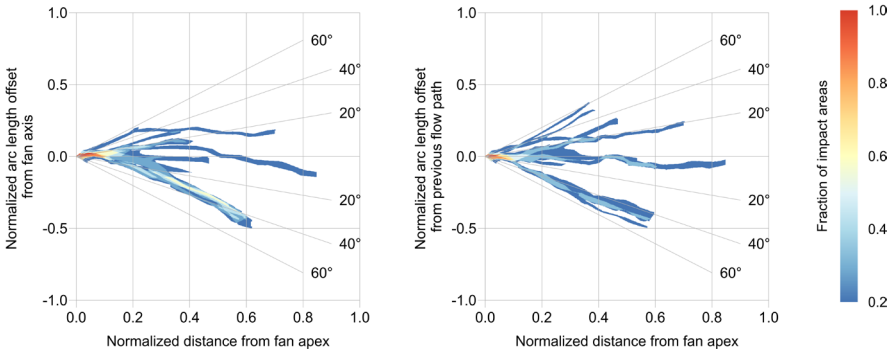

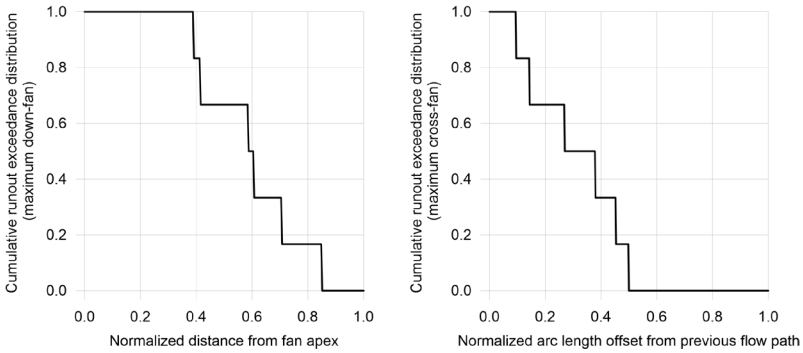

Site 2: Endurance

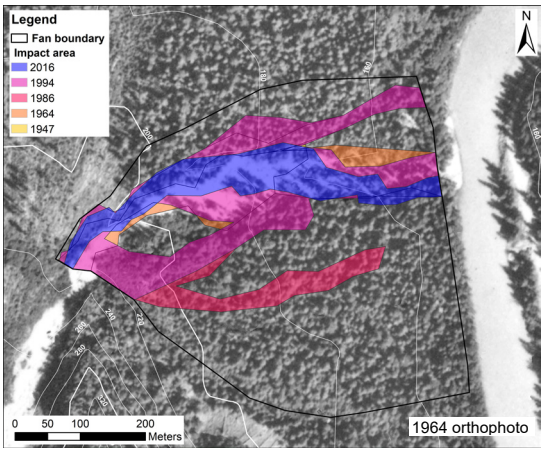

Easting (m)	473304
Northing (m)	5548766
No. impact areas:	5
No. events:	3
Normalizing fan length (m):	637
Normalizing fan arc-length (m):	555
Normalizing fan angle (°)	69
Watershed area (km^2):	8.68
Melton ratio:	0.66
Fan area (km^2):	0.23
Fan slope (°):	7.4
Average channel slope (°):	7.3
Fan ERR:	0.42
Normalized intersection point:	-
Truncated:	Yes
Bedrock geology:	Intrusive

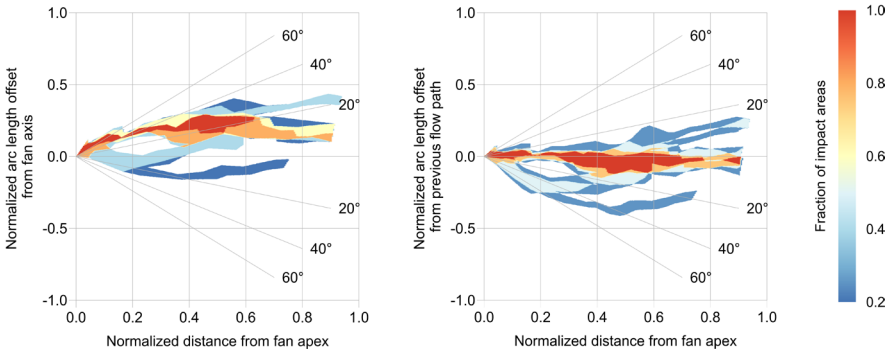

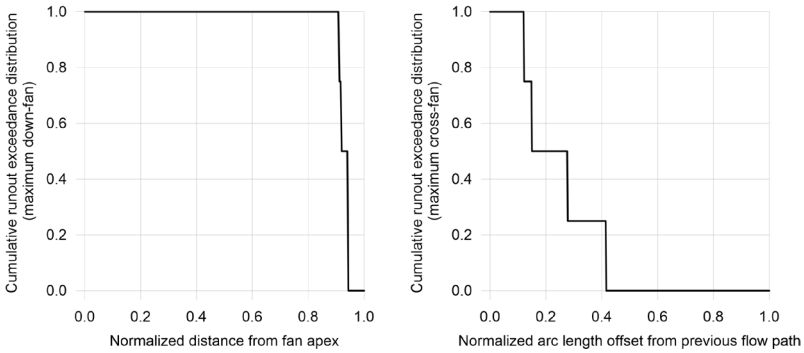

Site 3: Terminal

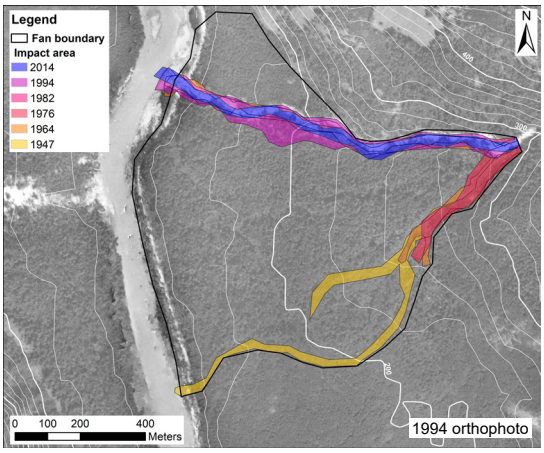

Easting (m)	475132
Northing (m)	5549082
No. impact areas:	6
No. events:	3
Normalizing fan length (m):	1292
Normalizing fan arc-length (m):	1199
Normalizing fan angle (°)	75
Watershed area (km^2):	9.49
Melton ratio:	0.68
Fan area (km^2):	0.78
Fan slope (°):	7.2
Average channel slope (°):	7.2
Fan ERR:	0.38
Normalized intersection point:	0.83
Truncated:	Yes
Bedrock geology:	Volcanic

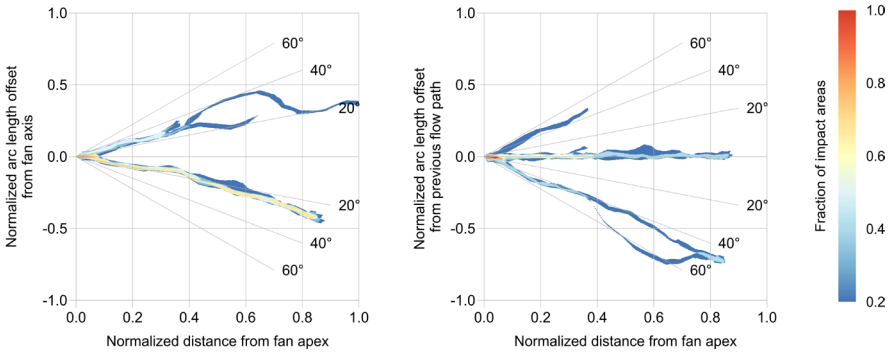

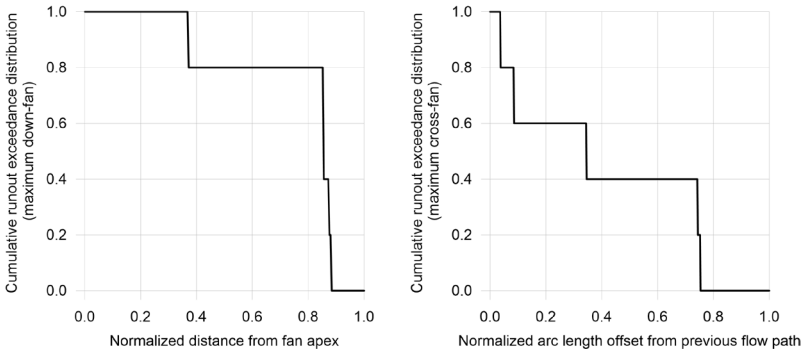

Northern channel at the fan toe, looking up-fan. Photo provided by Lauren Vincent.

Northern channel at the fan toe, looking down-fan toward Squamish River. Photo provided by Lauren Vincent.

Site 4: Middle Lillooet W

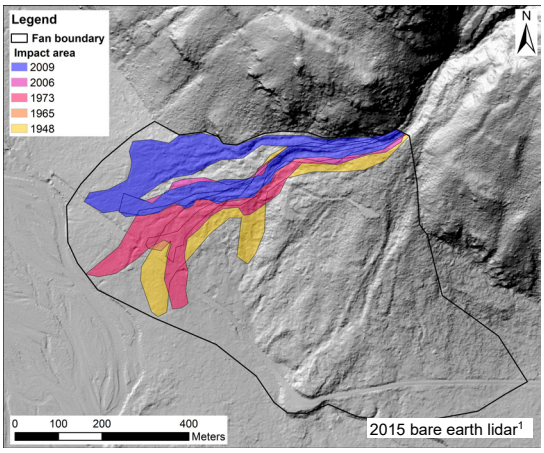

Easting (m)	474226
Northing (m)	5606122
No. impact areas:	5
No. events:	2
Normalizing fan length (m):	832
Normalizing fan arc-length (m):	1334
Normalizing fan angle (°)	115
Watershed area (km^2):	2.27
Melton ratio:	1.17
Fan area (km^2):	0.47
Fan slope (°):	12.7
Average channel slope (°):	9.8
Fan ERR:	0.25
Normalized intersection point:	0.48
Truncated:	Yes
Bedrock geology:	Intrusive

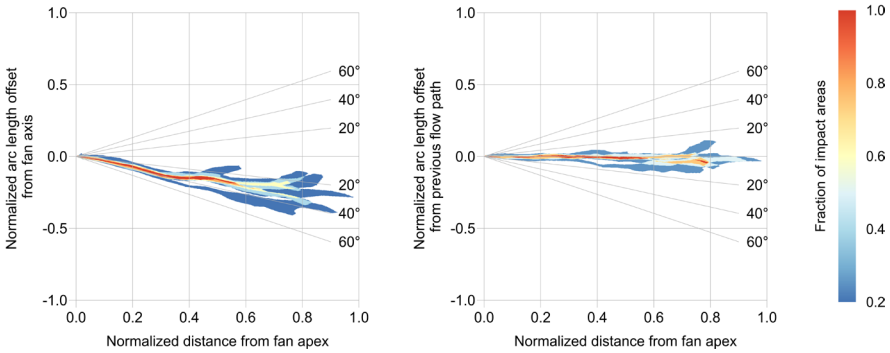

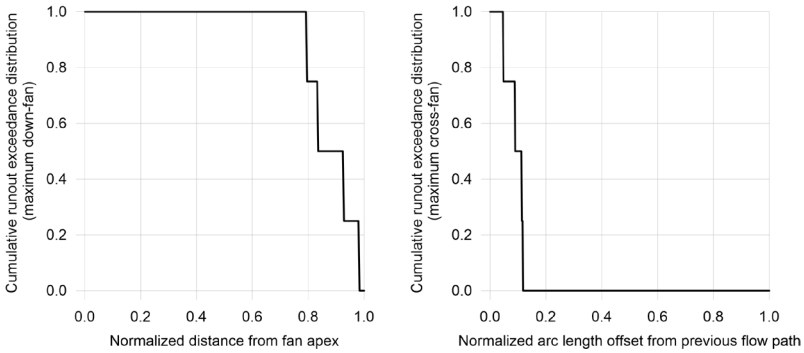

On left bank levee at fan apex looking upslope.

Debris at distal fan, upslope of logging road.

[1]ALS courtesy of Brian Menounos (University of Northern British Columbia), John Clague, and Gioachino Roberti (Simon Fraser University).

Site 5: Middle Lillooet C

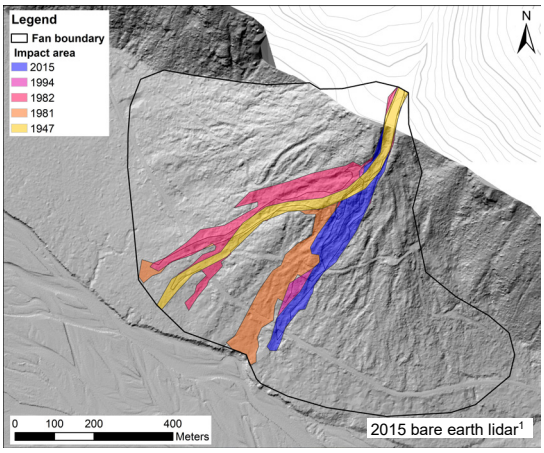

Easting (m)	475684
Northing (m)	5605380
No. impact areas:	5
No. events:	4
Normalizing fan length (m):	870
Normalizing fan arc-length (m):	1310
Normalizing fan angle (°)	112
Watershed area (km^2):	2.68
Melton ratio:	1.11
Fan area (km^2):	0.59
Fan slope (°):	13.7
Average channel slope (°):	11.9
Fan ERR:	0.26
Normalized intersection point:	0.54
Truncated:	Yes
Bedrock geology:	Intrusive

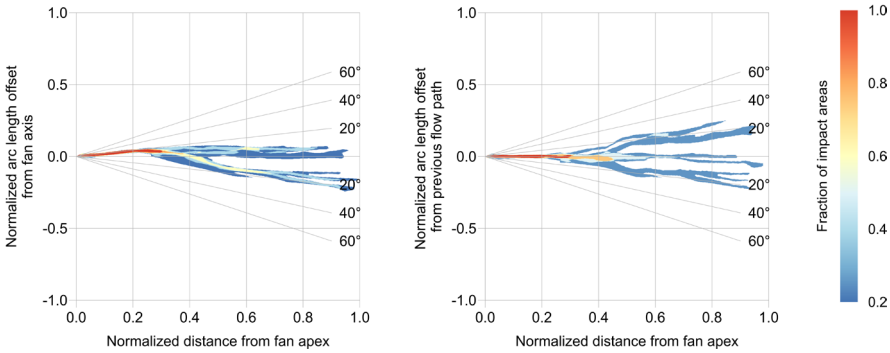

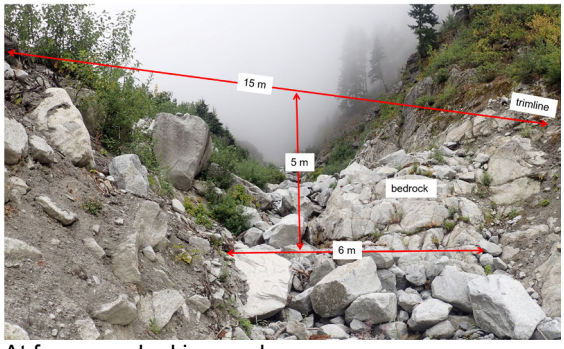

At fan apex, looking upslope.

Debris path on lower fan, overlooking Lillooet river valley.

[1]ALS courtesy of Brian Menounos (University of Northern British Columbia), John Clague, and Gioachino Roberti (Simon Fraser University).

Site 6: Middle Lillooet E

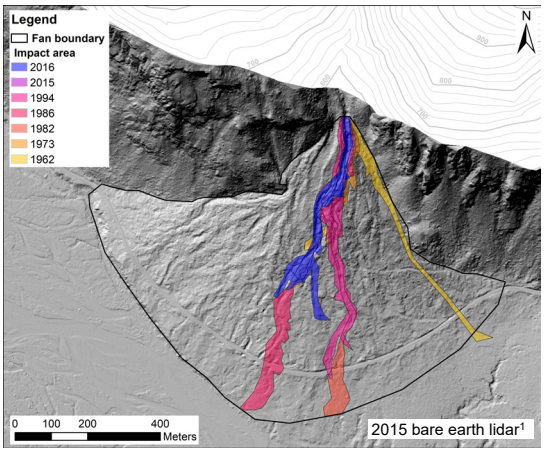

Easting (m)	477147
Northing (m)	5604529
No. impact areas:	7
No. events:	5
Normalizing fan length (m):	810
Normalizing fan arc-length (m):	1287
Normalizing fan angle (°)	115
Watershed area (km^2):	2.84
Melton ratio:	1.08
Fan area (km^2):	0.52
Fan slope (°):	13.1
Average channel slope (°):	12.5
Fan ERR:	0.27
Normalized intersection point:	0.58
Truncated:	Yes
Bedrock geology:	Intrusive

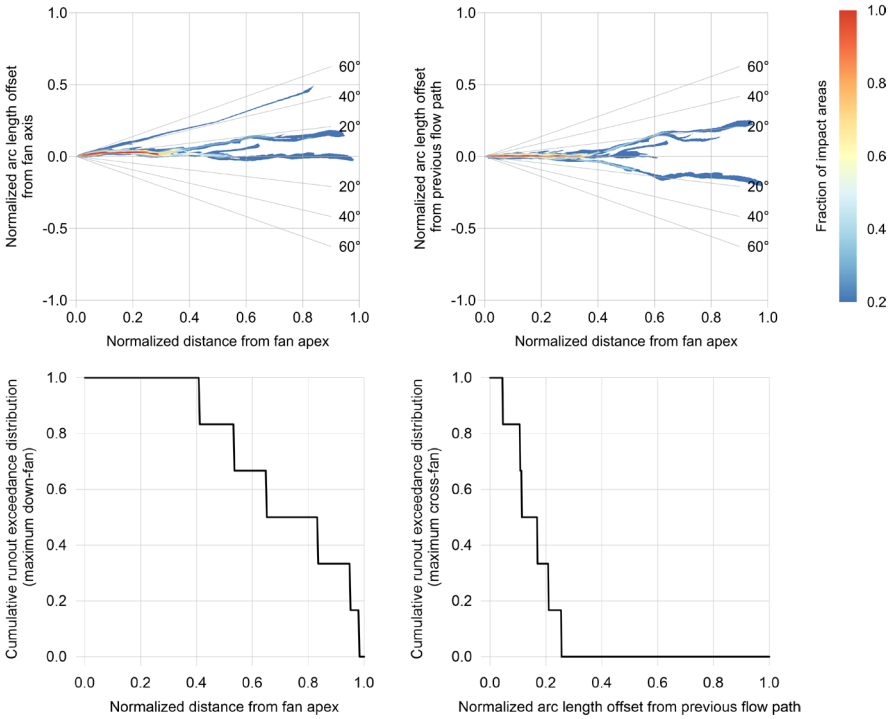

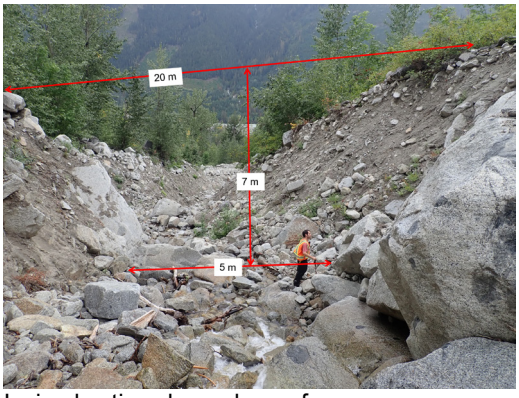

Incised active channel near fan apex.

Levee and mud line, mid-fan.

[1]ALS courtesy of Brian Menounos (University of Northern British Columbia), John Clague, and Gioachino Roberti (Simon Fraser University).

Site 7: Petersen

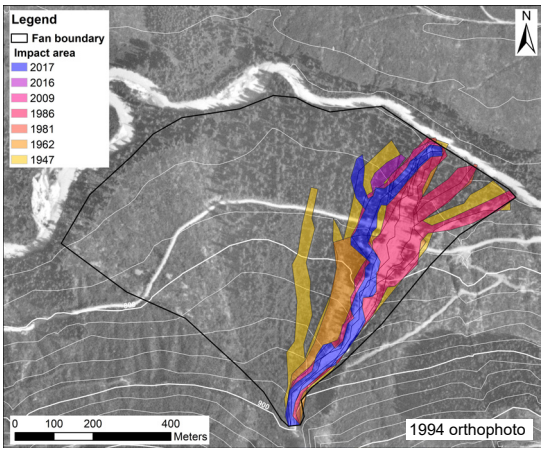

Easting (m)	488876
Northing (m)	5589224
No. impact areas:	7
No. events:	3
Normalizing fan length (m):	849
Normalizing fan arc-length (m):	1266
Normalizing fan angle (°)	95
Watershed area (km^2):	8.20
Melton ratio:	0.48
Fan area (km^2):	0.53
Fan slope (°):	10.7
Average channel slope (°):	10.7
Fan ERR:	0.28
Normalized intersection point:	-
Truncated:	Yes
Bedrock geology:	Intrusive

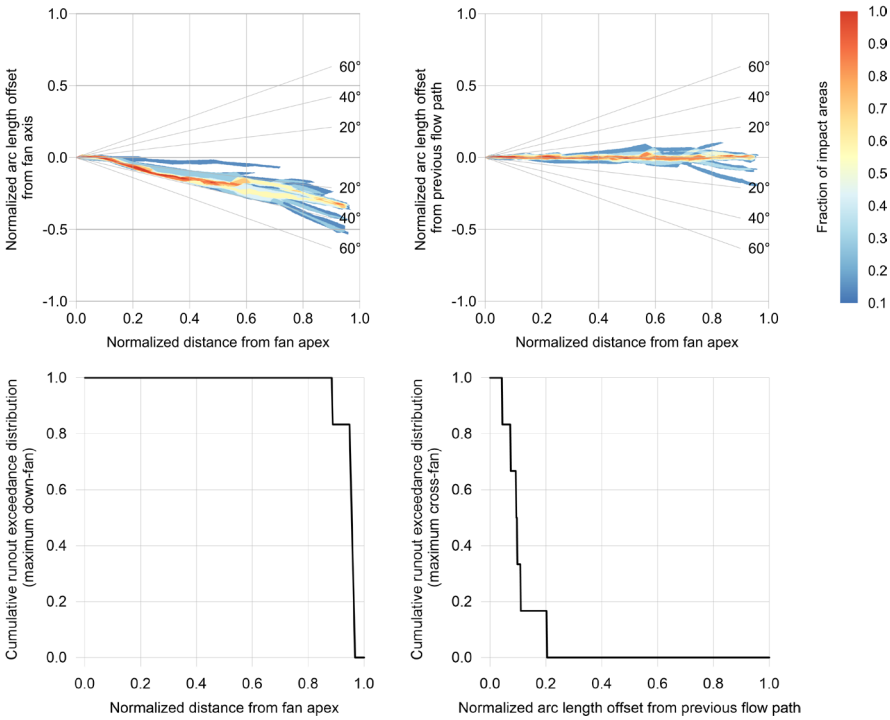

Site 8: Upper Rutherford

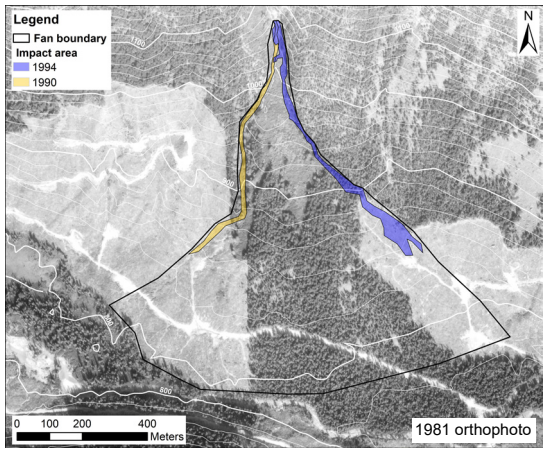

Easting (m)	498423
Northing (m)	5571312
No. impact areas:	2
No. events:	1
Normalizing fan length (m):	1206
Normalizing fan arc-length (m):	1168
Normalizing fan angle (°)	66
Watershed area (km^2):	2.72
Melton ratio:	0.88
Fan area (km^2):	0.59
Fan slope (°):	12.6
Average channel slope (°):	12.6
Fan ERR:	0.21
Normalized intersection point:	-
Truncated:	Yes
Bedrock geology:	Intrusive

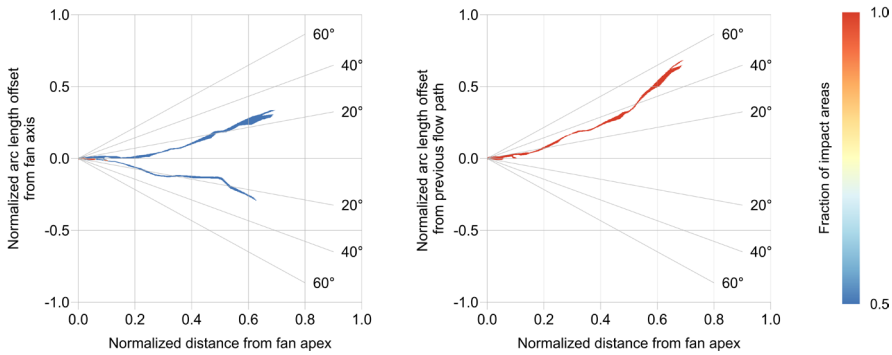

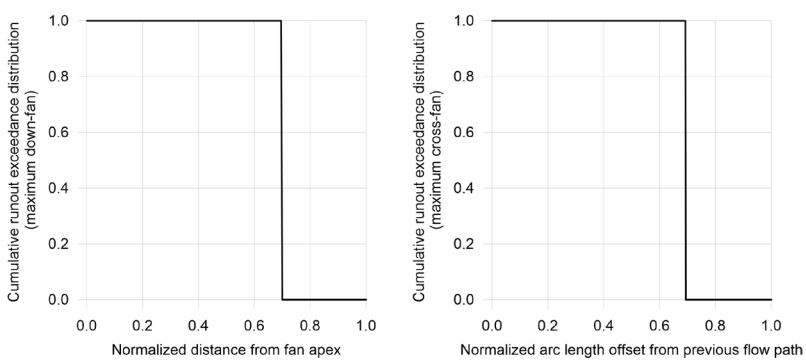

Lobe near fan apex, west of active channel.

Active channel on eastern side of lower fan.

Site 9: No Law

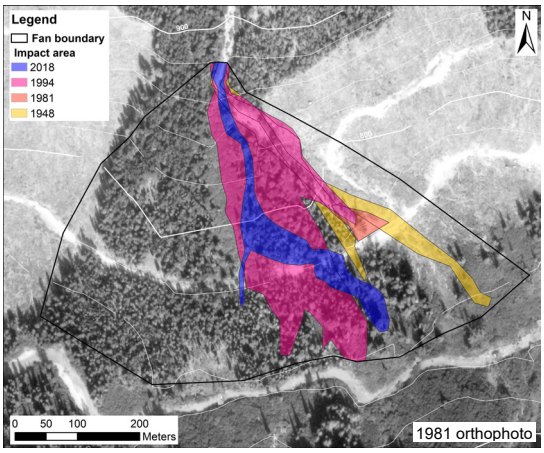

Easting (m)	500317
Northing (m)	5570349
No. impact areas:	4
No. events:	3
Normalizing fan length (m):	587
Normalizing fan arc-length (m):	790
Normalizing fan angle (°)	91
Watershed area (km^2):	3.37
Melton ratio:	0.89
Fan area (km^2):	0.24
Fan slope (°):	12.9
Average channel slope (°):	11.2
Fan ERR:	0.29
Normalized intersection point:	0.95
Truncated:	Yes
Bedrock geology:	Intrusive

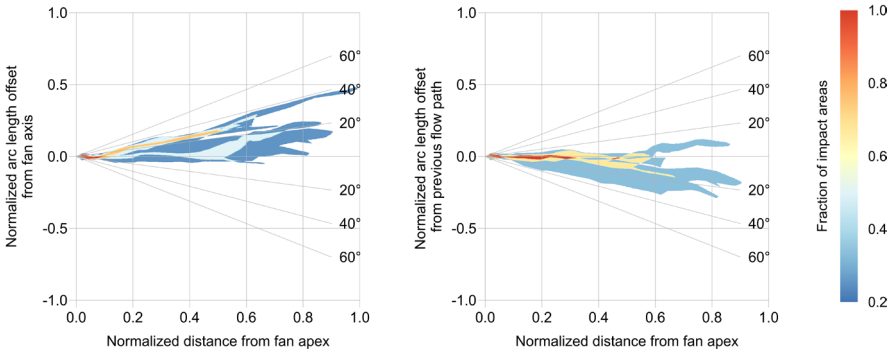

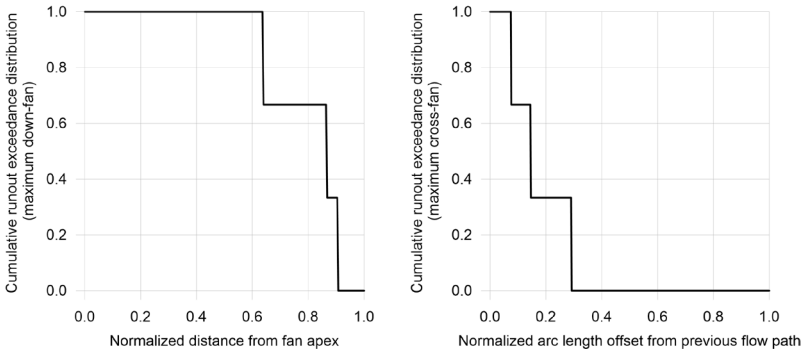

Debris on upper fan, looking upslope toward apex.

Debris field upslope of logging road, mid-fan.

Site 10: Sootip

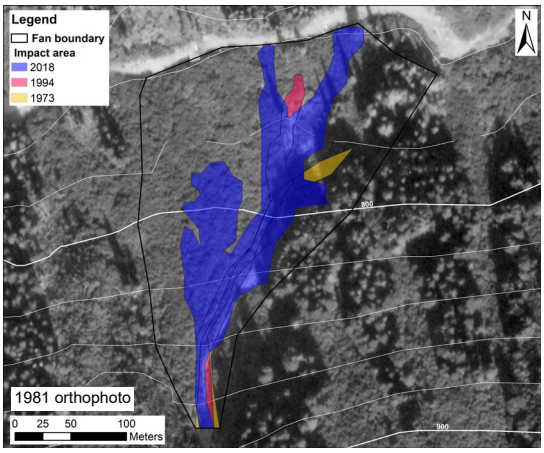

Easting (m)	500332
Northing (m)	5569470
No. impact areas:	3
No. events:	2
Normalizing fan length (m):	387
Normalizing fan arc-length (m):	240
Normalizing fan angle (°)	43
Watershed area (km^2):	0.83
Melton ratio:	1.26
Fan area (km^2):	0.05
Fan slope (°):	17.2
Average channel slope (°):	16.2
Fan ERR:	0.32
Normalized intersection point:	-
Truncated:	Yes
Bedrock geology:	Volcanic

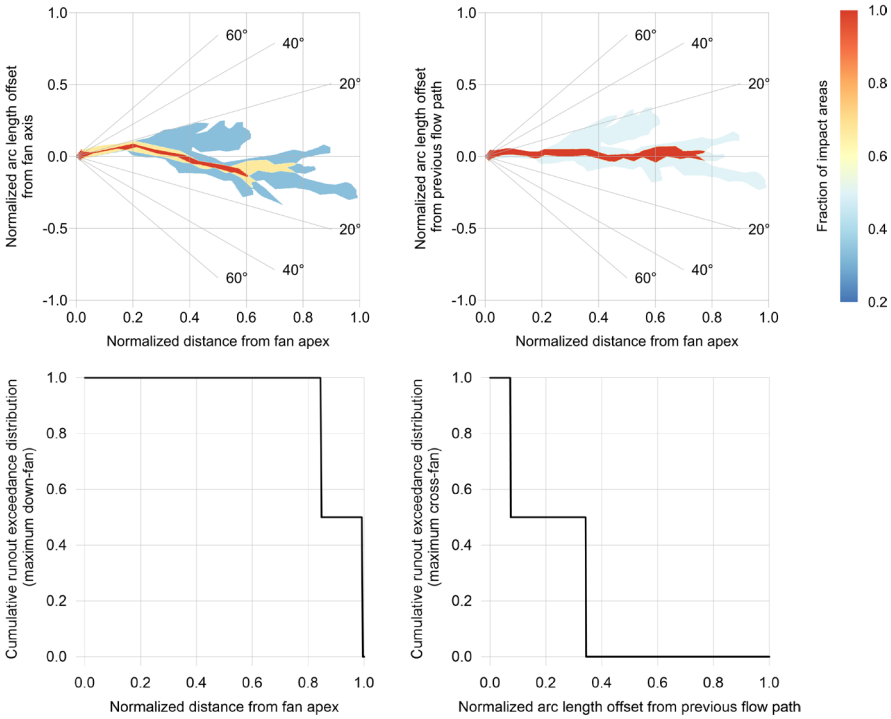

Overlooking avulsion lobe and watershed.
Photograph taken from opposite side of valley.

Site 11: Lower Rutherford W

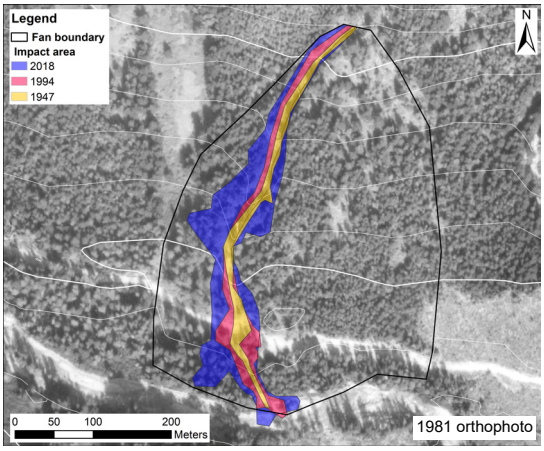

Easting (m)	503650
Northing (m)	5570723
No. impact areas:	3
No. events:	2
Normalizing fan length (m):	508
Normalizing fan arc-length (m):	375
Normalizing fan angle (°)	57
Watershed area (km^2):	2.02
Melton ratio:	1.04
Fan area (km^2):	0.14
Fan slope (°):	16.0
Average channel slope (°):	15.9
Fan ERR:	0.36
Normalized intersection point:	0.72
Truncated:	Yes
Bedrock geology:	Intrusive

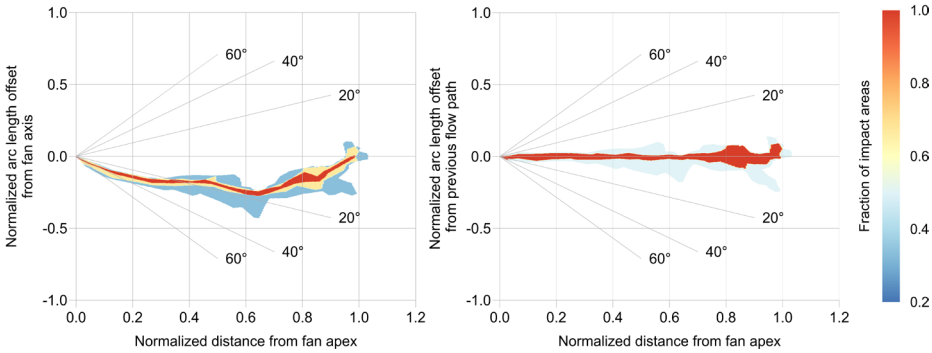

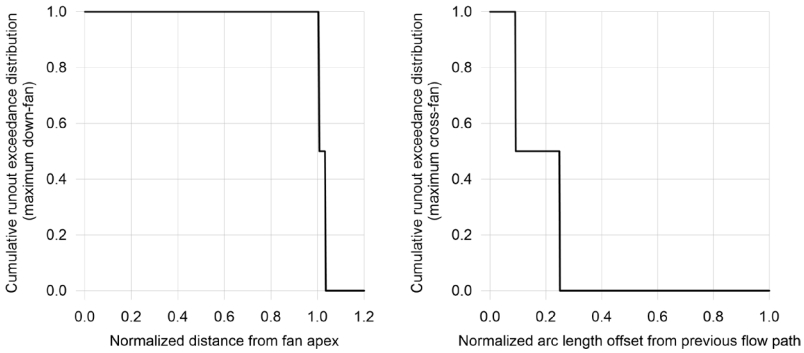

Boulder levee on upper fan, looking upslope.

Megaclast from 2018 event, upslope of logging road on lower fan.

Site 12: Lower Rutherford E

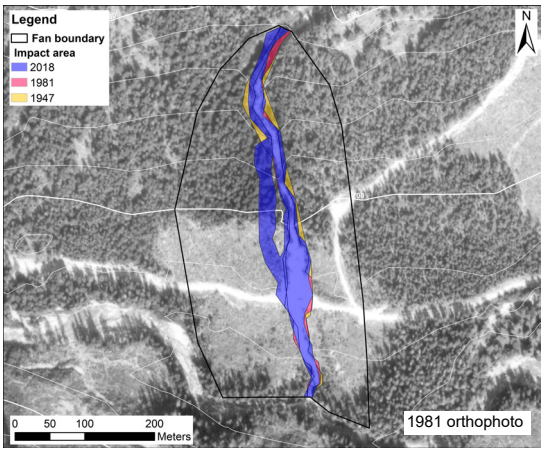

Easting (m)	503916
Northing (m)	5570658
No. impact areas:	3
No. events:	2
Normalizing fan length (m):	587
Normalizing fan arc-length (m):	268
Normalizing fan angle (°)	50
Watershed area (km^2):	1.45
Melton ratio:	1.12
Fan area (km^2):	0.12
Fan slope (°):	13.6
Average channel slope (°):	13.2
Fan ERR:	0.40
Normalized intersection point:	0.88
Truncated:	Yes
Bedrock geology:	Intrusive

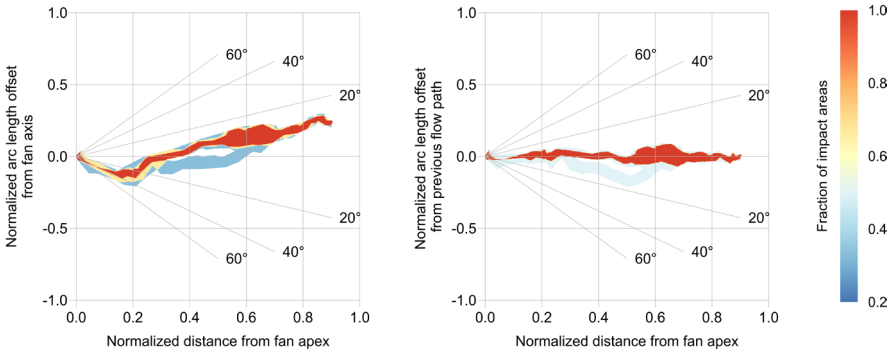

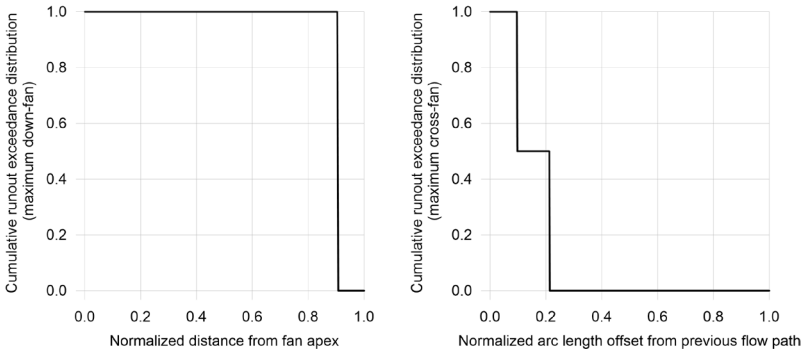

At fan apex looking downslope.

Bouldery channel plug on upper fan.

Site 13: Ross

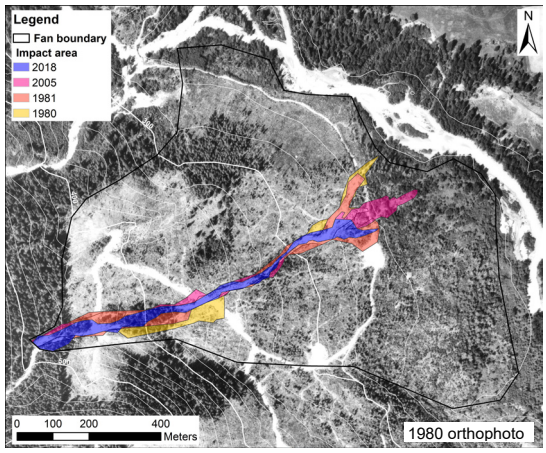

Easting (m)	503460
Northing (m)	5587279
No. impact areas:	4
No. events:	4
Normalizing fan length (m):	1348
Normalizing fan arc-length (m):	1098
Normalizing fan angle (°)	69
Watershed area (km^2):	5.79
Melton ratio:	0.78
Fan area (km^2):	0.81
Fan slope (°):	10.4
Average channel slope (°):	11.3
Fan ERR:	0.26
Normalized intersection point:	0.74
Truncated:	Yes
Bedrock geology:	Intrusive

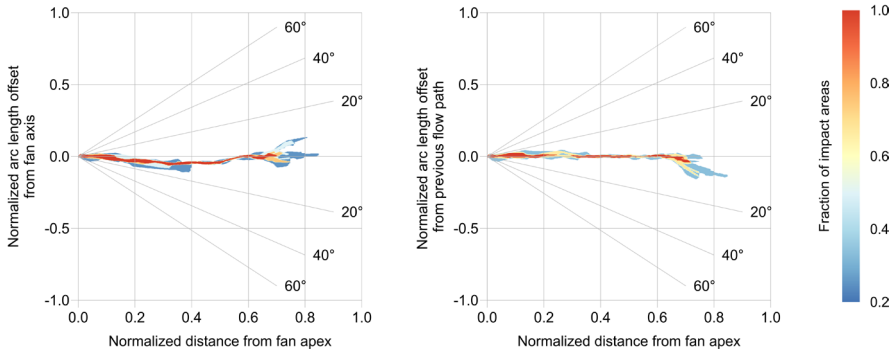

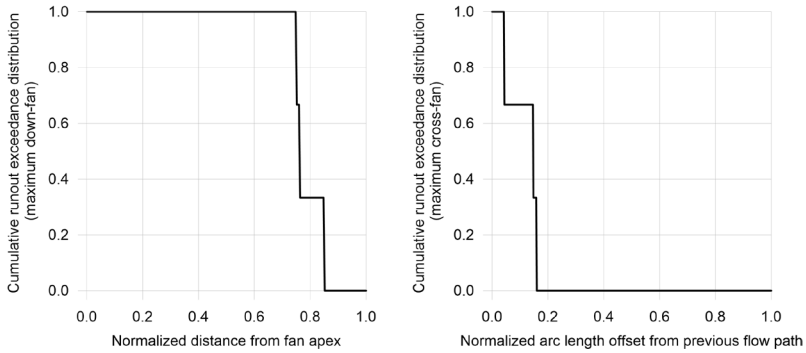

Debris path on upper fan.

Fine-grained deposits on distal fan.

Site 14: Nightmare

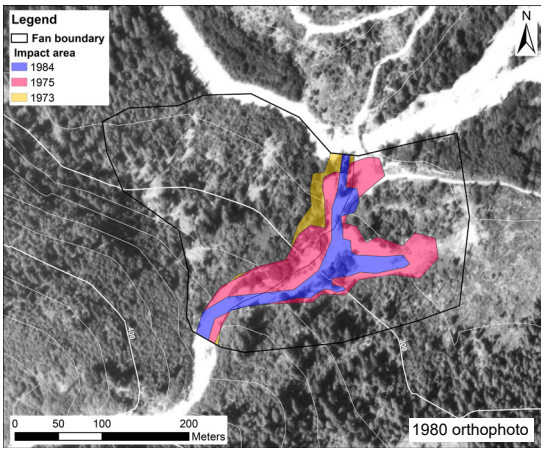

Easting (m)	503560
Northing (m)	5587870
No. impact areas:	3
No. events:	2
Normalizing fan length (m):	377
Normalizing fan arc-length (m):	501
Normalizing fan angle (°)	111
Watershed area (km^2):	1.46
Melton ratio:	1.47
Fan area (km^2):	0.09
Fan slope (°):	16.8
Average channel slope (°):	15.6
Fan ERR:	0.40
Normalized intersection point:	0.62
Truncated:	Yes
Bedrock geology:	Intrusive

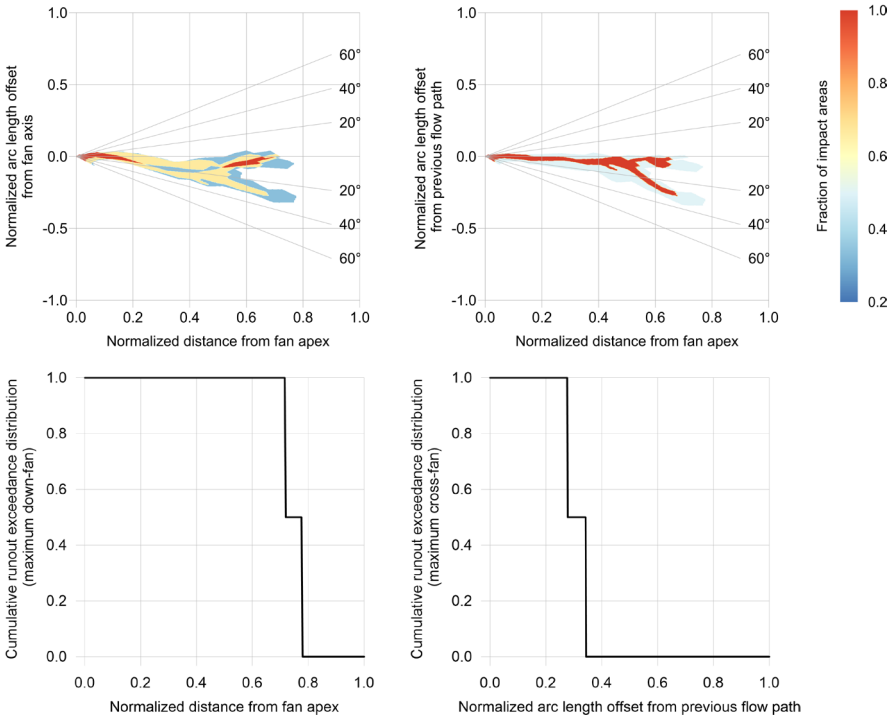

Overgrown lobe on lower fan.

Site 15: Fergusson

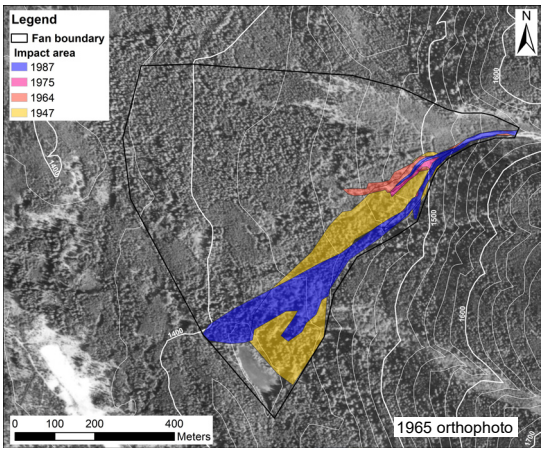

Easting (m)	515823
Northing (m)	5625672
No. impact areas:	4
No. events:	2
Normalizing fan length (m):	990
Normalizing fan arc-length (m):	974
Normalizing fan angle (°)	60
Watershed area (km^2):	1.36
Melton ratio:	0.87
Fan area (km^2):	0.46
Fan slope (°):	10.6
Average channel slope (°):	10.5
Fan ERR:	0.26
Normalized intersection point:	-
Truncated:	No
Bedrock geology:	Sedimentary

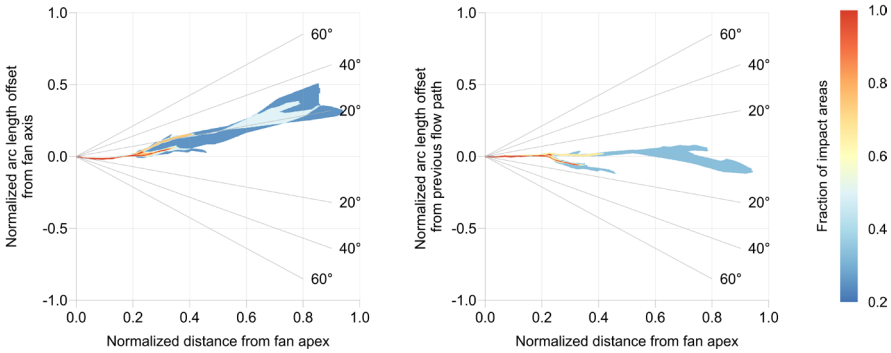

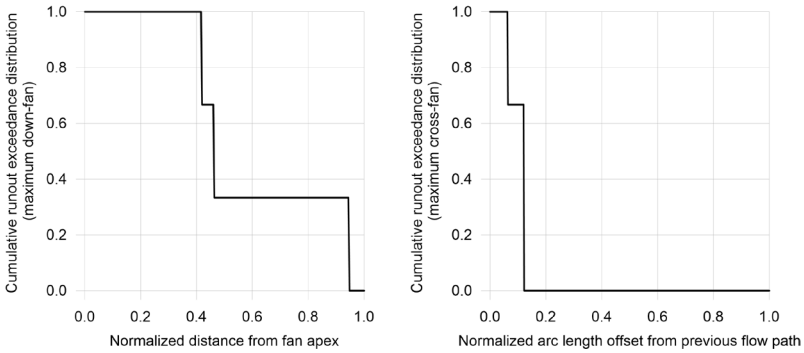

Site 16: Currie B

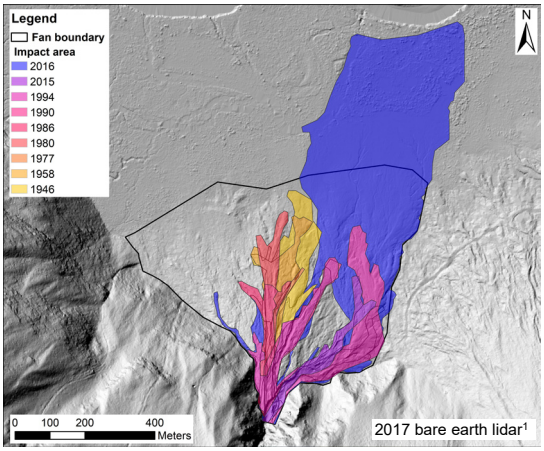

Easting (m)	515965
Northing (m)	5570375
No. impact areas:	10
No. events:	6
Normalizing fan length (m):	834
Normalizing fan arc-length (m):	865
Normalizing fan angle (°)	76
Watershed area (km^2):	2.70
Melton ratio:	1.30
Fan area (km^2):	0.36
Fan slope (°):	10.7
Average channel slope (°):	8.2
Fan ERR:	0.25
Normalized intersection point:	0.32
Truncated:	No
Bedrock geology:	Intrusive

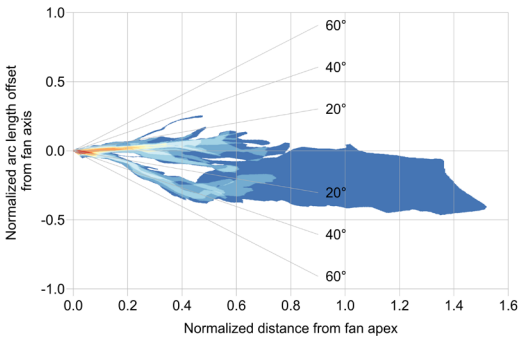

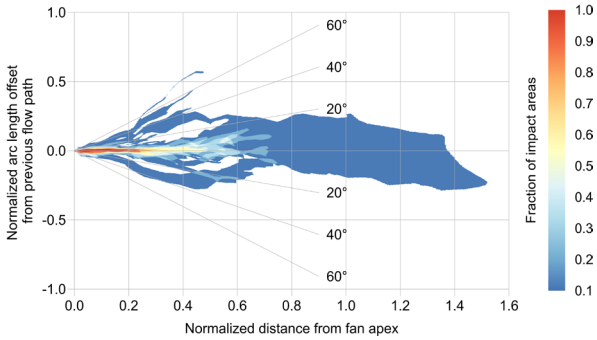

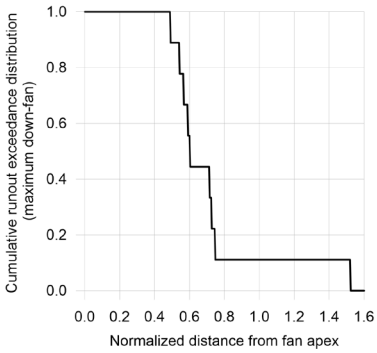

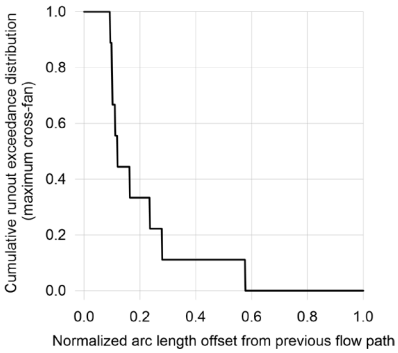

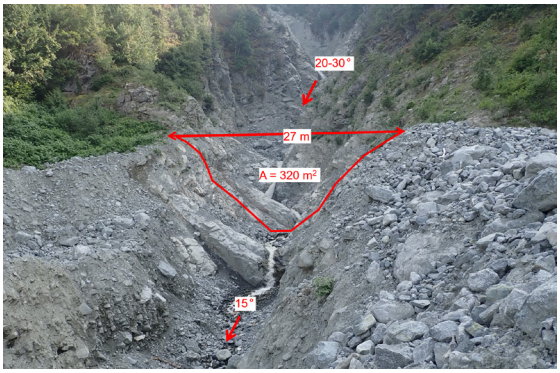

Looking upstream at fan apex.

Recent debris contact with mossy lobe, mid fan looking down slope.

[1]ALS courtesy of Squamish Lillooet Regional District.

Site 17: Currie C

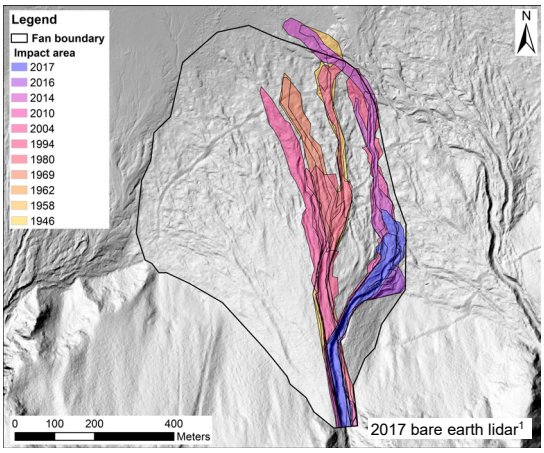

Easting (m)	516839
Northing (m)	5570140
No. impact areas:	11
No. events:	9
Normalizing fan length (m):	1045
Normalizing fan arc-length (m):	692
Normalizing fan angle (°)	58
Watershed area (km^2):	1.20
Melton ratio:	1.58
Fan area (km^2):	0.44
Fan slope (°):	17.5
Average channel slope (°):	15.8
Fan ERR:	0.32
Normalized intersection point:	0.66
Truncated:	No
Bedrock geology:	Intrusive

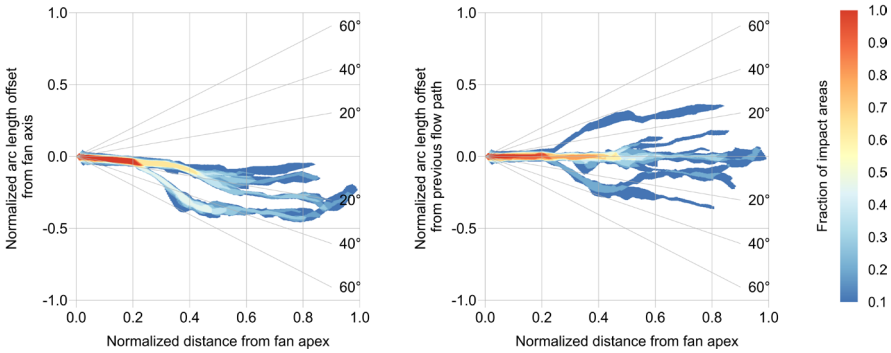

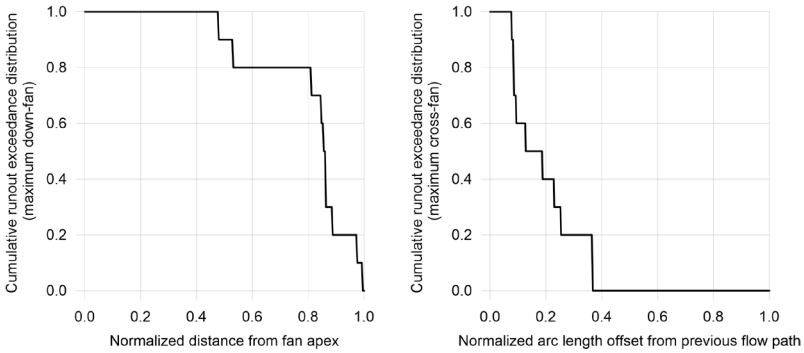

On the left bank of the incised channel near the fan apex overlooking Currie D deposits.

Paleochannel, mid fan.

[1]ALS courtesy of Squamish Lillooet Regional District.

Site 18: Currie D

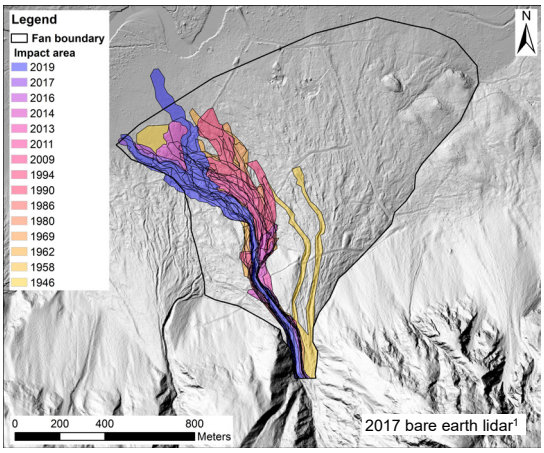

Easting (m)	517411
Northing (m)	5570114
No. impact areas:	15
No. events:	11
Normalizing fan length (m):	1655
Normalizing fan arc-length (m):	1612
Normalizing fan angle (°)	70
Watershed area (km^2):	1.66
Melton ratio:	1.14
Fan area (km^2):	1.28
Fan slope (°):	14.1
Average channel slope (°):	14.7
Fan ERR:	0.21
Normalized intersection point:	0.49
Truncated:	No
Bedrock geology:	Intrusive

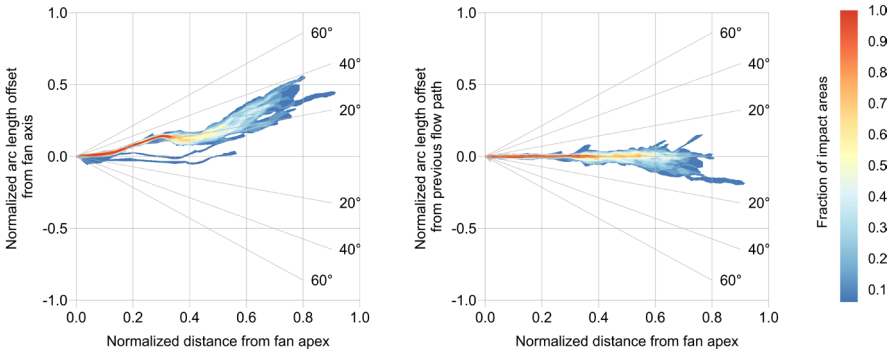

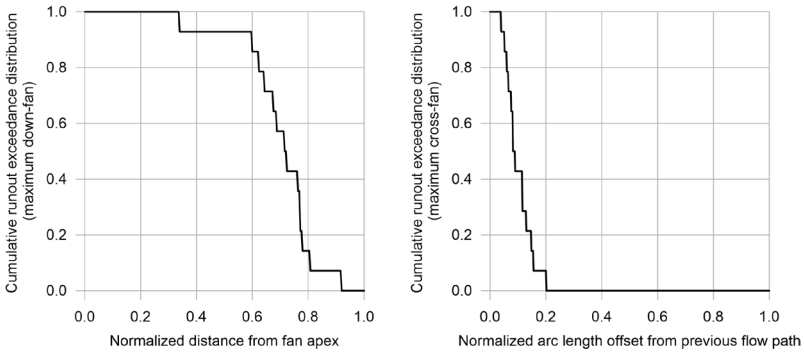

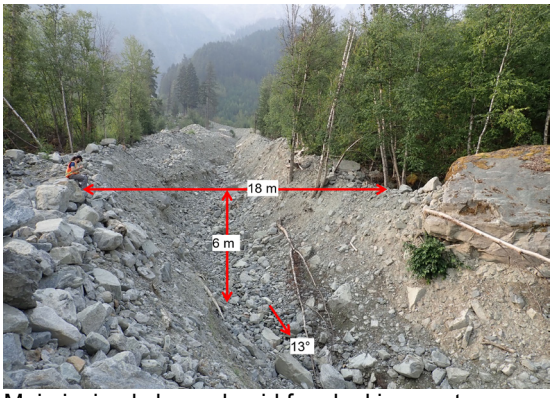

Main incised channel, mid fan, looking upstream.

Debris lobes on lower fan, looking west.

[1]ALS courtesy of Squamish Lillooet Regional District.

Site 19: Deepa

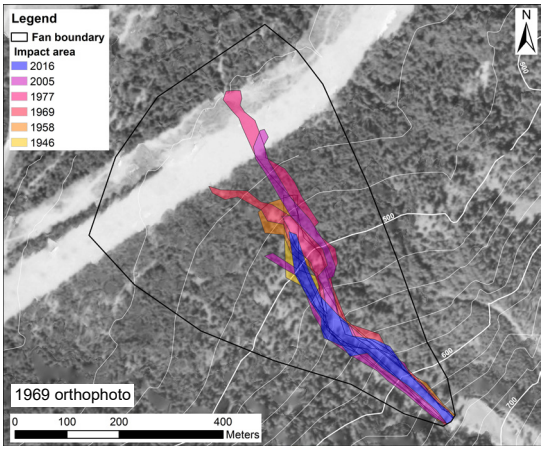

Easting (m)	523562
Northing (m)	5588576
No. impact areas:	6
No. events:	4
Normalizing fan length (m):	846
Normalizing fan arc-length (m):	549
Normalizing fan angle (°)	41
Watershed area (km^2):	1.12
Melton ratio:	1.22
Fan area (km^2):	0.29
Fan slope (°):	15.0
Average channel slope (°):	14.1
Fan ERR:	0.25
Normalized intersection point:	-
Truncated:	No
Bedrock geology:	Intrusive

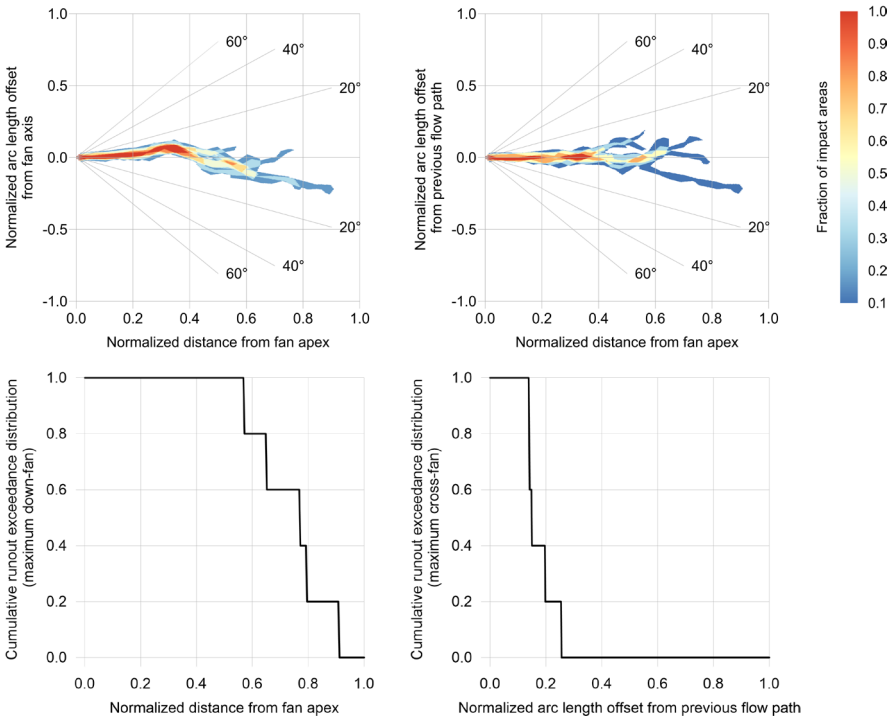

Site 20: Neff

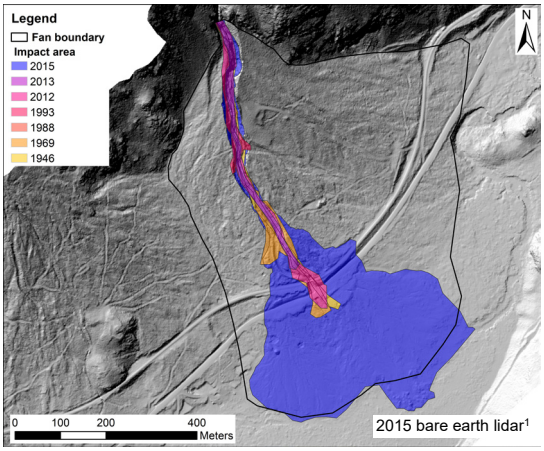

Easting (m)	529458
Northing (m)	5593780
No. impact areas:	7
No. events:	5
Normalizing fan length (m):	897
Normalizing fan arc-length (m):	824
Normalizing fan angle (°)	85
Watershed area (km^2):	3.29
Melton ratio:	1.02
Fan area (km^2):	0.42
Fan slope (°):	11.7
Average channel slope (°):	10.9
Fan ERR:	0.24
Normalized intersection point:	0.63
Truncated:	No
Bedrock geology:	Sedimentary

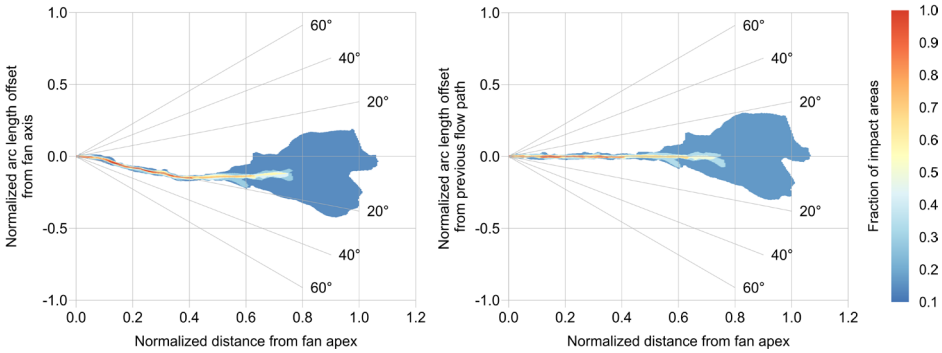

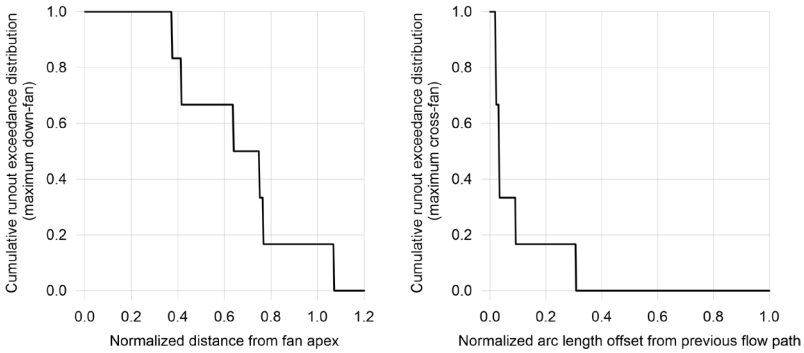

Main channel on upper fan, incised 10-12 m.

Debris on lower fan, looking southeast.

[1]ALS courtesy of BC Hydro.

Site 21: Catiline

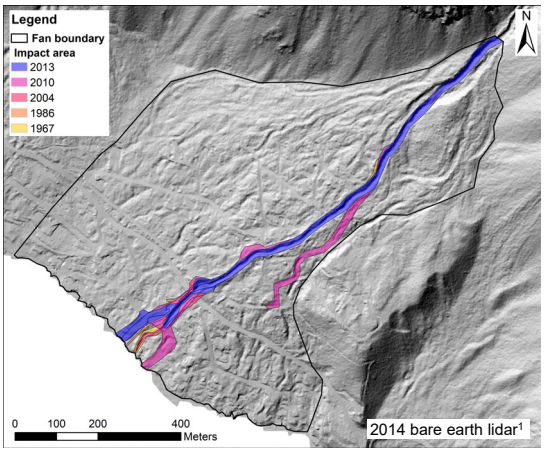

Easting (m)	535567
Northing (m)	5568500
No. impact areas:	5
No. events:	4
Normalizing fan length (m):	1278
Normalizing fan arc-length (m):	849
Normalizing fan angle (°)	46
Watershed area (km^2):	3.04
Melton ratio:	0.94
Fan area (km^2):	0.56
Fan slope (°):	14.4
Average channel slope (°):	13.8
Fan ERR:	0.32
Normalized intersection point:	0.91
Truncated:	Yes
Bedrock geology:	Intrusive

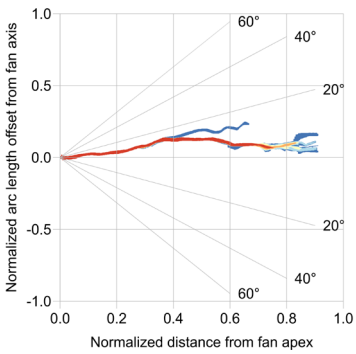

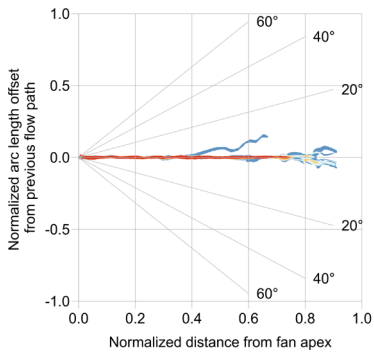

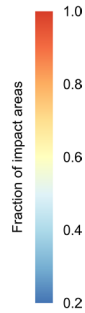

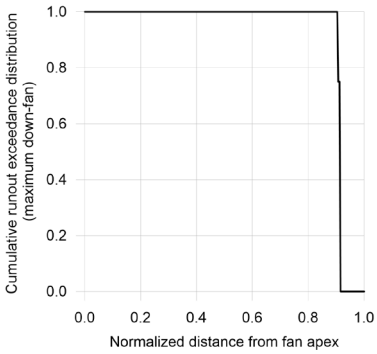

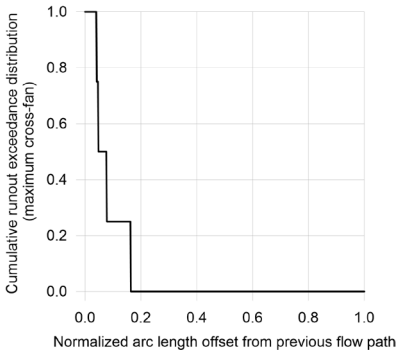

Upper fan channel plug. Photo courtesy of BGC.

Bridge on lower fan. Photo courtesy of BGC.

[1]ALS courtesy of Squamish Lillooet Regional District.

Site 22: Fern

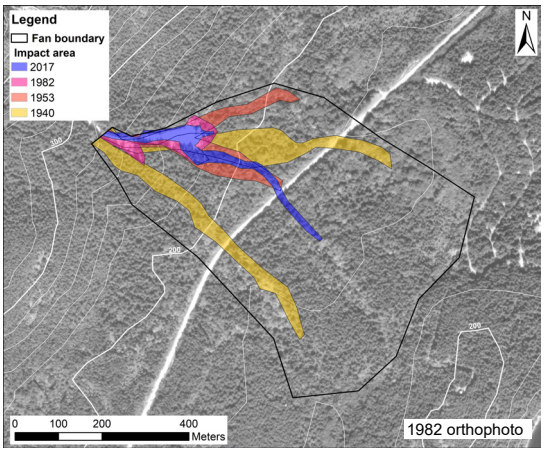

Easting (m)	537775
Northing (m)	5462900
No. impact areas:	4
No. events:	2
Normalizing fan length (m):	868
Normalizing fan arc-length (m):	636
Normalizing fan angle (°)	49
Watershed area (km^2):	0.86
Melton ratio:	1.16
Fan area (km^2):	0.35
Fan slope (°):	6.3
Average channel slope (°):	6.3
Fan ERR:	0.24
Normalized intersection point:	0.53
Truncated:	No
Bedrock geology:	Intrusive

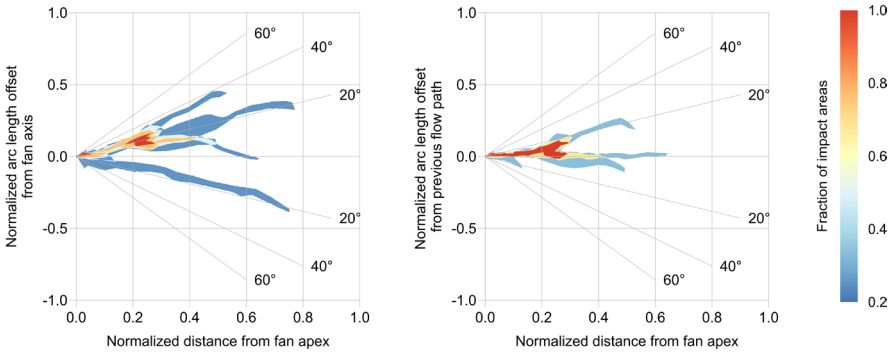

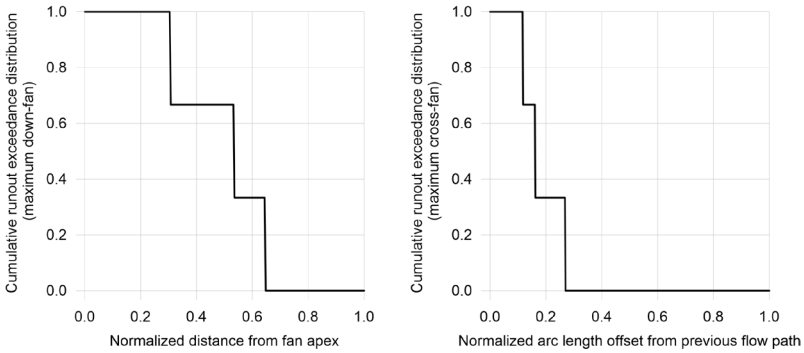

Debris on upper fan.

Debris on lower fan.

Site 23: Bear

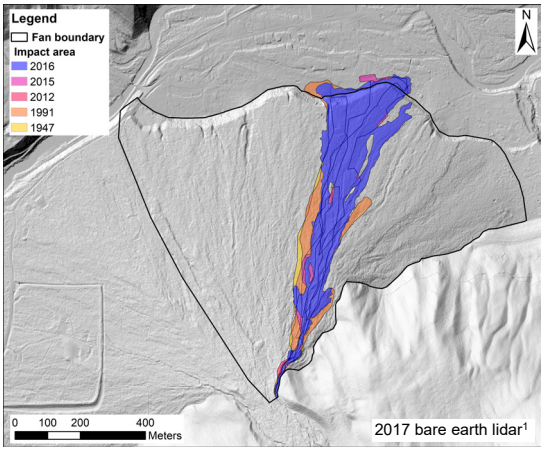

Easting (m)	550167
Northing (m)	5616375
No. impact areas:	5
No. events:	4
Normalizing fan length (m):	1030
Normalizing fan arc-length (m):	1319
Normalizing fan angle (°)	85
Watershed area (km^2):	2.20
Melton ratio:	1.22
Fan area (km^2):	0.67
Fan slope (°):	11.2
Average channel slope (°):	10
Fan ERR:	0.34
Normalized intersection point:	0.18
Truncated:	No
Bedrock geology:	Sedimentary

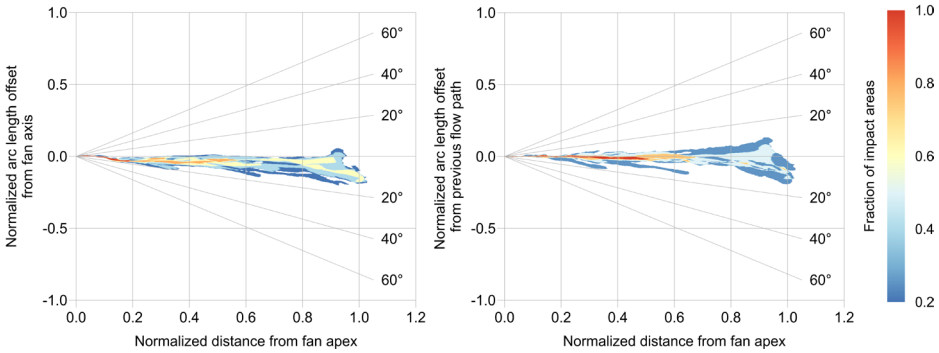

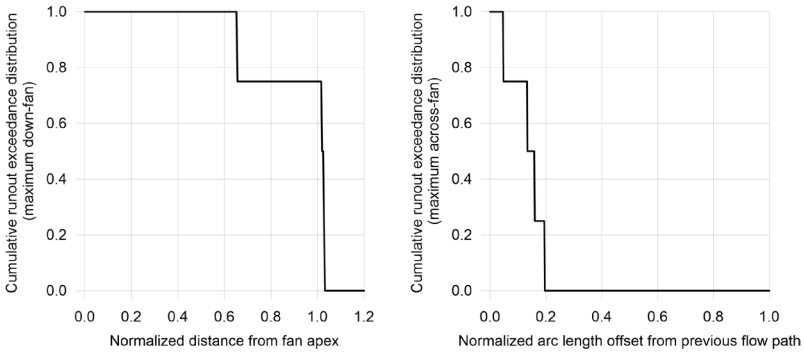

Incised channel on upper fan. Photo courtesy of BGC.

Channelized deposit, mid fan. Photo courtesy of BGC.

[1]ALS courtesy of Squamish Lillooet Regional District.

Site 24: Fountain N

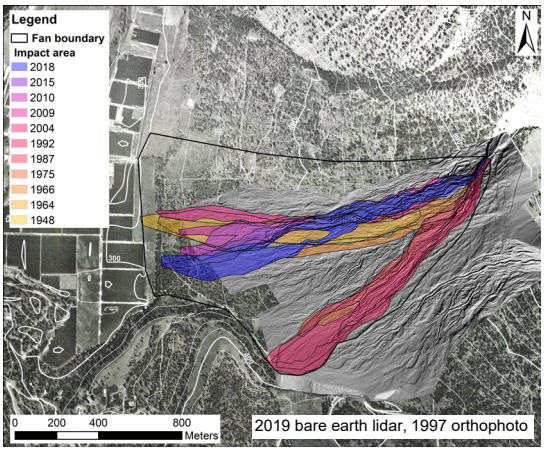

Easting (m)	578798
Northing (m)	5616465
No. impact areas:	12
No. events:	6
Normalizing fan length (m):	1729
Normalizing fan arc-length (m):	1267
Normalizing fan angle (°)	53
Watershed area (km^2):	0.94
Melton ratio:	1.16
Fan area (km^2):	1.25
Fan slope (°):	10.6
Average channel slope (°):	11.4
Fan ERR:	0.30
Normalized intersection point:	0.16
Truncated:	No
Bedrock geology:	Sedimentary

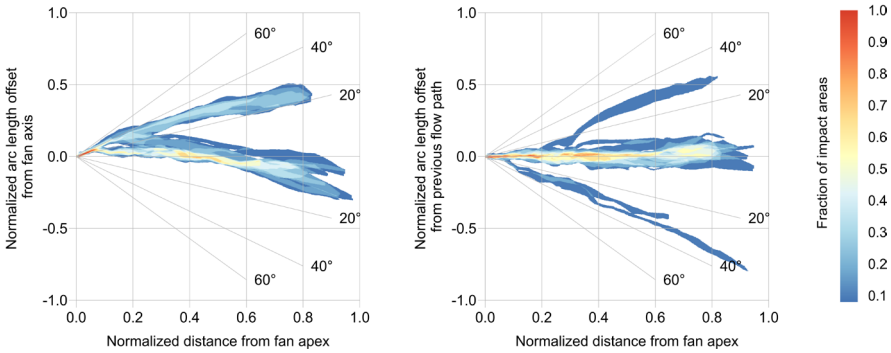

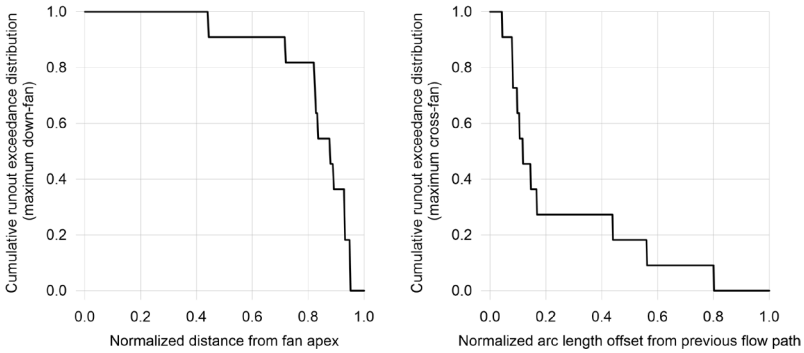

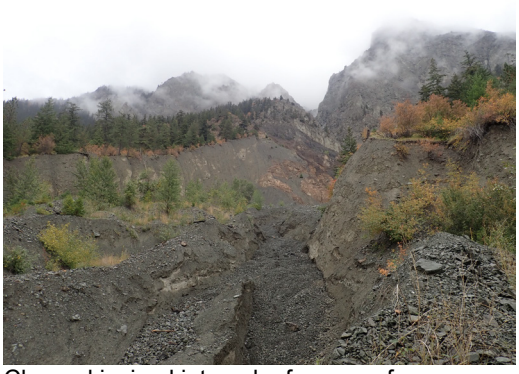

Channel incised into paleofan, near fan apex.

Channelized deposit, mid fan.

Site 25: Fountain S

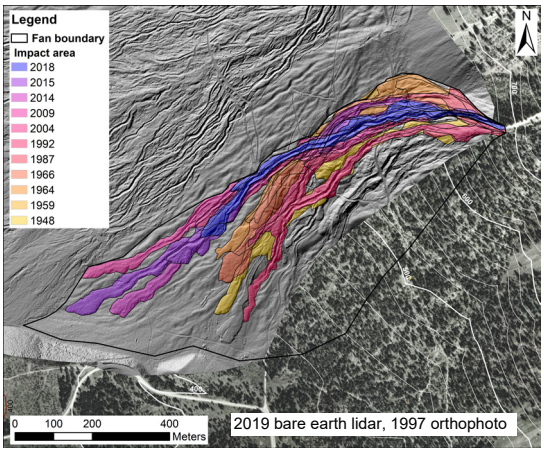

Easting (m)	579160
Northing (m)	5615932
No. impact areas:	11
No. events:	7
Normalizing fan length (m):	1347
Normalizing fan arc-length (m):	494
Normalizing fan angle (°)	41
Watershed area (km^2):	0.35
Melton ratio:	1.74
Fan area (km^2):	0.43
Fan slope (°):	14.3
Average channel slope (°):	12.4
Fan ERR:	0.34
Normalized intersection point:	0.45
Truncated:	No
Bedrock geology:	Sedimentary

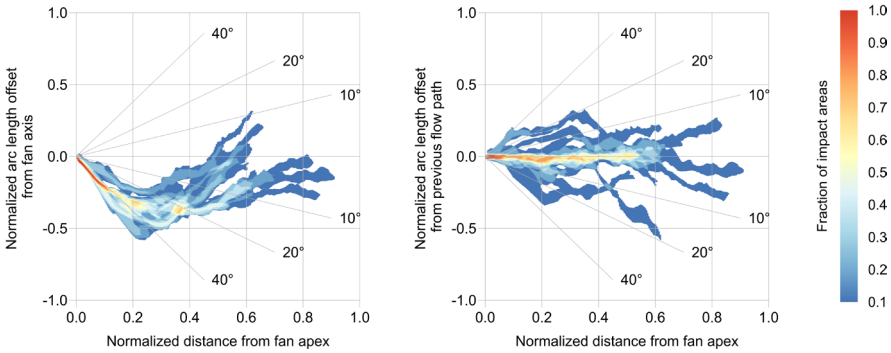

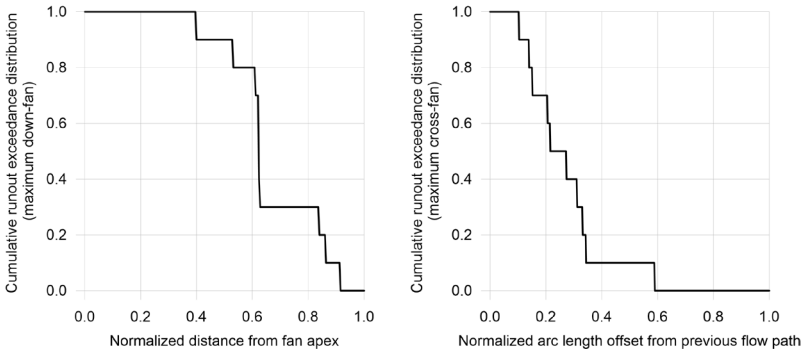

Channelized flow path, mid fan.

Terminal lobe.

Site 26: Cheam W

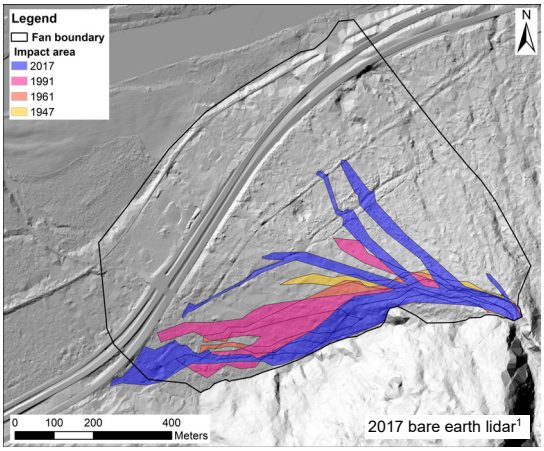

Easting (m)	594952
Northing (m)	5451397
No. impact areas:	4
No. events:	3
Normalizing fan length (m):	1088
Normalizing fan arc-length (m):	1094
Normalizing fan angle (°)	73
Watershed area (km^2):	1.87
Melton ratio:	1.38
Fan area (km^2):	0.63
Fan slope (°):	10.5
Average channel slope (°):	9.4
Fan ERR:	0.28
Normalized intersection point:	0.16
Truncated:	No
Bedrock geology:	Sedimentary

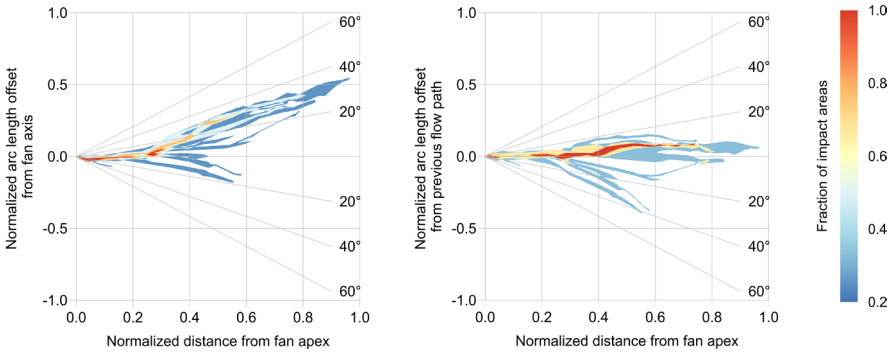

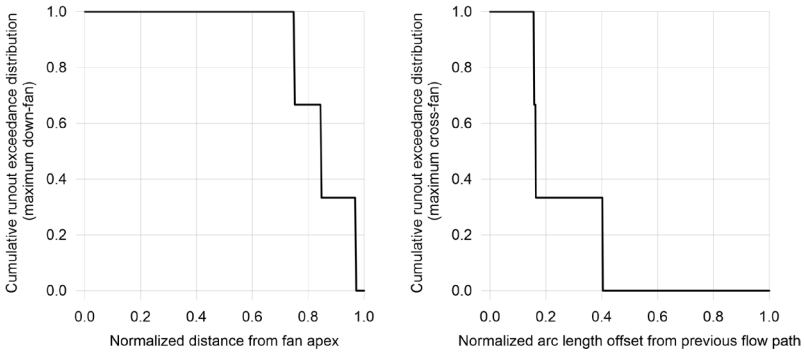

Debris near fan apex, looking upslope.

Recent deposition on lower-mid fan.

[1]ALS courtesy of BC Ministry of Transportation and Infrastructure.

Site 27: Cheam E

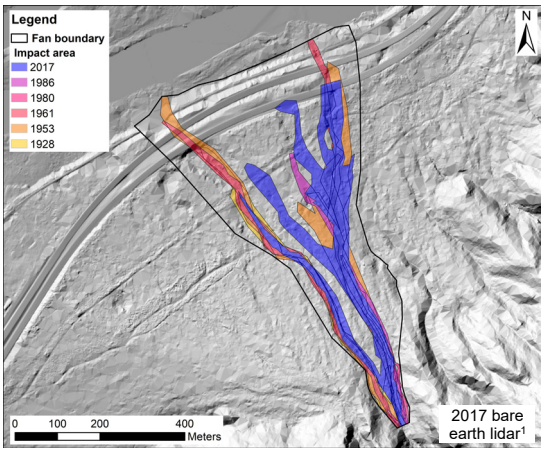

Easting (m)	595063
Northing (m)	5451381
No. impact areas:	6
No. events:	2
Normalizing fan length (m):	962
Normalizing fan arc-length (m):	555
Normalizing fan angle (°)	35
Watershed area (km^2):	2.25
Melton ratio:	1.26
Fan area (km^2):	0.25
Fan slope (°):	11.7
Average channel slope (°):	10.8
Fan ERR:	0.28
Normalized intersection point:	0.97
Truncated:	Yes
Bedrock geology:	Sedimentary

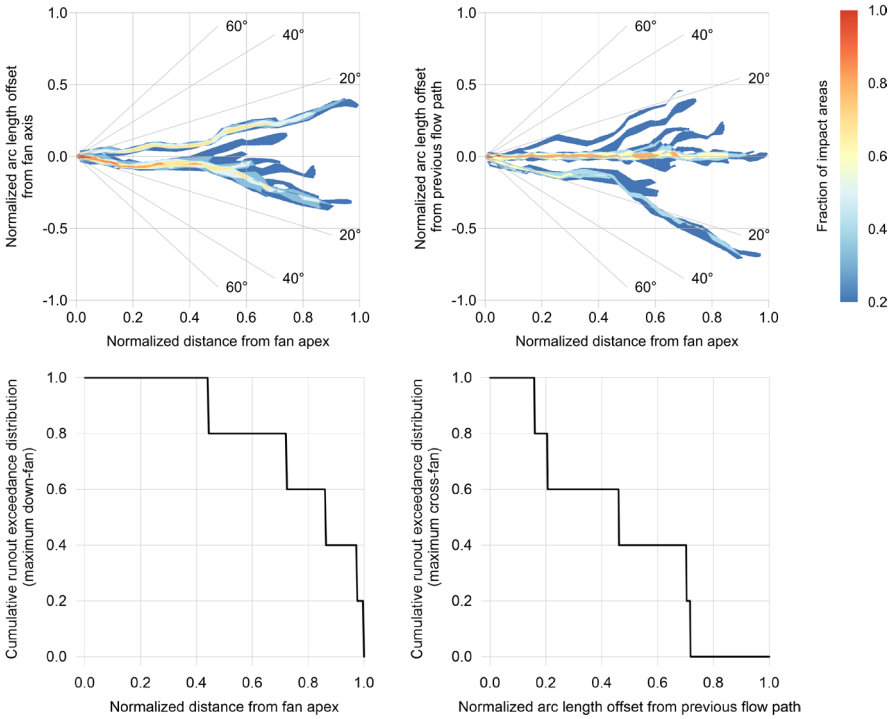

Fan apex.

Active channel, mid fan.

[1]ALS courtesy of BC Ministry of Transportation and Infrastructure.

Site 28: Hope

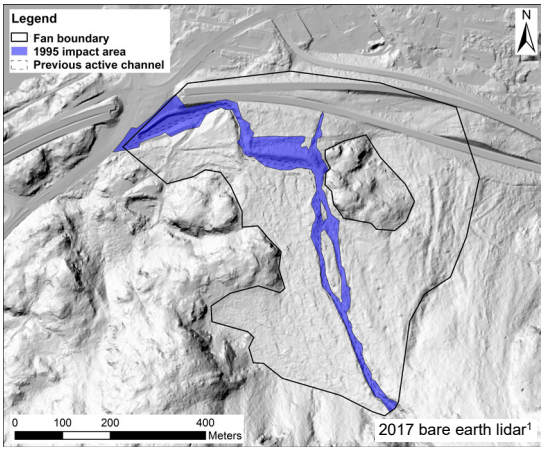

Easting (m)	613674
Northing (m)	5469474
No. impact areas:	1
No. events:	1
Normalizing fan length (m):	810
Normalizing fan arc-length (m):	595
Normalizing fan angle (°)	53
Watershed area (km^2):	0.65
Melton ratio:	1.37
Fan area (km^2):	0.28
Fan slope (°):	16.7
Average channel slope (°):	13.4
Fan ERR:	0.39
Normalized intersection point:	0.82
Truncated:	No
Bedrock geology:	Metamorphic

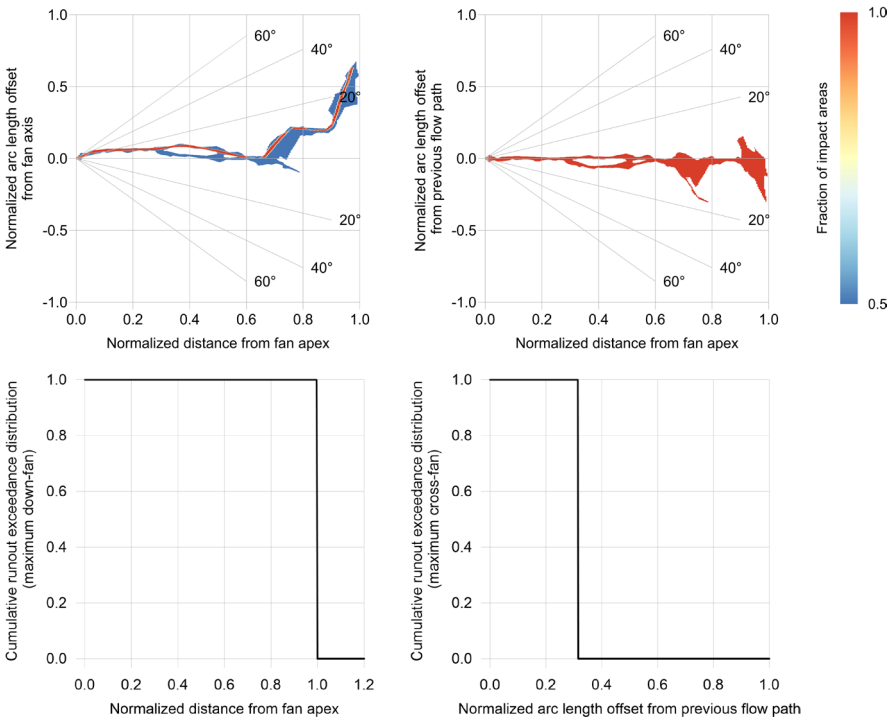

[1]ALS courtesy of BC Ministry of Transportation and Infrastructure.

Site 29: Allard

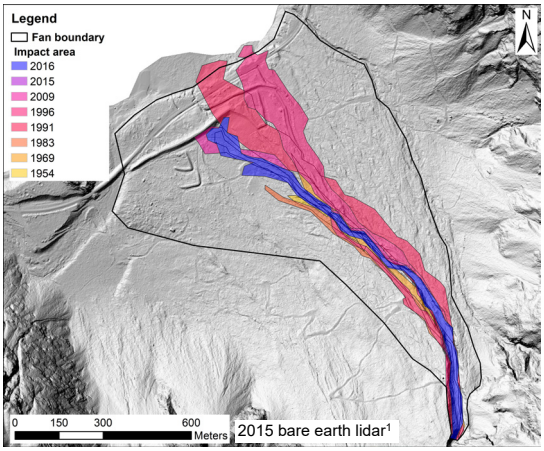

Easting (m)	616587
Northing (m)	5489888
No. impact areas:	8
No. events:	6
Normalizing fan length (m):	1566
Normalizing fan arc-length (m):	988
Normalizing fan angle (°)	43
Watershed area (km^2):	0.65
Melton ratio:	1.12
Fan area (km^2):	0.76
Fan slope (°):	15.5
Average channel slope (°):	12.5
Fan ERR:	0.24
Normalized intersection point:	0.70
Truncated:	Yes
Bedrock geology:	Intrusive

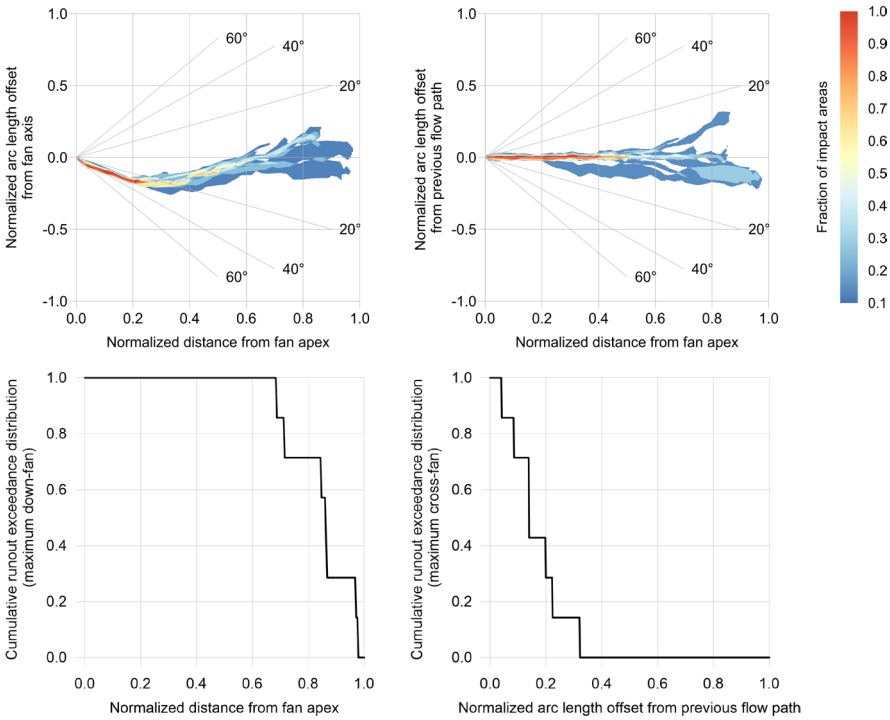

[1]ALS courtesy of Canadian National Railway.

Site 30: Anonymous

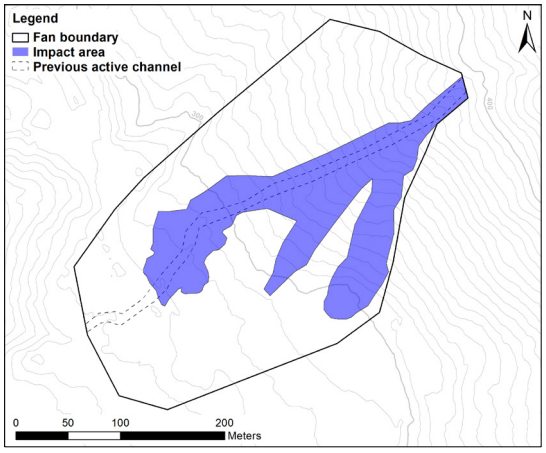

Easting (m)	-
Northing (m)	-
No. impact areas:	1
No. events:	1
Normalizing fan length (m):	445
Normalizing fan arc-length (m):	260
Normalizing fan angle (°)	64
Watershed area (km^2):	0.21
Melton ratio:	1.52
Fan area (km^2):	0.08
Fan slope (°):	14.7
Average channel slope (°):	14.2
Fan ERR:	0.32
Normalized intersection point:	0.52
Truncated:	No
Bedrock geology:	Intrusive

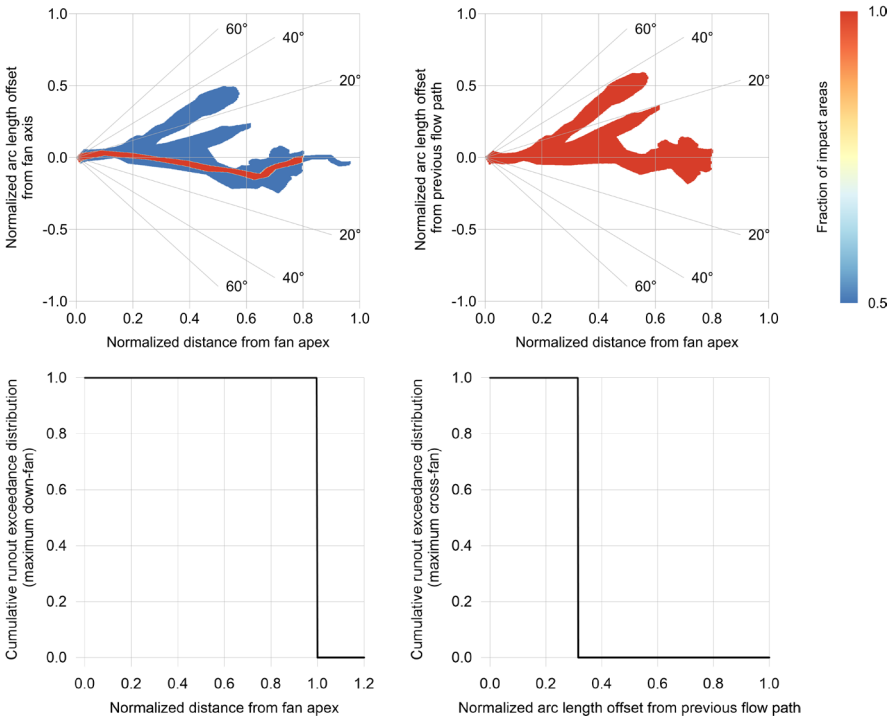

Appendix B

Supplementary Material: GIS Data

GIS data for the SWBC dataset (Anonymous case excluded) have been made available as supplementary material. The files listed below can be found on cIRcle (UBC digital repository) in a .zip file. Shapefiles are projected in the UTM NAD83 Zone 10 coordinate system. Metadata associated with each shapefile are listed below.

1. **apex**. Apex point locations. Metadata: fan ID, fan name, number of impact areas, number of events, number of observation years, observation length (years), normalizing fan radius (m), normalizing fan arc length (m), normalizing fan angle (°), fan area (km^2), overall fan slope (°), average fan channel slope (°), fan elevation relief ratio, normalized fan intersection point, watershed area (km^2), watershed relief (km), Melton ratio, fan truncation, geology (rock class).
2. **fan**. Fan boundary. Metadata: fan ID, fan name.
3. **watershed**. Watershed boundary. Metadata: fan ID, fan name.
4. **impact_areas**. Impact area boundaries. Metadata: fan ID, fan name, impact area ID, year, temporal certainty class, spatial certainty class, avulsion classification, event classification (boolean), impact area (m^2), deposit area (m^2), volume (m^3), volume estimation method, notes.
5. **flow_paths**. Flow path lines associated with each impact area. Metadata: fan ID, fan name, impact area ID.
6. **swbc_data.xls**. Metadata spreadsheet. First tab defines the metadata fields, and the remaining tabs correspond to data for each shapefile listed above.

Appendix C

Supplementary Material: MATLAB code

MATLAB code and example inputs for the workflow described in Section 4.5.1 have been made available as supplementary material. The files listed below can be found on cIRcle (UBC digital repository) in a .zip file.

1. **NERE-DF.m**. MATLAB code for the Normalized Empirical Runout Estimator - Debris Flow.
2. **swbc.grd**, **swbc_smoothed.grd**. Empirical fan-normalized impact area heatmaps (ASCII grid) for the SWBC dataset (raw and smoothed).
3. **apex.shp**, **fan.shp**, **channel.shp**. Example input geometry shapefiles.